Mitochondrial OxPhos:

The integrator of the cellular metabolic status

Ana Victoria Lechuga Vieco

Madrid, 2018



Universidad Autónoma de Madrid
Departamento de Biología Molecular

Universidad Autónoma de Madrid



Programa de Doctorado en Biociencias Moleculares

Tesis doctoral

Mitochondrial OxPhos:
the integrator of the cellular metabolic status

Ana Victoria Lechuga Vieco

Madrid 2018

Facultad de Ciencias

Universidad Autónoma de Madrid

Mitochondrial OxPhos:
The integrator of the cellular metabolic status

Doctorando:

Ana Victoria Lechuga Vieco

Licenciada en Biotecnología

Madrid 2018

Directores de tesis:

José Antonio Enríquez Domínguez

Jesús Ruíz-Cabello

El Dr. José Antonio Enríquez Domínguez , líder del grupo de investigación "Genética Funcional del Sistema de Fosforilación oxidativa" del Centro Nacional de Investigaciones Cardiovasculares (CNIC), y el Dr. Jesús Ruíz-Cabello, líder del grupo "Marcadores Moleculares y Funcionales" del Centro de Investigación Cooperativa en Biomateriales (CIC biomaGUNE)

CERTIFICAN

Que la Tesis Doctoral "*Mitochondrial OxPhos: the integrator of the cellular metabolic status"* ha sido realizada en la Fundación Centro Nacional de Investigaciones Cardiovasculares Carlos III, bajo su tutela, y que reúne las condiciones para optar al grado de Doctor.

Madrid, 2018





Fdo. José Antonio Enríquez

Fdo. Jesús Ruíz-Cabello



Agradecimientos

En primer lugar, quiero dar las gracias a mis directores de tesis, Toño y Jesús, por haberme dado la oportunidad de realizar este trabajo en vuestros grupos. Por todas y cada una de las reflexiones y sugerencias, por confiar en mi trabajo, por respetar mis ideas. Gracias Toño, por enseñarme que siempre hay una pregunta biológica nueva detrás de cada avance y gracias Jesús por involucrarte en cada una de ellas y hacer posible que consiga resolverlas por mí misma. Esta forma de integrar distintas materias es realmente lo que más me ha hecho disfrutar durante esta etapa.

Gracias Ana por la cantidad de conocimientos que me traspasaste. Porque con tu gran trabajo, tus ganas y dedicación hiciste que desde el primer momento estuviera ilusionada con este proyecto. Por hacerme ver desde el comienzo qué tipo de científica quería ser. Porque un trabajo de investigación es siempre fruto de ideas, proyectos y esfuerzos previos, gracias por todos ellos.

Me gustaría, en estas líneas, ser capaz de mostrar el infinito agradecimiento que tengo hacia las personas que con sus ideas, sugerencias y trabajo colectivo han hecho posible esta tesis doctoral. Porque sin ellas se hubieran perdido en el camino muchas de las conclusiones obtenidas.

En especial,

A Fátima, Carlos y Álvaro por todos los análisis realizados y vuestra gran profesionalidad en todo momento. A Jesús y Enrique, por hacer posible el exhaustivo análisis proteómico en nuestros modelos animales.

A Enzo. Gracias por aceptarme en tu grupo aún viniendo de ramas muy diferentes y Anne, por hacer posible toda la gestión. A Uzi, Aditi, Mattu y resto del grupo, por hacerme ver lo subjetiva que puede ser la palabra diferente e integrarme como una más. A Fabio, porque me encantan sus dibujos y esquemas, porque sin conocerlo personalmente puedo decir que es un artista! Y cómo no, gracias Gennaro (sólo esta vez te llamaré boss...), por toda tu ayuda durante los meses en tierras inglesas, por no dejarme sola en mi desastre, por no desesperar en los experimentos interminables y por todas las risas, cervezas y charlas que hicieron mi estancia mucho más llevadera.

A Marisa, por la cantidad de horas que hemos estado intentando entender qué ocurría en esos corazoncitos. Porque la fusión de esas desconocidas mitocondrias para ti y esa desconocida ultraestructura para mí han hecho un todo. Gracias por tu dedicación durante todo este tiempo.

A Andrés y Ángel, por hacernos partícipes de un proyecto apasionante. A Silvia, Demetrio y Francy. A Luis M. , Íñigo y María Dolores. A Juan Pedro y Daniel. A Cristina. ¡Muchísimas gracias por todos los análisis que habéis realizado y prestarme vuestra ayuda cuando la he necesitado!

A Mercedes y Raquel. Porque con vuestro trabajo habéis hecho posible el manejo de este gran número de modelos animales y que el trabajo sea más que riguroso en todas los procedimientos realizados. Gracias también a Antonio, Rubén y a toda la Unidad de Medicina Comparada del CNIC por toda la ayuda recibida y por darnos siempre buenos consejos y explicaciones.

Y agradecer el trabajo realizado por las diferentes Unidades Técnicas del CNIC, en especial a Bioinformática, Proteómica, Microscopía, Celómica, Transgénesis y Genómica, así como a la Unidad de Citometría del Weatherall Institute of Molecular Medicine de la Universidad de Oxford.

A Rebeca, Sara, Conchi, Umut y Fernando. Gracias por compartir vuestros conocimientos y experiencia, por ayudarme cada vez que me he perdido entre mi caos.

A Raquel, Mar, Andrés, Isabel y Clara, porque sin vosotros nada de esto habría podido ser así. Porque habéis dedicado mucho tiempo a hacer que este trabajo sea mucho mejor. Gracias por vuestra paciencia y profesionalidad.

A Rocío, Adela y Elena. Porque sin vosotras todo hubiera sido mucho más difícil. Porque habéis estado muy cerquita siempre y hemos podido compartir de todo…risas, lágrimas, experimentos, caos, resultados y la vida en general. Porque podría hacer una libreta de frases míticas y dejarla de libro de mesilla de noche para no parar de reír en años. Gracias por vuestra ayuda desinteresada, por enseñarme todo lo que vosotras ibais aprendiendo. Gracias por los consejos y gracias por ser como sois. Y porque os vuelvo a incluir junto al resto del equipo, Carol, Álvaro, Yolanda, Raquel, Marta, Maca…porque un café sin vuestras conversaciones, risas, trapicheo de dinero y reflexiones, para mí ya no tiene sentido!

A Kevin, Vanessa, María, Ana y Raquel, quienes con vuestras aportaciones al trabajo lo habéis hecho mucho mejor. Porque aunque soy malísima "jefa" me habéis enseñado otra de las facetas de la ciencia, saber transmitir ideas y compartir conocimientos.

A "esos químicos (y no químicos) de la cuarta" … ¡Gracias! Porque creo que sin ellos no hubiera sabido ver más allá de las "mitocosas". Porque me fascina vuestra forma de trabajar y pensar, y porque ello me ha llevado a saber respirar en los momentos de agobio. Por eso y porque habéis sido los que más conocimientos nuevos me habéis enseñado. A Marina, por ser mi gran maestra en la resonancia, por la implicación con el proyecto y por ser amiga en todo momento. Gracias Arnoldo, por demostrarme cómo la ciencia básica y aplicada van unidas de la mano.

Quería tener unas palabras especiales para las Raqueles: Rachel y Raquel. Quienes han hecho posible que los últimos meses hayan sido más llevaderos. Gracias por ayudarme en cada cosita ó cosaza que he necesitado. Por haber aguantado mis quejas cuando mi modo Zen se iba de paseo. Rachel, vaya gran corazón que tienes! Y Raquel...me ha encantado encontrarme al doble de mi "disaster person" en la etapa final de la tesis, ya sabes que tienes mucho que ver en que estas páginas estén hoy impresas!

No es fácil escribir estas palabras y más cuando han pasado tantas personas por ésta etapa. Espero no dejarme a nadie, y si lo hago, creo que cada uno sabe dónde incluirse dentro de este apartado.

A nivel personal, son muchas las personas que me han acompañado durante toda la vida pero muchas también las que he conocido durante ésta etapa y que de una forma u otra tengo que agradecerles el estar ahí. Porque mente sin corazón no tiene sentido, y vosotros completáis mi círculo.

A mi club del café, porque aunque ya os he mencionado anteriormente, creo que me llevo de esta etapa mucho más que compañeros, me llevo amigos con los que espero poder compartir muchas más experiencias!

Y de pura casualidad…os conocí! gracias a todos mis inmunólogos, biofísicos y bioquímicos de Oxford. Experiencia enriquecedora gracias a la cual me siento más segura de mi misma, porque me habéis hecho ver que teniendo enfrente a las personas adecuadas, no existe limitación de entendimiento alguna. En especial, gracias Falk, por leer y releer más de doscientas páginas una y otra vez, porque tus ganas de ayudar superan todo, porque eres de las mejores personas que te puedes encontrar en el camino.

A mis AJF….esas siglas que tan poco dicen para unos cuantos y que tanto significan para mí. Bea, Almu, David, Tere, Choni, Inma, Mayte, Sandra...GRACIAS! Y junto a ellos, el resto de Biotecs, porque a vuestro lado me he formado como científica y lo que es más importante, como persona (ó personaja). Juntos comenzamos a dar los primeros pasitos en la ciencia…quién nos lo iba a decir! Porque de la complejidad sale la armonía, y es increíble que personas tan distintas a la vez seamos tan iguales. Porque durante estos años cada vez que os he visto me habéis dado fuerza y risas suficientes para poder sobrevivir varios meses sin vosotros!

A los Viecos nerviosos y Lechugas relajados. Porque siempre he creído en los uno de cal y otro de arena para avanzar y aprender de cada circunstancia. Porque siempre encontramos un buen motivo de reunión y compartir vivencias, porque en la distancia se os echa mucho de menos. Y a mi nueva familia bejarana, quien me ha acogido y dado todo el cariño, motivación, risas, jamón y vino necesario para afrontar cada situación difícil. Gracias a todos, familia.

A mi hermana y a mis padres, esas personas que han apoyado cada decisión que he tomado, que sólo han tenido palabras bonitas cada vez que me he tropezado. Por no haberme negado nunca una sonrisa a pesar de mi pesimismo en algunos momentos. Gracias por las oportunidades que me habéis dado sólo para hacerme feliz. Por todo lo que he aprendido de vosotros, el tesón y la paciencia para acabar siempre lo que se empieza.

Al doble de mi mitad, a mi compañero, a mi amigo. Porque contigo lo empecé y más que contigo lo he acabado. No hay palabras para ti que puedan agradecer que hayas estado a mi lado en cada decisión, sonrisa, lágrima, discusión, experimento y en cada pase de tarjetas por el torno. Porque entrar contigo y salir contigo me ha hecho inmensamente feliz. Porque compartir es vivir y he tenido la suerte de poder compartir contigo absoluta y literalmente TODO.

Me gustaría acabar estas páginas con una dedicatoria especial hacia las personas que desde que era pequeña han querido que siempre arriesgara, que siempre indagara, que nunca pusieron límites a mi curiosidad, mis abuelos. A mi abuela, por llevar muy marcado el gen de la alegría y compromiso, de la vitalidad y de la perspicacia. Y, como no, a uno de mis referentes, quien me enseñó que el saber nunca ocupa lugar y quién siempre estuvo orgulloso de cada pasito que he dado. Gracias por hacerme ver desde que no tenía sentido de la razón...que siempre hay una razón para todo, y que hay que buscarla para ser feliz. A la persona más constante, tenaz e inteligente que he conocido nunca. Te quiero, abuelo.



Resumen

El sistema de fosforilación oxidativa (OXPHOS) es el único sistema en la célula animal cuyos componentes están codificados en dos genomas, el ADN mitocondrial (mtDNA) y el ADN nuclear (nDNA). El mtDNA es poliploide, de herencia materna y carece de un sistema de recombinación durante su replicación, cuyas consecuencias son una tasa de mutación un orden de magnitud mayor que el nDNA y el origen de diversos haplotipos mitocondriales. Las proteínas del sistema OXPHOS que son codificadas en el nDNA presentan opciones alternativas debido a las variantes alélicas y las variantes específicas de tejido. Es por ello que se pueden dar diversas combinaciones de nDNA y mtDNA en el mismo individuo. Esta asimetría podría provocar un desajuste entre componentes del sistema: las proteínas codificadas en el mtDNA tienen que interaccionar físicamente con las proteínas codificadas en el nDNA para formar los complejos respiratorios. Por otro lado, todas las copias de mtDNA de una misma célula son idénticas, situación llamada homoplasmia. La heteroplasmia es el término utilizado para referirnos a la coexistencia de más de un tipo de mtDNA en el mismo citoplasma celular. En la actualidad, aún quedan cuestiones por resolver: (i) ¿Son intercambiables los distintos haplotipos de mtDNA sin provocar ningún impacto funcional o fenotípico en el individuo? (ii) ¿Presenta la generación artificial de heteroplasmia un conflicto genómico capaz de provocar riesgos para la salud de los individuos? Durante el desarrollo de esta Tesis Doctoral se han estudiado (i) cómo las modificaciones en genes nucleares relacionados con la función mitocondrial impactan en la fisiología del individuo bajo la presencia de genomas mitocondriales alternativos, (ii) cómo la coexistencia de dos variantes de mtDNA en el mismo citoplasma celular afecta al metabolismo y (iii) la identificación de posibles mecanismos relacionados con esta regulación. Para responder estas preguntas se han utilizado modelos de ratones conplásticos (idéntico nDNA y dos variantes de mtDNA no patológicas intercambiables, C57 y NZB) y ratones heteteroplásmicos (coexistencia de ambas variantes de mtDNA en la misma célula).

La caracterización de los modelos animales conplásticos se ha llevado a cabo desde el desarrollo embrionario hasta la muerte natural de los mismos a través de diversas metodologías ómicas, análisis bioquímicos y diversos estudios fenotípicos. Se ha observado que los distintos haplotipos de mtDNA influyen en la producción de especies reactivas de oxígeno y en la homeostasis celular. Nuestros recientes análisis confirman que: (1) las variantes de mtDNA inducen diferencias en el sistema OXPHOS bajo un mismo contexto nuclear; (2) hay un proceso de adaptación celular que modula el rendimiento OXPHOS para mantener la salud del individuo a pesar del desajuste entre nDNA/mtDNA; (3) la sensibilidad frente a ese desajuste entre genomas es dependiente del tipo celular y (4), las diferencias en el ajuste nDNA/mtDNA dan lugar a alteraciones metabólicas, manifestadas en el animal adulto y que impactan dramáticamente en el proceso de envejecimiento.

En la naturaleza, la heteroplasmia es activamente combatida por diversos mecanismos, como es el caso de la degradación del mtDNA paterno tras la fertilización del ovocito o la existencia de un cuello de botella genético en el desarrollo del mismo. La condición de heteroplasmia puede generarse de forma natural durante la replicación del mtDNA por mutagénesis, pero también puede ser originada por nuevas tecnologías médicas. Entre ellas, cabe destacar aquellas empleadas para (i) la prevención de la transmisión de enfermedades mitocondriales, (ii) la mejora de la fertilidad a través de un rejuvenecimiento de ovocitos humanos y (iii) la recuperación de la función mitocondrial en células dañadas mediante la transferencia de mitocondrias exógenas. A lo largo de este trabajo se ha demostrado que la heteroplasmia puede modular la viabilidad y el metabolismo de las células embrionarias y del individuo adulto. En el período postnatal del individuo, la mayoría de los tejidos combaten la heteroplasmia eliminando y/o seleccionado una de las variantes de mtDNA, preservando de esta forma la función tisular. A pesar de ello, existen tejidos incapaces de eliminar la heteroplasmia, como es el caso del corazón, del pulmón o del músculo esquelético. Estos tejidos están sometidos a un estrés metabólico progresivo seguido de un fenotipo patológico en el animal adulto que incluye daño cardiopulmonar, pérdida de músculo esquelético, fragilidad y muerte temprana en el individuo.



Summary

The oxidative phosphorylation (OXPHOS) system is the only process in animal cells with components encoded by two genomes, mitochondrial DNA (mtDNA) and nuclear DNA (nDNA). MtDNA is polyploid, maternally inherited, suffers marginal recombination and has a rate of mutation which is one order of magnitude higher than nDNA, thus resulting in high variability of healthy mtDNA haplotypes. Nuclear OXPHOS genes present lower mutation rate and recombination. However they have alternative options due to allele variants and tissue-specific variants, which confront identical nDNA with diverse mtDNA within the same individual. This asymmetry leads to the physical match constraint: the fact that mtDNA-encoded proteins have to physically assemble with the nuclear-encoded ones to build the respiratory complexes.

All mtDNAs of a given cell are essentially identical, a situation termed homoplasmy. Heteroplasmy refers to the presence of more than one variant of mtDNA co-existing in the same cytoplasm. Two major interconnected questions remain to be solved: (i) are different versions of wild-type mtDNAs interchangeable without any phenotypic impact? And, (ii) does the iatrogenic introduction of heteroplasmy result in health risks for the offspring by triggering a genomic conflict between alternative mtDNA variants with potential negative consequences? We intend to understand the long-term consequences of mtDNA/nDNA mismatch and heteroplasmy. In particular, (i) whether or not modifications in key nuclear genes involved in mitochondrial function modulate the impact of alternative mtDNAs, (ii) whether or not the co-existence of two wild-type mtDNAs in the same cytoplasm impacts on metabolism, and (iii) the identification of the signals involved in regulation. To address these questions, we use conplastic mice (identical nucleus but interchanged mtDNAs, C57 and NZB non-pathological variants) and heteroplasmic mice (co-existence of both mtDNAs in the same cell).

Here, we systematically characterised conplastic mice throughout embryo development and during their lifespan through omics techniques and physiological and phenotyping studies. We report that the mtDNA haplotype profoundly influences the reactive oxygen species generation, energy homeostasis, metabolism and ageing parameters among others, resulting in different healthy longevities of conplastic strains. Our recent analysis supports: (1) mtDNA variants induce functional OXPHOS differences under the same nuclear background. (2) Cells can adapt their OXPHOS performance to generate healthy animals, regardless the nDNA/mtDNA match. (3) Different cell types show specific sensitivity to the nDNA/mtDNA match. (4) Changes in the nDNA/mtDNA match induce significant metabolic differences that are manifested in the adulthood and which dramatically impact on ageing and longevity.

Heteroplasmy is actively combated by several mechanisms, including the degradation of the paternal mtDNA upon fertilization, and the existence of a genetic mtDNA bottleneck in oocyte development. Heteroplasmy can be naturally generated by mutagenesis during mtDNA replication, but also can originate from novel medical technologies aiming (i) to prevent the transmission of mtDNA-linked diseases, (ii) to improve the fertility by human oocyte “rejuvenation”, and (iii) to restore the function of damaged cells using the transfer of foreign mitochondria. Here we show that mtDNA heteroplasmy modulates the viability and metabolism of embryonic cells, as well as their ability to become iPS. During post-natal life, most of the tissues can remove the remaining heteroplasmy and preserve life-long fitness. In contrast, critical tissues like cardiac and skeletal muscles as well as the lung maintain heteroplasmy and suffer a progressive metabolic stress leading to a severe adult pathologies, including cardiopulmonary failure, skeletal muscle wasting, frailty and premature death.



INDEX

INDEX

I. ABBREVIATIONS 21
II. INTRODUCTION 33

II.1. MITOCHONDRIAL STRUCTURE AND COMPARTMENTALIZATION 33

II.1.A. Functional morphology of the mitochondria 34

II.1.B. Mitochondria as signalling organelles 36

II.1.C. Reactive Oxygen Species: from physiology to pathology 36

II.1.D. Mitochondrial quality control 37

II.1.D.1. Mitochondrial unfolded protein response (mtUPR) 37
II.1.D.2. Translation attenuation process 38
II.1.D.3. Autophagy and Mitophagy 38

II.1.E. MtDNA and mitochondrial performance under stress conditions 38

II.1.E.1. Mitochondria and ageing 38
II.1.E.2. Mitochondria in lung pathophysiology 39

II.2. OXPHOS SYSTEM AS A UNIQUE FUNCTIONAL STRUCTURE 41

II.2.A. MtETC versatility and superassembly of mitochondrial respiratory complexes 42

II.3. OXPHOS SYSTEM: FUNCTIONAL INTEGRATION OF TWO GENOMES 43

II.3.A. Mitochondrial DNA particularities 45

II.3.B. MtDNA variability 45

II.3.C. The MitMatch paradox 47

II.3.D. Effects of simultaneous alternative combination of mtDNAs within the same cell. 48

II.3.E. Heteroplasmy: from natural to artificial generation 48

II.3.F. Mitochondrial DNA segregation 48

II.3.F.1. Segregation of genetically different mtDNA haplotypes 49
II.3.F.2. Impact of nuclear genes in mtDNA segregation 49

II.3.G. Heteroplasmy between mtDNA variants: evolutionary, physiological, pathological and ethical implications 50

II.3.H. Addressing the inheritance of mtDNA diseases 50

II.3.H.1. Classical approaches. 50
II.3.H.2. Modern strategies 51

III. OBJECTIVES 55
IV. MATERIALS AND METHODS 59

IV.1. CELL CULTURE PROCEDURES 59

IV.1.A. Cell line generation and cell culture conditions 59

IV.1.A.1. Mouse Adult Fibroblasts (MAFs) 59
IV.1.A.2. Mouse Embryonic Fibroblasts (MEFs) 59

IV.1.B. Growth curves 60

IV.2. CELLOMICS TECHNIQUES: FLOW CYTOMETRY AND CELL SORTING 60

IV.2.A. Reactive Oxygen Species (ROS) and Mitochondrial Membrane Potential (MMP) analysis 60

IV.2.B. Mitochondrial content assay 61

IV.2.C. Cardiac tissue inflammation assessment 61

IV.3. ANIMAL HANDLING PROCEDURES 62

IV.3.A. Experimental Mouse Models. 62

IV.3.A.1. Generation and breeding of Conplastic Mice 62
IV.3.A.2. Heteroplasmic Mice generation 62

IV.3.A.2.a. C57BL/6JOlaHsd and NZB/OlaHsd zygotes 62

IV.3.A.2.b. Generation of NZB/OlaHsd cytoplasts 63

IV.3.A.2.c. Production of "C57BL/6JOlaHsd zygote-NZB/OlaHsd cytoplast" couples 64

IV.3.A.2.d. Electrofusion of "C57BL/6JOlaHsd zygote-NZB/OlaHsd cytoplast" couples: Production of C57BL/6-mtC57+NZB zygotes 64

IV.3.A.2.e. Heteroplasmic mouse strains nomenclature 65

IV.3.A.3. Maintenance of heteroplasmic colonies 65
IV.3.A.4. Genetic modifications in heteroplasmic mice 65

IV.3.B. In vivo modulation of the mtDNA segregation 65

IV.3.C. Mouse embryo collection 65

IV.3.D. Growth curve analyses in mice 66

IV.3.E. Survival studies 66

IV.3.F. Blood and plasma analysis 66

IV.3.F.1. Haematology 66
IV.3.F.2. Biochemical profile 66

IV.3.G. Haematopoietic stem cell (HSC) analysis 66

IV.3.H. Adult cardiomyocyte isolation 66

IV.3.I. Chronic MitoQ administration in mice 67

IV.3.J. Histological Assays 67

IV.3.J.1. Cardiac tissue analyses 67
IV.3.J.2. Analysis of the ovary 68
IV.3.J.3. Morphometric analyses of retinal sections 68
IV.3.J.4. Superoxide levels in frozen tissues: DHE Staining 68
IV.3.J.5. Evans Blue assay 68
IV.3.J.6. Histological analysis of brain sections 68

IV.3.K. 3MC-Induced fibrosarcomas 69

IV.3.L. Partial hepactectomy 69

IV.3.M. Astrocytes and neurons isolation 69

IV.3.N. Mice immunization 69

IV.3.O. Assessment of heteroplasmy in T cell populations 69

IV.3.P. $CD8^+$ T cells isolation and in vitro activation 70

IV.3.Q. Intraventricular pressure measurement 70

IV.3.R. Gasometry analysis 71

IV.3.S. Glucose and insulin tolerance test 71

IV.3.T. In vivo ROS assessment 71

IV.4. HIGH-THROUGHPUT SCREENINGS: OMICS TECHNIQUES 71

IV.4.A. Transcriptomic assays 71

IV.4.A.1. RNA-seq 72
IV.4.A.2. Transcriptomic and bioinformatic analysis. 72

IV.4.B. Proteomic techniques *73*

IV.4.B.1. Quantitative proteomics 73
IV.4.B.2. PTMs analysis 73

IV.4.C. Metabolomic analysis *74*

IV.5. *IN VIVO* IMAGING TECHNIQUES. 75

IV.5.A. Magnetic resonance imaging (MRI) *75*

IV.5.A.1. Cardiac magnetic resonance imaging (CMR) 75
IV.5.A.2. MRI analysis of brain anatomy and tumour progression 76

IV.5.B. Magnetic resonance spectroscopy (MRS) *76*

IV.5.B.1. 31P/1H Magnetic resonance spectroscopy (31P/1H-MRS). 76

IV.5.C. PET/CT imaging *76*

IV.5.C.1. Molecular Imaging probes: Biodistribution and uptake 77
IV.5.C.2. *Ex vivo* biodistribution analysis 77
IV.5.C.3. MicroCT analyses 77

IV.5.D. Mouse transthoracic echocardiography *78*

IV.6. MOLECULAR BIOLOGY TECHNIQUES 78

IV.6.A. nDNA and mtDNA genotyping *78*

IV.6.A.1. DNA extraction and PCR 78
IV.6.A.2. DNA digestion, gel electrophoresis and heteroplasmy quantification 79

IV.6.B. In vivo modulation of mtDNA segregation *79*

IV.6.B.1. Nnt genotyping 79
IV.6.B.2. Scaf1 genotyping 80

IV.6.C. Mitochondrial Characterization *80*

IV.6.C.1. Mitochondrial Isolation 80
IV.6.C.1.a. Mitochondrial isolation from tissues *80*
IV.6.C.1.b. Mitochondrial isolation from cell lines *80*
IV.6.C.2. ATP synthesis 80
IV.6.C.3. Seahorse analysis 81

IV.6.C.4. Citrate synthase activity 81

IV.6.D. Protein analysis *82*

IV.6.D.1. Total protein cell extraction 82
IV.6.D.2. Protein quantification 82
IV.6.D.3. Gel electrophoresis 82
IV.6.D.4. Western Blot 83

IV.6.E. Transmission electron microscopy *85*

IV.6.F. Immunohistochemistry and Immunocytochemistry *85*

IV.6.F.1. *In situ* mitochondrial DNA detection 86

IV.7. STATISTICAL ANALYSIS 87

IV.7.A. Statistical analysis of heteroplasmy by mathematical modelling *88*

IV.7.B. Experimental statistical analysis. *88*

V.RESULTS AND DISCUSSION 91

V.1. RESULTS I: MITOCHONDRIAL AND NUCLEAR DNA MATCHING SHAPES METABOLISM AND HEALTHY AGEING 91

V.1.A. Previous results *91*

V.1.A.1. Conplastic mice model generation 91
V.1.A.2. Phenotypic variations in conplastic strains 92

V.1.A.2.a. Metabolic consequences *92*

V.1.A.2.b. Ageing phenotype *92*

V.1.B. Match between mitochondrial DNA and nuclear DNA *94*

V.1.B.1. Different mtDNA variants promote *in vivo* metabolic consequences 94
V.1.B.2. Cardiac and liver ultrastructural features 95

V.1.C. nDNA/mtDNA mismatch triggers a cellular adaptive response *97*

V.1.C.1. Role of Reactive Oxygen Species 97
V.1.C.2. Role of the mitochondrial unfolded protein response 98

V.1.D. Phenotypic differences: mtDNA variants modulate healthy ageing and lifespan ... *99*

V.1.E. Discussion *101*

V.2. RESULTS II: PHYSIOLOGICAL IMPLICATIONS OF HETEROPLASMY BETWEEN MTDNA HAPLOTYPES. 103

V.2.A. Previous Results *104*

V.2.A.1. Germline mtDNA selection 104
V.2.A.2. MtDNA competition at early embryonic stages 105
V.2.A.3. Embryonic mtDNA segregation is associated with pluripotency 105
V.2.A.4. Heteroplasmy is rejected in most of the tissues 105

V.2.B. MtDNA segregation in embryonic stage, fertility and ovarian ageing *106*

V.2.B.1. Variations in OXPHOS function influence mtDNA haplotype segregation 108
V.2.B.2. Heteroplasmy modulates embryonic cell metabolism 108

V.2.C. Heteroplasmic and homoplasmic animals are physiologically different *111*

V.2.D. Heteroplasmy, post-natal segregation and tissue performance *113*

V.2.D.1. Evaluation of OXPHOS function in post-natal segregation: *in vitro* mouse adult fibroblast analysis 113
V.2.D.2. Stable heteroplasmy impairs mitochondrial function and compromises tissue health 116
V.2.D.3. Cardiac tissue analysis in heteroplasmic mice 116

V.2.D.3.a. Biochemical profile and evaluation of heart anatomical features and ultrastructure *117*

V.2.D.3.b. Mitochondrial dynamics, OXPHOS performance and mtUPR assessment *120*

V.2.D.3.c. The presence of heteroplasmy at any level induces a defined cellular status *123*

V.2.D.3.d. Proteomic analysis determines why ATP production is decreased in heteroplasmic hearts *126*

V.2.D.3.e. Cardiac function assessment in heteroplasmic mice *127*

V.2.D.4. How non-pathological variants of mtDNA can affect pulmonary function 129
V.2.D.5. All tissues with stable heteroplasmy develop dysfunctional mitocondria 138

V.2.D.5.a. MtDNA heteroplasmy induces skeletal muscle degeneration with ageing *139*

V.2.D.5.b. Heteroplasmy induces structural and functional abnormalities in the eye *141*

V.2.E. Elucidating a new mechanistic model: why heteroplasmy is harmful in tissues that do not resolve it? *142*

V.2.F. Discussion *146*

V.3. RESULTS III: CROSSTALK BETWEEN MTDNA AND NDNA IN HEALTH, AGEING AND DISEASE 149

V.3.A. Elucidating the driving force of mitochondrial DNA segregation *149*

V.3.A.1. Nuclear control of mitochondrial DNA segregation 149

V.3.A.2. Previous results 149
V.3.A.3. Somatic mtDNA segregation and mitochondrial dynamics, redox balance and OXPHOS function....151
V.3.A.3.a. Effects of mitochondrial dynamics....151
V.3.A.3.b. Effects of cellular metabolism optimization....151
V.3.A.3.c. Effects of ROS detoxification in heteroplasmy....151
V.3.A.4. Generation of new heteroplasmic animal models 152
V.3.A.5. MtDNA haplotype preference in germline and embryo development 153
V.3.A.6. Post-natal analysis of selective mtDNA segregation in tissues 154
V.3.A.6.a. Effects of NNT mutation in post-natal mtDNA segregation....154
V.3.A.6.b. Effects of SC reorganization in post-natal mtDNA segregation....156
V.3.A.6.c. OMA1 does not have significant impact on the mtDNA segregation behaviour....157
V.3.A.7. Phenotypic and metabolic consequences of nuclear gene modifications....158
V.3.A.7.a. Assessment of metabolic performance and mitochondrial characterization in mouse adult fibroblasts....158
V.3.A.7.b. Study of cardiac and mitochondrial ultrastructure in genetically modified heteroplasmic mice....162
V.3.A.7.c. Analysis of mitochondrial performance....163
V.3.A.7.d. Impact on whole animal physiology....164
V.3.A.7.e. Lifelong consequences of nuclear gene modifications in heteroplasmic mice....167
V.3.A.8. Modulation of the cellular status by activation of physiological processes 168
V.3.A.8.a. MtDNA segregation in liver regeneration process....168
V.3.A.8.b. Tumour development....168
V.3.A.8.c. T cell activation in immune responses....169
V.3.A.8.d. Metabolic coupling between neurons and astrocytes....171
V.3.A.8.e. Analysis of mtDNA segregation in brain cell populations....172
V.3.A.8.f. Functional analysis of brain in heteroplasmic mice....173
V.3.B. Discussion 177
VI. CONCLUSIONS 179
VII. BIBLIOGRAPHY 183



Abbreviations

I. Abbreviations

ΔΨm:	mitochondrial membrane potential
Δp:	proton-motive force
[^{18}F]-FDG:	[^{18}F]-Fluorodeoxyglucose
[^{18}F]-FMISO:	[^{18}F]- Fluoromisonidazole
3-MC:	3-methylcholanthrene
AA:	antymicin A
Aa:	amino acid
ACO1:	cytoplasmic aconitate hydratase
ACO2:	mitochondrial aconitate hydratase
ADP:	adenosine diphosphate
AECs:	alveolar epithelial cells
AMP:	adenosine monophosphate
AMPK:	AMP-activated protein kinase
AMU:	atomic mass unit
amUPR:	unfolded protein response activated by misstargeted proteins
ANT:	adenine nucleotide translocator (ADP/ATP translocase)
ATP:	adenosine triphosphate
BAT:	brown adipose tissue
BEC:	bioenergetic Celullar (Index)
BNE:	blue native electrophoresis
Bp:	base pair
BSA:	bovine serum albumin
CI:	complex I

CII: complex II

CII: complex III

CIV: complex IV

CV: complex V

Ca^{2+}: calcium ions

CA1: *Cornu Ammonis*

CK: creatin kinase

CNS: central nervous system

CRD: cysteine-rich domain

CRP: C-reactive protein

CS: citrate synthase

CO: cardiac output

CoQ: coenzyme Q

COX: cytochrome c oxidase

Cyt c: cytochrome C

Cyt b: cytochrome B

DAPI: 4’,6-diamidine-2’-phenylindole

DCA: dichloroacetate

DEG: differential expressed genes

DHE: dehydroethidium

DM: Descemet’s membrane

DMEM: Dulbecco’s Modified Eagle’s Medium

DNA: deoxyribonucleic acid

MtDNA: mitochondrial DNA

nDNA: nuclear DNA

dNTP: deoxynucleotide triphosphate

DNTB: 5,5′-dithiobis (2-nitrobenzoic) acid

Dpc: days post coitum

DRP1: dynamin related protein 1

ECAR: extracellular acidification rate

EDTA: ethylenediaminetetraacetic acid

EF: ejection fraction

EFS: electrofusion solution

ER: endoplasmic reticulum

EtBr: ethidium bromide

F1: first filial generation

F2: second filial generation

FAD: flavin adenine dinucleotide

FAO: fatty acid oxidation

FAS: saturated fatty acids

FBS: fetal bovine serum

FCCP: carbonyl cyanide-4 (trifluoromethoxy) phenylhydrazone

FDR: false discovery rate

FISH: fluorescence *in situ* hybridization

Fw: forward

GABA: gamma-aminobutyric acid

GAPDH: glyceraldehyde-3-phosphate dehydrogenase

GC-MS: gas chromatography–mass spectrometry

GFAP: glial fibrillary acidic protein

GSEA: gene set enrichment analysis

GTP: guanosine triphosphate

GTT: glucose tolerance test

GO: glucose oxidation

GO: gene ontology

H: heteroplasmy

H_0: heteroplasmy in reference tissue

H^+: proton

H_20_2: hydrogen peroxide

HE: haematoxylin and eosin

HFD: high fat diet

HK: hexokinase

HSCs: haematopoietic stem cells

LT-HSCs: long- term HSCs

HSP: heat shock protein

HTC: haematocrit

HPV: hypoxic pulmonary vasoconstriction

IBA1: ionized calcium binding adaptor molecule 1

ID: injected dose

ILDs: interstitial lung diseases

IMF: intermyofibrillar mitochondria

IMJ: inter-mitochondrial junctions

IMM: inner mitochondrial membrane

IPA: ingenuity pathway analysis

IPF: idiopathic pulmonary fibrosis

ITT: insulin tolerance test

IVS: intraventricular septum

KO: knockout

KS: Kolmogorov-Smirnov test

LC-MS: liquid chromatography–mass spectrometry

LDH: lactate dehydrogenase

LOHN: Leber hereditary optic neuropathy

LV: left ventricle

MAF: mouse adult fibroblast

MAMs: mitochondria-associated endoplasmic reticulum membranes

MBq: megabecquerel

MEF: mouse embryonic fibroblast

MELAS: mitochondrial encephalomyopathy, lactic acidosis and stroke-like episodes

MICOS: mitochondrial contact site and cristae organizing system

MMP: mitochondrial membrane potential

MRI: magnetic resonance imaging

MRS: magnetic resonance spectroscopy

- ^{1}H-MRS: proton magnetic resonance spectroscopy
- ^{31}P MRS: phosphorus magnetic resonance spectroscopy
- ^{13}C MRS: carbon magnetic resonance spectroscopy

MSEA: metabolite set enrichment analysis

MS/MS: tandem mass spectrometry

MSR: mitochondrial stress response

Mt: mitochondria

MtDg: mitochondrial degradome

MtETC: mitochondrial electron transport chain

mtROS: mitochondrial reactive oxygen species

MRR: maximum respiration rate

mtUPR: mitochondrial unfolded protein response

MUFAs: monounsaturated fatty acids

NAC: N-Acetyl-L-Cysteine

NAD^+: nicotinamide adenine dinucleotide

NAO: N-nonyl acridine orange

NIR: near-infrared

NLS: nuclear localization sequence

NNT: nicotinamide nucleotide transhydrogenase

NSCs: neural stem/progenitor cells

O_2^-: superoxide anion

OAA: oxalacetic acid

OCR: oxygen consumption rate

OMM: outer mitochondrial membrane

ONL: outer nuclear layer

OXPHOS: oxidative phosphorylation

PAMPs: pathogen associated molecular patterns

PAH: pulmonary arterial hypertension

PBS: phosphate buffered saline

PC: primary cytoplast

PCA: principal component analysis

PCR: polymerase chain reaction

PCr: phosphocreatine

PGD: pre-implantation genetic diagnosis

PDH: pyruvate dehydrogenase

PDK: pyruvate dehydrogenase kinase

PET/CT: positron emission tomography and computed tomography

PH: pulmonary hypertension

Phb: prohibitin subunits

PHx: partial hepatectomy

Pi: inorganic phosphorus

PLS-DA: partial least squares-discriminant analysis

$pC0_2$: partial pressure of carbon dioxide

pO2: partial pressure of oxygen

POLG: mtDNA polymerase-γ

POLRMT: mitochondrial RNA polymerase

PPM: parts-per-million

PPP: pentose phosphate pathway

PTMs: postranslational modifications

PUFAs: polyunsaturated fatty acids

R5P: ribulose 5-phosphate

RCA: rolling-circle amplification

REDOX: reduction- oxidation (reactions)

RNA: ribonucleic acid

mRNA: messenger RNA

tRNA: transfer RNA

rRNA: ribosomal RNA

RNA-seq: RNA sequencing

ROS: reactive oxygen species

RT: room temperature

RV: right ventricle

Rv: reverse

RVSP: right ventricular systolic pressure

TCA: tricarboxylic acid cycle

T_E: effector T cells

TEM: transmission electron microscopy

T_M: memory T cells

TMT: tandem mass tags

T_N: naïve T cells

TOM: translocase of the outer membrane

SC: subsarcolemmal mitochondria

SCs: supercomplexes

SCAF1: supercomplex assembly factor 1

SD: standard deviation

SDS-PAGE: sodium dodecyl sulphate polyacrylamide gel electrophoresis

SDH: succinate dehydrogenase

SEM: standard error of the mean

SNPs: single nucleotide polymorphisms

SOD2: superoxide dismutase 2

SP-A: surfactant protein A

SSC: saline-sodium citrate

SUV: standardized uptake value

UPR: unfolded protein response

VCP: valosin-containing protein

VDAC: voltage-dependent anion channel

WAT: white adipose tissue

WB: western blot

WT: wild type

YBP: years before present

ZFNs: zinc-finger nucleases



Introduction

II. Introduction.

Mitochondria: more than a cell powerhouse

Mitochondria are subcellular organelles within eukaryotic cells with their own genetic material, responsible for producing energy in form of adenosine triphosphate (ATP) (Figure 1A). On average, the organelle is 1-2 µm in length and 0.5-1 µm in diameter but these parameters may vary between cell types[1]. Due to their evolutionary endosymbiotic origin, evolved from engulfed prokaryotes organisms that lived independently[2], mitochondria were considered for decades isolated, independent and functional organelles with the unique goal to provide energy for the cell. They are considered the "powerhouse" of the cell, providing ATP by aerobic respiration to maintain homeostasis and cell survival[3].

During the past two decades, new mitochondrial functions have been discovered. They act as mediators between different components in cytosol communication to initiate biological responses under different homeostatic and stress conditions (e.g. endoplasmic reticulum), but also forming part of the complex crosstalk between mitochondria and nucleus[4,5]. Mitochondria act as metabolic sensors and can induce specific gene expression programs. Furthermore, mitochondria take part in iron-sulfur clusters, heme groups and lipid biosynthesis. Due to their capacity to produce energy, integrate and converge anabolic and catabolic processes, they play an important role in cell differentiation, proliferation, adaptive mechanisms under stress conditions and in cell apoptosis and death[5].

II.1. Mitochondrial structure and compartmentalization

Mitochondrial architecture consists of two different membranes (outer and inner mitochondrial membrane) that separate two different compartments: the mitochondrial matrix and the intermembrane space[3] (Figure 1B).

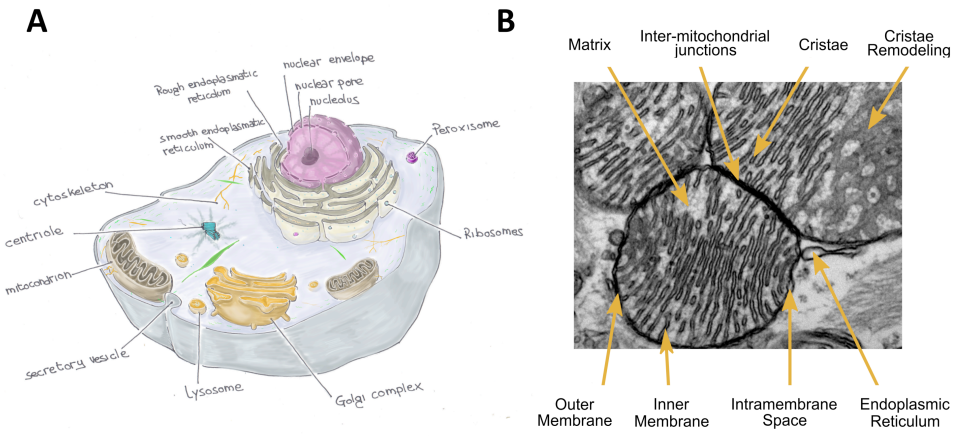

Figure 1. Structure of the eukaryotic cell and mitochondria. (A) Diagram of a typical animal cell showing the plasma membrane and cytoplasm; nucleus and ribosomes, mitochondria, cytoskeleton and the endomembrane system. *Designed by Fabio Rico.* **(B)** The mitochondrion as a multi-compartment system. Transmission electron microscopy (TEM) image of cardiac mitochondria illustrating the principal compartments of the organelle. Mitochondria-mitochondria junctions and mitochondria-endoplasmic reticulum interactions are crucial in high energetic tissues.

Outer mitochondrial membrane (OMM): This membrane contains porins, proteins that form large aqueous channels through the lipid bilayer allowing the permeation of small molecules and metabolites (< 5 kDa) into the intermembrane space. Nuclear-encoded proteins pass the membrane via the translocase TOM. The voltage-dependent anion channel (VDAC) permits the crossing of other metabolites.

Proteins involved in lipid synthesis and lipid metabolism are also present[6,7]. As specialized areas, the mitochondria-associated membranes (MAMs), where mitochondria and the endoplasmic reticulum (ER) are connected. They are involved in the regulation of calcium homeostasis and the reactive oxygen species (ROS) generation among others[8].

Mitochondrial Matrix: This compartment contains multiple copies of mitochondrial DNA (mtDNA), tRNAs and many enzymes required for mtDNA replication and gene expression, fatty acid oxidation and tricarboxylic acid cycle (TCA) [6,9].

Inner mitochondrial membrane (IMM): Selective for small molecules that cross between the cytosol and the mitochondrial matrix. It is responsible for maintaining the electrochemical proton gradient, a converted energy derived from oxidative phosphorylation (OXPHOS). The inner membrane defines two sub-compartments: the intermembrane space and the cristae lumen. The intermembrane space contains high number of small molecules and its chemical composition is similar to that of the cytosol. Here, the enzymatic reactions for phosphorylation of nucleotides occur by conducting ATP out of the mitochondrial matrix[6]. The invaginations of the IMM form the cristae, where is located the mitochondrial electron transport chain (mtETC)[9], that define the cristae lumen. Cristae junctions separate them from the rest of the IMM. Cristae morphology is modulated by the ATP synthase complexes located at membranes, which can bend them, and the mitochondrial contact site and the cristae organizing system (MICOS), which creates cristae junctions for compartmentalizing them (Figure 1B)[2].

II.1.A. Functional morphology of the mitochondria

Several proteins link the different functions of mitochondria: control of cell cycle, cell death, development or immune responses among others. It was at this point when mitochondrial dynamics started to be part of the functional output in the organelle, establishing the connection between ROS generation, ATP production and mitochondrial plasticity in their IMM and OMM[3].

Mitochondrial content and localization vary between cell types and tissues; e.g. in cardiac muscle, mitochondria are located in the region with the higher ATP requirement[6]. Mitochondrial morphology and dynamics, fusion and fission events in OMM and IMM, depend on the cellular type, and it can be modulated by metabolic requirements. Fission events cause mitochondrial network fragmentation. Also, uncoupling OXPHOS from ATP production could lead to fragmented mitochondria[10]. On the other hand, an unopposed fusion leads to an elongation of the mitochondrial network. This improves the cellular adaptation to an external stress that potentially can disrupt the cell metabolism (e.g. oxidative stress and ROS production)[1]. Mitochondrial dynamics is not only regulated by OXPHOS performance, but also by pathways like adrenergic signalling or AMPK signalling[11]. Changes in the dynamics also play a role in ROS production, apoptotic signalling and inter-organelle communication coordinating the inner mitochondrial membranes to form inter-mitochondrial junctions (IMJ). IMJ frecuency can be used as an index of energized mitochondria during the propagation of intracellular bioenergetics through mitochondrial networks in cells[12].

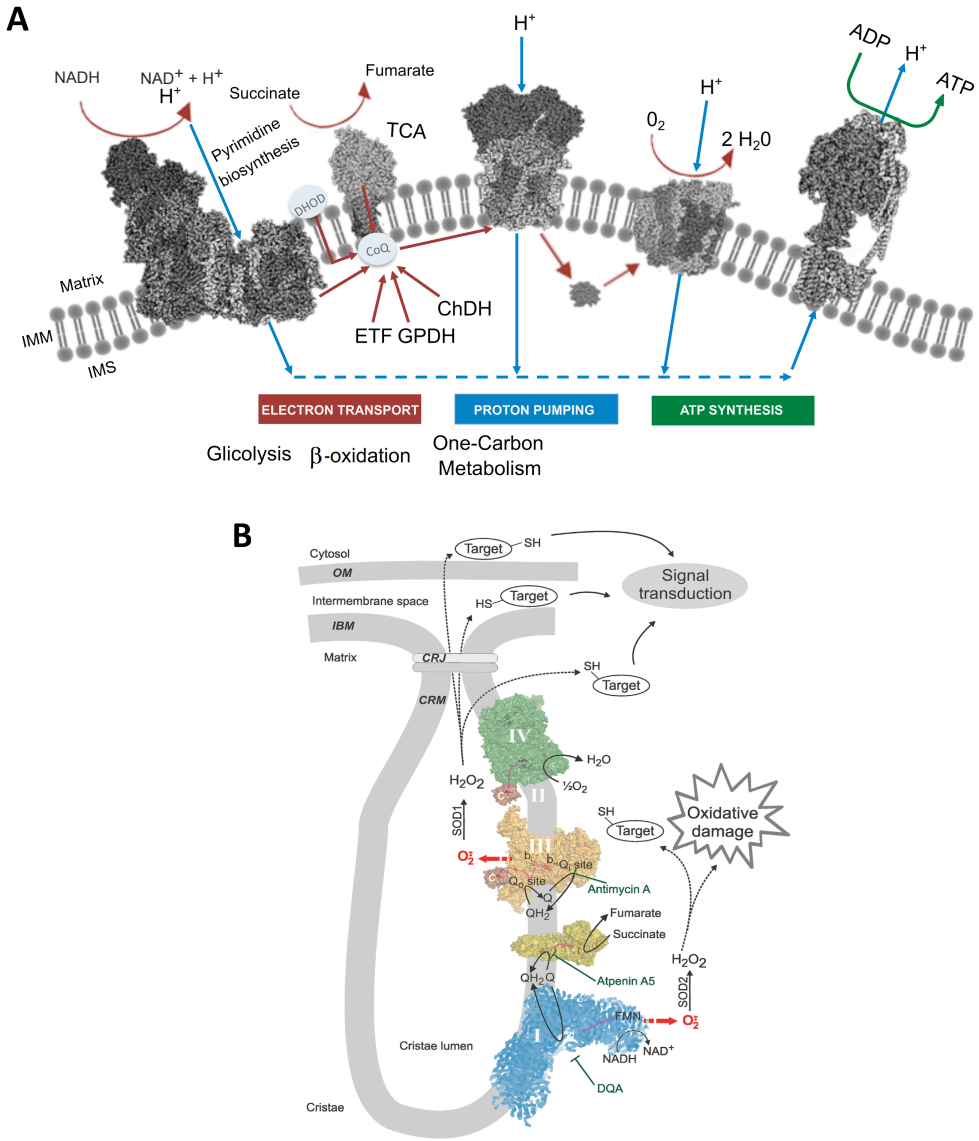

Figure 2. Mitochondria represent a hub in the overall REDOX status and metabolic network of the cells. **(A)** OXPHOS system. Three different processes are integrated in the same structure: ATP synthesis (blue lines and arrows), proton pumping (green lines and arrows) and electron transport (red lines and arrows). **(B)** How mitochondria produce ROS. mtETC CI presents two possible sites of ROS production: NADH and quinone-binding sites. Superoxide can also be generated by CIII at the ubiquinol oxidation site (centre P, Q_o site). Other sites of ROS production within mitochondria are the cytochrome (cyt c), monoamine oxidase (MAO), and the NADPH oxidase 4 (NOX-4). The antioxidative system is formed by thioredoxins (Trx), peroxiredoxins (Prx) and glutathione peroxidases (Gpx) proteins and glutathione (GSH). *Obtained from Bleier L. et al. (2015).*

Proteins related to mitochondrial shape such as the mitochondrial fission 1 protein (FIS1), and the mitofusins 1 and 2 (MFN1 and MFN2) are located in the OMM and are also involved in mediating mitochondria-mitochondria communication and in communication with other cytoplasmic components like the endoplasmic reticulum (mitochondria-associated endoplasmic reticulum membranes, MAMs)[7]. A family of GTP-dependent dynamin-like proteins mediates mitochondrial plasticity. Among the proteins involved in fusion are the optic atrophy 1 (OPA1) protein, MFN1 and MFN2 and profission proteins such as the dynamin like-1 (DRP1) protein[7,13]. Most of these proteins present post-translational modifications in order to regulate their function. E.g. OPA1 is processed by the proteases m-AAA, i-AAA (YME1L) and OMA1; in addition, MFN2 and DRP1, can be modified by ubiquitination, SUMOylation and phosphorylation[7,14,15]. Mitochondrial reorganization of the IMM and cristae shape is also regulated by complexes formed by different prohibitin subunits (Phb) and MICOS[7].

II.1.B. Mitochondria as signalling organelles

Mitochondria have a central role in the energy metabolism. Demands on catabolic and anabolic processes need to be reconciled. Activity of the organelle determines the equilibrium of the key cellular metabolic pairs ATP/ADP, NADH/NAD^+, $CoQH_2$/CoQ, and $FADH_2$/FAD (Figure 2A). They also act as regulators for critical signalling molecules (AMP, α-ketoglutarate, acetyl-CoA, succinate and citrate) and generation of cellular second messengers[16]. The significant impact on cell signalling also resides on events of acetylation, phosphorylation, oxidation-reduction, and protein stabilization and turnover[16]. Mitochondria from different tissues are subject to vary metabolic requirements and can be highly specialized on adapting to different fuels and physiological needs[17].

The proton (H^+) pumping from the mitochondrial matrix into the intermembrane space through the inner membrane forms the electrochemical gradient, also called proton-motive force (Δp)[18]. Two major components of Δp are the pH gradient and the mitochondrial membrane potential (ΔΨm)[19]. This gradient acts like a capacitor that stored energy to be used for calcium (Ca^{2+}) uptake into mitochondria, to transport proteins and metabolites across the membranes and to modulate the cellular oxidation-reduction (REDOX) reactions[20]. Proton motive force regulates ATP production, while the ΔΨm component provides the difference of charge that is required for mitochondrial Ca^{2+} sequestration, reactive oxygen species (ROS) production and programmed cell death, which are crucial for cell survival. ΔΨm can be altered by an unbalanced concentration of ionic charges (Ca^{2+}, K^+) in the intracellular medium, affecting the ATP production and thus, resulting in bioenergetics stress[19,21]. As a sensor of metabolic homeostasis, Ca^{2+} is buffered in the proximity of the ER and can modulate different signalling pathways in the cytosol[22].

II.1.C. Reactive Oxygen Species: from physiology to pathology

Retrograde signalling between mitochondria and nucleus is required to adapt the cellular responses under different physiological and stress conditions. Different signalling molecules, metabolites, ions and ROS play a crucial role in the process. Mitochondrial cellular energetics and redox signalling influence all cellular functions. ROS are critical for cell differentiation, regulation of the activity of the mitochondrial electron chain (mtETC) complexes[23], mitochondrial biogenesis[24,25] and for modulating disease penetrance by cell adaptation to pathological mutations[26]. These pathways can impact on the innate and adaptive immune responses, mitochondrial homeostasis and ageing. In physiological states, ROS are necessary to act as signal-transducing molecules but their production is minimized to avoid cellular and tissue oxidative damage. This damage generates the oxidation of DNA, lipids and proteins. The increase in ROS generation is counter-productive for ATP production, and in consequence, impairs tricarboxylic acid cycle, fatty acid oxidation, the urea cycle, amino acid metabolism, heme synthesis and FeS centre assembly processes, leading to cell death[24,27,28]. It is well documented that excess of ROS production triggers inflammation by cytokine production, cardiac ischemia-reperfusion injury and neurodegenerative diseases such as Parkinson's and Alzheimer's diseases among others[28–30]. New studies point to a new role of ROS in the attenuation of global protein synthesis[31].

Mitochondria are the major source of ROS (mtROS). Superoxide (O_2^-) is produced in the mitochondrial matrix or in the intermembrane space. Its generation is dependent on the proton motive force (Δp), concentration of electron donors (in the mtETC) and is also regulated by the oxygen concentration and NADH/NAD^+ and CoQH2/CoQ ratios[24,32]. Hydrogen peroxide (H_2O_2) is generated by the dismutation of O_2^- by the mitochondrial superoxide dismutase (SOD2). O_2^- and H_2O_2 also react with other molecules (eg. nitric acid and fatty acids) and generate hydroxyl (OH^-), alcoxyl (RO^-) and peroxyl (ROO^-) radicals. Among the mitochondrial enzymes that are well described to generate ROS are the aconitase (ACO), α-

ketoglutarate dehydrogenase (αKGDH), glycerol-3-phosphate dehydrogenase (GPDH), pyruvate dehydrogenase (PDH), monoamine oxidase (MAO) isoenzyme A and B, dihydroorotate dehydrogenase (DHOH), cytochrome b reductase (BR5) and the electron transfer flavoprotein:ubiquinone oxidoreductase (ETF-QO) . There is an increase in ROS production when the NAD^+ is limited[24,30]. Within the mtETC, there are three sites of ROS production: complex I (CI, NADH:ubiquinone oxidoreductase), complex II and complex III (CIII, cytochrome bc_1 complex, ubiquinol:cytochrome *c* oxidoreductase)[33–36] (Figure 2B). Complex I is formed by 44 different proteins[37], 30 of them involved in the assembly and stability of the complex and the rest, implied in the electron transfer and proton pumping processes. Complex I has two possible sites of ROS production, both of them in the peripheral arm, the flavin moiety and quinone-binding sites. ROS are generated during the forward electron transport (FET), from NADH to CoQ enzime[38]. It is known that during the reverse electron transport (RET), electrons pass from the ubiquinol to reduce the NAD+ when there is a high ratio of CoQH2/CoQ, coupled with the highest rate of ROS, but it is still unknown the specific site of their generation[24]. Further ROS produced by CIII are linked to the ubiquinol oxidation (centre P, Q_0 site). CIII-derived $O_2^{\cdot}$ is released to the intermembrane space and the $O_2^{\cdot}$ generated at CI is mostly located in the mitochondrial matrix and in the inner mitochondrial membrane[35]. Intermembrane proteins like the voltage-dependent anion channel isoform 3 (VDAC3) or the TOM/TIM (translocase of the outer and inner membrane, respectively) subunits are often oxidized by the complex III-derived ROS. Proteins like the 3-mercatopyruvate sulphurtransferase are, however, targets for ROS released by CI and CIII[35]. Enzymes like superoxide dismutase (SOD2), glutathione peroxidase (GPx), peroxiredoxins (PRDX3, PRDX5) and catalase are necessary to establish an equilibrium between ROS generation and detoxification[24]. Enzymatic antioxidant activity of SOD2 is being questioned; an increase in its expression can promote oxidative stress. The binding of iron (FeSOD2) instead of manganese (MnSOD2) as a metal cofactor can promote the shift in its enzymatic activity and the use of the H_2O_2 for the oxidation of other molecules [39].

II.1.D. Mitochondrial quality control

Mitochondria act as signalling effectors and need strict regulation of their homeostasis. Mitochondrial proteostasis is the term for the global process of homeostasis of mitochondrial proteins. It summarizes protein expression, correct localization and folding, acquisition of the correct conformational state and the protein degradation under different signals of damage (e.g. incorrect protein folding or oxidative PTMs)[40]. Multiple mechanisms play a crucial role in identifying and resolving mitochondrial dysfunction.

II.1.D.1. Mitochondrial unfolded protein response (mtUPR)

MtUPR was discovered in mammalian cells but the pathway was further characterized in *C. elegans*. In this animal model it was described that a reduction in the import of the ATFS-1 transcription factor into mitochondria can traffic it to the nucleus (by nuclear localization sequence, NLS) promoting the expression of more than 500 genes that can modulate diverse cellular pathways. This transcription factor also interacts with mtDNA to downregulate the accumulation of its transcripts. MtUPR promotes the transcription of mitochondrial proteases and chaperones (e.g. chaperone mtHSP70 and proteases m-AAA and i-AAA), proteins involved in mitochondrial dynamics (e.g. DRP-1), ROS detoxification enzymes and components that form the machinery for importing proteins into mitochondria (e.g. TIMM17 and TIMM23)[41]. Studies in mammalian systems have suggested a mechanistic overlap between *C. elegans* and mammalian mtUPR. Orthologous transcription factors have been identified (ATF4, ATF5 and CHOP)[42]. The metabolic remodelling triggered by the activation of mtUPR implies the down-regulation of OXPHOS genes and up-regulation of those involved in the glycolytic pathway[41]. It has been also described the unfolded protein response activated by mistargeted proteins (amUPR) in which the unusual location of mitochondrial

proteins in the cytoplasm activates the proteasome[43]. Recent advances have described the UPR as a cellular stress response related to the ER stress. The major pathways of ER stress are controlled by three different sensors: (a) inositol-requiring enzyme 1α (IREα), (b) the pancreatic endoplasmic reticulum kinase (PERK/EIF2AK3) and (c) the activating transcription factor 6 (ATF6). These sensors can activate the signalling cascade under conditions that compromise the cell homeostasis (i.e. nutrient starvation, imbalanced ion concentrations or hypoxia)[44–46].

II.1.D.2. Translation attenuation process

Alterations in mitochondrial performance (e.g. increase of ROS or ribosome stalling) can activate GCN2 kinase (GCN2/EIF2AK4). This kinase phosphorylates the eukaryotic initiation factor alpha (eIF2a) promoting the inhibition of the protein synthesis and a decrease on the amount of the proteins imported into mitochondria. Together with PERK/EIF2AK3 activity, it modulates ATF4 expression adapting the cell to stress conditions[47]. Other two eIF2α kinases (PKR/EIF2AK2 and HRI/EIF2AK1) can trigger translation attenuation upon different stresses in which mitochondria may participate (i.e. heme deficiency or viral infections).

II.1.D.3. Autophagy and Mitophagy

Autophagy is a catabolic process regulated by lysosomes that removes damaged organelles and macromolecules. Severely damaged mitochondria that are beyond repair are identified and degraded via mitophagy. During the process of mitochondria-specific autophagy, dysfunctional mitochondria can be sequestered within autophagosomes. That double membrane compartment fuses with lysosomes to deliver the content for degradation[48]. PINK1 is placed into OMM and promotes the recruitment of PARKIN to trigger the ubiquitination in OMM proteins and subsequent engulfment of labelled mitochondria into autophagosomes[49,50]. The mechanism of mitophagy blocks the excessive ROS production and accumulation of mtDNA mutations that can generate respiratory chain dysfunction, the release of pro-inflammatory signals, the opening of mitochondrial permeabilization pore, apoptosis and premature ageing[51].

II.1.E. MtDNA and mitochondrial performance under stress conditions

II.1.E.1. Mitochondria and ageing

Ageing refers to a cellular status characterized by a progressive loss of vitality of the cell as well as cellular integrity and tissue homeostasis, leading to impaired function and increased susceptibility to death[52]. Until now, there is no single theory of ageing that can explain the global process. A compilation of the nine tentative hallmarks of ageing in different organisms were defined: 1) genomic instability, 2) epigenetic alterations, 3) cellular senescence, 4) loss of proteostasis, 5) impaired nutrient sensing, 6) stem cell exhaustion, 7) disrupted intercellular communication, 8) telomere attrition and 9) mitochondrial dysfunction[52]. Premature ageing has been associated with alterations during development, genetic defects, disease conditions and environmental stress[53]. To improve human health during ageing and the design of new drugs, these targets are used to elucidate the relative contribution in the overall process.

From a molecular point of view, senescence involves a reduction in the activity of the proteasome, an increase of lipofuscin content, enlarged nuclei, impaired mitochondria and as a consequence, an increase in ROS generation and oxidation of biomolecules. Features of the associated secretory phenotype (SASP) in cells are the release of (a) fibronectin, (b) inflammatory cytokines (e.g. IL-6 and IL-1) and (c) growth factors (e.g. IGF-21), with the subsequent activation of the immune system[54].

It was more than fifty years ago, when mitochondria were placed in the centre of the longevity studies. The first proposal was the "free radical theory of ageing"[55]. Although the explanation of how OH^- and hydroperoxyl HO_2^- radicals interfered on cell physiology was still unclear, an increase of free radicals during ageing by enzymatic activity of respiratory complexes and deleterious consequences on cells were reported[55]. Since then, different updates of the original theory have been published[53,56,57]. The relationship between ROS and ageing has been supported by studies that show how an increase in the expression of ROS scavengers (e.g. MnSOD, methionine sulphoxide reductase and catalase) and molecules such as melatonin prolong lifespan at different levels of short-lived and long-lived strains[30,58].

During the last years, several studies have been focused on the alterations in mitochondria during ageing. Mitochondrial network dissociation within cells, impairment of mtETC functionality, increase of ROS generation and subsequent oxidation of mtDNA, proteins and lipids and accumulation of mtDNA mutations have been described[59]. Molecular and morphological changes in mitochondria during ageing can trigger cellular death[60]. In post-mitotic tissues, where there is no possibility of cell regeneration, the removal of impaired mitochondria is crucial. Defects in autophagic activity lead to accumulation of damaged organelles and oxidized biomolecules are commonly observed in age-associated pathologies such as heart failure[51,61]. The role of mitochondrial unfolded protein response in ageing has been related to the lifespan by a selective gene expression. New insights in the field suggested that chromatin remodelling might also activate the mtUPR which is well described in the process of transcriptional regulation[42,44]. For example, the dimethylation of the H3K9 histone (via MET-2 and co-factor LIN-65) condenses the chromatin whereas the histone demethylase activity gives to the promotors of mtUPR-induced genes the appropriate state for the initiation of the transcription in an independent manner of ATFS-1 in *C. elegans*. The full induction of the stress response also requires the activity of the mitochondrial proteases (CLPP1), the transcription factor DVE-1 and the co-factor UBL-5[62].

II.1.E.2. Mitochondria in lung pathophysiology

Pulmonary disorders are one of the most frequent causes of death worldwide. In Spain, diseases of the respiratory system were the third cause of death, accounting for 12.5% of the deaths in 2016[63]. Since the incidence of chronic pulmonary disease is rising, the health impact is expected to increase in the future. In spite of this forecast, the advances in the respiratory pathology treatment are very limited, focusing in the symptomatic treatment.

It has been proposed that mitochondrial dysfunction could contribute to the pathological process in some aetiologies of pulmonary diseases[64]. Until recently, the implication of the mitochondria in diseases was focused in their bioenergetic role. During the past years, it has been recognized that additional mitochondrial roles (i.e. apoptosis and inflammation or as a nutrient and oxygen sensor) may have critical importance (Figure 3). MtDNA haplotypes modulate the function of the mitochondria and the organismal metabolism, being in that way able to modulate the triggering, evolution and severity of the diseases[16,65]. In case of lung tissue, it has been postulated that mitochondria can act as oxygen sensors, modifying cytosolic redox state by producing ROS to regulate secondary effectors involved in hypoxic pulmonary vasoconstriction (HPV)[66] (Figure 3).

Mitochondrial function in lung is less understood in comparison with other tissues due to the complexity of the lung tissue structure and the challenges to optimize gas exchange in mammalian lungs[67]. Most of the pulmonary cells get energy from pyruvate as a primary carbon source through oxidative phosphorylation (OXPHOS). Oxygen consumption in lung is similar to other tissues, being the ATP generated comparable to hepatic, renal or even brain cells, which their main metabolism relies on mitochondrial performance. Lung mitochondria also need fatty acids, glutamate and glycerol 3-phosphate,

intermediates of tricarboxylic acid cycle (TCA), as energy sources. Their highest rate in oxygen consumption is with succinate as substrate[68].

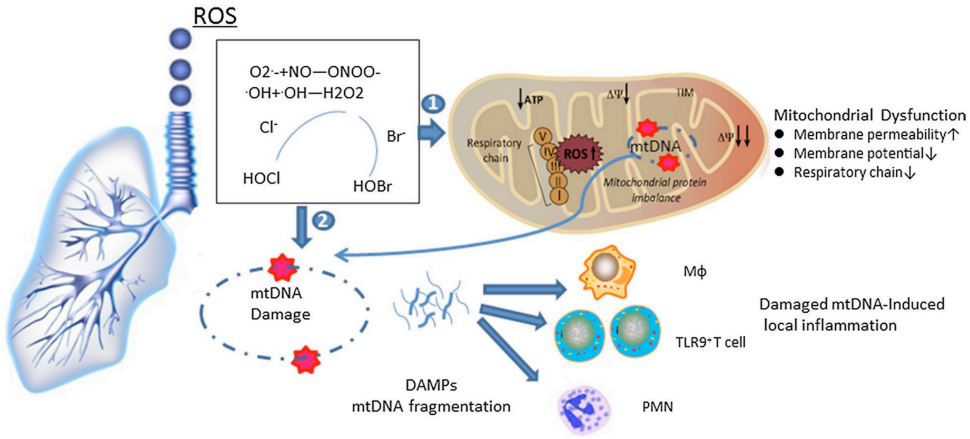

Figure 3. Mitochondrial dysfunction and pathogenesis in lung diseases. Mitochondrial impairment increases ROS production, decreases OXPHOS performance and develops mtDNA-associated immune response. O_2^- is generated in the intermembrane space, matrix and outer membrane of the mitochondria. (1) O_2^- can generate peroxynitrite ($ONOO^-$) when reacts with nitric oxide (NO^-) or H_2O_2 by dismutation (SOD2 enzymatic activity). In the presence of chloride (Cl^-) and bromide (Br^-) hydrogen peroxidase activity generates the very damaging oxidants hypochlorous (OHCl) and hypobromous (OHBr) acids. (2) MtDNA damaged fragments can be released from mitochondria and cells acting as immunogenic particles that recruit macrophages, T cells and neutrophils. *Obtained from Llu and Chen. J. Transl. Med (2017).*

Mitochondria may be implicated in pulmonary vascular remodelling. Mitochondrial hyperpolarization, has been described as a mechanism that affect cell proliferation in some respiratory disorders, as pulmonary hypertension (PH)[69]. In addition, alterations in mitochondrial dynamics could trigger the progression of a variety of pathologies[66]. Type II alveolar epithelial cells (AECs) are responsible for the synthesis, recycling and secretion of pulmonary surfactant, and they are rich in mitochondria. Irregularities in phospholipid production and in the mitochondrial carnitin-acyltransferase pathway alter surfactant composition, triggering alterations in pulmonary function[70]. Surfactant proteins A and D (SP-A, SP-D) are C-type lectins (collectins), that have a crucial role in the regulation of lung immune response, clearance of apoptotic and necrotic cells and enhancing the priming of adaptive immunity[71].

Interstitial lung diseases (ILDs) are a heterogeneous group of diseases that present, among others features, fibrosis and interstitial inflammation[72,73]. Idiopathic pulmonary fibrosis (IPF) is one of the most frequent ILD with an unknown aetiology that lacks of reliable biomarkers for diagnosis[72]. Accelerated lung ageing and associated mechanisms like telomere attrition, epigenetic modifications, genomic instability and mitochondrial dysfunction have been suggested to be involved in the development of the pathology. The most accepted theory of PF is based in the abnormal activation and miscommunication between type II AECs and fibroblasts. This promotes an exaggerated production and accumulation of extracellular matrix, formation of scars and end-stage fibrosis[72,73]. Mitochondrial impairment leads to an excessive ROS production and mitochondrial-mediated AECs apoptosis, both described in IPF patients[73,74]. Loss of NAD^+ and acetyl-CoA can lead to a reduced activity of sirtuins that inactivate AMPK and FOXO proteins and mitochondrial biogenesis factor PGC1-α (peroxisome proliferative activated receptor, gamma, coactivator 1 alpha), increasing mtROS[74]. This pathway is reported in the case of mtDNA mutator mice, in which there are high levels of point mutations due to the proofreading deficiency of the mtDNA polymerase-γ (POLG)[74,75], establishing mitochondrial age-related dysfunction with vulnerability to lung fibrosis.

IPF disease remains one of the common causes of PH[76,77]. Between 32-85% of diagnosed IPF patients develop it over the time[78]. PH is a multifactorial and progressive disease characterised by loss and narrowing of pre-capillary vessels (in some cases also post-capillary) and pulmonary vasoconstriction, resulting in right heart ventricle failure and death[79,69,80]. Recent studies define the pathobiology of this disease as a complicated interaction of fibroblasts, epithelial cells and vascular cells, having a crucial role in pulmonary artery wall remodelling[78]. PH shares most of the outstanding properties with cancer: dysregulated angiogenesis, alterations in energy metabolism and mitochondrial bioenergetics, an increase in cellular growth factors gene expression and resistance to apoptosis. The highly proliferative status of the cells is sustainable by the increase of fatty acid oxidation (FAO) instead of glucose oxidation (GO), promoting a metabolic shift to aerobic glycolysis (Warburg effect)[80]. Pyruvate dehydrogenase kinase (PDK) play a crucial role in the inhibition of the pyruvate dehydrogenase (PDH) and GO[81]. This metabolic status in pulmonary circulation and in the right ventricle (RV) is critical to asses pulmonary disfunction[82]. As a predictor of mortality in pulmonary arterial hypertension (PAH), RV failure is the best one although the molecular mechanism of uncoupling the adaptive hypertrophic response of RV and the pressure overload that causes it is still unknown[83]. Therapies for restoring RV function need to be improved, however, after lung transplant it is known that metabolic remodelling occurs in RV[83].

Mitochondrial dysfunction in pulmonary vascular cells was reported during PAH progression, being linked to the initial stage of the disease[84]. There is no consensus on how human mtDNA haplogroups modify the prevalence of specific diseases. In case of lung disorders, it was proposed that some mtDNA haplogroups increase the risk of PAH. The unique study that involves patients with this condition reveals that haplogroups M and N (branches HV, UK, JT) have a higher risk of PAH in comparison with haplogroup L. One of the limitations of the work was the small number of African Americans with PAH, but the results suggest that the high prevalence of PAH has been associated to the adaptation of people that emigrated from Africa to different environments[84]. Mitochondrial haplogroups with lower coupling efficiency are linked to diseases with energy deficient states. There are several limitations in the association between diagnosed patients and mitochondrial DNA haplogroups. Further work is needed to determine the interaction between mitochondrial and nuclear genomes in order to explain the susceptibility to different pathologies and their contribution in pulmonary diseases, one of the most energy demanding tissues.

II.2. OXPHOS system as a unique functional structure

The OXPHOS system is a functionally unique structure, one of the best-understood systems in the eukaryote cell. Although it has been deeply studied during years, it is still unknown how and why the impairment of OXPHOS affects phenotypically to different diseases[85]. OXPHOS presents different particularities: its structural components are encoded by two different genomes and three processes are integrated in the same structure: electron transport, proton pumping and ATP generation[86] (Figure 2A). The main role of these three processes is the energy production, but each one by itself has additional functions, for example, proton motive force is necessary to import metabolites into mitochondria and to generate heat instead of ATP (e.g. brown adipose tissue).

MtETC is linked to many other metabolic processes guided by the electron transport, as many enzymes require it. This is the case of succinate dehydrogenase (SDH or Complex II, tricarboxylic acid cycle), glycerol-3-phosphate dehydrogenase (mtGPDH, reducing equivalents from the cytoplasm), dihydroorotate dehydrogenase (DHOD, synthesis of pyrimidines), choline dehydrogenase (CHDH, metabolism of glycine)[87], electron transfer flavoprotein:ubiquinone oxidoreductase (ETF-QO, β-oxidation)[88], sulfide-quinone oxidoreductase (SQOR, sulphur and seleno-aminoacid metabolism)[89] and proline dehydrogenase (PRODH2, proline and arginine metabolism)[90]. The integration of different processes challenges the cells

with the coexistence of efficient and suboptimal functions. All these enzymes use FADH as cofactor to deliver electrons to CoQ without pumping protons. They can be called collectively as CII-type enzymes. The selection criteria between them depend on cell type and cell fate requirements under different stress conditions. An additional layer of complexity is that some OXPHOS structural subunits are expressed only in response to a defined stimulus, as in the case of hypoxia inducible subunits[91].

The OXPHOS system is composed of four respiratory complexes named complex I (CI, NADH-ubiquinone oxidoreductase), complex II (CII, succinate:ubiquinone oxidoreductase), complex III (CIII, ubiquinol-cytochrome c reductase) and complex IV (CIV, cytochrome c oxidase); two electron carrier molecules, ubiquinone (UQ or CoQ) and cytochrome c (cyt c) and the complex V (CV), the H^+-ATP synthase. Complex I is the largest integral membrane enzyme composed of 44 different proteins in humans and 45 in mice, complex II of 4 subunits, complex III of 11 subunits, complex IV 14 subunits, and complex V that contains 11 subunits. All these subunits have to assemble to form functional complexes. How the assembly factors work during this process is still largely unknown[85,92].

The generation of ATP by mitochondria is mediated by the electrochemical proton motive force (Δp) created by the reductive transfer of electrons through mtETC. This force allows condensing ADP and inorganic phosphate (Pi) for ATP synthesis in the ATP synthase. Δp is the combination of the mitochondrial pH gradient and the mitochondrial membrane potential (ΔΨm). Proton motive force regulates ATP production, while ΔΨm component provides the difference of charge that is required for active transport of metabolites across the mitochondrial inner membrane[33].

Fatty acid oxidation, glycolysis and Krebs cycle originate reducing equivalents: NADH or $FADH_2$. The oxidation of acetyl-CoA to CO_2 is coupled to the reduction of FAD and NAD^+ to $FADH_2$ and NADH, respectively. The four complexes integrated in the mtETC (Complex I, II, III and IV) perform the reduction of them. NADH and FADH enter the electron transport chain through Complex I and Complex II-type enzymes, respectively. The electrons are then transferred stepwise to coenzyme Q and from there to Complex III, cytochrome c, and finally to Complex IV, which passes them to molecular oxygen. The serial reduction of electrons through mtETC, with O_2 as a final acceptor in the inner mitochondrial membrane, produces the energy used to drive protons out of the mitochondrial matrix. This proton accumulation in the inter-membrane space flows back into the organelle through the ATP-synthase (complex V) producing ATP and completing the oxidative phosphorylation process[19,11,85,93].

II.2.A. MtETC versatility and superassembly of mitochondrial respiratory complexes

The functional organization of the mtETC complexes forming the OXPHOS system was widely debated until very recently. Many models have been suggested since 1947, when Keilin and Hartree proposed the first OXPHOS system organization[94]. The first model was the "solid model" (Figure 4A), in which the respiratory complexes assembly orderly in closed packages within the IMM. Based on proximity, mtETC could improve the efficiency of electron transfer between them and thus generate higher catalytic activity which has been supported by different kinetics studies[95–97]. Subsequently, in 1961 Mitchell's chemiosmotic model and the description of a new "fluid model" (Figure 4B) by Hackenbrook *et al*. (1986) replaced this theory after demonstrating the independent complexes[98,99]. This model, also called "classical model", supports the random collision of the electron transport chain components and could explain better the structural organization of the mtETC and how it forms a diffusion-dependent kinetic process. The importance of the velocity of diffusion of the two main carriers, the coenzyme Q (CoQ) taking electrons from CI and CII to CIII and the cytochrome c (cyt c) from CIII to CIV was pointed out [98,100]. Years later, Schägger and Pfeiffer presented a new way of analysing mitochondrial complexes, the blue native polyacrylamide gel electrophoresis (BN-PAGE)[101,102]. Using that technique they could observe individual

complexes but also associations between them, leading to the most recent model of mtETC organization: the "plasticity model" [103] (Figure 4C). This last model is based on stoichiometry between complexes, which can be functional either individually or assembled into functional quaternary structures or supercomplexes (SCs). Supercomplexes are formed by: complexes I and III, complexes III and IV and complexes I+III+IV (the so called respirasome)[85,103,104]. This functional reorganization optimizes cell adaptation to different conditions with varying substrate availability[105]. It is generally accepted that CII does not superassemble with other respiratory complexes. However, some functional evidences suggested that a small proportion of CII may be incorporated in SCs[103]. In the last years a possible higher-order assembly of respiratory complexes where complex II also takes part, called respiratory megacomplex, was proposed[106]. This megacomplex ($MCI_2III_2IV_2$) would form a ring in which CIII is in the centre[106]. The presence of CII in this megacomplex was inferred and a definitive probe of it remains to be demonstrated.

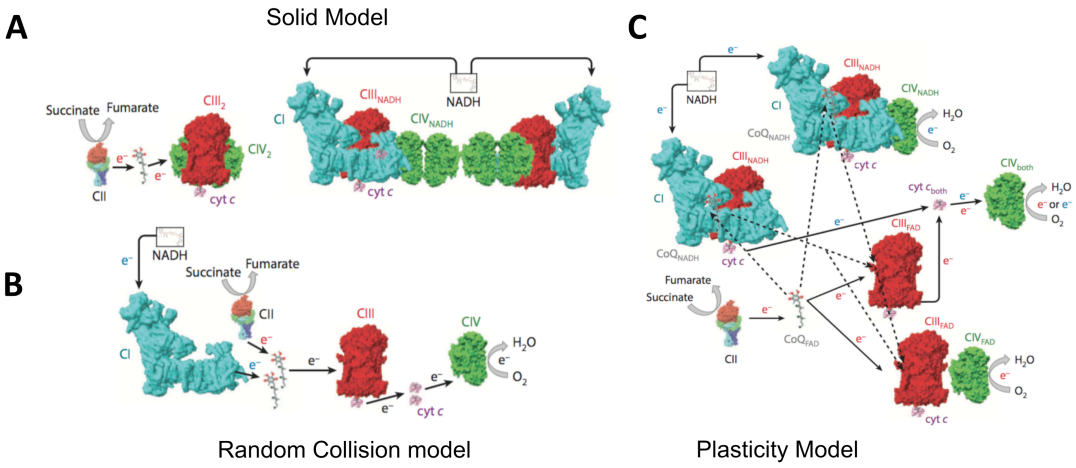

Figure 4. Supramolecular organization of respiratory complexes. (A) Solid-state model of the electron transport chain. Each complex only exists in a larger complex called oxysome (CI, CIII and CIV in different proportions) and electrons from NADH are transported by a diffusion-coupled process **(B)** Random collision model. Diffusible electron carriers can connect CI and CII to CII (CoQ) and CIII to CIV (cyt c). The model explains how multiprotein complexes can move freely in the IMM. **(C)** Plasticity Model. In this model, complexes can be functional in their free form or in supercomplexes. The majority of CI is found assembled with $CIII_2$ or with $CIII_2$ and CIV forming the respirasome. In these cases, CIII receives electrons from NADH. $CIII_2$, alone or only associated with CIV, transfers electrons from $FADH_2$. Solid lines: preferential routes for electrons. Dotted lines: undetermined functional pools, incomplete segmentation of CoQ and cyt c. *Modified from Enríquez JA (2016).*

II.3. OXPHOS system: functional integration of two genomes

The OXPHOS system is the unique physiological process in mammalian cells with components that are encoded by two different genomes, nuclear DNA (nDNA) and mitochondrial DNA (mtDNA). In order to generate the respiratory complexes, proteins that are encoded in nDNA and mtDNA have to physically interact with their counterparts, encoded in the other genome[16]. Due to the diverse metabolic roles that the OXPHOS system plays in different cell types, the combination between mtDNA-encoded subunits and nDNA-encoded subunits faces multiple challenges. The OXPHOS system cannot be genetically optimized for every physiological requirement. Therefore, alternative OXPHOS status should be able to feedback the system to tune its capacity according to the cell requirements. Thus, mitochondria need to signal to the nucleus to respond to different stimuli and on the other hand, several nuclear-encoded transcription factors are involved in mitochondrial maintenance.

A **NADH:ubiquinone oxidoreductase**

Approved Name	Chromosome
MT-ND1	mitochondria
MT-ND2	mitochondria
MT-ND3	mitochondria
MT-ND4	mitochondria
MT-ND4L	mitochondria
MT-ND5	mitochondria
MT-ND6	mitochondria
NDUFS1	2q33.3
NDUFS2	1q23.3
NDUFS3	11p11.2
NDUFS7	19p13.3
NDUFS8	11q13.2
NDUFV1	11q13.2
NDUFV2	18p11.22
NDUFAB1	16p12.2
NDUFA1	Xq24
NDUFA2	5q31.3
NDUFA3	19q13.42
NDUFA5	7q31.32
NDUFA6	22q13.2
NDUFA7	19p13.2
NDUFA8	9q33.2
NDUFA9	12p13.3
NDUFA10	2q37.3
NDUFA11	19p13.3
NDUFA12	12q22
NDUFA13	19p13.11
NDUFB1	14q31.3
NDUFB2	7q34
NDUFB3	2q33.1
NDUFB4	3q13.33
NDUFB5	3q26.33
NDUFB6	9p21.1
NDUFB7	19p13.12
NDUFB8	10q24.31
NDUFB9	8q24.13
NDUFB10	16p13.3
NDUFB11	Xp11.3
NDUFC1	4q31.1
NDUFC2	11q14.1
NDUFS4	5q11.2
NDUFS5	1p34.3
NDUFS6	5p15.33
NDUFV3	21q22.3

Cytochrome c oxidase

Approved Name	Chromosome
COX4I1	16q24.1
COX4I2	20q11.21
COX5A	15q24.2
COX5B	2q11.2
COX6A1	12q24.31
COX6A2	16p11.2
COX6B1	19q13.12
COX6B2	19q13.42
COX6C	8q22.2
COX7A1	19q13.12
COX7A2	6q14.1
COX7B	Xq21.1
COX7B2	4p12
COX7C	5q14.3
COX8A	11q13.1
COX8C	14q32.12
MT-CO1	mitochondria
MT-CO2	mitochondria
MT-CO3	mitochondria

ATP Synthase

Approved Name	Chromosome
ATP5F1B	12q13.3
ATP5F1C	10p14
ATP5F1D	19p13.3
ATP5F1E	20q13.32
ATP5MC1	17q21.32
ATP5MC2	12q13.13
ATP5MC3	2q31.1
ATP5MD	10q24.33
ATP5ME	4p16.3
ATP5MF	7q22.1
ATP5MG	11q23.3
ATP5MPL	14q32.33
MT-ATP6	mitochondria
MT-ATP8	mitochondria
ATP5PB	1p13.2
ATP5PD	17q25.1
ATP5PF	21q21.3
ATP5PO	21q22.11
ATP5IF1	1p35.3

Ubiquinol:cytochrome *c* oxidoreductase

Approved Name	Chromosome
CYC1	8q24.3
MT-CYB	mitochondria
UQCRB	8q22.1
UQCRC1	3p21.31
UQCRC2	16p12.2
UQCRFS1	19q12
UQCRH	1p33
UQCRQ	5q31.1
UQCR10	22q12.2
UQCR11	19p13.3

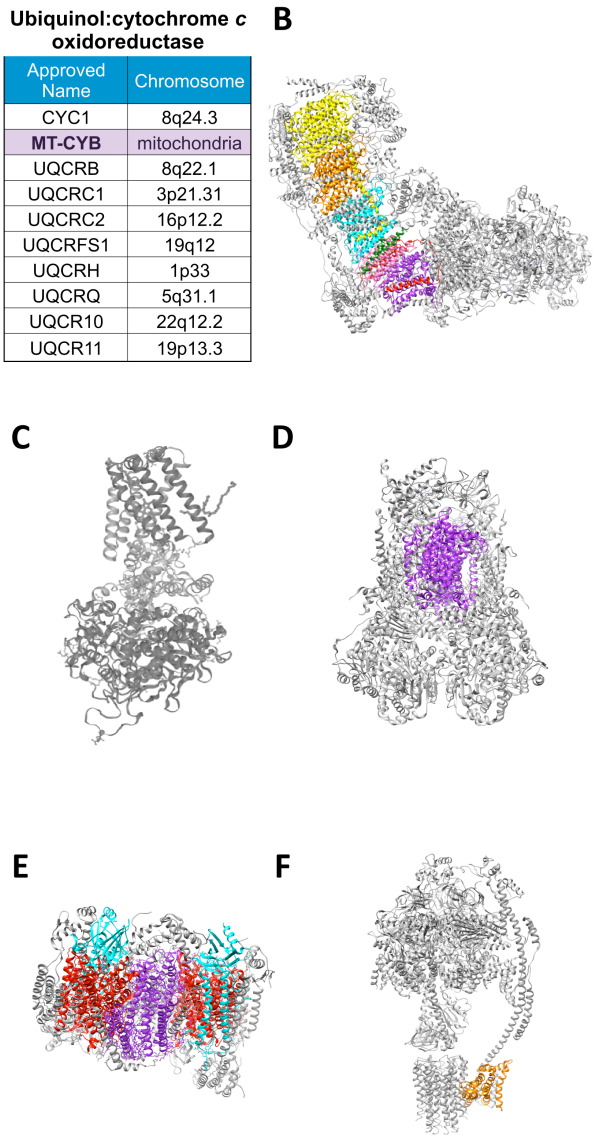

Figure 5. OXPHOS System: Overview of nuclear and mitochondrial-encoded proteins. **(A)** List of peptides forming complex I (NADH:ubiquinone oxidoreductase), complex III (Ubiquinol:cytochrome c oxidoreductase), complex IV (Cytochrome c oxidase) and ATP synthase. [Source: HGNC-HUGO Gene nomenclature Committee]. Complex IV is buit with 14 subunits. The altenative isoforms that substitute each other in different tissues, different supperassembled status or different physiological situations (i.e. COX4, COX6B, COX7A, COX7B and COX8) are listed. In addition, the fourteenth subunit of the CIV is NDUFA4 (termed COXFA4). **(B)** 3D structure of Complex I. In colour are the different peptides encoded in the mitochondrial genome. **(C)** 3D structure of the succinate dehydrogenase (Complex II). **(D)** Complex III 3D structure. In colour, mitochondrial-encoded cytochrome b. **(E)** Three-dimensional structure of Complex IV. Mitochondria-encoded peptides are in colour, mt-CO2; blue mt-Co1; orange, mt-CO3. The position of NDUFA4 remains to be described. **(F)** 3D structure of ATP synthase. B-F: In grey all the nuclear-encoded subunits. [Modified from PDBE-Protein Data Bank in Europe].

MtDNA in mammals encodes for 13 polypeptides (Figure 5A), but also for several rRNAs (2) and tRNAs (22) for the intra-mitochondrial protein synthesis system. Mammalian mtDNA encodes different proteins of the OXPHOS system: seven of the forty five peptides that form Complex I (ND1, ND2, ND3, ND4L, ND4, ND5 and ND6) (Figure 5A, B), one of the eleven peptides of Complex III (Cyt b) (Figure 5A, D), three of the fourteen peptides of complex IV (COI, COII and COIII) (Figure 5A, E), and two of the fifteen polypeptides of the ATP synthase (ATP6 and ATP8) (Figure 5A, F). None of the proteins of complex II are mitochondrially encoded[20] (Figure 5C). There are intrinsic difficulties to reach an optimal adjust between proteins encoded by the mtDNA and those encoded by nDNA because of the genetic

differences. For optimal OXPHOS functionality, structural and functional matching between protein subunits of the respiratory complexes is crucial[16].

II.3.A. Mitochondrial DNA particularities

Since the discovery of maternal inheritance of mitochondrial DNA[107–109], different particularities of the extranuclear genome have been reported and investigated. The mitochondrial genome is circular, double-stranded and has a size of 16.5kb in humans[110] (Figure 6A). Contrary to nuclear DNA that it is biparental inherited, mitochondrial DNA is exclusively maternally inherited and the sperm mtDNA is actively degraded, resulting in non-mendelian rules of inheritance. That means that mtDNA is transmitted between generations without germline recombination (clonal expansion). MtDNA is polyploid (multiple copies per cell) ranging from 100-200.000 copies in different mammalian cells types[17,111,112]. There are no introns (93% coding region instead of 3% nuclear DNA coding region) and no histones in mitochondrial genome, all genes are transcribed as large polycistrons and the intraorganella protein synthesis uses its own genetic code (AUA= Met, TGA= Tryp; AGA and AGG stop codons)[113]. All the 37 mitochondrial-encoded genes are expressed regardless of the cell type.

MtDNA has a replication rate 5-10 times faster than nuclear DNA and the accumulation of mutations in mtDNA is about ten-fold greater than in the nuclear genome[111]. Replication of mitochondrial genome is carried out by the mtDNA polymerase-γ (POLG), which has also a proofreading activity (3'-5' exonuclease). However, mutation rate is an order of magnitude higher for mtDNA than for nDNA and recombination rate is marginal in mtDNA[114]. It has been suggested that recombination can occur at a population level[113]. Therefore, mtDNA has a high susceptibility to different DNA damages (e.g. oxidative damage). Recent studies reported that PrimPol, and unusual mammalian primase-polymerase that belongs to archaeo-eukaryotic primases, can maintain mtDNA integrity by initiation of the replication after DNA damage[115]. Different proteins are important for mitochondrial genome maintenance. The levels of transcription factor A (TFAM) correlates with the number of copies of mtDNA regardless of the cell type[17]. Mitochondrial RNA polymerase (POLRMT) is recruited and its specificity is enhanced by TFB2M to increase the expression of mitochondrial-encoded genes[17].

II.3.B. MtDNA variability

MtDNA particularities are responsible for the high sequence variability within species; mutations have been accumulated historically and in consequence, mtDNA haplotypes are classified into haplogroups. Single nucleotide polymorphisms (SNPs) are the most common source of variance between mtDNA sequences. Segregation between them during human evolution and global migration flow resulted in different haplogroups. In the recent years, the complete sequence of mtDNA genome could improve the worldwide mtDNA tree, being fundamental for phylogeographic analyses[116,117]. The evolution of mtDNA was originated from the accumulation of mutations in its sequence during years of maternally inherited lineages. Nowadays the role of mtDNA mutations in phylogenetics and environment adaptation is still under debate, as well as the relationship between them and the differences in energy expenditure and metabolic status. One of the first hypothesis points to selection as a mechanism of adaptation to climate and nutrition after *Homo sapiens* left Africa approximately 130-200.000 years ago[118] (Figure 6C). Recent studies in disease-causing mutations estimate that they are more frequent in young mitochondrial genome sequences and these findings implicate that sequences with more variations have been purified through natural selection in older populations[119].

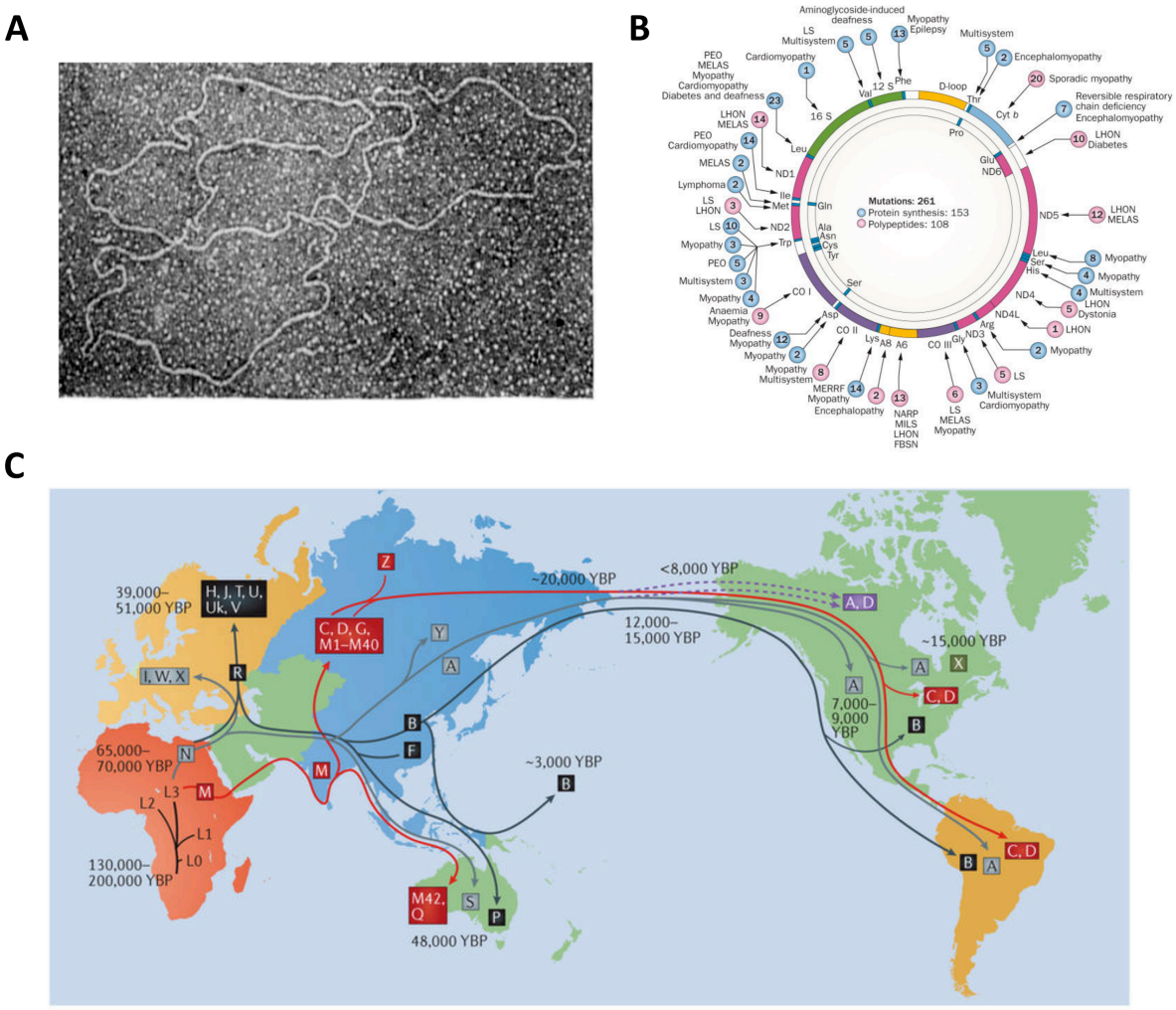

Figure 6. The complexity of mitochondrial genetics. (A) Catenated Circular DNA molecules in mitochondria of HeLa cell. *Obtained from Hudson, B. et al. (1967).* **(B)** Schematic map of mtDNA. Proteins of mtETC (CI, CIII, CIV and CV) complexes encoded by mtDNA are represented in different colours. 12S and 16S ribosomal RNA and 22 transfer RNAs with their own three-letter codes for the corresponding amino acids are represented in the inner circle. Different mitochondrial diseases associated with different mutations (the total number of them inside the circles). *Obtained from DiMauro S et al. (2013).* **(C)** Human haplogroups rise 40.000-150.000 years before present (YBP) and defined different populations as they migrated out of Africa (M and N haplogroups from L3). N is the eurasian haplogroup, giving rise in Europe the root haplogroup (R) for H, J, T, U haplogroups. A, B, C, D, G and F haplogroups emerged after the moving to Asia of N and M lineages. *Obtained from Stewart JB. and Chinnery PF. (2015)*

The role of mtDNA haplogroups in bioenergetics and their link with different longevities and pathological phenotypes remains controversial. It was first studied at the cellular and molecular level in cybrid cell lines and creating an association with human phenotypes in the clinic. Clinical data relating metabolic capacity and mitochondrial haplotype show that haplogroup L (L0, L2 and L3) has the lowest resting metabolic rate in comparison with the haplogroups presents in Europe (H, JT, UK)[120]. Among the mitochondrial parameters, the ones related with ROS production, apoptosis activation and OXPHOS performance are prone to have some pathological implications such as premature ageing, male subfertility, neurodegenerative diseases and cancer[84,121]. Disease-causing mtDNA mutations and metabolism (ROS generation, OXPHOS performance) and capacity of different mtDNA haplotypes for segregating pathogenic mtDNA are still under debate.

More than three decades ago it was discovered that deletions and point mutations of the mitochondrial genome could cause human diseases[122–124] (Figure 6B). Patients with mitochondrial myopathies presented a

variety of functional defects on the mtETC, most of them in complex I (NADH-CoQ reductase), complex III (ubiquinol-cytochrome c reductase) and complex IV (cytochrome c oxidase)[125,126]. The number of point mutations and deletions in mtDNA that cause human diseases (catalogued in the MITOMAP, http://www.mitomap.org) is still growing. Mitochondrial DNA rearrangements during reparation of double-strand breaks in mtDNA replication are also involved in mitochondrial disorders. In case of deletions, it has been suggested that they can be actively removed in proliferative cells, as they are only found in post-mitotic tissues[127]. Even though it is well known that SNPs influences the generation of different pathologies, it is not understood how different mtDNA haplogroups can impact the penetrance of autosomal genetic defects. Over the last years, the study of the neutrality of the different variants of mtDNA has been under debate. Some studies claim that different degrees of enzymatic activity present between haplotypes can explain the predisposition to a certain pathological status, having even more pronounced activity differences if the protein suffers the same mutation between haplogroups[11]. One of the examples are the patients that present clinical symptoms of LOHN syndrome (Leber Hereditary Optic Neuropathy), significantly associated with a specific mtDNA haplotype[128,129]. The marginal frequency of mitochondrial diseases in specific ethnic groups was revealed by the recent analysis of more than 30.000 mtDNA sequences from human macro-haplogroups L, M and N, which strongly associates the disease-causing mutations with mtDNA haplogroups. The study of the major alleles in each mtDNA sequence was assigned a pathogenicity score which is based on amino acid changes in mitochondria-encoded respiratory complexes subunits[119].

II.3.C. The MitMatch paradox

MitMatch refers to the requirement that the protein products of the mtDNA-encoded genes have to physically assemble with their counterparts encoded in the nucleus to build molecular machines called respiratory complexes. Mitochondrial encoded proteins need to match physically with up to 70 structural proteins of the same complexes that are encoded in nuclear genome. Failure in the interaction generates a non-functional OXPHOS system; consequently, rigorous limits for structural and functional matching are necessary.

The adjustment between nuclear and mitochondrial-encoded proteins is rapidly acquired in evolution as the optimal adjustment of both genomes requires co-evolution and is considered an important factor in the interspecies reproductive barrier[130]. It was long assumed that the fixed mtDNA polymorphic variants were phenotypically silent, but all these features of mtDNA and the concept of nDNA-mtDNA match changed this assumption. A controversy about the mtDNA haplogroups and disease association arose after reports connecting them[84,121,131–133] and studies not supporting that idea[134–138].

The mechanisms generating variability in genes of the OXPHOS system in nuclear and mitochondrial genome are different. In nuclear-encoded genes, the diversity is consequence of meiosis and recombination processes between individuals. Different combinations of alleles can be generated in this way but not with mitochondrial-encoded genes since they are maternally inherited. Variability can also be due to the tissue specific variants of the structural subunits of the respiratory complexes and/or expression of specific forms in conditions such as hypoxia (e.g. COX4-1 and COX4-2 subunits)[91]. The analysis performed by Lomax and Grossman (1989) in CIV (COX, cytochrome c oxidase) was the first evidence of the tissue-specific isoforms of nuclear-encoded OXPHOS subunits[139]. In a posterior study, COX nuclear-encoded subunits were analysed in the liver, kidney, heart and brain showing the kinetics of COX in each tissue. Differences of expression between the tissues and in areas within the same tissue were evident. These results combined with differences in the kinetic parameters of the enzyme based in the subunit variability, suggest a correlation between tissue metabolic oxidative demands and COX subunit composition[140,141,142]. But CIV

is not the only respiratory complex in which tissue-specific subunit isoforms were found. NDUFV3 is a nuclear-encoded subunit of CI that is present in different isoforms (NDUFV3-L, long; NDUFV3-S, short) originated by alternative splicing[143].

II.3.D. Effects of simultaneous alternative combination of mtDNAs within the same cell

All mitochondrial DNAs (mtDNAs) of a given cell in our organism are essentially identical, a situation named homoplasmy. Heteroplasmy refers to the presence of more than one variant of mtDNA co-existing in the same cytoplasm.

II.3.E. Heteroplasmy: from natural to artificial generation

Heteroplasmy is actively combated by several mechanisms, including degradation of the paternal mtDNA upon fertilization, and the existence of a genetic mtDNA bottleneck in oocyte development. Although the exclusive maternal inheritance in mammals, heteroplasmy has been described in humans, and the transmission of paternal mtDNA in interspecific mice crosses. The entire mechanism that permits degradation of paternal mtDNA is still undisclosed. Mitochondria from paternal origin suffer mitophagy inside the fertilized mammalian oocytes being ubiquitinated and degraded. The mechanism of removal in mammals is based on a combination between SQSTM1-dependent autophagy, VCP-mediated dislocation and the presentation of the ubiquitinated mitochondria of the sperm to the 26S proteasome[144].

On the other hand, natural or artificial processes can cause variability in mtDNA and following heteroplasmy. As mentioned above, mutation rate is higher for mtDNA in comparison with nDNA. Heteroplasmy is the most common feature in mtDNA-linked diseases, where mutated copies of mtDNA are inherited from maternal oocytes. Random mutation, segregation and amplification occur in somatic mitochondrial genome. Skin fibroblasts and blood mtDNA is reported that contains low amount of somatic mutations while iPSCs in elderly individuals present a larger number[145]. It is also known that mtDNA heteroplasmy can be used as a marker for most of types of tumours and during ageing process[146–148]. New insights into the field suggest trans-cellular migration or internalization of isolated functional mitochondria that could also cause heteroplasmy[149–151].

Novel medical techniques have come to the forefront of the public awareness because they generate heteroplasmy through artificial procedures. They rose up with three main objectives: 1) to prevent the transmission of mtDNA-linked diseases 2) to improve female fertility (oocyte rejuvenation) by injecting young donor oocyte cytoplasm into oocyte of subfertile women and 3) to restore mitochondrial performance by transfer of foreign mitochondria in some tissues.

II.3.F. Mitochondrial DNA segregation

Although mtDNA has a very high mutation rate, deletions in mitochondrial genome are controlled by mother ovary, as a mechanism of selection[20].

Many of the mitochondrial diseases are associated with heteroplasmy: mtDNA mutated copies coexist with wild type mtDNA in the same cytoplasm. In humans, heteroplasmy was first identified in studies with clinical patients that have variable levels of deletions or mutations[152]. Clinical symptoms usually appear when the patient has more than 70% of heteroplasmy, but this is not the same for all the patients with mtDNA disorders. The majority of the disorders in which heteroplasmy is present have the highest levels of mutated mtDNA in post-mitotic tissues such as skeletal muscle, cardiac muscle or brain[153].

The inheritance of mtDNA disease is marked by the large shifts of heteroplasmy between the mother and the offspring. Dynamics in mitochondrial DNA segregation during embryo development is poorly understood. The change of the proportion of mtDNA mutated copies is probably due to the so-called "bottleneck effect", whose underlying mechanism is still under debate. Most of the accepted theories are related to the large decrease of mtDNA copy number in germinal cells, the partitioning of clusters of mtDNA during cell division and the rate of replication of a subset of mtDNA during embryo development[153].

II.3.F.1. Segregation of genetically different mtDNA haplotypes

There are differences in rates of mtDNA proliferation between different mtDNA pairs in heteroplasmic cells, but the mechanisms are still unknown. Interestingly, mtDNA segregation seems not to be random. When confronted NZB mtDNA with Balb/c, or 129 variants, the same tissue always selected positively or negatively the NZB mtDNA[7-10]. Confrontation of mtDNAs of wild captured mice with that of C57BL/6 mouse strain also causes a characteristic pattern of segregation[153,154]. Different studies demonstrate that mtDNA segregation is the rule, not the exception, in pairing from diverse populations[154].

II.3.F.2. Impact of nuclear genes in mtDNA segregation

To elucidate the underlying rules of mtDNA segregation is necessary for understanding the clinical implications of heteroplasmy. Segregation patterns of mutant mtDNAs involved in mitochondrial diseases are important to determine the severity and the nature of the pathology. The rate of segregation of pathological mtDNAs depends on mitochondrial DNA copy number and the turnover rate.

The nuclear background can interfere with these patterns. In 2003, the study published by Battersby *et al*. provided the first evidence for nuclear control of mammalian mtDNA segregation[155]. Although there is an open debate about the randomness of mtDNA segregation of wild type (wt) variants of mtDNA in embryo development, most of the postnatal studies done in tissues support that nuclear factors can modulate the segregation behaviour.

The active molecular mechanisms driving non-random mtDNA segregation are poorly understood. But it is known that heteroplasmy changes with time for diverse mtDNA pairs[154]. In mouse models, it has been described that in some tissues heteroplasmy becomes stable, but others can resolve it. In some studied tissues (e.g. liver), the rate of selection is constant with time, independently of the initial mtDNA genotype[156,157] and more diverse mtDNA pairs exhibit stronger segregation[154]. Recently, the nuclear gene Gimap3, a non-mitochondrial GTPase, with unknown function, was identified to be responsible for the biased accumulation of Balb/cJ mtDNA in blood cells[158]. However, Gimap3 is not responsible for the biased accumulation of NZB mtDNA in liver or kidney. The discovery of this protein has two major consequences. First, the crosstalk of mtDNA with the nucleus is cell-type specific. Second, it resolves the controversy between the confronted explanations commented above. Since Gimap3 is not a mitochondrial protein, it cannot directly interact with a specific regulatory sequence of mtDNA that could be diverse between the two haplotypes. And since it can explain only the biased segregation in leukocytes but not in liver and kidney, it reinforces the view that functional crosstalk between mtDNA and nDNA may be on the bases of the segregation phenotype. MtDNA haplotypes can modulate the pathological effects of mutated nuclear encoded genes, as well as the nuclear genetic background and the environment can interfere with mtDNA variants[159,158,160,161].

II.3.G. Heteroplasmy between mtDNA variants: evolutionary, physiological, pathological and ethical implications

The interaction between different mtDNAs within the same cytoplasm is a fascinating biological problem with evolutionary, physiological, pathological and ethical implications. It has being suggested that heteroplasmy of neutral mtDNA variants may induce physiological differences[162] and may negatively affect behaviour and cognition[163]. This lead to propose that heteroplasmy may be maladaptive[164] and therefore, the driving force for mtDNA segregation would be improved cell fitness. Although appealing, a major weakness in this proposal is that in mtDNA in critical tissues for organismal fitness (e.g. post-mitotic heart, brain and skeletal muscle), little mtDNA segregation occurs even in the case of pathological mutations. However, some wild-derived haplotypes do exhibit segregation in a subset of these tissues[154].

Whether or not the presence of heteroplasmy itself presents health risks for the offspring by triggering a genomic conflict between alternative mtDNA variants with potential negative consequences is still under debate. A spectrum of physiological consequences have been reported, from none[154,157,165] to mild impact on physiology, such as transient hypertension or alterations in behaviour and cognition[162,163]. However, all reports have shown that mtDNA heteroplasmy between two non-pathological mtDNA haplotypes allows healthy development and the generation of stable and fertile heteroplasmic mouse colonies. Those reports documented heteroplasmic shifts in some tissues as an intriguing observation, without observing a functional relevance. This has led to the perception that heteroplasmy between non-pathological mtDNA haplotypes is, in most part, harmless, and of negligible concern in the medical applications that may generate it. However, most of these studies focused on young animals, and we are not aware of any longevity studies of the physiology of heteroplasmic animals reported to date. The potential health risk produced by heteroplasmy in the offspring is still a matter under debate.

II.3.H. Addressing the inheritance of mtDNA disease: classical and modern approaches

Currently, there is no cure for mitochondrial pathologies because of the heterogeneity in mutated mtDNA segregation, lack of disease progression rules and the huge difference between the clinical symptoms of the patients. One example is the 2,243 mutation in mitochondrial genome that affects the gene sequence of the $tRNA^{LeuUUR}$. It presents different clinic manifestations between patients (MELAS syndrome or diabetes and deafness)[166]. Only CoQ deficiencies have some alternatives of treatment[167,168]. Specific approaches to remove mutated mtDNA copies such as zinc-finger nucleases[169] (mtZFNs) and mitoTALENS[170,171] have been described to decrease the grade of heteroplasmy in tissues by cutting and degrading specific mtDNA sequences.

Most of the efforts are concentrated on the developing of new reproductive strategies to combat the inheritance of mitochondrial disorders (Figure 7A). Reproductive techniques can be separated into classical or modern strategies[153].

II.3.H.1. Classical approaches.

Oocyte donation. With this approach, it is possible to remove the risk of inheritance of mutated mtDNA copies from the mother. The fertilization is done between sperm, with the paternal nuclear background, and an external donor oocyte, with no representation of the mother nuclear background.

Mother's oocyte selection. With this technique is possible to choose the oocyte with less number of mutated mtDNA copies. This can only be used in heteroplasmic diseases where the heteroplasmy threshold has been established to avoid risk of clinical symptoms in the offspring.

Embryo heteroplasmy monitoring: pre-implantation genetic diagnosis (PGD). This is the most established technology to select low risk early embryos. It is necessary to evaluate heteroplasmy after the fertilization of the oocyte and in the early embryo stages (the variation in mutant mtDNA load is small between blastomeres). A variant of this approach, focus on blastocyst biopsy, does not guarantee the post-natal heteroplasmy because of the rapid mtDNA segregation in pre-implantation embryos[172] (Figure 7B).

II.3.H.2. Modern strategies.

Pronuclear transfer. After oocyte fertilization between mother oocyte (patient) and paternal sperm, the two pronuclei are transferred into the enucleated recipient oocyte (Figure 7C).

Spindle transfer. In this technique, the first step is the transfer of the chromosomal spindle from a patient donor oocyte into the recipient enucleated oocyte with the complete cytoplasm. The second step is the fertilization of the oocyte with the paternal sperm (Figure 7D).

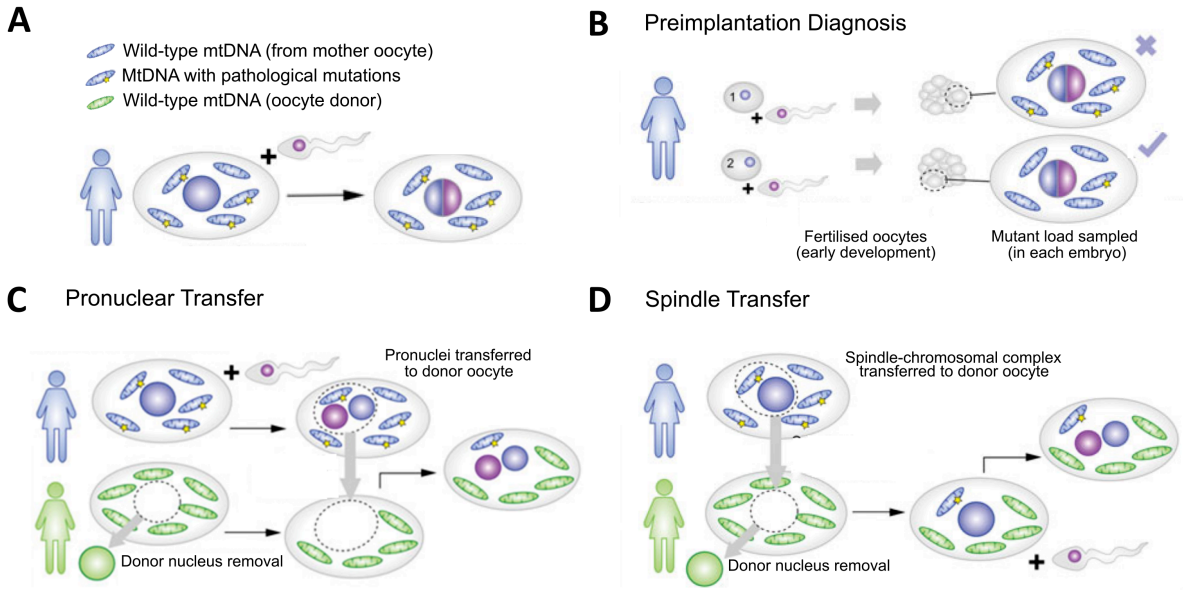

Figure 7. Mitochondrial replacement therapies. (A) MtDNA from the mother presents a percentage of mutated copies, and subsequently, high risk of inheritance between the mother and the offspring **(B)** Preimplantational genetic diagnosis (PGD). With this technique, low early risk embryos are selected; embryos are sampled to determine the mutant load. **(C)** Pronuclear transfer. Removal of the nucleus from the healthy donor oocyte to transfer the pronuclei inside it (from the mother oocyte and father sperm) **(D)** Spindle transfer. Chromosomal spindle from a healthy donor oocyte is transferred into an enucleated recipient oocyte before the fertilization. *From Burgstaller, J. P et al (2015).*

In these cases, most of the mtDNA belongs to the recipient oocyte and there would be a mixture between nuclear genomes from the mother and the father. However, none of the previous methods can eliminate the complete donor mtDNA carryover, some of the mitochondrial DNA from the mother is retained by definition. In these cases, the mutated and wt mtDNA (haplotype A) of the mother co-exist with the mtDNA of the recipient oocyte (haplotype B). Although the average of carryover is between 0.01-2% of the maternal mtDNA, it is still unknown if there could be negatives consequences of this phenomenon, which anyhow implies a low-level of heteroplasmy in the embryo. Because there would be three different mtDNA variants within the same cytoplasm (mutated mtDNA, haplotype A and haplotype B), the generation of impaired crosstalk between mtDNA-nDNA or a mismatch within mtDNA variants appears to

be possible [16,25,154]. Differences between pairwise comparisons in human mtDNA variants present more than 130 SNPs, 20 of them result in amino acid changes in OXPHOS proteins that can modify OXPHOS performance or change cellular environmental adaptation capacity. The evidences to support a positive segregation of mutant mtDNA are limited in those cases. However, small amount of carryover wild type mtDNA haplotype could segregate and dominate the cellular population[153].

In summary, heteroplasmy is a situation that has recently attracted the attention of the biomedical community because it may be produced during mitochondrial replacement therapies aiming to prevent transmission of pathogenic mutations in mitochondrial DNA[173] or to treat infertility[174]. Two major interconnected questions remain to be solved: 1) whether different versions of wild type mtDNAs are interchangeable without any phenotypic impact on function, which is highly debated in the scientific community; 2) whether the iatrogenic introduction of heteroplasmy presents health risks for the offspring by triggering a genomic conflict between alternative mtDNA variants with potential negative consequences.

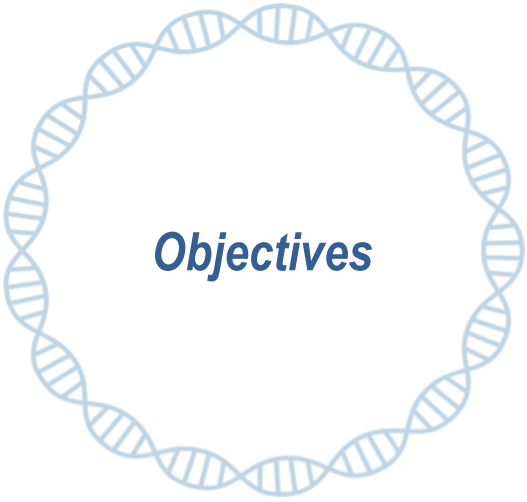

Objectives

III. Objectives

1. Analysis of the potential phenotypic consequences of the complete substitution of one mtDNA by another (both genetically wild type variants).

2. Evaluation of the functional impact of the mtDNA/nDNA match in different tissues in mice with identical nucleus but different mtDNA (conplastic mice).

3. Study of the possible generation of diverse functional OXPHOS systems with combinations of different nuclear and mitochondrial respiratory complexes encoded gene variants.

4. Study of the implication of the variable nuclear and environmental context on the functional impact and amplitude of the mtDNA/nDNA match.

5. Analysis of the physiological consequences of the generation of heteroplasmic embryos that contain a mixture of two wild type mtDNAs in the same zygote.

6. Establishment of the molecular basis of how the co-existence of two non-pathological variants of mtDNA within the same cytoplasm can affect the cardiopulmonary function, as well as the specific role of mitochondria in it.

7. Evaluation of how different conditions can modulate the mtDNA segregation behaviour by challenging heteroplasmic animals with a variety of genetic, environmental and pharmacological interventions to alter the organismal metabolism.

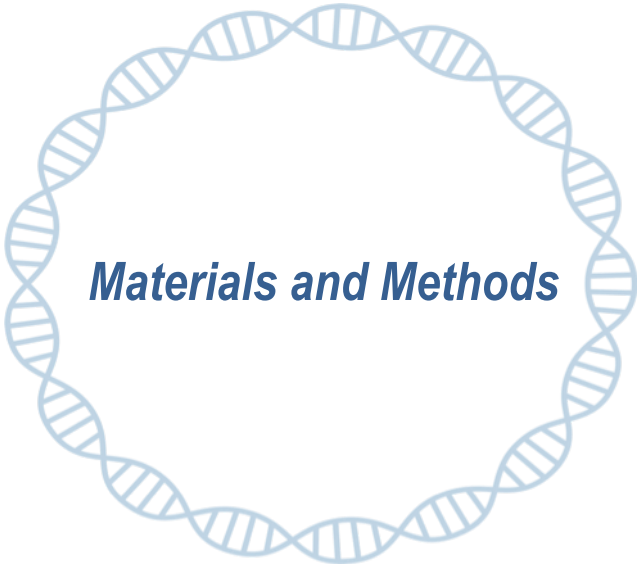

Materials and Methods

IV. Materials and Methods

IV.1. Cell Culture Procedures

IV.1.A. Cell line generation and cell culture conditions

IV.1.A.1. Mouse Adult Fibroblasts (MAFs)

Fibroblasts from homoplasmic and heteroplasmic mice were isolated from mouse ear and immortalized by transfection with pLOX-Ttag-iresTK (Addgene). Mouse ears were cut, digested with trypsin (30 minutes at 37 ºC) and seeded in 24-well plates with complete cell culture media adding 1% fungizone. Remaining tissue was removed after first adhesion of fibroblasts on the plate. Medium was changed daily. Immortalization was performed when the isolated cells reached 70-80% confluence.

Cell lines were grown in Dulbecco's Modified Eagle's Medium (DMEM, Sigma D5796) contaning 4500 mg/L glucose, 2 mM L-glutamine, supplemented with 5% fetal bovine serum (Sigma F7524), 1% penicillin-streptomycin (Lonza, 100 units/ml of potassium penicillin and 100 µg/ml of streptomycin sulphate per 1 ml of culture medium) and 1mM sodium pyruvate (Sigma). When indicated, the carbon source was 5 mM Glucose (Sigma) or 5 mM Galactose (Sigma). Culture media was changed every 2 days. Cell lines were grown at 37ºC in an atmosphere of 5% CO_2 / 95% air.

Table 1. Overview of the generated MAF cell lines

Cell Line	Cell type	Features	Mutation	Growth Media	Reference
BL/6^{C57}	MAFs	nDNA: C57BL/6(N) mtDNA: C57	-	Complete DMEM 5% FBS	Generated during the thesis
BL/6^{NZB}	MAFs	nDNA: C57BL/6(N) mtDNA: NZB	-	Complete DMEM 5% FBS	Generated during the thesis
BL/6$^{C57\text{-}NZB}$	MAFs	nDNA: C57BL/6(N) mtDNA: C57+NZB	-	Complete DMEM 5% FBS	Generated during the thesis
BL/6$^{C57\text{-}NZB}$ NNT^{KO}	MAFs	nDNA: C57BL/6(J) mtDNA: C57+NZB	*Nnt*$^{-/-}$	Complete DMEM 5% FBS	Generated during the thesis
BL/6$^{C57\text{-}NZB}$ SCAF1^{113}	MAFs	nDNA: C57BL/6(N) mtDNA: C57+NZB	*Scaf1*$^{113/113}$	Complete DMEM 5% FBS	Generated during the thesis
BL/6$^{C57\text{-}NZB}$ SCAF1$^{111/113}$	MAFs	nDNA: C57BL/6(N) mtDNA: C57+NZB	*Scaf1*$^{111/113}$	Complete DMEM 5% FBS	Generated during the thesis
ρ_0	MAFs	nDNA: L929 No mtDNA	-	Complete DMEM 5% FBS 50 µg/ml uridine	Moreno-Loshuertos *et al.* 2006

IV.1.A.2. Mouse Embryonic Fibroblasts (MEFs)

MEFs were isolated from E13.5 embryos using a previously described protocol[175]. Briefly, each embryo was dissected into 10ml of sterile PBS and internal organs as well as head and legs were removed. After 30

minutes incubation with gentle shaking at 37 ºC using 5ml 0.1 % trypsin, cells were plated on two 100 mm dishes and incubated for 24-48h.

MEFs immortalization and culture. To establish the immortalized MEFs, an early passage of MEFs was seeded in 60mm plates and infected with 10^5 IU/ml packaged retrovirus E6/E7. Selection was performed with 400 µg/ml of G418 over the course of 10 days.

Immortalized MEFs were grown in DMEM (Gibco 11966-025 without glucose) supplemented with 10% fetal bovine serum (FBS; Sigma), 1% penicillin-streptomycin (100 units of potassium penicillin and 100 µg of streptomycin sulphate per 1 ml of culture media, Lonza) and 1mM sodium pyruvate (Sigma). When indicated, the carbon source was: 4.5 g/l of glucose (Sigma), 0.9 g/l of glucose or 0.9 g/l of galactose (Sigma). Culture medium was changed every 2 days. Cell lines were grown at 37 ºC in an atmosphere of 5 % CO_2 / 95 % air.

Table 2. Overview of the generated MEF cell lines

Cell Line	Cell type	Features	Growth Media	Reference
BL/6^{C57}	MEFs	nDNA: C57BL6(N) mtDNA: C57	DMEM 10% FBS	Generated during this thesis and Latorre-Pellicer (2014)
BL/6^{NZB}	MEFs	nDNA: C57BL6(N) mtDNA: NZB	DMEM 10% FBS	Generated during this thesis and Latorre-Pellicer (2014)
BL/6$^{C57\text{-}NZB}$	MEFs	nDNA: C57BL6(N) mtDNA: C57+NZB (Different proportions)	DMEM 10% FBS	Latorre-Pellicer (2014)

IV.1.B. Growth curves

Cells were seeded in 96-well plates (2,500 cells/well) and grown in DMEM supplemented with glucose (5 mM) or galactose (5 mM). Cells with deficiency in respiratory function were not able to grow in medium with galactose as substrate due to the low ATP production. Multi-day test (0-96 hours) of a total of 8 replicates per cell line or cell clone were made by high throughput screening using CYQUANT™ NF Cell Proliferation Assay Kit (ThemoFisher Scientific C35006). CYQUANT™ is a fluorescent dye, which exhibits strong fluorescence enhancement when bounds to nucleic acids. Incubation of 30 minutes at 37 °C in the dark was needed prior to the fluorescence measurement (Excitation: 488 nm; Emission: 535nm).

IV.2. Cellomics Techniques: Flow cytometry and cell sorting

IV.2.A. Reactive Oxygen Species (ROS) and Mitochondrial Membrane Potential (MMP) analysis

ROS and MMP were measured in MAFs and MEFs using 2´-7´dichlorofluorescein diacetate (H2-DCFDA, ThermoFisher, 0.4 µM final concentration), and tetramethylrhodamine methyl ester perchlorate (TMRM, Sigma, 100 nM final concentration). A total of 10,000 events were recorded for each sample using the FACSCanto™ II system (BD Biosciences). All experiments were performed in triplicates. Samples were analysed with the BD FACSDivaTM software package and the average of the medians and corresponding standard deviations were calculated using the FlowJo software (v10).

IV.2.B. Mitochondrial content assay

Mitochondrial content was measured by flow cytometer using the probe N-Nonyl acridine orange (NAO, ThemoFisher Scientific A1372). Cells were collected and incubated with 10 µM NAO during 10 minutes at 37ºC. (Excitation: 450 nm; Emission: 530 nm). 4',6-diamidine-2'-phenylindole (DAPI) was used to discard necrotic cells from the analysis using FlowJo software (FlowJo LLC, Ashland, OR).

IV.2.C. Cardiac tissue inflammation assessment

Table 3. Antibodies used to define cardiac cell populations

Conjugated primary Antibodies	Clone	Source	Reference	Experiment
CD11b-PE	M1/70	Tonbo Biosciences	50-0112-U100	Flow cytometry/Sorting
F4/80-Biotin	BM8	eBioscience	14-4801-82	Sorting
F4/80-APC	BM8	Bio-RAD	MCA497A647	Flow cytometry
CD45-PerCP Cy5.5	A20	Biolegend	103132	Flow cytometry/Sorting
Ly6C-FITC	HK1.4	Biolegend	128006	Flow cytometry
CD31-PE/Cy7	390	eBioscience	25-0311-81	Flow cytometry/Sorting
CD115-PE	AFS98	eBioscience	12-1152-83	Sorting
MHCII-PECy7	M5/114.15.2	Biolegend	107629	Flow cytometry/ sorting
Ly6G-AF647	HK1.4	Biolegend	127610	Sorting

Tissue preparation, flow cytometry and cell sorting. Hearts from different mice strains were collected, cut and digested in HBSS with liberase (1 U/ml, Roche) and DNase I (10 mU/ml, Sigma) for 40 min at 37 °C. After digestion, single-cell suspensions were obtained by gentle pipetting and mechanical dissociation of the remaining tissue through cell strainers (BD Falcon). Single-cell suspensions were incubated with the indicated antibodies for 15 min at 4°C (Table 3). Samples were acquired in a LSRII Fortessa (BD Biosciences) or Canto HTS (BD) equipped with the BD FACSDivaTM Software. We use the FlowJo software (FlowJo LLC, Ashland, OR) to analyse the data.

The absolute number of cells per tissue was estimated using fluorescent beads. Beads (BD Biosciences) were prepared at a concentration of 10,000 beads per ml in a buffer containing 0.5 M EDTA (Sigma), 0.5 % FBS and 0.1 µg/mL DAPI (Life Technologies) in PBS. 500 µl of this PEB/DAPI buffer containing beads were added to the single cell suspensions and stained for flow cytometry as indicated above. To estimate the absolute number of cells, 500-1,000 beads were acquired per tube in order to ensure accuracy.

The different cardiac cell populations were sorted (myeloid cells, lymphoid cells and endothelial cells) and collected into 1.5 ml eppendorf tubes. Cell suspensions were centrifuged 7 minutes 1500 rpm and DNA was extracted from the pellet. Heteroplasmy was assessed in all the different populations (Material and methods, nDNA and mtDNA genotyping).

IV.3. Animal Handling Procedures

All animal procedures conformed to the EU Directive 86/609/EEC and Recommendation 2007/526/EC regarding the protection of animals used for experimental and other scientific purposes, enforced by Spanish law under Real Decreto 1201/2005. Approval of the different experimental protocols requires the estimation of the adequate sample size as well as the definition of the randomization and blinding criteria. Mice under endpoint criteria were excluded from analysis in long-term experiments. The mice were fed a standard chow diet (5K67 LabDiet) or, when indicated, a high-fat diet (D12492, Open Source Diets). The mice used for the studies were males or, when indicated, females.

IV.3.A. Experimental Mouse Models

IV.3.A.1. Generation and breeding of Conplastic Mice

Parental C57BL/6JOlaHsd and NZB/OlaHsd strains were purchased from Harlan Laboratories. The C57BL/6JOlaHsd strain was derived in 1974 from the C57BL/6J strain by the Jackson Laboratories but differs from the parental strain. The C57BL/6JOlaHsd strain does not harbour the nicotinamide nucleotide transhydrogenase (NNT) deletion due to a spontaneous mutation that renders the encoded enzyme undetectable, which is characteristic of the C57BL/6J strain provided by Jackson Laboratories. To avoid confusion, we call C57BL/6JOlaHsd mice C57BL/6 throughout the thesis. Conplastic strains were obtained by backcrossing females (mitochondrial donors) with males of the parental recipient strain for more than 20 generations to create a new line harbouring the nuclear genome of one strain and the mtDNA of the other. Conplastic strains were maintained by backcrossing females of the conplastic strain with males of the parental recipient strain. The offspring after the tenth generation of backcrossing were considered conplastic. Total DNA was extracted from tissues and genotyped by PCR restriction-fragment length polymorphism analysis (RFLP) and by Affymetrix mouse Diversity Genotypinc Array to verify the identical nuclear background.

IV.3.A.2. Heteroplasmic Mice generation

Heteroplasmic mouse embryos carrying two mtDNA genotypes were generated by the transgenesis unit at CNIC by electrofusion of cytoplasts from NZB/OlaHsd (NZB) zygotes to recipient C57BL/6OlaHsd (B6) one-cell embryos. They were cultured overnight and transplanted as two-cell embryos into pseudo pregnant Hsd:ICR (CD-1®) females to complete development to term. The procedure is based on the method described for pronuclear transfer between single-cell embryos[176], and other reports[156,177–179] .

IV.3.A.2.a. C57BL/6JOlaHsd and NZB/OlaHsd zygotes

Sexually immature 3-5 weeks-old C57BL/6JOlaHsd (B6) and NZB/OlaHsd (NZB) females were induced to superovulate by intra-peritoneal injection of 5 IU pregnant mare serum gonadotropin (PMSG) (FOLLIGON 5000, MSD Animal Health) and given 5 IU human chorionic gonadotropin (hCG) (VETERIN CORION®, DIVASA-FARMAVIC S.A., Spain) 48 later. After hCG injection, females were mated 1:1 with fertile B6 and NZB males respectively and examined the following morning for the presence of vaginal copulatory plugs. Plugged females were sacrificed to obtain the corresponding zygotes

by oviduct flushing. Fertilized embryos were flushed from the oviducts[180] at 21-22 h after hCG injection using homemade HEPES-buffered KSOM medium (FHM)[181], and were cultured in KSOM medium (KSOMaa-Evolve, Zenith Biotech, Cat. #ZEKS-050) in a humidified incubator at 37 ºC and 5 % CO_2 in air; KSOM contained 1 mg/ml bovine serum albumin (BSA) (Sigma-Aldrich, Cat. #A3311-10G), which was filtered through 0.22 µm pore size membrane filter (Millex™-GP, Millipore, Cat. #SLGPO33RS) before use.

IV.3.A.2.b. Generation of NZB/OlaHsd cytoplasts

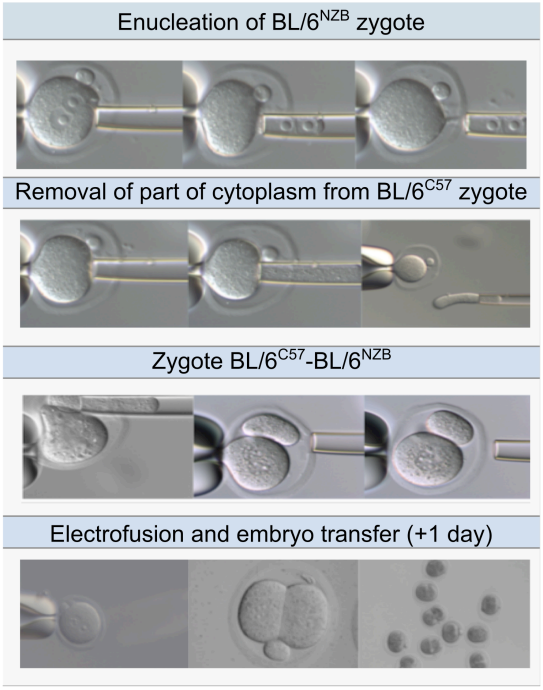

Figure 8. Generation of heteroplasmic mice. Work done by Transgenesis Unit (CNIC). *Adapted from Latorre-Pellicer (2014).*

The visual area through the microscope was divided into four quadrants by X and Y-axis; the X-axis was given along the enucleation pipettes that were placed at the left and right sides of the microscope, respectively. After collection of B6 and NZB zygotes, ten NZB zygotes were cultured in KSOM medium containing 5 µg/mL of cytochalasin-B (Sigma-Aldrich, Cat. #C6762-1MG) and 0.1-µg/mL of demecolcine (Colcemid™ Sigma-Aldrich, Cat. #D1925-20ML) that was previously equilibrated at 37 ºC and 5 % CO_2 in air for 2-3 hours; the zygotes were cultured under these conditions for 15-45 minutes until use. At 15 minutes of incubation, just before starting the production of cytoplasts from the NZB zygotes, twenty B6 zygotes were also placed into another dish of KSOM+CB+D and incubated at 37 ºC and 5 % CO_2 in air for 15-45 minutes, so that incubations of NZB and B6 zygotes into KSOM+CB+D were delayed for 15 minutes each other during the whole process. Immediately after, five NZB zygotes were washed in FHM medium containing 5-µg/mL of Cytochalasin-B (Sigma-Aldrich, Cat. #C6762-1MG) and 0.1 µg/mL of demecolcine (Colcemid™) (Sigma-Aldrich, Cat. #D1925-20ML) (FHM+CB+D) and placed at the Southwest quadrant of the microsurgery chamber. This chamber was built by gluing one 75x25mm and 1-mm thick microscope glass slide to a perspex frame (75x25mm external dimensions, 50x18mm internal dimensions, and 5-mm thick), and contained a 20 µl drop of FHM+CB+D medium covered with sterile light paraffin oil (NidOil™, Nidacon). Microsurgery was performed at room temperature (21-22 ºC) using an inverted microscope (AxiObserver-D1, Zeiss, Germany) equipped with a differential interference contrast (DIC) optical system as well as micromanipulators (TransferMan®-NK2, Eppendorf, Germany)

and microinjectors (CellTram® Vario, Eppendorf, Germany). Using the holding pipette (Sunlight Medical Inc., Cat. #SHP-100-25), one NZB zygote was taken and maintained in place at the central area of the chamber, and its zona pellucida was pierced using a 15-µm ID glass pipette (Eppendorf Custom Tip Type I: ID, 15-m; Angle, 25º; Limb length, 1000-µm; Front surface, round) attached to a piezoactuator (Piezo Micro Manipulator PMM-150FU, Prime Tech Ltd., Japan). Afterwards, the zygote was enucleated by suction of the two visible pronuclei surrounded by a small portion of cytoplasm (karyoplast) producing the so called "primary cytoplast" (PC), the cytoplasm without nuclear genetic material, and karyoplasts were left at the Northeast quadrant of the chamber; then, using the same pipette, two smaller "secondary cytoplasts" (SCs), about 1/3 of the original zygote in size, were produced from the PC, and were placed in the Southeast area of the microsurgery chamber until their introduction into the perivitelline space of the recipient B6 zygotes for electrofusion. Finally, the residues of the NZB zygotes were removed from the chamber.

IV.3.A.2.c. Production of "C57BL/6JOlaHsd zygote-NZB/OlaHsd cytoplast" couples

Immediately after the production of ten SC from five NZB zygotes, ten B6 zygotes maintained in KSOM+CB+D (≈ 15-20 min of incubation) were removed from the incubator, washed in FHM+CB+D medium, and placed at the Southwest area of the microsurgery chamber. The zona pellucida of each B6 zygote was drilled using the piezoactuator, and then a B6-PC similar in size to the NZB-SC was taken and placed at the Northeast area of the chamber together with the NZB-karyoplasts. Then, one NZB-SC previously obtained was recovered with the glass pipette (I.D. = 15-µm) and introduced into the perivitelline space of the B6 zygote. The resulting "B6 zygote-NZB cytoplast" couple remained in the North area of the microsurgery chamber and the process was repeated until ten couples were made. At the end, the couples were taken out of the microsurgery chamber and washed in 2-3 ml of FHM medium at room temperature (21-22 ºC) to eliminate cytochalasin-B and demecolcine. Right after, they were submitted to the electrofusion protocol. The entire process of cytoplast production, couple formation, and electrofusion was repeated until more than 30 heteroplasmic zygotes were produced.

IV.3.A.2.d. Electrofusion of "C57BL/6JOlaHsd zygote-NZB/OlaHsd cytoplast" couples: Production of C57BL/6-mtC57+NZB zygotes

Electrofusion was carried out using a BTX ECM 2001 Electro Cell Manipulator (BTX®, Harvard Apparatus,) and a BTX Model 450-1 Microslide 1-mm gap chamber (BTX®, Harvard Apparatus, Cat. #45-0104). The electrofusion solution (EFS) was 0.3 M mannitol (Sigma-Aldrich, Cat. #M4125) containing 0.3%w/v BSA (Sigma-Aldrich, Cat. #A3311), with pH adjusted to 7.2-7.4 and filtered through 0.22-µm pore size membrane filter (Millex™-GP, Millipore, Cat. #SLGPO33RS). Before electrofusion, the couples were washed in 3-4 ml of EFS and placed into a 100-µl EFS drop placed between the electrodes. Electrofusion was carried out using the following parameters: (a) Orientation: AC 2V; AC Duration 6 sec, (b) Fusion: Voltage, 120V; Pulse, 25-µsec, number of pulses, 2, and (c) Postfusion: AC, 2V; Duration 6 sec. Afterwards, electrically treated couples were removed and washed first in 3-4 ml of FHM at room temperature (21-22 ºC) and then in 80 µl drops of Evolve-KSOM covered with paraffin oil and previously equilibrated at 37 ºC and 5 % CO_2 in air, and let to fuse inside the incubator in another drop of Evolve-KSOM also covered with paraffin oil. equilibrated at 37 ºC, and 5 % CO_2 in air. The KSOM dish containing the treated couples was visually checked for electrofusion, and electrofused couples were recorded; non-electrofused couples were removed to another dish in case that electrofusion was delayed. Only confirmed fused couples were cultured overnight at 37 ºC and 5 % CO_2 in air. Next day, the resulting embryos at two-cell stage were transferred via oviduct to the reproductive tract of +0.5dpc pseudo pregnant Hsd:ICR (CD-1®) mouse females until birth[180].

IV.3.A.2.e. Mouse heteroplasmic strains nomenclature

To the best of our knowledge, no consensus nomenclature for heteroplasmic mouse strains exists. Here, we propose and use the following designation to name heteroplasmic mouse strains: NUCLEAR GENOME-mtCYTOPLASMIC GENOME #1 + CYTOPLASMIC GENOME #2 (i.e., C57BL/6J-mtC57BL/6+NZB, a strain with the nuclear genome of C57BL/6J and the cytoplasmic (mitochondrial) genome of C57BL/6J and NZB) [182]. We short the nomenclature to BL/6$^{C57\text{-}NZB}$ to simplificate it.

IV.3.A.3. Maintenance of heteroplasmic colonies

Heteroplasmic strains were maintained by outcrossing heteroplasmic females (BL/6$^{C57\text{-}NZB}$) with BL/6^{C57} males. Only females with an initial level of NZB heteroplasmy above 30 % were used for colony maintenance.

IV.3.A.4. Genetic modifications in heteroplasmic mice

To produce heteroplasmic mice OMA1^{KO}, BL/6$^{C57\text{-}NZB}$ females were outcrossed to OMA1^{KO} males (C57BL/6JOlaHsd background) to generate the F1 heterozygote mice, which were then intercrossed to obtain the F2, OMA1^{KO} heteroplasmic mice. The strain was maintained by outcrossing heteroplasmic females (BL/6$^{C57\text{-}NZB}$ OMA1^{KO}) with BL/6^{C57} OMA1^{KO} males.

To produce heteroplasmic mice PGC1α^{KO}, BL/6$^{C57\text{-}NZB}$ females were outcrossed to PGC1α$^{\text{-}KO}$ males (C57BL/6 JOlaHsd background) to generate the F1 heterozygote mice, which were then intercrossed to obtain the F2, PGC1α^{KO} heteroplasmic mice. Heteroplasmic strains were maintained by outcrossing heteroplasmic females (BL/6$^{C57\text{-}NZB}$ PGC1α^{KO}) with males BL/6^{C57} PGC1α^{KO}.

To produce heteroplasmic mice NNT^{KO}, BL/6$^{C57\text{-}NZB}$ females were outcrossed to NNT^{KO} males (C57BL/6J background) to generate the F1 heterozygote mice, which were then intercrossed to obtain the F2 NNT^{KO} heteroplasmic mice. Heteroplasmic strains were maintained by outcrossing heteroplasmic females (BL/6$^{C57\text{-}NZB}$ NNT^{KO}) with BL/6^{C57} NNT^{KO} males.

To produce heteroplasmic mice SCAF1^{113}, BL/6$^{C57\text{-}NZB}$ females were outcrossed to SCAF1^{113} males (C57BL/6JOlaHsd nuclear background) to generate the F1 heterozygote mice, which were then intercrossed to obtain the F2 SCAF1^{113} heteroplasmic mice. Heteroplasmic strains were maintained by outcrossing heteroplasmic females (BL/6$^{C57\text{-}NZB}$ SCAF1^{113}) with BL/6^{C57} SCAF1^{113} males.

IV.3.B. *In vivo* modulation of the mtDNA segregation

Mice were fed with high-fat diet (HFD) (D12492 Open Source Diets) from 28 days of age until being sacrificed. Mice treated with N-acetyl-L-cysteine (NAC) or dichloroacetate (DCA), were given 61.2 mM of NAC (Sigma-Aldrich) or 66.2 mM of DCA (Sigma-Aldrich) in drinking water from 28 days of age until being sacrificed.

IV.3.C. Mouse embryo collection

Heteroplasmic and homoplasmic females were mated with BL/6^{C57} males. The presence of a vaginal plug was taken as evidence for pregnancy, and 11.5 and 12.5 dpc embryos were collected. Their positions in the uterus were annotated for posterior genotyping (Material and methods, nDNA and mtDNA genotyping).

IV.3.D. Growth curve analyses in mice

To calculate growth curves, 15-20 animals per strain were weighted at the starting age and every week/month thereafter for the period indicated in each experiment.

IV.3.E. Survival studies

Mice that were found dead at daily inspections were considered as censored deaths. Criteria for euthanasia were based on an independent assessment by a veterinarian, and only cases where the condition of the animal was considered incompatible with continued survival are represented as deaths in the curves. Survival curves and weight gain were performed in the same group of animals.

IV.3.F. Blood and plasma analysis

All blood samples were obtained from cardiac puncture early in the morning. Mice were not fasted before the analysis.

IV.3.F.1. Haematology

Blood was collected in Microvette® 100 ethylenediaminetetraacetic acid (EDTA) tubes and kept at 4ºC until the analysis. Haematological analysis was assessed with a Pentra 80 automated blood cell analyser. White blood cells (WBC), red blood cells (RBC), haemoglobin (HGB), haematocrit (HCT), mean corpuscular volume (MCV), mean corpuscular haemoglobin (MCH), mean corpuscular haemoglobin concentration (MCHC), red cell distribution width (RDW), platelets (PLT), mean platelet volume (MPV), plateletcrit (PCT), platelet distribution width (PDW) and percentage and total number of neutrophils, lymphocytes, monocytes, eosinophils and basophils were analysed.

IV.3.F.2. Biochemical profile

Blood was collected using EDTA tubes. For plasma isolation, samples were centrifuged 15 minutes at 4 ºC at 2000 x g. The biochemical profile was assessed with a Dimension RxL Max® automated analyser. The parameters measured were: alkaline phosphatase (ALP), sodium (Na), chlorine (Cl), creatine kinase-MB (CK-MB), Creatine kinase (CK), Myoglobin (Myo), Creatinine (Crea), Glucose (Gluc), aspartate transaminase (AST), lactate dehydrogenase (LDH), potassium (K), total proteins (TP), blood urea nitrogen, protein C reactive (PCR) and albumin. All reagents used for the different tests were purchased from Siemens.

IV.3.G. Haematopoietic stem cell (HSC) analysis

80-weeks-old mice of $BL/6^{C57}$ and $BL/6^{NZB}$ strains were used for the experiment. The femur bone was excised from the mice and crashed and HSCs were purified from bone marrow. The antibodies used in the analysis were CD150 (PECy7), anti-SCA1 (PB), CD48 (APC, X), anti-cKit (APCeF780, X) and the LIN mix (anti-CD4, anti CD8a, anti-CD5, anti-Gr1, anti-Mac1, anti-B220, anti-Ter119). For all experiments, LT-HSCs were analyzed as LSK $CD150^{+}$ $CD34^{-}$ $CD48^{-}$.

IV.3.H. Adult cardiomyocyte isolation

Animals were heparinized (1,000 units/mouse) and euthanised. The hearts were surgically excised and immediately immersed in Ca^{2+}-free ice-cold buffer containing 10 mM of the contractile inhibitor 2,3-

butanedione monoxime (13 mM NaCl, 4.7 mM KCl, 0.6 mM KH_2PO_4, 0.6 mM Na_2HPO_4, 1.2 mM $MgSO_4$, 0.032 mM phenol red (to verify perfusion of the coronaries), 12 mM $NaHCO_3$, 10 mM $KHCO_3$, 10 mM HEPES, 30 mM taurine, 10 mM 2,3-butanedione monoxime and 5 mM glucose, the pH was adjusted to 7.46 with NaOH. The heart was then cannulated and connected to a Langendorff apparatus for retrograde perfusion with the flow rate adjusted to 3 ml/minute. The cannulated heart was first perfused with perfusion buffer at 37 °C for 4 minutes, and then digested at the same temperature for 22-24 min with the above perfusion buffer supplemented with 0.2 mg/ml liberase (Sigma), 0.14 mg/ml trypsin and 12.5 µM Ca^{2+}. To stop digestion the heart was removed from the Langendorff apparatus, mechanically minced with forceps and progressively introduced to a series of "digestion stop" solutions which are based on the above perfusion buffer with 12.5 µM Ca^{2+} added, and additionally contain variable percentages of fetal bovine serum: first 10%, then 5%. Cells were mechanically dissociated by gentle agitation of the heart debris with a Pasteur pipette. Physiological Ca^{2+} levels were slowly re-introduced by applying several steps of increasing Ca^{2+} concentration. Heteroplasmy was assessed in single myocytes after isolation one by one in a multiwell plate. Genotyping of mtDNA was performed as previously mentioned (See Material and methods, DNA extraction and PCR).

IV.3.I. Chronic MitoQ administration in mice

MitoQ (0.15 mg/day) was chronically administered. Mice were deeply anesthetized with sevoflurane (2,5-3.5 % and 1 % O_2) and osmotic minipumps (Mini-Osmotic Pump Model 2004, Alzet) were subcutaneously implanted for continuous doses during 28 consecutive days.

IV.3.J. Histological Assays

Table 4. Histological stains

Stains	Comments	Samples
Picrosirius Red (PSR)	Staining for collagen depositions (usually type I collagen)	OCT-embedded tissue section
F4/80	The antibody recognises the mouse F4/80 antigen, a 160kD glycoprotein expressed by murine macrophages	Paraffin-embedded tissue section
Masson's Trichrome	Three dyes are employed to selectively stain muscle, collagen fibers, fibrin, and erythrocytes	Paraffin-embedded tissue section
Hematoxylin and Eosin (H&E)	Staining for nucleus and cytoplasmic inclusions	Paraffin-embedded tissue section
COX/SDH	Staining for cytochrome oxidase and succinate dehydrogenase	OCT-embedded tissue section
Evans Blue	In presence of plasma membrane damage, the dye enters in the cytoplasm and nucleus. Used for cell necrosis	OCT-embedded tissue section

IV.3.J.1. Cardiac tissue analyses

Tissue samples were fixed in 4% paraformaldehyde, processed and embedded in paraffin. Sections (6-12 µm) were prepared and mounted on coverslips for staining with different reagents (Table 4). Tissue

images were captured using a NanoZoomer 2.0RS digital slide scanner (Hamamatsu), digitalized using NDP view2 Software and analysed by ImageJ v.1.6.0 software (NIH).

Samples were digitalized using NDP view2 software and collagen fibres were calculated as staining positive area *vs.* total area for heart sections or as staining positive area *vs.* total perimeter for tissue sections. The ratios were calculated using Fiji (http://fiji.sc/Fiji) and ImageJ v.2.0.0 Software (NIH)[183,184].

IV.3.J.2. Analysis of the ovary

The ovaries were collected from the homoplasmic and heteroplasmic females, fixed with 4% PFA for 24 hours and sectioned at 5 µm. Four sections from each ovary at three different levels of the tissue (40 µm between every section was discarded) were processed, mounted on a glass slide, stained with H&E and digitalized using NDP view2 Software. Ovaries from females of 3,6, 9 and 12 months of age were analysed by ImageJ v.1.6.0 Software (NIH) to assess the percentage of lipofuscin in ovaries with the age of the mice. Definition of primordial follicle, primary follicle and growing follicle was done according to Treuting P. and Dintzis S. (2012)[185].

IV.3.J.3. Morphometric analyses of retinal sections

Complete eye was dissected and fixed in Davidson´s fixative (2% formaldehyde, 35% ethanol, 10% glacial acetic acid), embedded in paraffin, sectioned with a microtome (10 µm) and mounted on glass slides. The retina was divided into superior and inferior sections. Outer nuclear layer (ONL) analysis was performed using Fiji image processing package (NIH)[184].

IV.3.J.4. Superoxide levels in frozen tissues: DHE Staining

Cardiac tissue was dissected, mounted in OCT embedding compound and cryostat-sectioned (12 µm). Slides were defrosted and incubated for 45 minutes at 37ºC with 5 mM dihydroethidium (DHE). Samples were washed twice with PBS and incubated 5 minutes at RT with DAPI solution (0.1 mg/ml) for counterstaining of all nuclei. Slides were washed twice with PBS and water and mounted in ProLong® Gold Antifade Reagent. Confocal fluorescence microscopy images were obtained on a Leica SPE-Upright confocal microscope using a HCX PL APO CS 40x 1.25 oil objective. Images were acquired with LAS-AF V 2.3.6 acquisition software (Leica Microsystems). DHE and DAPI fluorescence of cardiac sections was quantified using ImageJ v. 2.0.0 (NIH). The mean DHE fluorescence was quantified and expressed relative to values obtained for DAPI mean fluorescence.

IV.3.J.5. Evans Blue assay

Evans blue dye (Sigma E2129-50G) was used as an indicator of cardiomyocyte membrane permeability and viability. The compound was injected intravenously in 20-weeks-old mice (100mg/kg body weight). After 24 hours, mice were sacrificed and tissue slides were processed for counterstaining of the samples. Cardiac sections were quantified using ImageJ V2.0.0 (NIH).

IV.3.J.6. Histological analysis of brain sections

30 weeks-old mice were deeply anesthetized with pentobarbital (50 mg/kg body weight) and perfused through the left cardiac ventricle, first with 0.9 % NaCl and then for 5 min with 4 % paraformaldehyde in 0.1 M phosphate buffer pH 7.4. Brains were post-fixed for 4 h at 4 °C in the same fixative and washed three times with 0.1 M phosphate buffer, pH 7.4 at room temperature. Coronal sections of the brain

(50 µm) were obtained using a Vibratome (VT 1000S, Leica Microsystems, Wetzlar, Germany). Immunohistochemistry was carried out in free-floating sections under moderate shaking. All washes and incubations were done in 0.1 M phosphate buffer pH 7.4, containing 0.3% bovine serum albumin and 0.3% Triton X-100. After several washes in buffer, the sections were incubated overnight at 4 °C with a rabbit antibody against glial fibrillary acidic protein (GFAP; diluted 1:1000; DAKO), as a marker of reactive and resting astrocytes, or with rabbit polyclonal antibody for IBA1 (ionized calcium-binding adaptor molecule 1), as a marker for microglia (Wako Chemical Industries, Japan; diluted 1:2000). Sections were rinsed in buffer and incubated for 2 h at room temperature with the corresponding anti-mouse or anti-rabbit biotinylated secondary antibodies (diluted 1:300 and 1:1000 respectively, Pierce). After several washes in buffer, sections were incubated overnight at 4 °C. Glass coverslips were mounted on slides using Vectashield antifade mounting medium with DAPI (Vector Laboratories, Burlingame, CA, USA). The Z-stack images were visualized on a Leica TCS-SP5 confocal system3D images of $IBA1^+$ cells were obtained from stacks of 0.25 µm and quantified using the ImageJ Software.

IV.3.K. 3MC-Induced fibrosarcomas

For the induction of fibrosarcomas, 8-weeks-old mice received a single intra-muscular injection of 40 µl solution containing 3-methyl-cholanthrene (3MC) (Sigma-Aldrich) in one of the rear legs. 3MC was used at a concentration of 25 µg/µl and dissolved in sesame oil (Sigma). Mice were monitored regularly and sacrificed 150 days after the injection.

IV.3.L. Partial hepactectomy

For partial hepatectomy (PHx), adult mice (10-weeks-old males) were anaesthetized using a mixture of isoflurane/oxygen. Seventy percent of the liver was excised, which involves removal of the medial and left lateral lobes (used for initial estimation of heteroplasmy). Liver proliferation, regeneration and mitochondrial DNA analysis were performed at 15 days after PHx. Transformed heteroplasmy was calculated to analyse the change in NZB mtDNA proportion before and after liver regeneration. Liver samples obtained from the surgery were used as the reference tissue.

IV.3.M. Astrocytes and neurons isolation

Brains from adult mice were dissociated using Neuronal Tissue Dissociation Kit followed by cell separation using either the astrocyte-specific anti-ACSA-2 Microbead Kit (mouse) (Miltenyi) or the neuron-specific mouse Neuron Isolation Kit (Miltenyi) according to the manufacturer's protocol (MACS technology). The identity of the isolated fractions was confirmed by Western blotting against neuronal [neuron-specific class III beta tubulin (TUJ1) and MAP2]- or astrocytic (GFAP)-specific markers[186].

IV.3.N. Mice immunization

Adult heteroplasmic mice received a boost immunization intravenously using OVA (600 µg/mouse), IMM60 (1 µg/mouse) and MPLA (25 µg/mouse). Mice were sacrificed and spleens were analysed after 7 days of the immunization.

IV.3.O. Assessment of heteroplasmy in T cell populations

Cell suspensions were obtained after chopping the spleens and incubated them with collagenase-D (Sigma, 1 mg/ml) and DNAase (Sigma, 0.5 mg/ml) during 15 minutes at 37 ºC. Enzymatic activity was inactivated with R10 media. The resulting cell suspension was filter (70 µm strainer) and resuspended in

red blood cell lysis buffer (RBC lysis buffer, Qiagen) and washed before the staining with the specific antibodies. Sorting panel was designed using the following antibodies: anti-B220 (APC-Cy7, RA36B2, Biolegend), anti-CD3 (BV510, 17A2, Biolegend), anti-CD4 (BV421, RMA4-5, Biolegend), anti-CD8 (PE-Cy7, 53-6.7, Biolegend), anti-CD62L (FITC, MEL-14, eBioscience), anti CD44 (APC, IM7, Biolegend). L/O Near IR (Invitrogen) was used to discard necrotic cells. The concentrations of the antibodies in the final solution were specified in the manufacturer instructions.

R10 medium: RPMI medium (Sigma, R5878), 10% FBS, 2 mM L-glutamine, 100 U/ml penicillin-streptomycin (Sigma, P0781).

$CD4^+$ T cells (naïve, memory and effector T cells) and $CD8^+$ T cells (naïve, memory and effector T cells) were sorted and collected (25.000 cells per population). DNA was extracted using 10 µl of NaOH 50 mM, incubation of 10 minutes at 95 ºC, and neutralization with 2 µl of TrisHCl 1M pH=7.5. The level of heteroplasmy was assessed by PCR (Materials and methods, nDNA and mtDNA genotyping). Transformed heteroplasmy was calculated using tail as the tissue of reference.

IV.3.P. $CD8^+$ T cells isolation and *in vitro* activation

Cell suspensions were obtained after chopping the spleens and incubated them with collagenase-D (Sigma, 1 mg/ml) and DNAase (Sigma, 0.5 mg/ml) during 20 minutes at 37 ºC. Cell suspension was filter (70 µm strainer) and mixed with red blood cell lysis buffer (RBC lysis buffer, Quiagen) and washed before the staining with the specific antibodies.

$CD8^+$ T cells were collected using the $CD8^+$ T cell isolation kit according to manufacturer instructions (CD8α negative selection kit, MACS Miltenyi Biotec, ref: 130-104-075) and seeded into a p96 wells plate (clear round bottom, Corning®) with R10 media. Mouse $CD8^+$ T-cells were primed with a mix of the antibodies CD3/CD28 (dynabeads mouse T-activator CD3/CD28, ThermoFisher Scientific). The vial contains 4×10^7 beads/ml and 0.5 µl of the volume was added to each well for the activation and expansion of them for 3 days. Activation status of the cells was assessed by light confocal microscopy. Cells were collected every 24 hours to analyze the changes in the heteroplasmy level.

IV.3.Q. Intraventricular pressure measurement

Due to the high technical difficulty to directly measure pulmonary artery pressure in mice, the right intraventricular pressure was used instead. The difficulties arise mainly from the small lumen of vessels in mice, resulting in the impossibility to reach the pulmonary artery using floating catheters. The right ventricle pressure and, in particular, the systolic ventricular pressure has been described as a good surrogate of the systolic pulmonary artery pressure in several models and species. The experiments were performed as follows:

Surgical procedure. Mice were anesthetized using inhaled sevoflurane through a custom-built mask. Once the animal was anesthetized, skin was dissected at the right anterior portion of the neck and a dissection by planes was performed until finding the superior cava vein. Superior cava vein was carefully dissected and then a small hole was done with a needle to introduce a mikrotip catheter (SPR-671NR Millar Catheter, ADInstruments, Dunedin, New Zealand). Then the catheter was advanced until the right ventricle and the measurements performed. After the procedure, the catheter was removed and the skin and cellular subcutaneous tissue closed by stitches.

Measurement. The mikrotip catheter was advanced through the cava vein until reaching the right ventricle, which was attested by observation of the typical square waveform characteristic. Then the right ventricle pressure was continuously acquired during free breathing.

Data acquisition and processing. The mikrotip catheter was attached to a bridge amplifier (Bridge Amp FE221, ADInstruments, Dunedin, New Zealand) and data were collected using a PowerLab system (PL3504/P, ADInstruments, Dunedin, New Zealand) at 1,000 Hz sample rate. A second order Savitzky-Golay filter with a 35 samples window was applied to smooth the data. The systolic pressure was defined as the maximum pressure during each cardiac cycle and measured beat by beat during a 15 s period at which a stable measurement was observed. The average of this time period was used as representative of each animal and studied situation. Data were processed using custom-written routines programmed in Labchart v7.3.8 (ADInstruments, Dunedin, New Zealand) and Microsoft Excel (Microsoft Corporation, Albuquerque, New Mexico, USA).

IV.3.R. Gasometry analysis

Blood was obtained by cardiac puncture of 12 weeks-old and 80 weeks-old mice (n=6-8) and analysed with Alere EPOC^{TM} analysis system. EPOC test cards comprise of a biosensor array which uses calibration solution and fluidics to assess ions (Na^+, K^+, Ca^{2+}), glucose, lactate, $pC0_2$ and pO_2 parameters in blood.

IV.3.S. Glucose and insulin tolerance test

Mice were fed in high fat diet (HFD) (Research Diets Inc, 60 % kcal fat, 1.5% kcal cholesterol) for 8-10 weeks and weighted every week. For glucose tolerance tests (GTT) and insulin tolerance tests (ITT) mice were fasted for 16 or 2 h with free access to water, respectively. For intraperitoneal (IP) GTT, the mice received glucose injections of 1 mg/kg. For IP ITT, the mice received insulin injections of 0.75 U/kg. Mice were bled from a tail clip. Blood glucose was measured with a handheld glucometer before injection (time 0) and at the indicated times after injection.

IV.3.T. *In vivo* ROS assessment

In vivo mitochondrial hydrogen peroxide was measured using the MitoB mass spectrometric probe as described previously[187,188]. Briefly, 25 nmol MitoB was injected into the tail vein between 8 a.m. and 10 a.m. After 6 h, mice were euthanized by cervical dislocation and tissues were harvested and flash frozen in liquid nitrogen. The compounds (MitoB and MitoP) were extracted using Solution I (60 % ACN / 1 % FA) and homogenized in ultraturrax (100 mg of each tissue + 0.5 ml of solution I). Deuterized standards, d_{15}-MitoB/ d_{15}-MitoP, added to the homogenates. Samples were centrifuged for 10 minutes at 16,000 g and supernatants were filtered and dried in a SpeedVac (Savant) overnight. Dry samples were stored at −80 °C and the LC-MS/MS analysis performed in Mike Murphy's lab (Cambidge, UK).

IV.4. High-throughput screenings: OMICs techniques

IV.4.A. Transcriptomic assays

RNA-Seq primary data analysis (quality control of sequenced raw data) was performed by the team of the CNIC Genomics Unit. Further analysis was performed by the CNIC Bioinformatics Unit.

IV.4.A.1. RNA-seq

12-week-old BL/6$^{C57\text{-}NZB}$, BL/6^{C57} and BL/6^{NZB} males were killed by cervical decapitation, and heart (left ventricle) was dissected and immediately frozen in liquid nitrogen. Total RNA was extracted with TRIzol reagent and then purified on RNeasy spin columns (Qiagen). RNA integrity (RNA Integrity Score ≥ 7.9) and quantity were determined with an Agilent 2100 Bioanalyzer. RNA libraries were produced using TrueSeq RNASeq kit from Illumina and sequenced in the HiSeq2500 Illumina Sequencer. Reads were pre-processed with Cutadapt 1.7.1 to remove the TrueSeq adaptors. RSEM v1.2.2 and Bowtie 0.12.4 were used to map the reads against the GRCm38 reference and ensembl genebuild v84 (www.ensembl.org) modified to remove pseudogenes and adding the genes of the two mitochondrial references (C57 and NZB) as isoforms. Expected counts at gene level were normalized (TMM) and transformed using VOOM function from "limma" R package.

IV.4.A.2. Transcriptomic and bioinformatic analysis

Analysis of conplastic strains Mitochondrial reads were identified and removed by aligning all reads to mitochondrial DNA using Tophat. Resulting reads (nuclear genes) were mapped on the mouse transcriptome (Ensembl gene-build GRCm38.v70) and genome, using RSEM v1.2.3 and Bowtie2 v2.0.6. Genes with at least one count per million in at least three samples were considered for downstream analysis. As the data were generated in two different sequencing runs, we used the R Function Combat (http://www.bu.edu/jlab/wp-assets/ComBat/Download.html) to adjust for potential batch effects. Statistical analysis was performed on the remaining set of genes using the bioconductor package EdgeR[189]. Raw reads and TMM-normalized batch corrected counts have been deposited in GEO with the accession number GSE56933. Sets of differentially expressed genes across conditions were analysed for functional associations using IPA (Ingenuity Knowledge Database, http://www. ingenuity.com). Benjamini–Hochberg adjusted p-values were reported for differential gene expression and IPA functional analysis. Gene Set Enrichment Analysis (GSEA[190]) identified sets of co-expressed genes that are functionally linked based on different ontologies and/or pathways. Gene sets with a FDR < 0.25 were considered functionally related.

Heteroplasmic Analysis. Conplastic and wild type samples were retrieved and re-analysed from GSE56933. In the new experiment (GSE93920) one sample from conplastic hearts and one sample from wild type hearts were also included to allow for batch correction. Differential expression analysis was tested using a linear model with sequencing batch as a random variable to correct for batch effects. For representation purposes in HeatMaps and PCAs the normalized data were corrected using ComBat as implemented in the "sva" R package[191]. Functional analysis of sets of differentially expressed genes across conditions were analysed using DAVID and Ingenuity Pathways Analysis Suite (IPA). Benjamini-Hochberg adjusted p-values were used for both differential gene expression and functional analysis. Raw reads and TMM-normalized counts were deposited in GEO with accession number: GSE93920.

A novel function was implemented to compare IPA and GO terms based on the number of shared genes. This approach allowed us to cluster functional terms and to identify the most relevant terms without the loss of information that results from choosing a given level in the hierarchy of ontologies. Plotting the average expression of the genes in each functional category and in each condition, revealed also information about the coordination of the expression profiles.

IV.4.B. Proteomic techniques

IV.4.B.1. Quantitative proteomics

High-Throughput protein profiling was performed at the CNIC-proteomics Unit. Total heart, skeletal muscle (gastrocnemius), liver and lung protein extracts from 12-week-old BL/6^{C57}, BL/6^{NZB} and BL/6$^{C57-NZB}$ males were digested with trypsin and labelled with tandem mass tags TMT (10plex), according to manufacturer's instructions. Resulting peptides were injected onto a C-18 reversed phase (RP) nano-column (75 µm I.D. and 50 cm, Acclaim PepMap, Thermo Fisher, San José, CA, USA) and analysed in a continuous acetonitrile gradient consisting of 8-31% B-solution (B=0.5% formic acid in acetonitrile) for 240 min, 50-90% B for 1 min. Peptides were eluted from the RP nano-column at a flow rate of ~200 nL/min to an emitter nanospray needle for real-time ionization and peptide fragmentation in a Q-Exactive HF mass spectrometer (Thermo Fisher). Mass spectra were acquired in a data-dependent manner, with an automatic switch between MS and MS/MS using a top 20 method. The raw files were analysed with Proteome Discoverer (version 2.1, Thermo Fisher Scientific), using a Uniprot database containing a joint Mouse Swissprot database (Uniprot release 57.3 May 2009; 26.885 entries). For database searching, parameters were selected as follows: trypsin digestion with 2 maximum missed cleavage sites, precursor mass tolerance of 800 ppm, fragment mass tolerance of 0.03 atomic mass unit (amu). We allowed variable methionine oxidation and fixed cysteine carbamidomethylation, and all lysines and N-terminals were modified in + 229.2634 amu. MS/MS spectra were also queried against inverted databases constructed from the same target databases. Peptide identification from MS/MS data was performed using the probability ratio method[192]. False discovery rates (FDR) of peptide identifications were calculated using the refined method described in references[45,46]. 1 % FDR was used as criterion for peptide identification. Each peptide was assigned only to the protein with the highest score as identified by the Proteome Discoverer algorithm.

Quantitative information were extracted from MS/MS spectra, from TMT reporter ions, using an in-house developed program (QuiXoT), as described previously[193] and protein abundance changes were analysed using the Generic Integration Algorithm, as described in[194] and using the same procedure, we integrated the protein quantitative information from several experiments to unique protein quantitative values. Calculation of statistical weights of each quantification at the spectrum level was performed according to the WSPP model[195]. The validity of the null hypothesis at each one of the levels (spectrum, peptide, protein within an experiment and protein) was carefully checked by plotting the cumulative distributions, as described in [195]. Normalized Zq from identified proteins were analysed with MetaboAnalyst 3.0 software (http://www.metaboanalyst.ca)[196].

IV.4.B.2. PTMs analysis

All the experimental designs and methods are explained in more detail in [197].

Protein Extraction. The effect of heteroplasmy on the post-translational modifications of the proteome of different tissues was studied in liver, heart, skeletal muscle (gastrocnemius) and lung samples. Mice (12 weeks-old) were sacrificed by cervical dislocation and liver, heart and skeletal muscle tissues were extracted. Tissues were cleaned and homogenized in buffer (10mM Tris-HCL pH7.4, 1 mM EDTA, 0.32 M sucrose) by 20 strokes using a Heidolph mechanical homogenizer with a dounce tissue grinder pestle. Homogenates were centrifuged at 1000 x g for 5 minutes at 4ºC to remove the remaining cells and debris.

Protein digestion, peptide labelling and fractionation. Proteins were treated with 50 mM iodoacetamide (IAM) and digested with trypsin using the Filter Aided Sample Preparation (FASP) digestion kit

(Expedeon)[198] according to manufacturer's instructions. Dried peptides were labelled using 10 plex-TMT reagents according to manufacturer's instructions (Thermo Fisher Scientific), desalted on OASIS HLB extraction cartridges (Waters) separated into 7 fractions using the high pH reversed-phase peptide fractionation kit (Thermo Fisher Scientific) and dried before MS analysis.

LC/MS analysis. Each fraction of the labelled peptide samples was analysed using an Easy nano-flow HPLC system (Thermo Fisher Scientific) coupled via a nanoelectrospray ion source (Thermo Fisher Scientific, Bremen, Germany) to a Q Exactive HF mass spectrometer (Thermo Fisher Scientific, Bremen, Germany). C18-based reverse phase separation was used with a 2-cm trap column and a 50-cm analytical column (EASY column, Thermo). Peptides were loaded in buffer A (0.1% formic acid (v/v)) and eluted with a 240 min linear gradient of buffer B (80% acetonitrile, 0.1% formic acid (v/v)) at 200 nL/min. Mass spectra were acquired in a data-dependent manner, with an automatic switch between MS and MS/MS using a top 15 method. MS spectra were acquired in the Orbitrap analyser with a mass range of 400–1500 m/z and 60,000 resolution. HCD fragmentation was performed at 27 of normalized collision energy and MS/MS spectra were analysed at 60,000 resolution in the Orbitrap.

Database search and analysis. Unless indicated otherwise, all searches were performed using Comet release 2016.01 using trypsin digestion with 1 missed cleavages and fixed Cysteine carbamidomethylation (57.021464 Da). For heteroplasmic mice data, TMT labelling at N-terminal end and Lysins were also considered as a fixed modification (229.162932 Da). Fragment ion tolerance was 0.02 bin, 0 mass offset. Precursor tolerance type and isotope error were set to 1. Precursor charge range was 2-4, maximum precursor charge 5 and maximum fragment charge 3. Only y- and b-ions were used for scoring. Closed searches (CS) were performed at 5 ppm precursor ion tolerance, using three dynamic modifications: Methionine oxidation (15.994915), Asparagine and Glutamine deamidation (0.984016) and Serine and Threonine phosphorylation (79.966331). Peptide identification from MS/MS data was performed using the probability ratio method. False discovery rates (FDR) of peptide identifications were calculated using the refined method[199]. 1 % FDR was used as criterion for peptide identification. Open searches (OS) with Comet and Comet-PTM were performed in the same conditions as CS, except that precursor ion tolerance was set to 500 Da.

Design of new a bioinformatic tool for comprehensive quantification of the modified proteome. Comet.PTM was developed by modifying the open-source database search engine. For every sequence candidate Comet-PTM calculates the difference between theoretical and experimental precursor mass (ΔMass) and adds up this mass iteratively to each one of the amino acid masses in the peptide sequence, calculating a Xcorr score in each one of the possible modified forms of the peptide. The selected candidate is the modified peptide form that produces the highest Xcorr. Comet-PTM was developed to take full advantage of the multi-thread design of Comet. Comet-PTM used less than 4 hours to perform a 500 Da-wide open search of 16 LC-MS runs, containing an average of 44.390 MS/MS spectra each, using a computer cluster with 16 nodes, where each node is built of 2 x Intel Xeon E5-2695v2 at 2.40 GHz and contained 46 threads/124 gigabytes. SHIFTS (Systematic hypothesis-free identification of modifications with controlled FDR based on ultra-Tolerant database search) is a program that identifies peaks in the ΔMass distribution, assigns PSM to peaks and calculates FDR for peptide identification SHIFTS uses as input the Thermo.raw files and the files obtained from Comet-PTM search.

IV.4.C. Metabolomic analysis

Samples of liver and plasma from 10-week-old mice (n = 6 per genotype) were collected, frozen in liquid nitrogen and sent to Metabolon (Durham, NC, USA) for metabolomics analysis according to their

proprietary methodology. The analysis profiled 313 metabolites in liver samples and 287 in plasma, with 197 common to both sources.

For the multivariate model analysis, between-group differences in the abundance of metabolites identified by mass spectrometry (LC–MS and GC–MS) were assessed by Welch's two-sample *t*-test. Differences were considered statistically significant at $p < 0.05$. Chemometric statistical analysis was performed using R scripts (http://cran.r-project.org/) and the mixOmics package (v. 5.0.1) executed in RStudio (v. 0.98.501) for MacOSX. Most metabolomic analysis employs unsupervised principal components analysis (PCA) to explore the quality of data and detect possible outliers and a supervised partial least squares-discriminant analysis (PLS-DA) to determine the number of metabolites responsible. PLS-DA is a supervised extension of PCA used to distinguish two or more classes by searching for original metabolic variables (*X* matrix) that are correlated to class membership (that is, liver, plasma, and mouse model) (*Y* matrix). Results of the PCA and PLS-DA were visualized by a scatter score plot of different PCs (PCA) and the first two latent variables (PLS-DA). The original *X* matrix contains the metabolic variables, while the *Y* matrix contains the class variable for which values are chosen to be the class descriptor. We performed the analysis by comparing BL/6^{C57} samples with BL/6^{NZB} samples, and liver samples with plasma samples. False discovery rate and overfitting were avoided by using a leave-one-out cross-validation, performed with the calibration data set, to determine the number of latent variables for each fold and to construct a model. The resulting model was applied to the test data set, including the 287 plasma metabolites and the 313 liver metabolites, to compute the predicted Y values. Due to the small number of samples, this process was repeated the number of times needed in each analysis so that every sample served as an independent test sample only once. The predicted Y values produced by the cross-model validation were used to examine the classification error and determine the number of most discriminant metabolites. Based on this, we selected only those metabolites that appear in at least 50% of the repeated analysis. For metabolomic set enrichment analysis (MSEA)[200], raw data from the metabolic analysis were normalized by quantiles using the Bioconductor LIMMA package. Metabolites with missing values were excluded. A moderated *t*-test, also implemented in the LIMMA package, was used to calculate log fold-differences between male BL/6^{NZB} and BL/6^{C57} mice for liver and plasma samples separately, together with raw and Benjamini–Hochberg adjusted *p*-values. MSEA was then run on the normalized samples and the signal-to-noise ratio statistic was used to rank metabolites in each pathway of interest. A false discovery rate (FDR) < 0.25 was considered significant. We considered sets of at least 10 metabolites in all analyses, except for bile acid, which required at least 5 metabolites to be in the same class for a result to be considered significant.

IV.5. *In vivo* imaging techniques

IV.5.A. Magnetic resonance imaging (MRI)

IV.5.A.1. Cardiac magnetic resonance imaging (CMR)

Animals were anaesthetized with isoflurane and were monitored for core body temperature, cardiac rhythm and respiration rate using a specific monitoring system (SA Instruments Inc. New York, NY). *In vivo* cardiac images were acquired using an Agilent VNMRS DD2 7T MRI system (Agilent Varian, Palo Alto, USA) with an active shielded gradient 115/60 insert coil with 433 maximum gradient strength and a four-channel receiver. A k-space segmented ECG-triggered short-axis cine gradient-echo sequence was used with a Helmet hundred-element surface coil (Extend MR, Silicon Valley, California). After shimming optimization, cardiac four-chamber and left two-chamber views were acquired and used to plan the short axis sequence. Mice were imaged with the following parameter settings: number of slices, 11-13; slice

thickness, 0.8 mm; gap, 1 mm; data matrix size, 128x128; field of view, 30x30 mm^2; gating: ECG and respiratory triggered; cardiac phases, 20; averages, 4; minimum TE, ~1.25 ms and TR, 7 ms; flip angle, 15º.

CMR images were exported to Dicom format and analysed with Segment software (Mediso AB v.1.9R3819). The short-axis dataset and cine modus short-axis view were analysed quantitatively by manual detection of RV and LV endocardial borders in end diastole and end systole without exclusion of papillary muscles and trabeculae to obtain both left and right end-diastolic volume, end-systolic volume, ejection fraction (%EF) and cardiac output (CO).

IV.5.A.2. MRI analysis of brain anatomy and tumour progression

In vivo MRI in mice was performed with an Agilent/Varian scanner (Agilent, Santa Clara, USA) equipped with a DD2 console and an active-shielded 205/120 gradient insert coil with 130 mT/m maximum gradient strength and a combination of volume coil/two channel phased-array (Rapid Biomedical GmbH, Rimpar, Germany). Mice were anaesthetised with 2% isoflurane (Abbott) and oxygen and positioned on a thermoregulated (38.7ºC) mouse bed with continuous monitoring of the respiratory cycle. Ophthalmic gel was placed in the eyes to prevent retinal drying. Consecutive axial 1 mm thick slices were acquired to image the tumour. Images were acquired in free-breathing animals, using a gradient echo sequence with 4 ms/40 ms echo/repetition times, a 20º flip angle, 100 kHz bandwidth, 6 cm x 6 cm FOV, for a total acquisition time of 80 sec.

IV.5.B. Magnetic resonance spectroscopy (MRS)

IV.5.B.1. 31P/1H Magnetic resonance spectroscopy (31P/1H-MRS)

Males $BL/6^{C57}$, $BL/6^{NZB}$ and $BL/6^{C57\text{-}NZB}$ weighing approximately 30-50g were housed in groups of 4-5 with unrestricted access to food and water. Spectroscopy examinations were performed *in vivo* on a 7T preclinical system (Agilent Varian, Palo Alto, USA) equipped with a DD2 console and an active shielded 115/60 gradient insert coil with 433 mT/m maximum strength. Double-tuned circular transmit/receive coils were used for phosphorus/proton (20 mm), placed over soleus muscle, cardiac muscle and liver (Rapid Biomedical GmBH, Rimpar Germany).

Proton tissue spectra were acquired by 128 transients with 2048 complex points with a spectral bandwidth of 10 kHz and a repetition time of 1.2 ms. Phosphorus tissue spectra were acquired by 1000 transients with 8192 complex points with a spectral bandwidth of 7 kHz and a repetition time of 800 ms. Spectra were acquired with adiabatic radiofrequency pulses to improve sensitivity and minimize spectral distortions with an Ernst flip angle. Chemical shifts were expressed relative to the water signal (4.7-4.8 ppm) in 1H-MRS and phosphocreatine (0 ppm) in 31P-MRS. Signals in nuclear magnetic resonance spectra were determined quantitatively by integration after automatic or manual baseline correction, with fitting of each peak of the spectrum (after phase and baseline correction) to a Lorentzian function using the Mestrenova program (Mestrelab Research, Santiago de Compostela, Spain; released 2015-02-04 version:10.0.1-14719) on a Macintosh computer. An exponential line broadening (3 Hz for proton) was applied before Fourier transformation.

IV.5.C. PET/CT imaging

In vivo positron emission tomography–computed tomography (PET/CT) imaging was performed with a nanoPET/CT small-animal imaging system (Mediso Medical Imaging Systems, Budapest, Hungary). List-

mode PET data acquisition commenced 30 min post intravenous injection of 15 MBq of [^{18}F]-fluorodeoxiglucose ([^{18}F]-FDG) in 20-weeks-old-mice, 2 hours post intravenous injection of 18 MBq [^{18}F]-FDG or 30 MBq [^{18}F]-fluoromisonidazole ([^{18}F]-FMISO) in 12.5 dpc embryo imaging, continued for 20 minutes PET acquisition. At the end of PET, scan microCT was performed for attenuation correction and anatomical references. The resulting dynamic PET images were reconstructed in a 105x105 matrix (frame rates: 3 x 10 min, 1 x 30 min, 1 x 60 min) using a Tera-Tomo 3D iterative algorithm. Acquisition and reconstruction were performed with proprietary Nucline software (Mediso, Budapest, Hungary) and saved in Dicom format. The images were imported into OsiriX software (Pixmeo, Switzerland v.8.0.1) and were analysed qualitatively comparing [^{18}F]-FDG uptake in different anatomical regions in case adult mice.

IV.5.C.1. Molecular imaging probes: Biodistribution and uptake

Cardiac and lung tissue analysis. All acquisitions were performed with a small-animal PET/CT scanner (nanoScan, Mediso). PET studies were acquired 30 minutes after intravenous administration of 17 MBq of [^{18}F]-FDG. During FDG uptake, the animals were kept awake and warm to prevent brown fat uptake. PET data were then collected for 30 minutes with the mice anesthetized using 1.5% sevoflurane in oxygen at 3 L/min and reconstructed using Tera-Tomo 3D with 6 subsets, 4 iterations, an energy window of 400-600 keV and a coincidence mode of 1-5. The voxel size of the reconstructed images was 0.399 mm in the transaxial plane and 0.399 mm in the axial plane. After the PET scan, a helicoidal CT study was acquired using an X-ray beam exposure of 89 μAs and a tube voltage of 45 kVp and reconstructed using a Ramlack algorithm. These CT scans were used as anatomical templates. PET values were measured as standardized uptake value (SUV). On the PET images, the regions of interest (left ventricle and right venticle, LV/RV) were delimited over the whole hearts to measure their corresponding SUV (SUV mean)

Embryo analysis. List-mode PET data acquisition commenced 30 min post bolus injection of 15 MBq of [^{18}F]-FDG through the tail vein and continued for 20 minutes during PET acquisition.

IV.5.C.2. *Ex vivo* biodistribution analysis

Biodistribution studies were performed 6 hours post intravenous injection of 15 MBq [^{18}F]-FDG in a Wizard 1470 Gamma Counter (Perkin Elmer). Animals were sacrificed in a CO_2 chamber. Afterwards, blood was extracted and animals perfused with 8 mL of PBS. Tissues were extracted and counted for 1 min in the gamma counter. Decay correction was performed and data represented as relative %ID/ g.

Ex vivo [^{18}F]-FDG and [^{18}F]-FMISO embryo biodistribution analysis. Embryo biodistribution studies were performed 4 hours post intravenous injection of 18 MBq [^{18}F]-FDG or 30 MBq [^{18}F]-FMISO. Animals were sacrificed in a CO_2 chamber. 12.5 dpc embryos were extracted and counted for 1 min in a Wizard 1470 Gamma Counter (Perkin Elmer). Decay correction was performed and data represented as relative %ID/ g.

IV.5.C.3. MicroCT analyses

Micro-CT was performed with a nano-PET/CT small-animal imaging system (Mediso Medical Imaging Systems, Budapest, Hungary). Whole-body helical scans were captured with a 142 micrometre spatial resolution at a voltage 45 kVp. For the study of kyphosis, curve progression was measured using a modification of the Cobb method. High-resolution CT images were processed using OsiriX software (Pixmeo, Switzerland). The rotation angle was calculated using properly aligned references lines drawn perpendicular to the lines drawn along the fourth thoracic (T4) endplate and the inferior fourth lumbar (L4) end vertebra. The angle between these two lines was measured as the kyphotic angle. The kyphosis was

calculated after tracing the line between the anatomical landmarks of these two bones using standard length ROI tools included in this software. Tibia and femur length were measured on volume-rendering 3D CT scans with OsiriX imaging software.

IV.5.D. Mouse transthoracic echocardiography

Two-dimensional and M-mode echocardiography longitudinal studies were performed in 3 months intervals during the whole mice lifespan. Males (n=15-20) were anesthetized (1.5-2% isoflurane in a mixture with oxygen) and the analysis was carried out using a Vevo770 system (Vevo 2100, Visualsonics Inc., Canada) equipped with a 30-MHz linear transducer probe. To avoid night-day circadian variations, echocardiographies were performed in the mornings. Before echocardiography, animal fur was removed with a depilatory agent and animals were warmed to maintain body temperature. The heart was imaged in the 2D parasternal long- and short-axis projections with guided M-mode recordings at the midventricular level in both views. Images were recorded and transferred to a computer for posterior blinded analysis using the Vevo 2100 Workstation software. LV end-diastolic diameter (LVEDD), LV-systolic diameter (LVESD), end-diastolic LV anterior wall thickness (LVAW), and LV posterior wall thickness (LVPW) were measured from images obtained by M-mode echocardiography. LV fractional shortening (FS) and aortic cardiac output (CO) was calculated.

LV ejection fraction (EF) by Teichholz formula[201] has been assessed using the M-mode images displayed over time and obtained from a single line in the middle of LV. The LV mass has been calculated from the same M-mode images by using diastolic LV diameters of LV internal diameter (LVID), posterior wall (PW) and interventricular septum (IVS) as follow: LV Mass (mg) = 1.05 (LVIDd + LVPWd + $IVSd^3$ – $LVIDd^3$). Corrected LV Mass = (LV Mass) 0.8.

IV.6. Molecular biology techniques

IV.6.A. nDNA and mtDNA genotyping

IV.6.A.1. DNA extraction and PCR

All mice were genotyped at post-natal day 21 using DNA extracted from tail tip. Total genomic DNA was PCR amplified using standard conditions with the REDExtract-N-Amp™ PCR ReadyMix™ (Sigma-Aldrich R4775).

To determine the heteroplasmy levels of each tissue or cell culture, total genomic DNA was isolated using DNeasy Blood &Tissue kit (Qiagen 69506) or from the REDExtract-N-Amp™ PCR ReadyMix™ (Sigma-Aldrich R4775):

- Liver, lung, kidney, ovary, testes, heart (left ventricle), brain (cerebral cortex), skeletal muscle (gastrocnemius muscle), bladder, gut (duodenum), thymus, eye, pancreas, spleen, bone marrow, blood, brown adipose tissue and white adipose tissue (gonadal adipose tissue), sperm, oocytes, fibrosarcoma samples and embryos.

To assess mtDNA from cell populations in cardiac tissue, blood, bone marrow, isolated cardiomyocytes, MAFs and MEFs, DNA was isolated using 50 mM NaOH at 95 ºC and neutralization with TrisHCl pH 7.5.

IV.6.A.2. DNA digestion, gel electrophoresis and heteroplasmy quantification

The polymorphic G4276A nucleotide was used to genotype individual animals and tissues. This polymorphism in C57 mtDNA formed part of a BamH1 restriction site, which is absent in NZB mtDNA. Total genomic DNA was PCR amplified using standard conditions with a kit (5Prime Master Mix), using the following primers: 5'-AAGCTATCGGGCCCATACCCCG-3' (3862-3884) and 5'-GTTGAGTAGAGTGAGGGATGGG-3' (4503-4525), with PCR settings as follows: 95ºC, 30s; 58ºC, 30s; 72ºC, 45s for 30 cycles. A 15 µl aliquot of PCR product was digested with 20 units of BamH1 (New England Biolabs) at 37ºC for 2 hours. After 1.5 % agarose gel electrophoresis, DNA was visualized with a Gel Doc XR+System using ethidium bromide (EtBr, Bio-Rad), and band intensity was quantified with Quantity One 1-D Analysis Software. The proportion of C57 mtDNA was calculated by adding the intensities of the 414 bp and 250bp BamH1 fragments and was divided by the sum of the intensities of the undigested 664 bp fragments and the 414 bp and 250 bp BamH1-digested fragments.

IV.6.B. *In vivo* modulation of mtDNA segregation

Total genomic DNA was PCR amplified using standard conditions with the REDExtract-N-Amp™ PCR ReadyMix™ (Sigma-Aldrich R4775).

Oma1 gene was genotyped as described in [19] and *Ppargc*1α gene was genotyped as described in [41].

Table 5. Primer sequences

PCR	Forward Primer (Fw)	Reverse Primer (Rv)
Mitochondrial DNA (*Nd2* Polymorphic G4276A nucleotide)	5'-AAGCTATCGGGCCCATACCCCG-3' (3862-3884)	5'-GTTGAGTAGAGTGAGGGATGGG-3' (4503-4525)
Nnt	COM 5'-GTAGGGCCAACTGTTTCTGCATGA-3' WT 5'-GTGGAATTCCGCTGAGAGAACTCTT-3' MUT 5'-GGGCATAGGAAGCAAATACCAAGTTG-3'	
Oma1	5'-GAGTGCTGTTTCTCTGGGTGT3'	WT 5'-TGCCCTAAACTGAAGGTGTG-3' KO 5'-TAGACCGCGGCTAGAGGTA-3'
Scaf1	5'-CTT TCT TGC TTT GCA GAA GGC-3'	5'-GAA GGC CTC GTT TCA GGT GG-3'
Pgc1α (Ppargc1a)	5'-TCCAGTAGGCAGAGATTTATGAC-3'	5'-GCAACTGTCTATAATTCGAGTTC-3'

IV.6.B.1. Nnt genotyping

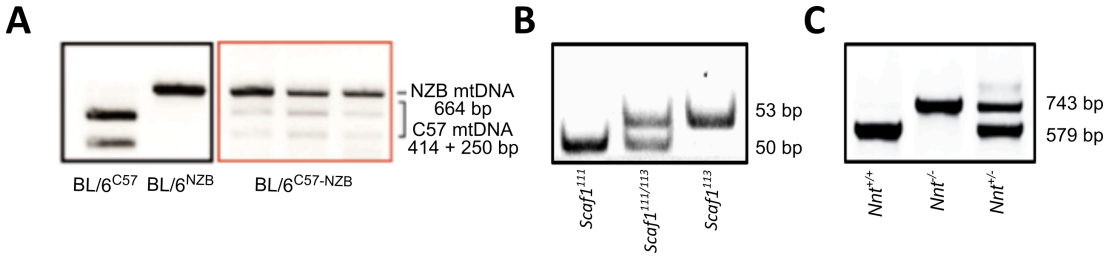

Figure 9. PCR products from *Nd2*, *Scaf1* and *Nnt*. **(A)** PCR and following restriction endonuclease digestion products from homoplasmic and heteroplasmic samples (1.5 % agarose gel). **(B)** PCR products of the different DNA sequences of *Scaf1* gene (10% acrylamide gel). **(C)** PCR products of *Nnt*, wild type and mutant DNA sequence (2% agarose gel).

Tissue genotyping for the *Nnt* gene was performed as follows. Total DNA was extracted and amplified using the following primers, 5'-GTAGGGCCAACTGTTTCTGCATGA-3', 5'GTGGAATTCCGCTGAG AGAACTCTT-3', 5'-GGGCATAGGAAGCAAATACCAAGTTG-3' with PCR settings as follow: 95ºC, 5 minutes; [95ºC, 45s, 58ºC, 30s; 72ºC, 45s] for 35 cycles; 72ºC 5 minutes. After 2% agarose gel electrophoresis, DNA was visualized with a Gel Doc XR+System (Bio-Rad). 579 bp fragments correspond to wild type *Nnt*, 743 bp to mutated Nnt^{202}.

IV.6.B.2. Scaf1 genotyping

The genotype of the different SCAF1 isoforms was determined by PCR. Total DNA was extracted and amplified using the following primers, 5'-CTT TCT TGC TTT GCA GAA GGC-3' (Fw) and 5'-GAA GGC CTC GTT TCA GGT GG-3' (Rv) and the PCR performed as follow: 95ºC, 2 minutes; [95ºC, 30s, 56ºC, 45s; 72ºC, 30s] for 30 cycles; 72ºC 5 minutes. After 10% acrylamide gel electrophoresis and EtBr staining, DNA was visualized with a Gel Doc XR+System (Bio-Rad). Fragments correspondent to 50 bp (*Scaf1*^{111}) and 53 bp (*Scaf1*^{113}) were obtained.

IV.6.C. Mitochondrial Characterization

IV.6.C.1. Mitochondrial Isolation

Mitochondria were isolated from mice and cells as described previously [203]. Samples were stored at -80 ºC in 50 mM Bis-Tris, 1M aminocaproic acid medium.

IV.6.C.1.a. Mitochondrial isolation from tissues

Mice were killed by cervical dislocation and the different organs were removed and immediately cooled down to 4 ºC in medium A (320 mM sucrose, 10 mM Tris-HCl, 1mM EDTA, pH 7.4). For cardiac mitochondria isolation, fatty acid-free BSA was added. The tissues were cut and homogenised with a glass tissue grinder using a motor-driven Teflon pestle (Heidolph RZR 2041) with 10-15 strokes at 600 rpm. Then the samples were centrifuged for 5 minutes at 4 ºC at 1,000 x g and the supernatant was collected, centrifuged for 10 minutes at 4 ºC at 13,000 x g and the mitochondria containing pellets were washed with medium A.

IV.6.C.1.b. Mitochondrial isolation from cell lines

Cells were trypsinised and pelleted from 10 plates 150 mm of diameter (Corning™ Falcon™ tissue culture dish). Pellets were washed with cooled PBS and stored at -80 ºC prior to extraction. Hypotonic medium (sucrose 83 mM, MOPS 10 mM, pH 7.2) was added to resuspend the pellet (7-fold increase in pellet volume). After 2 minutes on ice, the pellet was placed into a glass tissue potter and homogenised with a motor-driven Teflon pestle (Heidolph RZR 2041) with 10-15 strokes at 600 rpm. Then, the same volume of hypertonic medium (250 mM sucrose, 30 mM MPS pH 7.2) was added and centrifuged for 5 minutes at 4 ºC at 1,000 x g. Supernatants were centrifuged for 5 minutes at 4 ºC at 13,000 x g and pellets resuspended in medium A.

IV.6.C.2. ATP synthesis

Mitochondria were isolated from different mouse tissues as described previously[105] and ATP productions were measured. ATP synthesis was assessed in isolated mitochondria by a kinetic

luminescence assay[204]. The produced light was proportional to the amount of ATP with maximum emission at 560 nm. The luciferin/luciferase fluorometric method is based on the following reactions:

- Luciferase (Luciferase from *Photinus pyralis*, Roche) + Luciferin (Beetle Luciferin, Potassium Salt, Promega) + ATP→ Luciferase-Luciferil-AMP + PPi
- Luciferase-luciferil-AMP + O_2 → Luciferase + oxyluciferin + AMP + CO_2 +*hv*

Mitochondria (25-50 µg mitochondrial protein depending on the tissue) were resuspended in 160 µl of buffer A (150 mM KCl, 25 mM Tris-HCl, 2 mM EDTA, 0.1 % BSA fatty acid free 10 mM KPO_4, 0.1 mM $MgCl_2$, pH 7.4) at room temperature (RT) and dispensed into the wells (96-well luminescence reading plate, Costar). Substrate cocktail and buffer B (0.5 M Tris-acetate, pH 7.75, 0.4 mM luciferine, 10 µg/ml luciferase) were added, and luminescence was measured over 2 minutes in a plate luminometer (Orion Microplate Luminometer, Simplicity 4.2 software). Substrate cocktails were composed of 6 mM diadenosin pentaphosphate and 6 mM ADP supplemented with 0.1 M glutamate/malate for determination of CI activity or with 0.1 M succinate for CII activity. A standard ATP curve was performed (0-10 mM final concentration of ATP). A regression curve was calculated by correlation of ATP concentration and luminescence. ATP production rate is expressed as percentage of 'nmol of ATP/min/mg of protein *vs.* control'. In the final plots, each dot represents mitochondria from an individual mouse; each sample has a technical duplicate.

IV.6.C.3. Seahorse analysis

Oxygen consumption in mouse adult fibroblasts (MAFs) and mouse embryonic fibroblasts (MEFs) (15,000-20,000 cells/well) was measured using the XF96 MitoStress Test (Seahorse Bioscience). The SeaHorse cartridge with the oxygen sensors was hydrated overnight (O/N) with the calibration medium at 37 °C in atmosphere without CO_2. Seahorse XF Base medium supplemented medium (1 mM pyruvate, 2 mM glutamine, 1 M glucose, pH 7.4) was added to the cells and incubated for 30-45 minutes before the analysis at 37 °C in an incubator without CO_2. Oligomycin (1st injection) was used to inhibit ATP synthase, and the decrease in oxygen consumption rate (OCR) following injection of oligomycin correlates to the mitochondrial respiration associated with cellular ATP production. Carbonyl cyanide-4 (trifluoromethoxy) phenylhydrazone (FCCP, 2nd injection) uncouples oxygen consumption, collapses the proton gradient and disrupts the mitochondrial membrane potential. Antimycin A (AA) and rotenone (3rd injection) were used to inhibit complexes III and I, respectively to enable the calculation of non-mitochondrial respiration. Final drug concentrations were 1 µM. Oxygen consumption rates were normalized to cell number using CyQuant (Molecular Probes).

IV.6.C.4. Citrate synthase activity

Citrate synthase activity was determined spectrophotometrically as described elsewhere[205]. The assay was performed at 30 °C. As electron donors and acceptors we used 50 mM oxalacetic acid (OAA, Sigma O4126), acetyl-CoA 7 mg/ml (Sigma, A2181) and 5,5′-dithiobis(2-nitrobenzoic acid) (DTNB, Sigma D8130-5G). 10 mM Tris–HCl, pH 7.5 buffer containing 0.1 % Triton X-100, 0.1 mM DTNB, 3.3 µl of acetyl-CoA 7mg/ml and 10 µg of protein from tissue homogenates were used for the assay. The reaction started by adding 5 µl of OAA (50 mM). The reaction was followed for 1-2 minutes by measuring the increase in absorbance at 412 nm as a course of the reduction of the DTNB compound.

IV.6.D. Protein analysis

IV.6.D.1. Total protein cell extraction

Cells were collected from 150 mm plates at ~ 80 % of confluence and centrifuged at 4ºC (5 minutes, 2500 rpm). The pellet was resuspended in 250 µl RIPA buffer (1 % Triton-X-100, Tris-HCl 50 mM pH 7.4, NaCl 50 mM, Sodium deoxicholate 0.5 % and EDTA 5 mM) and incubated at 4 ºC for 5 minutes. Cells were centrifuged at 15,000 x g for 15 minutes at 4 ºC and the supernatant was collected. Protease inhibitor cocktail mix (Sigma P8340) was added to the RIPA solution when proteins from tissues were extracted.

IV.6.D.2. Protein quantification

Protein quantification was performed by a colorimetric assay. The assay measures total protein concentration using a basic dye, the Bradford method[206] (BioRad, 5000001) in 96-well microplates. 200 µl H_2O, 50 µl Bradford reagent and 1 µl of the samples was added per well. A protein calibration curve was done using 0, 1, 2, 4, 8, 10 and 15 µg/µl of bovine serum albumin (BSA). Spectrophotometer measurements were carried out at 595 nm (BioRad microplate spectrophotometer).

IV.6.D.3. Gel electrophoresis

I.1.1.1.a. Denaturing electrophoresis: SDS-PAGE

Sodium dodecyl sulphate polyacrylamide gel electrophoresis (SDS-PAGE) was performed for protein separation. Loading buffer (50 mM Tris-HCl pH 6.8, 2 % SDS, 10 % glycerol, 1 % β-mercaptoethanol, 0.02 % bromophenol blue) was added to protein samples and were incubated for 5 minutes at 90 ºC. Subsequently 25-30 µL of each protein sample were loaded onto a 7% or 12.5% acrylamide gel, depending on the expected molecular weight. The electrophoresis was done in Mini-PROTEAN Tetra cell (Biorad) using Tris-glycine buffer (Tris 25 mM, glycine 20 mM, SDS 0.5 %), amperage of 10 mA during the stacking of the proteins and 20 mA once the samples reached the running gel.

Table 6. Recipes for stacking and resolving SDS-PAGE gels

Reagents	Resolving 7% A/BA	Resolving 12.5% A/BA	Stacking
TrisHCl 1M pH 8.8	1.87 ml	1.87 ml	-
TrisHCl 1 M pH 6.8	-	-	0.25 ml
H_2O_{mq}	1.94 ml	1.05 ml	1.417 ml
A/AB (30%) 29:1	1.16	2.08	0.33
SDS (20% stock)	25	25	10
APS (20 % stock)	15	15	10
TEMED	5	5	5

I.1.1.1.b. Non-denaturing electrophoresis: Blue Native-PAGE

Table 7. Recipes for stacking and resolving BNE gels

Reagents	Acrilamide Solution 3%	Acrilamide Solution 13%	Stacking
A/BA 48:1.5	0.305 ml	0.866 ml	0.25 ml
Buffer 3x (Bis-Tris 150 mM, aminocaproic acid 1.5 M, pH 7)	1.667 ml	1.111 ml	1 ml
H_2O_{mq}	3 ml	0.713 ml	1.75 ml
Glycerol (85% stock solution)	-	0.643 ml	-
APS (20 % stock solution)	20µl	7µl	12.5µl
TEMED	4µl	3µl	3 µl

Supercomplex levels and compositions were analysed in isolated mitochondria from different tissues and cells by blue native electrophoresis (BNE) as described previosuly[103]. Mitochondrial proteins from heart tissue were solubilized with 10% digitonin (4g/g) (Sigma D5628) and run on a 3%–13% gradient Blue Native gel. The gradient gel was prepared in 1.5 mm glass plates using a gradient former connected to a peristaltic pump.

Digitonized mitochondrial samples were loaded onto gels and run in a mini-PROTEAN Tetra Cell apparatus (BioRad). Buffers and experimental conditions are presented in Table 8.

Table 8. Recipes for BNE running buffers.

Buffer	Composition	Voltage	Time
Cathode A	50 mM Tricine, 7.5 mM imidazole 0.02% Coomassie Blue G-250 pH 7	150	40 min
Cathode B	50 mM Tricine, 7.5 mM imidazole, pH 7	300 V	1 hour
Anode	25 mM imidazole, pH 7	-	-

IV.6.D.4. Western Blot

Proteins were electroblotted onto PVDF transfer membrane (Immobilon-FL, 0.45 µm, Merck millipore, IPFL00010) for 1 h at 100 V in transfer buffer (48 mM Tris, 39 mM glycine, 20 % EtOH). A Mini Trans-Blot Cell system (BioRad) was used. Sea Blocking buffer (Thermo Scientific 37527) or PBS with 5 % BSA was used for 1 hour at room temperature (RT) to avoid non-specific binding of antibodies.

For protein detection, antibodies were incubated with the membrane for 2 hours at RT. Secondary antibodies were incubated for 45 minutes at RT. The membrane was washed with PBS 0.1 % Tween-20 for

5 minutes three times between primary and secondary antibodies and after secondary antibodies, the last wash was only PBS. The antibodies used are summarized in Table 9.

To study supercomplexes assembly, the PVDF membrane was sequentially probed with antibodies Complex I (anti-NDUFA9), Complex III (anti-UQCRC2), Complex IV (anti-COI) and Complex II (anti-SDHA) (Table 10).

Table 9. List of antibodies used for western blot (WB)

Antibody	Clon	Isotype	Source	Reference no.
α-ACTIN	Polyclonal	Rabbit IgG	Sigma	A1066
ATG5	Monoclonal	Rabbit IgG	Cell Signaling	4445
ATG7	Monoclonal	Rabbit IgG	Cell Signaling	4445
ATG3	Polyclonal	Rabbit IgG	Cell Signaling	4445
BECLIN2	Monoclonal	Rabbit IgG	Cell Signaling	4445
LC3A/B	Monoclonal	Rabbit IgG	Cell Signaling	4445
GRP75	Monoclonal	Mouse IgG3	Abcam	Ab2799
HSP60	Monoclonal	Mouse IgG1	Sigma	H4149
PINK1	Polyclonal	Rabbit IgG	Abcam	Ab23707
GAPDH	Monoclonal	Mouse IgG1	Abcam	Ab8245
ATP-B	Monoclonal	Mouse IgG1	Abcam	Ab14730
DRP-1	Monoclonal	Mouse IgG1	BD Biosciences	611113
HTRA2	Polyclonal	Rabbit IgG	Cell Signaling	2176
OPA1	Monoclonal	Mouse IgG1	BD Biosciences	612606
SOD2	Monoclonal	Mouse IgG1	Abcam	Ab16956
TOM20	Polyclonal	Rabbit IgG	Santa Cruz	Sc-11415
LONP1	Polyclonal	Rabbit IgG	Abcam	Ab103809
COXIV	Monoclonal	Mouse IgG	Abcam	Ab14744
SDHA (Fp70)	Monoclonal	Mouse IgG1	Abcam	Ab168536
COI	Monoclonal	Mouse IgG2a	Invitrogen	459600

Table 10. List of antibodies used to study SCs assembly

Antibody	Features		Source	Reference no.	mtETC
NDUFA9	Monoclonal	Mouse IgG1	Abcam	Ab14713	CI
NDUFS3	Monoclonal	Mouse IgG1	Abcam	ab110246	CI
SDHA (Fp70)	Monoclonal	Mouse IgG1	ThermoFisher	459200	CII
UQCRC2 (Core2)	Polyclonal	Rabbit IgG2a	ProteinTech	14742-I-AP	CIII
COI	Monoclonal	Mouse IgG2a	Invitrogen	459600	CIV
COX5a	Polyclonal	Rabbit IgG2a	Abcam	Ab110262	CIV
VDAC1	Monoclonal	Mouse IgG2b	Abcam	Ab147334	VDAC1
ATP-β	Monoclonal	Mouse IgG1	Abcam	Ab14730	CV

Analysis and quantification of signals arising from near-infrared (NIR) fluorophores conjugated to secondary antibodies (Table 11) was performed by a two-channel infrared (IR) scanner (Odyssey v.3.0).

Table 11. List of fluorochrome-conjugated secondary antibodies

Antibody	Conjugation	Source	Reference no.
Mouse IgG (H+L)	DyLight™ 800	Rockland	610-145-121
Mouse IgG (H+L)	Alexa Fluor 680	Life Technologies	A21057
Rabbit IgG (H+L)	DyLight™ 800	Rockland	610-145-122
Rabbit IgG (H+L)	Alexa Fluor 6808	Life Technologies	A210766

IV.6.E. Transmission electron microscopy

Cardiac muscle (LV), liver, skeletal muscle (gastrocnemius), cornea, brain (hippocampus) and lung samples from 12-week-old and 80-week old mice were obtained. Tissues were immediately dissected after animals were euthanized by cervical dislocation (n=3-5). Samples were fixed in 2.5 % glutaraldehyde (Sigma-Aldrich) 4 % formaldehyde (Electron Microscopy Sciences) in 0.1 M HEPES buffer for 4-5 h at 4 ºC. After buffer washes, samples were post-fixed for 1h at room temperature in a 1:1 solution of 2 % osmium tetroxide (Electron Microscopy Sciences) and 3 % aqueous potassium ferrocyanide (Sigma-Aldrich). Samples were rinsed with distilled H_2O. Tissues were dehydrated through a graded acetone series and embedded in Spurr's Low Viscosity embedding mixture (Electron Microscopy Sciences). Ultrathin sections (60 nm) were then mounted on copper grids and stained with lead citrate. Samples were examined on a JEOL 10-10 electron microscope and analysed by ImageJ v.1.6.0 Software (NIH).

IV.6.F. Immunohistochemistry and Immunocytochemistry

Table 12. Leica TCS SP5 confocal microscope specifications.



	Leica SP5 Confocal
Detectors	4 spectral PMT detectors 1 spectral Hybrid Detector 1 PMT for transmitted light
Objectives	HCX PL APO lambda blue 63x 1,40 oil HCX PL APO CS 40x 1,25 oil HCX PL APO CS 10x 0,4 dry
Illumination Source	Diode 405 nm Argon Ion Laser: 458,476,488, 496, 514 nm Diode 561 nm HeNe 594 nm HeNe 633 nm
Scanner	Galvano/Resonant

Tissue slides were deparaffined and rehydrated (5 min xylene, 5 min xylene, 3 min 100 % ethanol, 3 min 100% ethanol, 30 sec 95-90-80-70-50% ethanol, 5 min deuterated water). Heat-induced epitope retrieval with citrate buffer (10 mM pH 6) was conducted at 100 °C for 15 minutes. Slides were allowed to cool 20 minutes, and then washed 3 times for 5 min each in PBS containing 0.5 % Tween 20 (PBS-T) and

permeabilised for 15 min PBS-T. After 3 further washes in PBS-T, non-specific binding was blocked for 1 hour with 1 % BSA in PBS-T. Primary antibodies were added in blocking solution and incubated 2 hours at RT. Sections were washed 3 times with blocking solution for 5 minutes each and incubated for 45 minutes with the secondary antibodies (Alexa Fluor antibodies, 1:500). Slides were washed twice and mounted in glass coverslips using ProLong® Gold Antifade Reagent with DAPI. Confocal fluorescence microscopy images were obtained at a Leica TCS SP5 inverted confocal microscope using HCX PL APO CS 40x 1.25 oil and HCX PL APO lambda blue 63x 1.40 oil objectives. Images were acquired with LAS-AF 2.6.0 acquisition software (Leica Microsystems).

IV.6.F.1. *In situ* mitochondrial DNA detection

Single nucleotide polymorphisms (SNPs) can be detected by padlock probes approach. The assay was based in fluorescence *in situ* hybridization (FISH) using probes labelled with single fluorophores. The specific probes are converted into circular molecules by ligation upon perfect hybridization to the target sequence following by rolling-circle amplification (RCA) is performed *in situ*[207].

Cells were seeded in Superfrost plus slides (Thermo Scientific) using complete DMEM media lacking phenol-red (10% FBS, 290 µg/mL L-glutamine, 50 µg/mL uridine, 5 mM glucose) and allowed to attach. When the cells reached 80% of confluency they were fixed in 4% (w/v) paraformaldehyde (Sigma) in DMEM media for 15 minutes at 37 ºC. In case of heart analysis, cardiac tissue was fixed in 4% paraformaldehyde for 24 hours RT and tissue slides were cut (6 µm). Cell and tissue permeabilization was performed with 95% EtOH and 5% acetic acid for 10 minutes at RT. Then, slides were washed with PBS. Enzymatic target preparation was performed with SspI (R0132S) for 30 minutes at 37 ºC. Two washes were done with Buffer A (0.1M Tris-HCl pH 7.5, 0.15 M NaCl and 0.05% Tween-20). 0.2 U/µL of λ-exonuclease (New England Biolabs M0262S) was used for exonucleolysis for 15 minutes at 37 ºC adding 10% glycerol to the corresponding enzyme buffer. The slides were washed twice with Buffer A. Oligonucleotide sequences were designed (Table 13). Padlock probes (1 and 2) were incubated in a specific hybridization buffer (2X saline-sodium citrate (SSC) buffer, 20% formamide, 0.5 µg/µL salmon sperm DNA) for 15 minutes at 37 ºC. To remove the excess of the probe, Buffer B was used (2X SSC, 0.05% Tween-20) for 5 minutes at 37 ºC. DNA padlock probes were circularized by T4 DNA ligase (New England Biolabs M0202M) for 15 minutes at 42 ºC in Buffer B supplemented with 20% formamide and 1 mM EDTA. Then, slides were washed in Buffer A and dehydrated in ethanol. RCA was performed using 1U/ µL of ϕ29 DNA polymerase (New England Biolabs M0269L) for 1 hour at 37 ºC in a shaking platform. Slides were washed three times with Buffer A and Lin15 and Lin33 fluorescence-labelled oligonucleotide (100 nM) hybridization was performed in the hybridization buffer for 30 minutes at 37 ºC. Then, slides were washed with Buffer A followed by PBS-0.01% Tween-20 and dehydrated in ethanol. Vectashield with DAPI mounting media were used for nuclei staining. Specificity of the probes and staining were confirmed by using homoplasmic cell cultures (100% NZB and 100% C57 mtDNA). Leica SP5 confocal and ImageJ v.1.6.0 software were used for image acquisition and data analysis respectively.

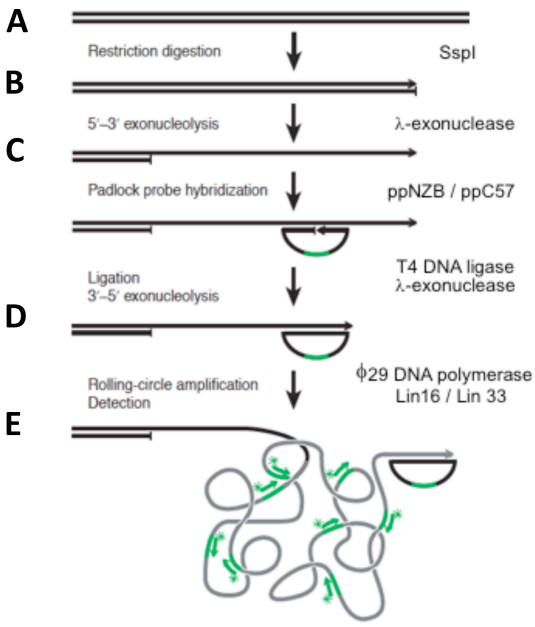

Figure 10. ***In situ*** **detection of mitochondrial DNA using padlock probes.** **(A)** Restriction digestion (*SspI*) at one of the SNPs presented between the two mtDNA sequences. **(B)** Single stranded DNA was generated by strand-specific 5'-3' exonucleolysis **(C)** Padlock probes hybridization to target sequences and **(D)** joint through ligation (DNA ligase) and posterior exonucleolysis to initiate the amplification. **(E)** RCA (ϕ29 DNA polymerase) using fluorescence-labelled oligonucleotides to tag sequences. *Modified from Larsson et al. (2004).*

Table 13. Padlock probes and padlock probe primers

Probe	Sequence
ppC57	5'-P- ATTACTCTCTTCTGG TTCCTTTTACGA**CCTCAATGCTGCTGCTGTACTAC**TCTTC ACAGTGTACAGGTTA -3'
ppNZB	5'-P- ATTACTCTCTTCTGG**CCTTTCCTACGACCTCAATGCACATGTTTGGC**TCCTCTTC ACAGTGTACAGGTTC -3'
Lin33 (ppC57)	5'-Cy3-CCTCAATGCTGCTGCTGTACTAC-3'
Lin16 (ppNZB)	5'-FITC-CCTCAATGCACATGTTTGGCTCC-3' 5'-Cy5-CCTCAATGCACATGTTTGGCTCC-3'

IV.7. Statistical Analysis

Sample size for each measurement was based on previously reported results, and varied depending on the type of data and/or study. The experiments were not randomized. The investigators were blinded to animal genotype and strain in the *in vivo* imaging analysis.

IV.7.A. Statistical analysis of heteroplasmy by mathematical modelling

Heteroplasmy dynamics were modelled in collaboration with Iain G. Johnston and Nick S. Jones (University of Birmingham and Imperial College London, United Kingdom) The model yields $h(t) = 1 / (1 – (1-h_0)/h_0 e^{-\beta t})$, where h is heteroplasmy, t is time after conception, h_0 is initial heteroplasmy at conception, and β is segregation rate. For each dataset the values of h_0 for each sample and of β for each tissue were simultaneously inferred using a maximum likelihood approach implemented with MCMC, assuming normally-distributed measurement noise, with confidence intervals derived using bootstrapping with the percentile method[208]. To assess the influence of chemical and genetic perturbations, the model was expanded to allow β to be a function of time (β_0 before treatment and β_1 after treatment) or a function of a particular mouse strain (β_0 for control mice and β_1 for treated mice). To assess the influence of time, β was modelled as β_0 before a threshold time τ and β_1 afterwards, and the value of τ was jointly inferred. In these cases, a significant difference between β_0 and β_1 implies a difference in segregation behaviour between treatment and control cases, or before and after the threshold time. Model selection using the likelihood ratio test was performed to distinguish the most supported model. When reporting a change in heteroplasmy h with respect to a reference value h_0 (for example, a previous measurement, or a reference tissue), we use the transformation $\Delta h = \beta t = \ln ((h(h_0-1))/(h_0(h-1)))$, motivated by the above model as in Ref [208].

IV.7.B. Experimental statistical analysis.

Data are represented as mean values ± standard error of the mean (SEM) or ± standard deviation (SD) in dot, box and whiskers plots. Where applicable, normality was estimated using D'Agostino & Pearson or Shapiro-Wilk normality test. For comparison between 2 groups, paired or unpaired t-test was used. When data presented normal distribution, a paired test was used and Mann-Withney test otherwise. For more than 2 groups, data were evaluated by one-way analysis of variance (ANOVA) with Dunnett's multiple comparison when data presented normal distribution and Kruskal-Wallis with Dunn´s multiple comparison when data did not follow a normal distribution. Statistically significant outliers were identified using Grubb's test (ESD method). All statistical analyses were performed using Prism v6 (GraphPad Software, California, USA) if is not specified. A p-value below 0.05 was considered statistically significant (*). p-values $p \leq 0{,}01$ (**) and $p \leq 0{,}001$ (***), as well as non-significant differences (n.s.) are indicated.



Results and Discussion

V. Results and Discussion

V.1. Results I: Mitochondrial and nuclear DNA matching shapes metabolism and healthy ageing

The mitochondrial DNA (mtDNA) sequence variability in human population is extensive[209]. Association studies supporting the link between non-pathological mtDNA variants with a growing variety of diseases or conditions are overwhelming, both for human and rodents. However, successful reproducibility of these association studies is just marginal and no convincing support at a molecular level has been achieved. Therefore, the physiological relevance of mtDNA sequence variability remains uncertain. Excellent tools to address the potential role of mtDNA variants are the conplastic animal models. Thus, individuals harbouring identical nuclear background with different mtDNA variants can be compared. Analysis in invertebrates have raised concerns about the consequences of the nuclear and mitochondrial genome mismatch on altered respiratory metabolism or changes in the global organismal behaviour[210,211]. Previous reports using conplastic mice or rats are contradictory; both support or reject the notion that mtDNA variability may impact on organismal physiology. The neutrality of mtDNA variants has been defended for years[212,213]. However, most of the studies that did not confirm the conplastic status of the animals investigated were focused on young animals, and did not investigate the full range of physiological and phenotypic variability.

V.1.A. Previous results

V.1.A.1. Conplastic mice model generation

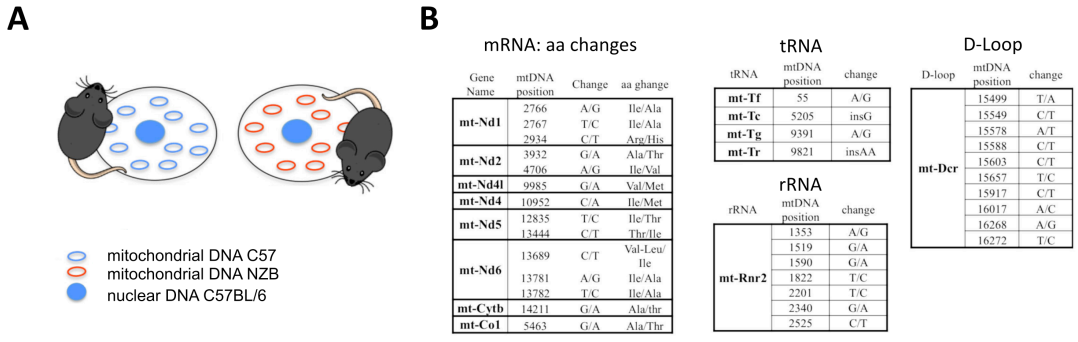

Gene Name	mtDNA position	Change	aa ghange
mt-Nd1	2766	A/G	Ile/Ala
	2767	T/C	Ile/Ala
	2934	C/T	Arg/His
mt-Nd2	3932	G/A	Ala/Thr
	4706	A/G	Ile/Val
mt-Nd4l	9985	G/A	Val/Met
mt-Nd4	10952	C/A	Ile/Met
mt-Nd5	12835	T/C	Ile/Thr
	13444	C/T	Thr/Ile
mt-Nd6	13689	C/T	Val-Leu/ Ile
	13781	A/G	Ile/Ala
	13782	T/C	Ile/Ala
mt-Cytb	14211	G/A	Ala/thr
mt-Co1	5463	G/A	Ala/Thr

tRNA	mtDNA position	change
mt-Tf	55	A/G
mt-Tc	5205	insG
mt-Tg	9391	A/G
mt-Tr	9821	insAA

rRNA	mtDNA position	change
mt-Rnr2	1353	A/G
	1519	G/A
	1590	G/A
	1822	T/C
	2201	T/C
	2340	G/A
	2525	C/T

D-loop	mtDNA position	change
mt-Dcr	15499	T/A
	15549	C/T
	15578	A/T
	15588	C/T
	15603	C/T
	15657	T/C
	15917	C/T
	16017	A/C
	16268	A/G
	16272	T/C

Figure 11. Conplastic mouse models. (A) Schematic diagram of the conplastic strains BL/6^{C57} and BL/6^{NZB}. **(B)** Differences between C57 and NZB mtDNA. The sequences previously published in C57BL/6J (NC_005089) and NZB/B1NJ (L0705) mice were validated in our conplastic mice using RNAseq analyses. *Modified from Latorre-Pellicer (2014).*

Conplastic mice are defined by having the same nuclear DNA but different mtDNA variants. Previous work from our group done by Moreno-Loshuertos *et al.* (2016) using transmitochondrial cybrid cell lines led to the proposal that different mouse mtDNA variants modify the efficiency of the OXPHOS system and the level of ROS production by mitochondria in cell culture[25]. We generated conplastic mice by backcrossing NZB/OlaHsd females, as mtDNA donors, with C57BL/6 males for more than 20 generations. The result was the generation of animals with the C57BL/6 nuclear genome and the NZB/OlaHsd mtDNA (BL/6^{NZB})[175].

Both strains were obtained from Harlan (today re-brand as Envigo). The original mice with the nuclear and mitochondrial genome from C57BL/6 will be referred along this thesis as BL/6^{C57}. The mtDNAs of both strains differ by 12 missense mutations, 4 transfer RNA (tRNA) mutations, 8 ribosomal RNA (rRNA) mutations, and 10 non-coding-region mutations (Figure 11B). We confirmed the nuclear genome identity between both strains by comparing the nuclear sequence derived from liver and heart RNASeq analyses[16,175].

V.1.A.2. Phenotypic variations in conplastic strains

V.1.A.2.a. Metabolic consequences

Conplastic animals, BL/6^{C57} and BL/6^{NZB}, were fertile and showed apparently no differences in phenotype at young ages. When animals reached the adult stage, they revealed metabolic differences since BL/6^{C57} animals presented lower capacity of insulin regulation and plasma glucose clearance (Figure 12A). At younger age (12-weeks-old mice), plasma and liver metabolomics confirmed that the mtDNA haplotypes differ in three relevant metabolic pathways: glutathione metabolism, digestion/absorption, and lipid and membrane metabolism. (Figure 12B). At the same age, RNAseq analysis revealed strain specific gene expression signatures in molecular functions related to lipid and carbohydrate metabolism in the liver and heart (Figure 12C). Free radical scavenging genes were also found among the most differentially expressed genes (DEG) in both tissues, particularly in the liver.

Mitochondria from liver and heart tissue harbouring NZB mtDNA produce more ROS, what is accompanied with higher mtDNA copy number but similar mitochondrial ATP synthesis rate. We equalized the level of ROS and mtDNA copy number providing N-Acetyl-L-Cysteine (NAC) to the animals in drinking water during several weeks. This treatment also caused the reduction in oxygen consumption and ATP synthesis only in mitochondria harbouring NZB mtDNA (Figure 12D) [16,175].

V.1.A.2.b. Ageing phenotype

Several characteristic signs of ageing were less evident in the elderly BL/6^{NZB} individuals when compared with age-matched BL/6^{C57} mice (Figure 12E). Four days after birth, the respiration and ATP synthesis rates in liver mitochondria were lower in organelles from BL/6^{NZB} mice. Both variables were subsequently equalized, but from 100-days-old onwards, the rates in BL/6^{C57} liver mitochondria decreased progressively. These changes were due to a steady decline of BL/6^{C57} respiration with ageing. However, BL/6^{NZB} respiration remained constant between days 20 and 300 (Figure 12F). Analysis of the telomere-length attrition rate with age in the hair follicle stem cell compartment reinforced the observation that the NZB mtDNA haplotype promotes healthier ageing when compared with the C57 mtDNA haplotype in the context of the C57BL/6 nuclear background. (Figure 12G). The transcriptomic and metabolic profiling in the liver and heart confirmed a difference in ROS handling between mtDNA variants. The elevated levels of mitochondrial ROS in BL/6^{NZB} young mice were inverted in animals above 28 weeks of age. Then, BL/6^{NZB} liver mitochondria from young and middle-aged maintained similar ROS production whereas BL/6^{C57} mitochondria showed a sharp age-related increase in ROS production (Figure 12H).

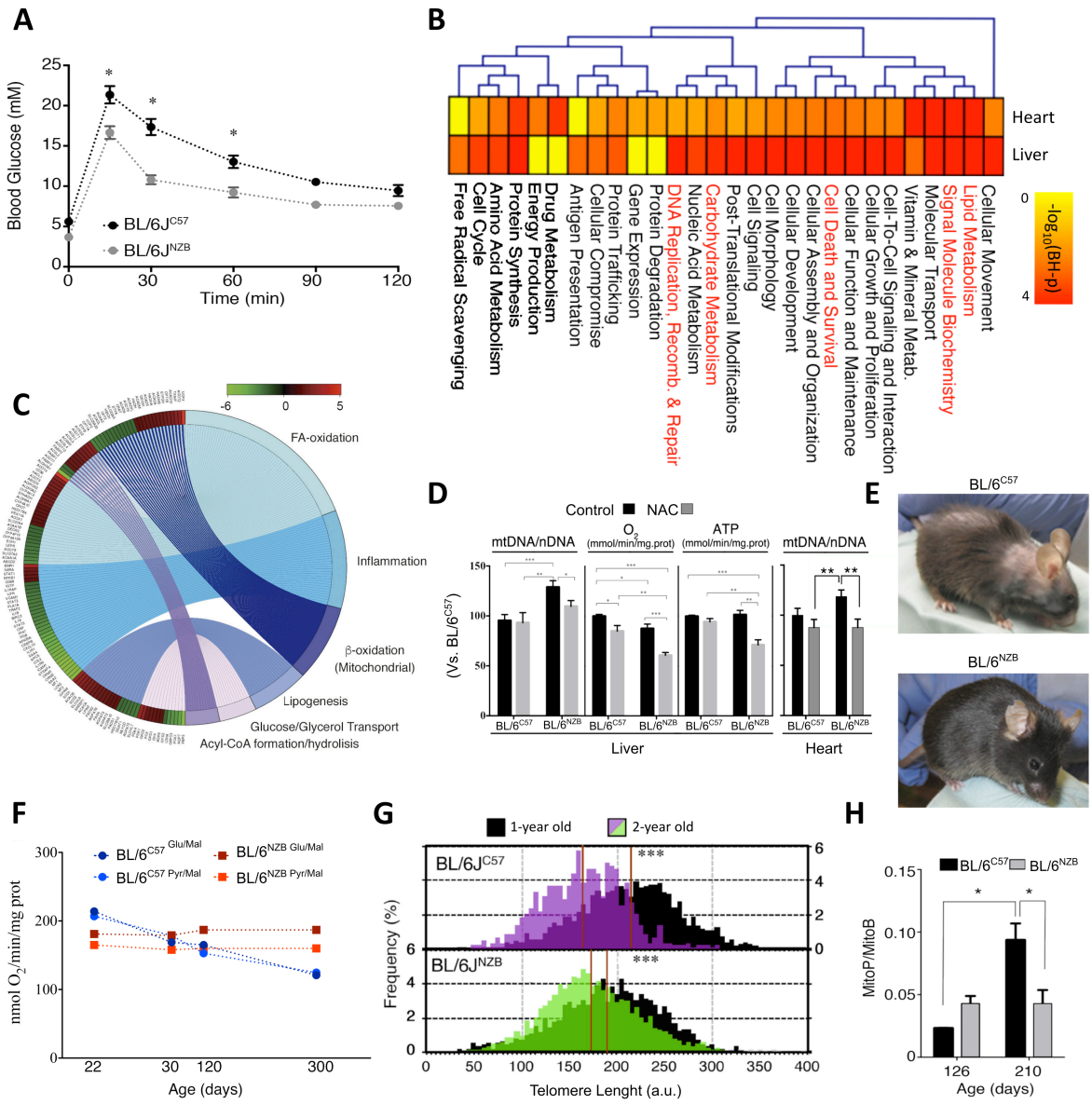

Figure 12. Functional differences among conplastic strains. **(A)** Glucose tolerance test in starved mice (14 months old, *n* = 7 per genotype). **(B)** Heatmap and hierarchical clustering of enrichment ($-\log_{10}$ Benjamini–Hochberg (BH)-adjusted *p-value*) of the functions defined by the ingenuity pathway analysis (IPA) in the set of genes differentially expressed between conplastic mice ($BL/6^{NZB}$ *vs.* $BL/6^{C57}$) in heart (H) (top) and liver (L) (bottom). Yellow, non-significant (BH $P = 1$); red, highly significant (BH $P \leq 10{-}4$) (10-weeks-old mice, *n* = 6 per genotype). **(C)** Chord plot comparing liver gene expression in conplastic mice. The chord plot shows gene changes (logFC) and relates them to their functional categories. (10-weeks-old mice, *n* = 6 per genotype). **(D)** Mitochondrial performance in control *vs.* treated mice (NAC). Liver: relative mtDNA amount; oxygen-dependent (coupled) respiration; pyruvate + malate-driven ATP production in isolated mitochondria. Heart: relative mtDNA amount. (12-week-old animals; *n* = 6 per genotype). **(E)** Representative image of 2-year-old conplastic animals. **(F)** O2 consumption (coupled) respiration in liver mitochondria simultaneously isolated from 22-, 30-, 120- and 300-days-old males (*n* = 8) **(G)** Telomere length in hair follicle cells of 1- (*n* = 6 per group) and 2-year-old mice ($n = 5$ for $BL/6^{NZB}$, $n = 4$ for $BL/6^{C57}$). Red lines indicate mean length (*** p-value < 0.001, Wilcoxon's rank sum test). **(H)** Relative liver mitochondrial H_2O_2 generation (126-days-old mice, *n* = 2 per genotype; 210-days-old mice, *n* = 6 per genotype).

V.1.B. Match between mitochondrial DNA and nuclear DNA

The OXPHOS system in animal cells is the only macromolecular structure formed with components encoded in two genomes. We hypothesized that diverse wild type mtDNA haplotypes, when confronted with the same wild type nDNA background, may generate an array of mtETC with slight differences in performance and we postulated that these differences could impact on organismal metabolism.

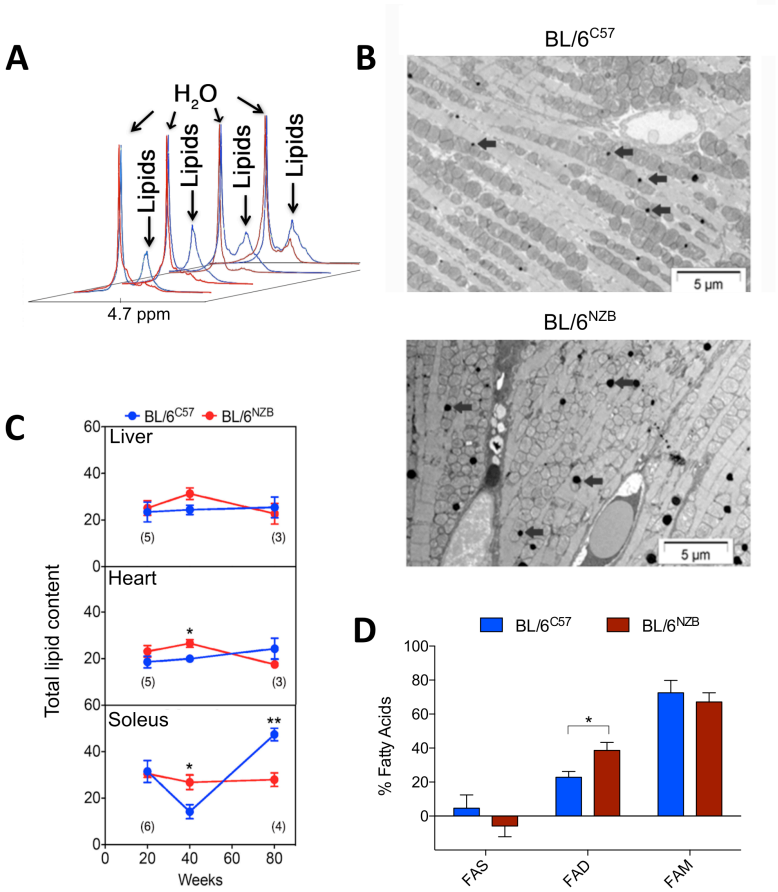

Figure 13. Differences in lipid metabolism in conplastic mice. (A) Representative ^{1}H-MRS spectra of soleus skeletal muscle. In blue, BL/6^{C57} strain; in red BL/6^{NZB} strain (80-weeks-old animals, n=4 per genotype). **(B)** Representative heart TEM images illustrating differences in mitochondria and lipid droplets (black arrows) between 20-weeks-old conplastic mice (n=5). **(C)** ^{1}H-MRS longitudinal analysis of lipid content in the indicated tissue, age and genotype (number of individuals in brackets). **(D)** ^{13}C-MRS of the fatty acid accumulation in WAT of 80-weeks-old mice (n=5). Data are means ± s.e.m, **p-value* < 0.05, ***p-value* < 0.01, two-tailed *t*-test.

V.1.B.1. Different mtDNA variants promote *in vivo* metabolic consequences

In vivo ^{1}H Magnetic Resonance Spectroscopy (^{1}H-MRS) revealed that different mtDNA haplotypes influence both, the lipid and glucose metabolism. BL/6^{C57} mice gain more weight in the middle age[16]. In agreement with that, it was found more accumulation of epididymal lipid storages in the control mice BL/6^{C57} at 40 weeks of age (Figure 13A). Longitudinal analyses of lipid content in the liver, heart and skeletal muscles showed no differences in lipid content at 20 weeks (Figure 13C). However, transmission electron microscopy analysis (TEM) of cardiac fibres revealed that 12-weeks-old BL/6^{NZB} mice have higher content and size of lipid droplets (Figure 13B). The explanation may reside in the use of fat, suggesting a more active mobilization of lipids for degradation and consumption in peripheral tissues. The accumulation of lipid droplets by healthy cardiomyocytes is for fuel purposes not for lipid storage[214]. Mature BL/6^{NZB} mice (40-weeks-old males) had higher tissue lipid content despite their lower body weight

(Figure 13C). At 80 weeks of age, lipid content in both strains was similar in the liver and in the heart although was significantly higher in BL/6^{C57} muscle (Figure 13C). This may reflect the accelerated deterioration of aged BL/6^{C57} mice, with replacement of muscle mass and gain in fat content.

Next, the nature of the lipid storages was determined by ^{13}C MRS in white adipose tissue (WAT) of the mouse epididymis (Figure 13D). Variations in the content of polyunsaturated fatty acids (PUFAs) and monounsaturated fatty acids (MUFAs) were found in young mice (12 weeks of age). Among the different PUFAs, we were able to distinguish di-unsaturated (FAD) and mono-unsaturated (FA) fatty acids. Together with the evaluation of the saturated fatty acids (FAS) content, the results revealed differences in lipid metabolism between the two strains. The average number of moles of oxygen required to oxidize PUFAs is about 10% higher than that required for MUFAs, and this observation has been described in relation to the use and accumulation of different varieties of FA[215,216]. We found that each strain is associated with a characteristic accumulation of FA in the WAT. More precisely, the amount of polyunsaturated fatty acids, specifically FAD, is higher in presence of mtDNA NZB and FAS are not accumulated in these animals (Figure 13D).

V.1.B.2. Cardiac and liver ultrastructural features

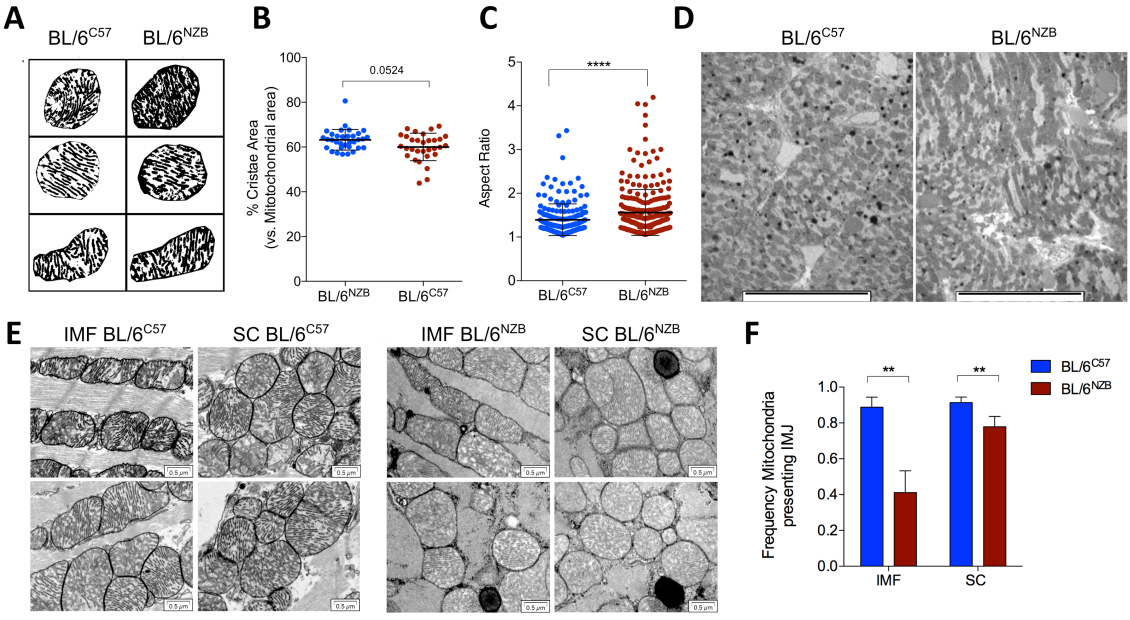

Figure 14. Comparative ultrastructural analysis of mitochondria in conplastic mice. (A) Representative image masks of individual heart mitochondria from 12-week-old mice (n = 3 per genotype). **(B)** The cristae area per mitochondria was estimated from masks. Bars and whiskers represent means ± SD; each point represents the percentage of cristae area in an individual mitochondrion; (BL/6^{NZB}, n = 33; BL/6^{C57}, n = 31). **(C)** Aspect ratio of cardiac mitochondria of conplastic mice (each spot corresponds to a different mitochondrion). ****p-$value$ < 0.0001, nonparametric Mann–Whitney U-test. **(D)** Representative TEM images of mouse left ventricle (80-weeks-old mice, n=3 animals per genotype). The scale bars correspond to 20 µm. **(E)** Representative TEM images of intermyofibrillar (IMF) and subsarcolemmal (SC) mitochondria in cardiac fibres illustrating the differences in mitochondrial shape and distribution in 12-weeks-old BL/6^{C57} and BL/6^{NZB} mice. The scale bars correspond to 0.5 µm. **(F)** Quantification of inter-mitochondrial junctions (IMJ) in IMF and SC cardiac mitochondria. ** p-$value$ < 0.01; two-tailed t-test.

Transmission electron microscopy (TEM) in cardiac tissues revealed between-strain differences in mitochondrial aspect and dynamics, affecting density, morphology and cristae area when the animals were young (12 weeks of age) (Figure 14A-C). In aged animals, we could observe that the mitochondria from control mice (BL/6^{C57}) were more fragmented than in the conplastic ones (Figure 14D). In both strains, a

decrease in the lipid droplets inside the cardiomyocytes could be appreciated with the age (Figure 14D). These results were accompanied with differences between the two strains in cristae remodelling and intermembrane junctions (IMJs) in intermyofibrillar (IMF) and subsarcolemmal (SC) mitochondria in young animals (Figure 14E-F). The IMJs organize cristae from adjacent mitochondria to favour electrochemical coupling and a better propagation of bioenergetic waves into mitochondrial networks[12]. The combination of these results confirm the previous analysis where BL/6^{C57} mice presented higher rates of ATP synthesis per cardiac mitochondria[16,175].

Quantitative proteomics revealed between-genotype differences in the structural proteins of all the respiratory complexes, independently of whether or not they are encoded by nuclear or mtDNA genes (Figure 15A). The proportion of respiratory complexes is lower in young BL/6^{NZB} livers but they are better preserved with age in comparison with that of the BL/6^{C57} livers (Figure 15A). Changes in the proportion of free vs superassembled CIII and CI is required to adapt the cell to different fuels. Thus, a reduction in supercomplex CI+CIII$_2$ favours fatty acid oxidation[32]. The proportion of free CI vs CI forming supercomplexes (CI+CIII$_2$) is lower in livers of BL/6^{NZB} mice regardless of the age, suggesting a preference for fatty acid oxidation (Figure 15B, C). In agreement with that, quantitative proteomics revealed an overall reduction in glycolytic enzymes and an increase in those responsible for β-oxidation in BL/6^{NZB} mice (Figure 15D).

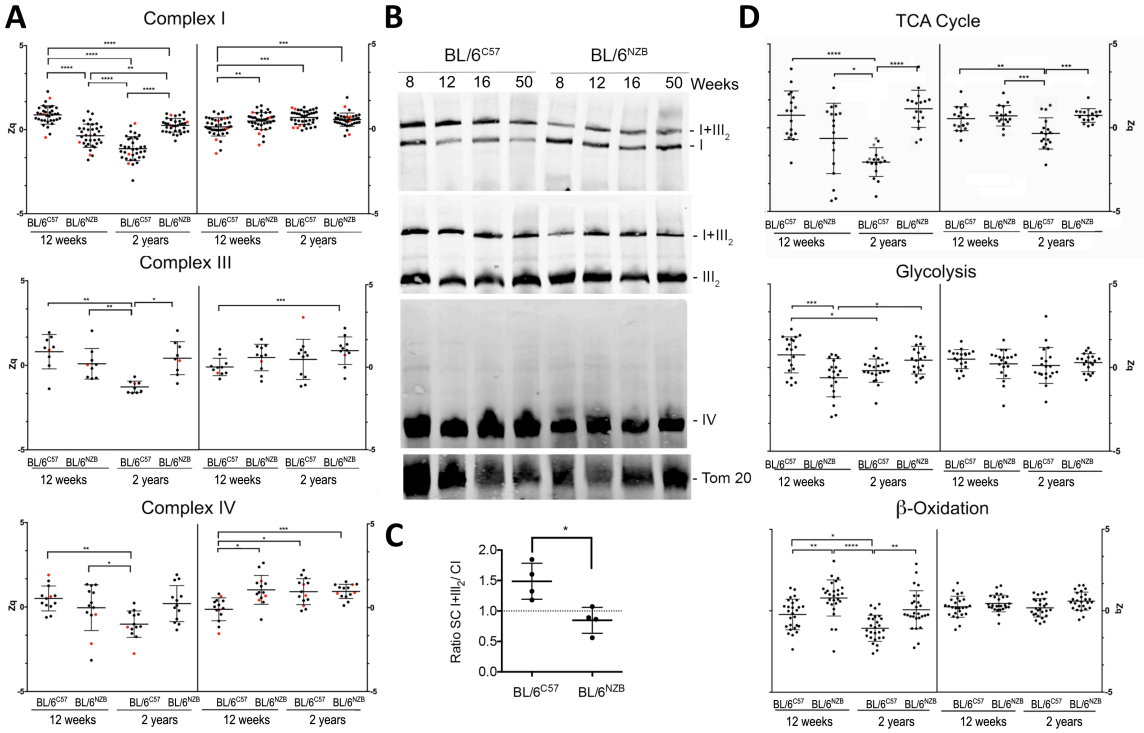

Figure 15. Quantitative proteomics analysis of mitochondrial complexes and functional categories. (A) Relative abundance of component proteins of CI, CIV and CIII detected by iTRAQ quantitative proteomics in heart and liver of the indicated mouse strain at 12 weeks and 2 years of age. Each dot represents a single protein (red dots represent mtDNA-encoded proteins)**. (B)** Blue native electrophoresis of liver samples from 8-, 12-, 16- and 50-week-old conplastic mice. Top: complex I, (NDUFA9); middle: complex III (UQCRC2); bottom: complex IV (COX5b) and TOM20. **(C)** Ratio of supercomplexed to free complex I, determined from the CI western blot in B. **(D)** Relative abundance of proteins of the TCA cycle, glycolysis, or β-oxidation detected by iTRAQ quantitative proteomics in heart and liver of the indicated mouse strains at 12 weeks and 2 years of age.

V.1.C. nDNA/mtDNA mismatch triggers a cellular adaptive response

V.1.C.1. Role of Reactive Oxygen Species

Quantitative proteomics revealed a differential profile for the ROS defence proteins (Figure 16A). In liver, the major mitochondria-located redox regulators GLRX2, GLRX5 and TXNRD2 were increased in young and old BL/6^{NZB} mice, whereas cytosolic ϒ-glutamyltranspeptidase 1 (glutathione pool maintenance) and four mitochondrial redox regulators (PRDX3, TXNRD2, SOD2 and NNT) were decreased in young BL/6^{NZB} mice, but then strongly increased with age (Figure 16B). Ageing has a profound and different effect on the ROS handling proteomes of the two conplastic mouse strains (Figure 16A).

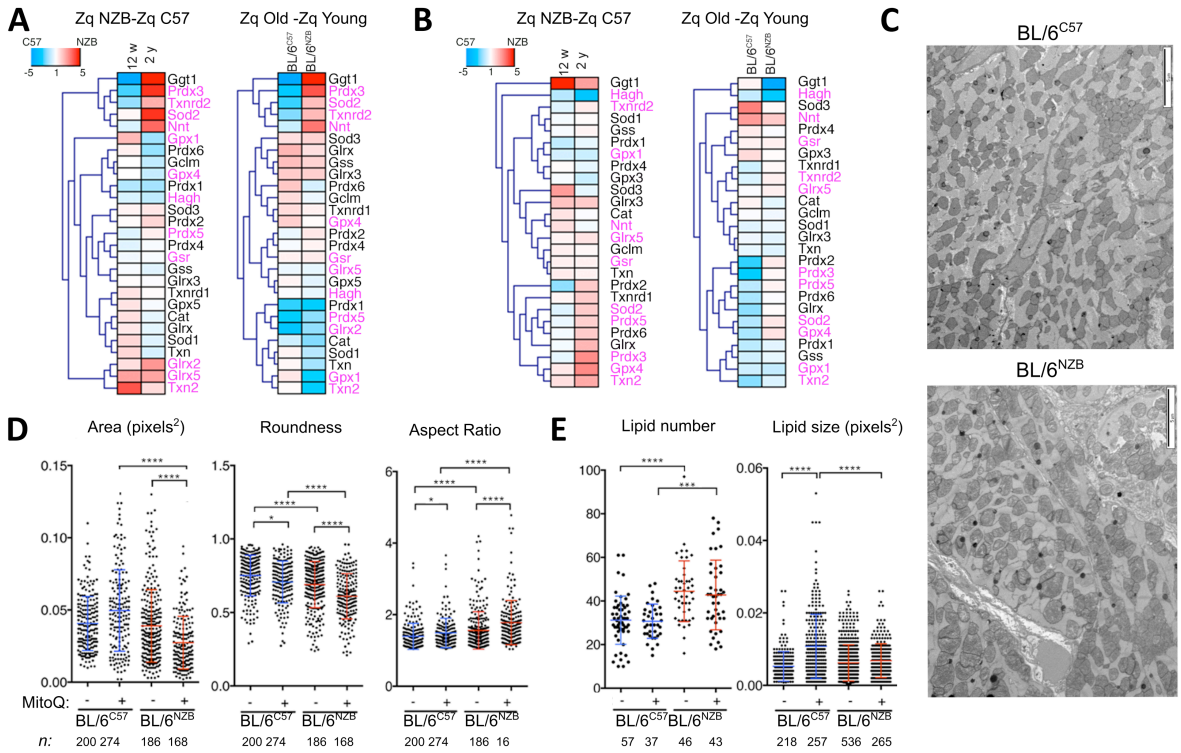

Figure 16. Differential handling of ROS in conplastic mice. (A-B) Heat maps and hierarchical clustering of enrichment (*Zq* differences between indicated genotypes and/or ages) of the proteins quantified by iTRAQ involved in ROS metabolism in either liver (A) or heart (B). Text in purple colour corresponds to mitochondrial located proteins (n=3). **(C)** Heart representative TEM images of 12-week-old animals treated with MitoQ (n=3 per genotype). **(D)** Morphometric analysis of mitochondria in TEM images of heart left ventricle (n=3 per genotype). **(E)** Lipid composition and content analyses in cardiac myographs of 12-weeks-old conplastic mice with or without MitoQ treatment. Data in D-E are given as means ± s.e.m. **p-value* < 0.05; ***p-value* < 0.01; ****p-value* < 0.001; *****p-value* < 0.0001, non-parametric Kruskal–Wallis test.

To determine the role of mtROS, young mice (12-weeks-old males) were treated with the mitochondria-specific antioxidant molecule, MitoQ[217]. Chronic administration of MitoQ for 28 days with an osmotic minipump modified significantly the overall ultrastructure of heart mitochondria in young BL/6^{NZB} mice (Figure 16C, D). TEM analysis was performed using different shape descriptors (i.e. lower roundness-sphericity- and an increase in aspect ratio, defined as the ratio between the major and minor axis lengths of an ellipsoidal shape)[184]. Very interestingly, the overall mitochondrial area was similar between control and conplastic hearts in the absence of treatment and significantly smaller in the BL/6^{NZB} mice when exposed to MitQ. MitoQ did not affect the lipid droplet accumulation between BL/6^{C57} and BL/6^{NZB} cardiomyocytes, but increased the droplet size in BL/6^{C57} animals (Figure 16E). Changes in mitochondrial morphology were

more pronounced in BL/6^{NZB}. There was an increase in the area of mitochondria of the conplastic mice, being more rounded in the presence of treatment, suggesting an increase of the mitochondrial fragmentation in that case.

V.1.C.2. Role of the mitochondrial unfolded protein response

The iTRAQ quantitative proteomics revealed also that the proteins involved in mitochondrial dynamics and mtUPR are increased in BL/6^{NZB} mice and that these differences are sensitive to age and vary between the tissues studied (Figure 17 A-D).

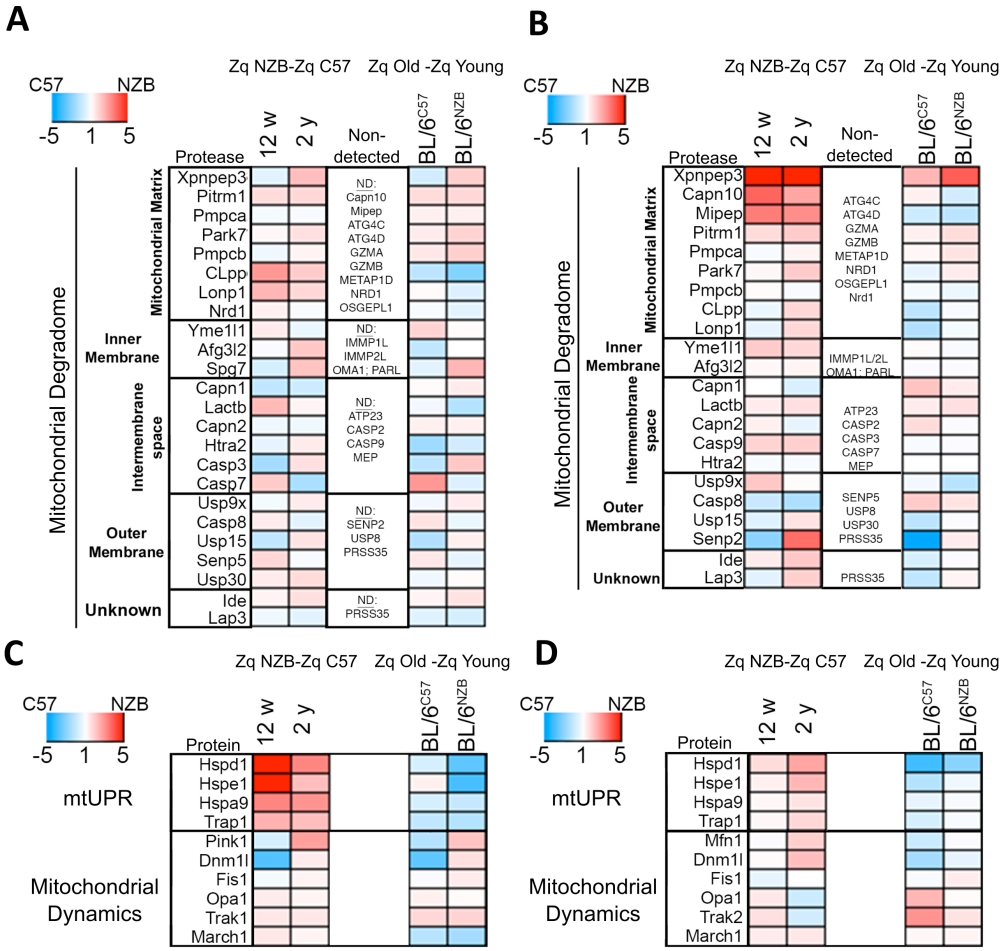

Figure 17. Proteostasis, mitochondrial UPR and dynamics. **(A-B)** Proteomic analyses of the mitodegradome in liver (A) and heart (B) total protein samples. **(C-D)** Detected proteins involved in the mitochondrial UPR and dynamics in liver (C) and heart (D) total protein samples. Data are expressed as *Zq* differences between BL/6^{NZB} and BL/6^{C57} mice with 12 weeks (w) or 2 years (y) of age, or between old and young animals of the same genotype (n=3).

The mitochondrial degradome (mtDg) is defined as the set of proteases located in mitochondria involved in the protein synthesis regulation, quality control, biogenesis, dynamics, mitophagy, and apoptosis[218]. Quantitative proteomics revealed between-strain differences in the mitochondrial degradome, especially in the heart, that were strongly influenced by age (Figure 17A, B). Matrix proteases and chaperones involved in the mitochondrial unfolded protein response (mtUPR) were elevated in BL/6^{NZB} animals, suggesting more active proteostasis (Figure 17C, D). This was especially prominent in the liver,

where an elevation in stress chaperones was accompanied by an elevation of characteristic proteases of the mitochondrial matrix (LONP1 and CLPP) involved in mtUPR (Figure 17C).

V.1.D. Phenotypic differences: mtDNA variants modulate healthy ageing and lifespan

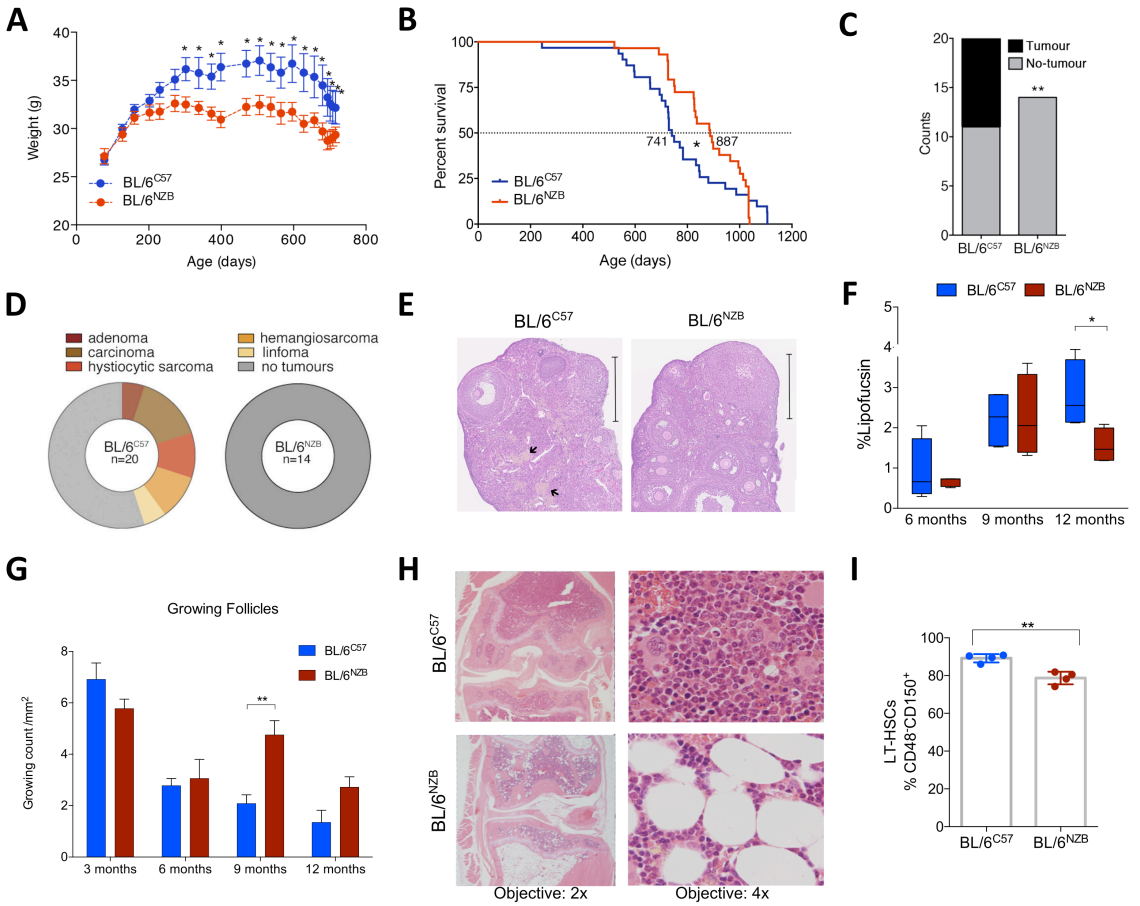

Figure 18. Ageing phenotype in conplastic mice. **(A)** Weight gain (chow diet, n = 19 males per genotype, mean ± s.e.m. **p-value* < 0.05, two-tailed *t*-test). **(B)** Survival curves (n = 31 BL/6^{C57} and n = 29 BL/6^{NZB}); Gehan–Breslow–Wilcoxon test **p-value* < 0.05. **(C-D)** Tumour incidence and classification detected upon liver necropsy of animals dying from natural causes (BL/6^{NZB}, n=14; BL/6^{C57}, n=20 mice). **(E)** Representative histological preparations of ovaries from animals of the indicated age and genotype (black arrows, lipofuscin pigment granules). **(F)** Lipofuscin accumulation over the reproductive period of conplastic females (n = 5 females per genotype and age). **(G)** Ovarian primary follicles quantification in female mice of different ages (n=5 females, in total 10 ovaries per group and age). **(H)** Histological analysis of the bone marrow of 75-weeks-old BL/6^{C57} and BL/6^{NZB} mice (n=4 males and 5 females per group). **(I)** Flow cytometry analysis of bone marrow multipotent long-term haematopoietic stem cells (LT-HSCs) in elderly conplastic mice (80-weeks-old mice, n = 4). **p-value* < 0.05, ***p-value* < 0.01, two-tailed *t*-test.

As a follow-up of previously research in our group[175], we decided to study the mismatch between nDNA/mtDNA during ageing in more detail. The existence of intrinsic mismatch between mtDNA and nDNA causes lifelong metabolic consequences. Phenotypically, we found an early loss of weight in BL/6^{C57} mice and a protection against frailty in BL/6^{NZB} mice (Figure 18A). BL/6^{NZB} mice increase median lifespan more than 16% (741 days for BL/6^{C57} and 887 days for BL/6^{NZB}) without modifying maximum lifespan (Figure 18B).

Healthier ageing of BL/6^{NZB} mice was characterized by a reduced tumour incidence (i.e. adenomas or carcinomas but also lymphomas), suggesting lower genome instability in BL/6^{NZB} mice (Figure 18C, D). We noticed, however, a higher incidence of extramedullary haematopoiesis in the spleen of the BL/6^{NZB} mice. Ovary deterioration was delayed in BL/6^{NZB} females, determined by the accumulation of lipofuscin

and the quantification of primary/primordial follicles, corpus luteum (CL) and atretic follicles as some signs of ageing (Figure 18E-G). The number of ovarian follicles is reduced by maturation until the exhausted capacity of the ovary at the menopause. Non-growing primordial follicles are used as a critical indicator of female fertility[219]. Primordial follicles are recruited into the growing follicle pool to follow with further stages of follicle development[220]. The decrease of primordial and primary follicles and primary and growing follicles in control mice in comparison to the conplastic mice indicates that ovary function is better preserved in BL/6^{NZB} females[16] (Figure 18F). Consistent with these results, the accumulation of lipofuscin at 12 months of age was significantly lower in BL/6^{NZB} females (Figure 18G).

The histological analysis of bone marrow (closer region of knee joint) revealed a very different composition between 75 weeks-old BL/6^{NZB} and BL/6^{C57} mice (Figure 18H). Thus, we documented an increased incidence of myeloproliferative disease in aged individuals with mtDNA C57. Normal ageing causes a diminished capacity of maintaining homeostasis with stem cell decline[221]. This is the cause of the described increase of the stem cell pool size, myeloid lineage potential and the expression of myeloid leukaemia genes in advanced age animals. On the other hand, lymphoid lineage potential and lymphoid progenitors are diminished during ageing and are related to the diminution of adaptive immune system[221]. To evaluate the age-related changes in hematopoietic stem cells (HSCs), bone marrow from the two strains were collected at 75 weeks of age. Analysis of the haematopoietic stem and progenitor cells (KLS) and multipotent long- term HSCs (LT-HSCs) by flow cytometry revealed a higher content of LT-HSC cells in BL/6^{C57} in comparison with BL/6^{NZB}, suggesting an increase in self-renewal of the stem cell pool due to the necessity of replenish the hematopoietic system in aged mice[222] (Figure 18I).

V.1.E. Discussion

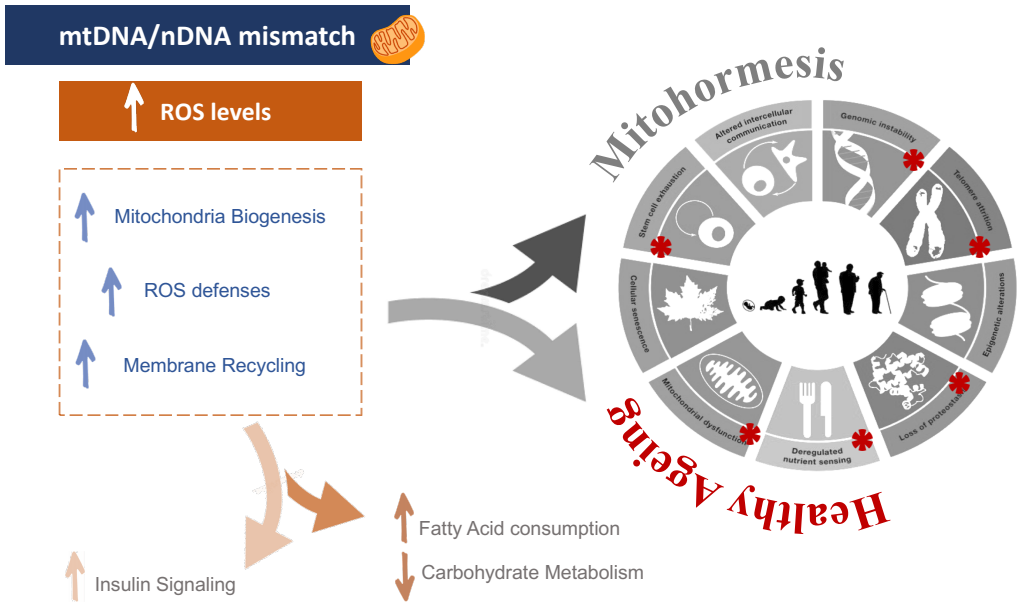

Figure 19. Model of the temporal integration of phenotypic differences between BL/6^{C57} and BL/6^{NZB} conplastic mouse models. MtDNA haplotype induces mtDNA/nDNA mismatch that causes a slight constitutive elevation of reactive oxygen species (ROS) in BL/6^{NZB} mice and an initially poorer OXPHOS performance. This promotes activation of mitochondrial biogenesis and improved efficiency of the defences against ROS and associated cell damage (membrane recycling). As a consequence, fatty acid metabolism is enhanced, with the concomitant reduction in carbohydrate metabolism, leading to improved insulin signalling. This, together with the generalised activation of the mitohormesis response, leads to the healthier ageing observed in BL/6^{NZB} mice.

The metabolic profile of conplastic mice is an indication of the influence of mitochondrial genome on lipid and carbohydrate metabolism, as well as on the contribution of xenobiotics and antioxidant metabolism and on several other physiological processes (e.g. inflammation, oxidative stress, energetic metabolism and ageing among others). The adjustment between structural and functional parameters of nDNA/mtDNA may determine the equilibrium of many metabolites that are essential for cell physiology (FAD, NAD, ATP, AMP...), ROS production and signalling. These factors have been implicated as major drivers of ageing in a context of mitochondrial function. Changes in OXPHOS performance may be silenced or induced by the combination of environmental factors and a specific mtDNA variant. The result of the alteration in physiology might modify the metabolic requirements and be either more or less permissive to minor discordance between mtDNA and nDNA. Our experiments demonstrate that mtDNA haplotype profoundly influences the generation of reactive oxygen species by mitochondria, the energy homeostasis metabolism, and several ageing markers among others, resulting in different healthy longevities of conplastic strains. Our results show that substitution of different wild type mtDNA variant is sufficient to promote measurable differences in mitochondrial function and a concomitant cellular adaptive response likely orchestrated by the complex network of mitochondrial stress response (MSR) pathways. The modest but continuously elevated basal levels of ROS do not seem to promote oxidative damage. This is perhaps due to the increased expression of antioxidant defences that can prevent injury and thereby ameliorate the damaging consequences of the elevated ROS without blocking their signalling role. The initially poorer performance of mitochondria in conplastic animals, caused by the mismatch between nDNA- and mtDNA-encoded genes, appears to trigger a compensatory response that, in the long term,

promotes a healthier ageing. This is a robust example of mitohormesis[223–225]. This scenario connects mitohormesis with several hallmarks of ageing, and establishes a temporal connection between them[52].

The results of the analysis of mtETC support the hypothesis that the double genetic origin of OXPHOS complexes gives rise to an array of alternative interaction modes between mtDNA-encoded and nDNA-encoded protein/complex subunits, and that these differences in interaction between proteins forming SCs, promote characteristic changes in the performance of the OXPHOS system. The adaptive response involves post-translational modifications and the activation/deactivation of regulatory pathways, and not only requires additional changes in gene expression. In summary, animal models with identical nuclear genomes but with different mtDNA haplotypes generate functionally different OXPHOS systems that shape the organismal metabolism, supporting the conclusion that different wild type mtDNA haplotypes are phenotypically relevant[16].

V.2. Results II: Physiological implications of heteroplasmy between mtDNA haplotypes.

Heteroplasmic mice were generated after fusing the cytoplast obtained from BL/6^{C57} and BL/6^{NZB} zygotes (Figure 8, Figure 20; See material and methods). The idea of using these two non-pathological mitochondrial DNA (mtDNA) variants is based on the deep characterization of the physiological differences in mice having one or the other mtDNA variant. We evaluated the effect of the co-existence in the same cytoplasm of the two-mtDNA haplotypes using as controls the homoplasmic strains (BL/6^{C57} and BL/6^{NZB}).

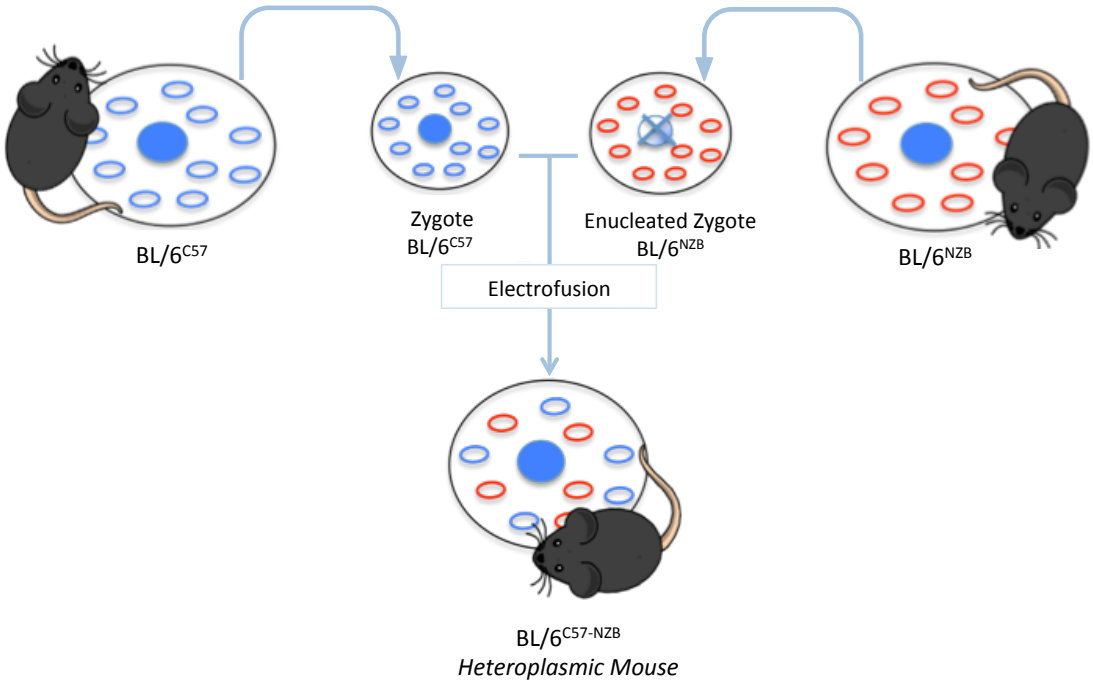

Figure 20. Diagram of heteroplasmic mice generation. Heteroplasmic mice were generated by fertilization process. Electrofusion of cytoplast from conplastic BL/6^{NZB} zygotes to recipient C57BL/6JOlaHsd (BL/6^{C57}) enucleated zygotes.

C57 and NZB mtDNA haplotypes differ by 12 missense mutations, 4 mutations in tRNA and 8 mutations in rRNA (SNPs) (Figure 11). Heteroplasmy is defined by the co-existence in the same cytoplasm of two or more mtDNAs that show divergence in their sequences, regardless of the number of SNPs. The differences depending on each haplotype can be modulated by the adaptive response of the cells to reach the required performance of the OXPHOS system. What is likely to impact more in OXPHOS function is the divergence caused by the individual single nucleotide polymorphism (SNP) variation, rather than the absolute amount of differences in the sequence. This fact was demonstrated previously in our group in human and mouse transmitochondrial cybrid cell lines with different mtDNA haplotypes[26,121].

V.2.A. Previous Results

V.2.A.1. Germline mtDNA selection

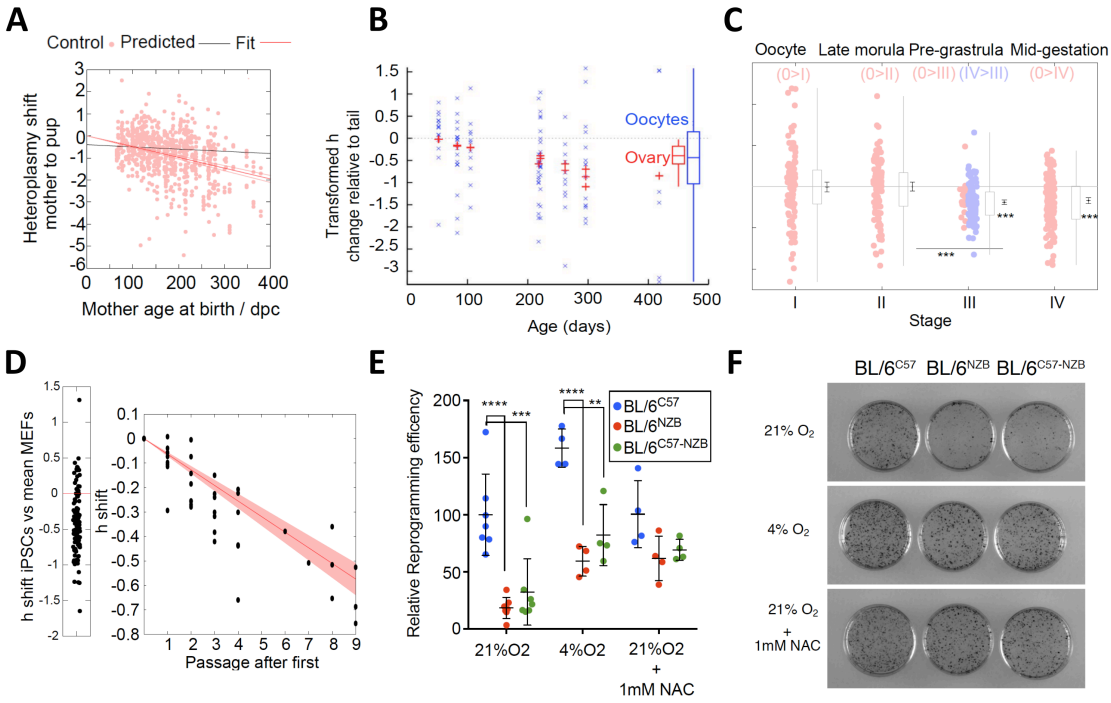

Figure 21. Heteroplasmy is sensed and mtDNA segregated prenatally. **(A)** Heteroplasmy shift between mother's tail sampled aand pup's tail sampled at 21 days of age (vertical axis), as a function of the mother's age when the pup was born (horizontal axis). Red lines show a fit with 95% c.i.s to a linear decrease in transformed heteroplasmy with mother's age. The black line shows the predicted trend from the inferred developmental shift and ovarian segregation that cannot explain the observed shift in heteroplasmy between mothers and their offspring; (pups = 819 from 43 BL/$6^{C57\text{-}NZB}$ females, ovary = 73 BL/$6^{C57\text{-}NZB}$ females). **(B)** Convergence in heteroplasmic proportions between ovary and oocytes; (n = 110 oocytes from 13 BL/$6^{C57\text{-}NZB}$ females). **(C)** Shift in heteroplasmy observed upon a change into each pluripotency class relative to ovary heteroplasmy. Classes are: 0 (ovary); I (oocyte, n = 100); II (2.5 dpc embryos, n = 101); III (5.5 dpc embryos, n = 21); IV (13.5 dpc embryos, n = 161). Pink dots represent heteroplasmy level in the indicated embryo class samples and blue dots represent heteroplasmy in MEF cell lines stablished from class IV embryos. Significant changes are shown. **(D)** (D-left) Heteroplasmy shift between the mean of the MEFs set and individual iPSCs, showing a significant deviation from zero (n = 80 iPSCs clones from 4 different MEFs BL/$6^{C57\text{-}NZB}$ lines). (D-right) Heteroplasmy changes with iPSCs passage, with the heteroplasmy of the first passage as the reference value, and the x-axis labelling subsequent passages (n = 8 iPSCs BL/$6^{C57\text{-}NZB}$ clones). Lines show mean linear fit and 95% c.i.s. **(E)** Reprogramming iPSCs efficiency of BL/6^{C57}, BL/6^{NZB} and BL/$6^{C57\text{-}NZB}$ MEFs under 21% O_2 (n = 7 per genotype), 21% O_2 plus 1mM NAC (n = 4 per genotype) and 4% O_2 (n = 4 per genotype). Data are represented as mean ± SD. **p-value* < 0.05, ***p-value* < 0.01; ****p-value* < 0.001), two-tailed *t*-test. **(F)** Representative images of AP-stained plates 14 days after reprogramming.

The selection between non-pathological mtDNA haplotypes along female germline transmission was first thought not to exist[178], although it has been recently proposed[163]. During maturation, female germline mtDNA suffers a bottleneck where either random-drift or positive selection strongly reduces the heteroplasmy[226]. Previous results indicate the presence of heteroplasmy shifts between mother tails at 21 days post coitum (dpc) and neonatal mice tails at day 21 after birth (Figure 21A)[175]. The change in heteroplasmy is accentuated with mother's age at pup birth (Figure 21A).

In our heteroplasmic model, ovary showed a significant tendency to accumulate C57 mtDNA while testis accumulated NZB mtDNA (Figure 21B). Oocytes have the highest mtDNA content of any cells, up to

200,000 copies per cell[227], while sperm mtDNA content is among the lowest (70 copies per cell)[121]. Most of the mtDNA extracted from ovaries originates from the oocytes and therefore ovary analysis reflected the behaviour of oocytes. The contribution of sperm mtDNA to the total analysis of the testis is minimal and the evaluation of testis cannot inform on the preference of sperm for one or the other mtDNA. In parallel, the assessment of heteroplasmy in gonads (ovary, testis) compared to the analysis in germline cells (oocytes and spermatozoa) revealed that both, the oocytes and sperm cells, positively select for C57 mtDNA, despite their highly divergent differentiation process (Figure 22).

V.2.A.2. MtDNA competition at early embryonic stages

The female germline segregation inferred through ovary mtDNA dynamics cannot account in full for the observed mother-to-pup shift in mtDNA heteroplasmy. This suggests that an additional selection in favour of C57 mtDNA haplotype takes place during gestation. It was found that a very fast shift in heteroplasmy occurrs in the early development around the pre-implantation step, between 5.5 and 6.5 dpc embryos[175] (Figure 21C). In this step, our results describe a new checkpoint for mtDNA segregation during embryonic development.

V.2.A.3. Embryonic mtDNA segregation is associated with pluripotency

Mouse embryonic fibroblasts (MEFs) from post-implantation embryos of the three strains (BL/6^{C57}, BL/6^{NZB} and BL/6$^{C57\text{-}NZB}$) and induced pluripotent stem cells (iPSCs) generated from them were used to generate induced pluripotent stem cells (iPSCs) in order to regress their differentiation status[175]. It was observed that NZB mtDNA was preferentially lost upon reprogramming (Figure 21D). Furthermore, a striking decrease in the reprogramming efficiency of MEFs obtained from BL/6^{NZB} and BL/6$^{C57\text{-}NZB}$ animals was observed (Figure 21E-F). Using culture conditions with 4% oxygen, the reprogramming efficiency increased in MEFs regardless of their mtDNA content, but oxygen concentration did not impact the heteroplasmic shift (Figure 21E-F). However, in the presence of 1 mM N-Acetyl-L-Cysteine (NAC) in the medium, the reprogramming efficiency of MEFs derived from BL/6^{NZB} and BL/6$^{C57\text{-}NZB}$ embryos increased significantly, without affecting that of BL/6^{C57} MEFs (Figure 21E-F). The heteroplasmic shift during MEFs to iPSCs reprogramming was eliminated adding NAC to cell culture media. This behaviour is reminiscent of the observed reduction in iPSCs reprogramming efficiency associated with elevated mitochondrial ROS and the demonstration of a negative selection against mutant mtDNA by pluripotent stem cells[228].

It was demonstrated that mtDNA heteroplasmy modulates the viability of embryonic cells, its metabolic fitness and their ability to become iPSCs[175] (Figure 21E-F). This is the cause of a strong competition among mtDNA haplotypes at early embryonic stages, adding a new mechanism to fight heteroplasmy. In conclusion, iPSC generation efficiency is strongly influenced by the mtDNA haplotype.

V.2.A.4. Heteroplasmy is rejected in most of the tissues

Segregation of C57 mtDNA and NZB mtDNA was analysed in 19 different tissues (brain, liver, heart, skeletal muscle, kidney, spleen, thymus, testis, ovary, bladder, gut, lung, pancreas, blood, tail, bone marrow, brown adipose tissue (BAT), white adipose tissue (WAT) and eye) of the heteroplasmic mice across the life span (Figure 22). Most of the tissues progressively selected for one of the alternative variants of mtDNA while in other tissues heteroplasmy remains largely stable[175], as previously reported[156,163,179,229]. We conclude that the segregation of one or the other mtDNA is the norm, and that only a limited number of

tissues are unable to select against heteroplasmy. Futhermore, we observed that the kinetics of segregation is specific for each tissue (Figure 22).

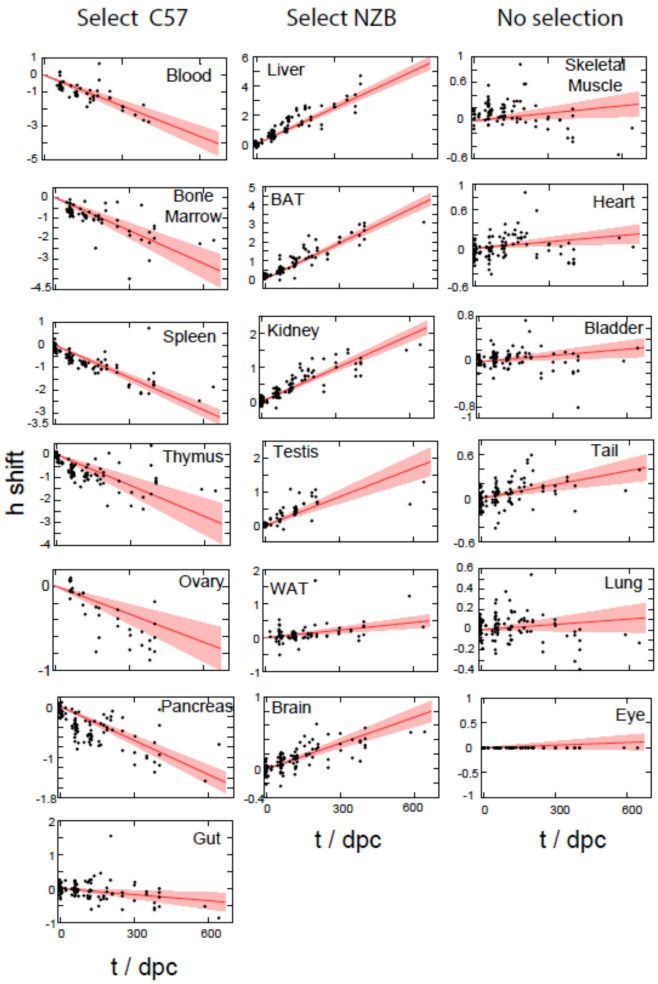

Figure 22. MtDNA segregation in tissues. Tissue-specific patterns of segregation. Red lines provide inferred mean segregation behaviour with 95% confidence intervals (n=119 BL/6$^{C57-NZB}$ mice). Black points show heteroplasmy data in the given tissue plotted relative to eye, which is inferred to have a low segregation rate and is hence used as an approximate control tissue. Each dot represents a different mouse.

V.2.B. MtDNA segregation in embryonic stage, fertility and ovarian ageing

The heteroplasmy levels of over 900 pups at birth were analysed and it was found that C57 mtDNA was significantly favoured, and that the proportion of near to homoplasmic C57:NZB was 45:1 (Figure 23A). The results agree the previous findings that the content of C57 mtDNA in mature oocytes was increased, and the shift between mother tail and neonatal mice indicates a positive segregation in favour of C57 mtDNA variant from heteroplasmic mother to pups. Interestingly, the first litter size was significantly smaller in heteroplasmic mothers than in the homoplasmic ones (Figure 23B) suggesting either that heteroplasmic mothers cannot deliver the regular number of pups or that heteroplasmy may diminish the likelihood of successful embryo development.

To analyse if the heteroplasmy condition or the presence of one or the other mtDNA variants can interfere with the maturation of the oocytes, we investigated the proportion of follicles in different stages of maturation, during the sexual maturity in control, conplastic and heteroplasmic females of different ages (3 to 12-months-old mice) (Figure 23C-F). We found that the proportion of primordial follicles at early age is

lower in the presence of C57 mtDNA with respect to that shown in homoplasmic NZB mtDNA or in heteroplasmic females. The analysis of the ovarian follicle reserve is reduced by maturation until the exhausting capacity of the ovary failure or menopause. Non-growing primordial follicles are used as a critical indicator of female fertility[219]. Primordial follicles are recruited into the growing follicle pool to follow with further stages of follicle development[220]. The systematic reduced content of primordial follicles and primary and growing follicles in control mice *vs.* conplastic mice support the idea that there is an earlier ovarian degeneration in BL/6^{C57} females[16] (Figura 18E, F). The proportion of primordial follicles at early age is increased also in heteroplasmic females with respect to homoplasmic BL/6^{C57}(Figure 23C). The degree of follicle activity can be measured by the number of growing follicles, and occurs in advanced stages of the ovary, when there are fewer amounts of them. There was a significant increase in growing follicles in conplastic females in comparison with control and heteroplasmic females at 12 months (Figure 5E). In summary, with age and using the approach to the mouse equivalent of menopause, follicle counts showed a larger primordial and growing follicle pool in conplastic females BL/6^{NZB} (Figure 5C-F) being an additional indication of their healthier ageing.

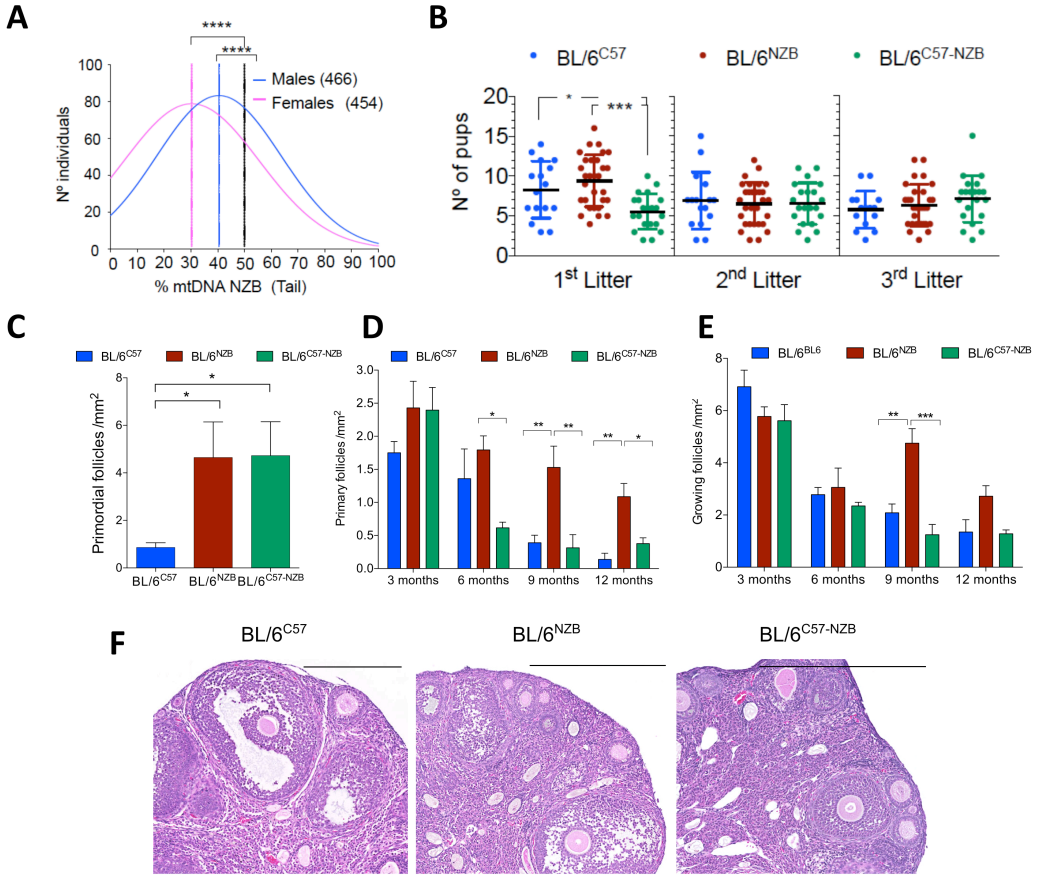

Figure 23. Female germline mtDNA segregation and fertility. **(A)** Distribution profiles in the level of heteroplasmy of the offspring for males and females. Distribution profiles for both sexes are not normal (skewness 0.135 and 0.476. and kurtosis -0.7114 and -0.5474 for males and females, respectively). **(B)** Litter size in homoplasmic and heteroplasmic mouse models. Each dot represents a different litter, only females with three litters are considered. **(C-E)** Histological analyses of follicles in ovaries. (C) Number of primordial follicles in 3-months-old females. Evolution of primary (D) and growing (E) follicles at the indicated ages of the conplastic and heteroplasmic females (n = 5 BL/6^{C57} and BL/6^{NZB}; n = 6 BL/6$^{C57\text{-}NZB}$ per indicated age). **p-value* < 0.05, ***p-value* < 0.01, ****p-value* < 0.001 assessed by ANOVA. **(F)** Representative histological images of the ovaries of 3-months-old conplastic and heteroplasmic females. Scale bar correspond to 0.5 mm.

These results may also suggest an earlier maturation of oocytes with higher content of NZB mtDNA in the heteroplasmic females. In this way, the shift in heteroplasmy towards more C57 mtDNA with the age of the mother could be explained. Also, it could be related with the reduced number of pups in the first litter of the heteroplasmic mice (Figure 23B). Additional support for this conclusion can be found in the study of Wai and Shoubridge (2008) where differences in primary follicles and secondary follicles between post-natal day 1 and post-natal day 29 heteroplasmic mice with co-existing Balb/c and NZB mtDNA haplotypes were observed. They found an increase of NZB mtDNA in more mature oocytes, although they did not attribute any functional role to the level of heteroplasmy[230].

V.2.B.1. Variations in OXPHOS function influence mtDNA haplotype segregation

First, to analyse if the OXPHOS performance can modulate the selection towards one of the mtDNA haplotypes during development, an *in vitro* model was used. MEFs obtained from post-implantation embryos of the BL/6^{C57}, BL/6^{NZB} and BL/6$^{C57\text{-}NZB}$ strains were generated. Three different levels of heteroplasmy were chosen for the analysis (17%, 51% and 79% of mtDNA NZB). Despite the differences in proportion of heteroplasmy, all the heteroplasmic clones showed a reduction in basal and maximum respiration capacity in glucose and in galactose (Figure 24A, B). Also, we observed an increase of mitochondrial membrane potential (MMP) (Figure 24C) and ROS production (Figure 24D). The ROS production was even one order of magnitude higher in heteroplasmic MEFs when normalized per the maximum respiration rate (MRR) (Figure 24E). MEFs could maintain stable heteroplasmy under regular conditions (glucose over-rich medium, 25 mM glucose), they favoured NZB mtDNA at physiological concentrations of glucose (5 mM) and 5 mM galactose medium induced a shift towards C57 mtDNA[175]. (Figure 24F). To guarantee that they were true heteroplasmic cells and not a mix of homoplasmic cells with different mtDNAs, we assessed heteroplasmy using padlock probes to detect each mitochondrial DNA haplotypes by fluorescence in confocal microscopy. In this way, we could conclude that heteroplasmy was intracellular and not intercellular (Figure 24G), both mtDNA variants co-exist in the same cytoplasm.

V.2.B.2. Heteroplasmy modulates embryonic cell metabolism

Embryonic metabolism relies on glycolysis but also on β-oxidation metabolism[231]. To determine *in vivo* whether or not mtDNA heteroplasmy levels establish functional differences among the embryos, we assessed [^{18}F]-Fluorodeoxyglucose ([^{18}F]-FDG) and [^{18}F]-Fluoromisonidazole ([^{18}F]-FMISO) uptake by positron emission tomography and computed tomography (PET/CT) (Figure 25A, C-D) and measured the uptake by gamma counter in 12.5 dpc embryos (Figure 25A, B and E). Previous studies with [^{18}F]-FDG, an analogue of glucose, studied the maternal-fetal drug pharmacokinetics and pharmacodynamics showing high uptake of the probe in early and late pregnancy in humans and primates, but not in rodents[232,233]. We needed to optimize the fetus absorption dose to obtain the uptake as an indicator of their glucose metabolism. [^{18}F]-FDG is taken up by glucose transporters and is phosphorylated by the enzyme hexokinase (HK) to [^{18}F]-FDG-6-phosphate. This product cannot be metabolized in the glycolytic pathway and remains trapped inside the cells[234]. [^{18}F]-FMISO is a PET radiotracer for visualizing regions with low oxygen or hypoxia. It presents higher sensitivity in living tissues than MRI and optical-based techniques (i.e. [^{19}F]-MRI, Near-infrared spectroscopy (NIRS) or phosphorescence)[235]. The uptake of the radioisotope is based on the reduction under hypoxic conditions of the compound to R-NO and RNHOH, and then, covalently bound to macromolecules[235].

Thus, the hypoxic status or oxygen consumption was measured with the [^{18}F]-FMISO. The higher probe uptake corresponded to the lower oxygen levels due to the higher rate of oxygen consumption. When NZB mtDNA predominated the uptake of the glucose analogue decreased, suggesting lower demand of

glucose (Figure 25A, C) that correlates with an increase of the oxygen level measured (Figure 25 B, C). When we compared them with the homoplasmic embryos, the uptake of [^{18}F]-FMISO relied more on the proportion of NZB mtDNA as a dominant effect. It can be observed that there is an overall impact of the balance between the two tendencies promoted by the different homoplasmic embryos (Figure 25D). The results obtained in embryos are evocative of our previous results showing that NZB mtDNA promotes a lower glucose use in favour of a higher lipid metabolism and a decreased rate of oxygen consumption[16].

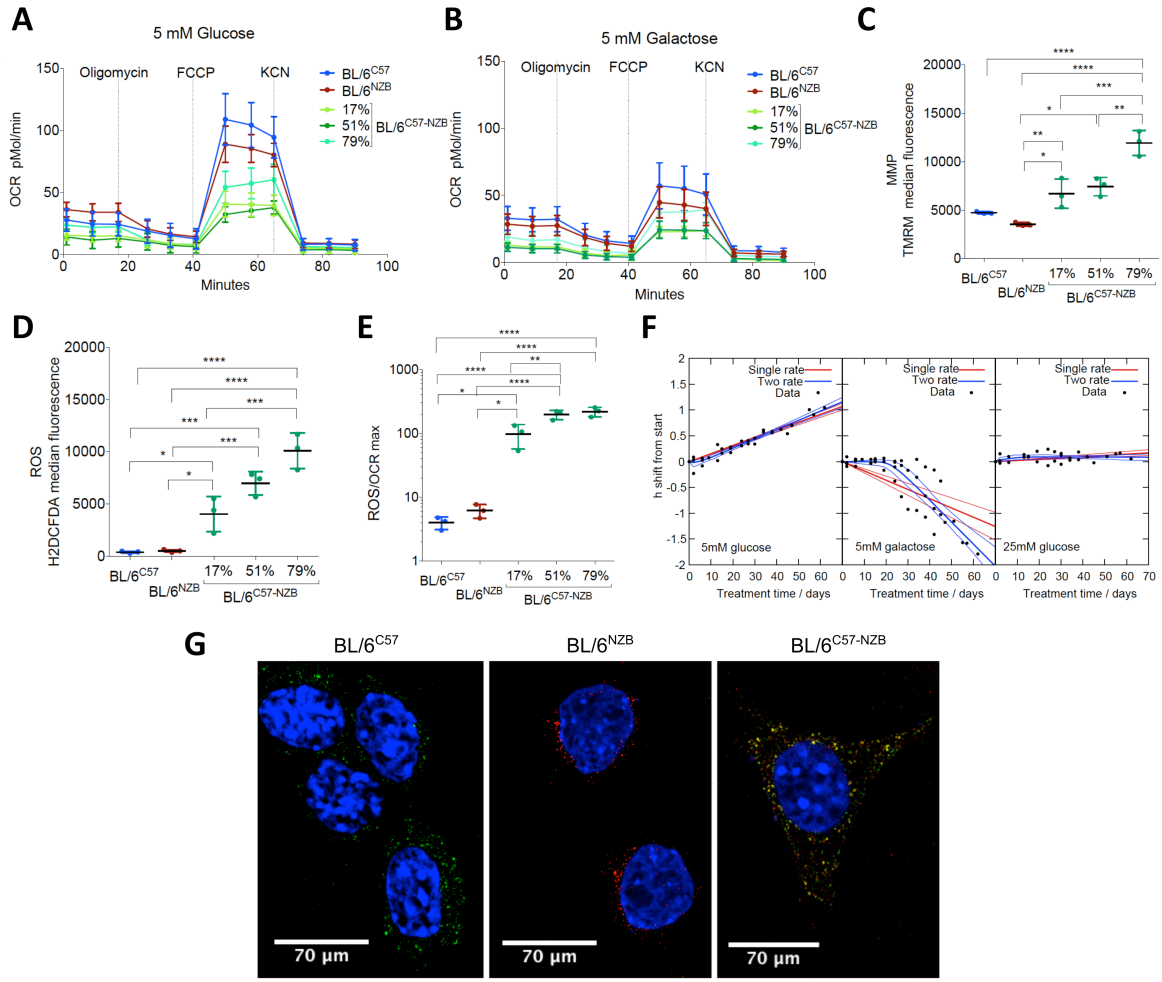

Figure 24 Metabolic performance of mouse embryonic fibroblasts. **(A-E)** Metabolic performance of mouse embryonic fibroblasts (MEFs) derived from 13.5 dpc embryos of homoplasmic or heteroplasmic mice. (A-B) Respiratory capacity of intact cells estimated by SeaHorse^{TM} at the indicated sugar supply. (C) Mitochondrial membrane potential (MMP) and ROS production per cell (D) or per oxygen consumption rate (OCR) capacity (E). **(F)** Dynamics of the mtDNA segregation in MEFs under different nutritional conditions. 25 mM of glucose displays no segregation (right); 5mM of glucose displays linear segregation (left); 5mM of galactose shows significant support for a model where there are no heteroplasmy changes in early treatment, followed by a fast decrease after 21 days (centre). N=3 BL/6$^{C57\text{-}NZB}$ MEFs immortalized lines per treatment during 62 days of culture. Initial heteroplasmy levels: 43, 46 and 47% of NZB mtDNA respectively. *Modified from Latorre-Pellicer (2014)*. **(G)** *In situ* detection of mtDNA sequences in mouse embryonic fibroblasts. In green, C57 mtDNA; in red, NZB mtDNA sequence, in blue, cell nucleus. The percentage of NZB mtDNA in BL/6$^{C57\text{-}NZB}$ MEF cell culture assessed by PCR and RFLP was 43% mtDNA NZB.

The PET/CT analyses indicated that the energetic metabolism of the embryos can be different and that the balance between oxidative *vs.* glycolytic metabolism may vary. We described elsewhere that in most of the tissues from C57BL/6 mice the respiratory CI is mainly distributed between free monomer CI and superassembled CI+CIII$_2$[142]. We also showed that the relative ratio of CI+CIII$_2$/CI is adapted to the fuel use, being higher value when glutamate or pyruvate is the main source of electrons. On the other hand, the

lower ratio is in presence of fatty acids as the predominant source[32]. In fact, we have already described in adult liver that the shift from C57 to NZB haplotype in homoplasmic animals reduces the CI+CIII$_2$/CI ratio[16]. To obtain an alternative confirmation of the different metabolic set up observed *in vivo*, we isolated 12.5 dpc embryos from the homoplasmic and heteroplasmic strains and performed a BNE to evaluate the organization of the mitochondrial electron transport chain. We confirmed in embryos that the CI+CIII$_2$/CI ratio is decreased in homoplasmic NZB animals with respect to homoplasmic C57 (Figure 25F, G). That decrease was also observed in heteroplasmic mice (Fig 25F-G). We further assessed the relative proportion between glycolytic and oxidative metabolism in the embryos using the Bioenergetic Cellular Index (BEC)[236]. The BEC index is calculated by the ratio of the expression of a critical protein of the OXPHOS system, the beta subunit of the mitochondrial H^+-ATP synthase (ATP-β) and a critical protein of the glycolysis (GAPDH) by western blot. This index was decreased in heteroplasmic embryos, confirming in that way the impact of the co-existence of different mtDNA variants on the embryo metabolism (Fig. 25H).

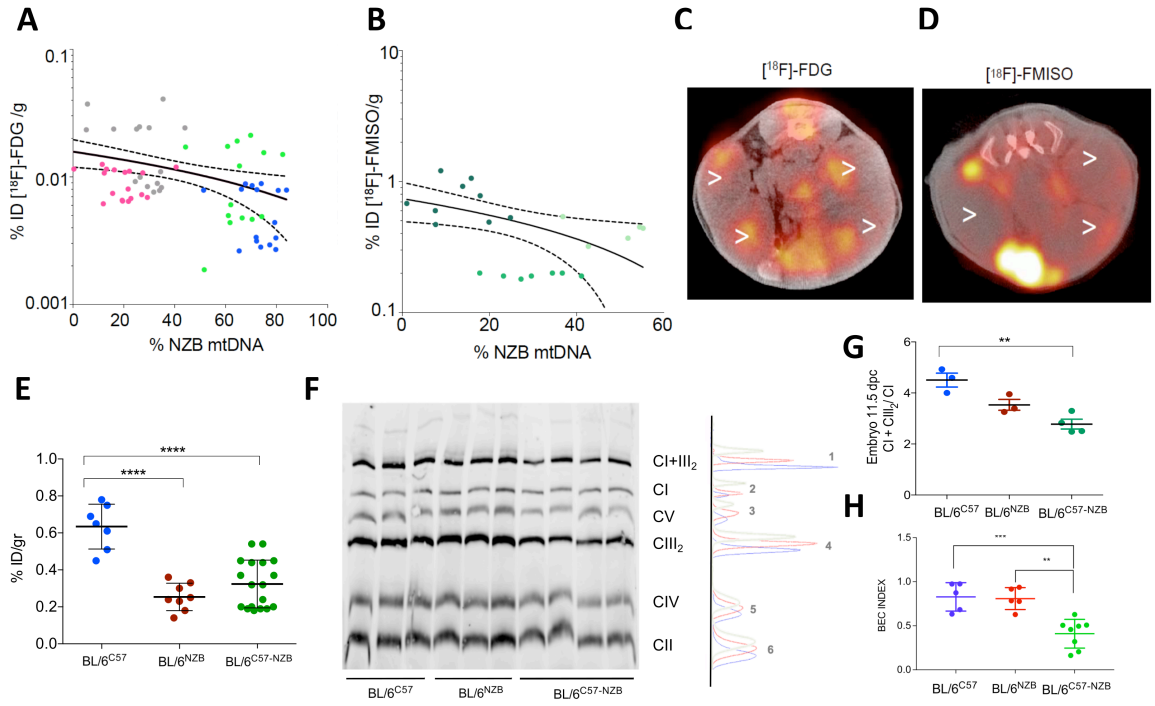

Figure 25. Heteroplasmy modulates embryo metabolism. **(A-B)** *Ex vivo* determination of [^{18}F]-FDG (A) or [^{18}F]-FMISO (B) uptake measured by gamma counter in 12.5 dpc heteroplasmic embryos with different mtDNA NZB content. Each dot represents an individual embryo, colors indicate embryos from the same litter. (n=4 litters per genotype). %ID: % of the injected dose. **(C-D)** *In vivo* analysis of embryo metabolism. Axial fused PET/CT representative images of [^{18}F]-FDG (C) and [^{18}F]-FMISO (D). Uptake in 12.5 dpc pregnant heteroplasmic females. White arrowheads indicate the position of the embryos. **(E)** *Ex vivo* comparative analysis of [^{18}F]-FMISO uptake between conplastic and heteroplasmic 12.5 dpc embryos. Each dot represents an individual embryo (n= 2 litters for homoplasmic mice and n=4 for heteroplasmic mice). **(F)** (left) BNE analysis of 12.5 dpc embryos. The antibodies used for immunodetection were NDUFA9 (CI), UQCRC2 (CIII), COI (CIV) and ATP-β (CV). (Right) Representative densitometry of BNE analysis (left) quantifying changes between homoplasmic and heteroplasmic embryos. **(G)** Ratio of supercomplexes to free complex I, determined from the BNE blot in (F). **(H)** Bioenergetic cellular (BEC) index in 12.5 dpc embryos from BL/6^{C57-}, BL/6^{NZB} and BL/6$^{C57-NZB}$ females. Each dot represents an individual embryo (n=3 homoplasmic and n=4 heteroplasmic embryos). ***p-value* < 0.01, **** *p-value* <0.0001 assessed by ANOVA. Data are given as means ± SD.

In summary, we found that heteroplasmy can be sensed but does not significantly impair embryo and fetal development. Therefore, these studies reinforce our previous proposal showing that the mtDNA variants have a functional impact. The combined analysis of the *in vivo* (embryo) and *in vitro* (MEFs) allow us to conclude that those features that depend only on the proportion of each mtDNA variant are not associated with dysfunction (i.e. oxygen level and glucose demands). Additionally, parameters such as

decreased MRR, OCR and increased MMP, associated with the heteroplasmy condition are strong indicators of dysfunction.

V.2.C. Heteroplasmic and homoplasmic animals are physiologically different

MtDNA heteroplasmy between two non-pathological mtDNA haplotypes allows healthy development and the generation of stable and fertile heteroplasmic mouse colonies, and has been considered as harmless[156,237]. However, other published works reported that heteroplasmy can induce alterations in mice physiology, such as systemic hypertension and increased body mass[162] resulting in harmful effects on cognition and behavior[163].

The three strains (BL/6^{C57}, BL/6^{NZB} and BL/6$^{C57\text{-}NZB}$) were studied during their whole lifespan. It was important to assess differences in adult mice after sexual maturity (8 weeks of age). Between 3-6 months of age, mice are still growing although are already sexually mature and can be consider young adults. The period between 8-12 months of age is the mouse adulthood in which animals do not grow but maintain healthy status. The period between 13-17 months of age can be considered middle age, where first signs of ageing may appear. Old or aged mice stage starts around 18-24 months of age, when most of the animals revealed ageing features.

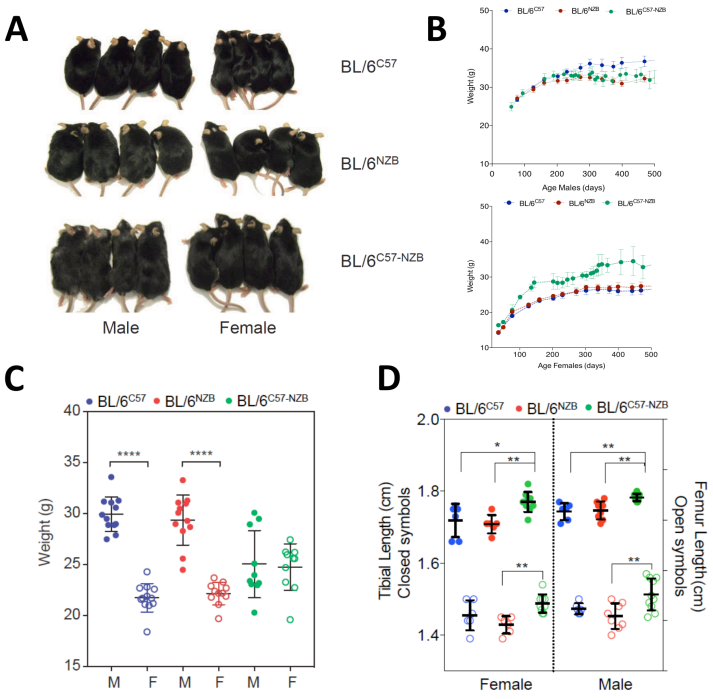

Figure 26. Heteroplasmic mice show altered differences between males and females. **(A)** Picture illustrating the appeareance of adult heteroplasmic mice compared to homoplasmic mice (20 weeks of age). An unusual increase in size of heteroplasmic females was observed. **(B)** Body weight gain in males (top) and females (bottom) of the different genotypes fed with the standard chow diet. (n = 19 homoplasmic and 20 heteroplasmic males; n = 15 homoplasmic and n = 20 heteroplasmic females). Data sets are represented as mean ± s.e.m. **(C)** Weight differences between males and females in homoplasmic and heteroplasmic animals (≈100 days old). Asterisks indicate significant differences assessed by ANOVA analysis. Data are given as means ± SD. F: females; M: males. **(D)** MicroCT assessment of tibia and femur length differences between homoplasmic and heteroplasmic males and females. Each dot represents a single animal. **p-value* < 0.05, ***p-value* < 0.01, ANOVA analysis.

A longitudinal analysis of the weight evolution in heteroplasmic and homoplasmic males revealed no significant differences (Figure 26A, B). Conversely, we found that the heteroplasmic females had higher weight than their homoplasmic counterparts (Figure 26B, C). Therefore, at ages where no loss of skeletal muscle was observed, we found a gender-specific impact of heteroplasmy on body weight. We observed an overgrowth of females with respect to homoplasmic animals. Thus, when the animals were around 100 days of age, male and female body weights were similar only in heteroplasmic animals (Figure 26C). Heteroplasmic mice seem to be bigger in size than the homoplasmic mice at these stages (Figure 26A, D). MicroCT analysis revealed an increase in tibia and femur length in heteroplasmic mice, exacerbated in females (Figure 26D).

Features of accelerated ageing were found in heteroplasmic mice regardless of their gender. However, females tend towards a more severe phenotype. One of the particularities was the early appearance of kyphosis which was evident at 25 weeks of age in females and at 60 weeks in males (Figure 27A-B) whereas similar findings were visible at 80-90-weeks-old homoplasmic animals. The animals that showed high degree of kyphosis usually died earlier. Some of the pathological features seemed to be triggered above a threshold of heteroplasmy while others presented a linear correlation with the degree of heteroplasmy. One example is the kyphosis angle and the grade of heteroplasmy. Females developed higher kyphosis when the heteroplasmy grade was closer to 50%, while males showed no correlation above the threshold that trigger early kyphosis (Figure 27C).

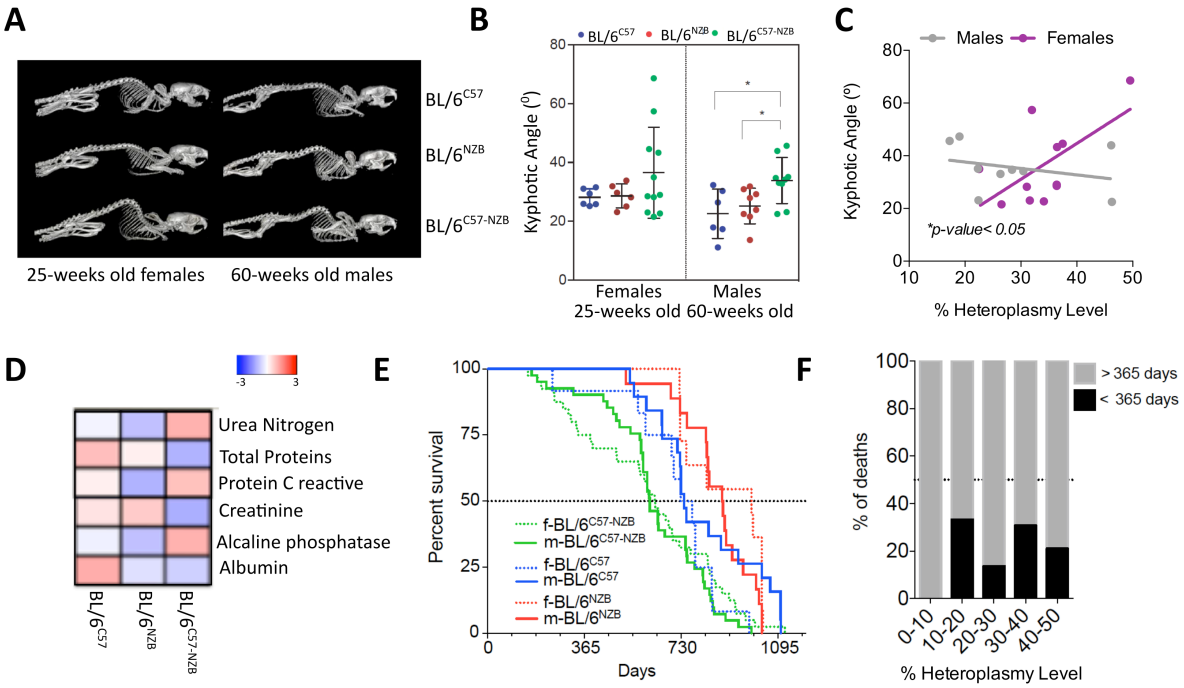

Figure 27. Heteroplasmy promotes premature ageing. **(A-B)** Representative CTs scans (A) and measured kyphotic angle (B) in homoplasmic and heteroplasmic 25-weeks-old females and 60-weeks-old males. **p-value < 0.05* assessed by ANOVA test. **(C)** Correlation between the kyphotic angle measured in (B) and the level of heteroplasmy in females and males. **p-value < 0.05.* **(D)** Heat map of age-related changes in biochemical parameters of 80-weeks-old homoplasmic and heteroplasmic males (n= 9 per genotype). **(E)** Longevity curves of heteroplasmic and homoplasmic individuals separated by sex. ($BL/6^{C57}$ 19 males and 12 females; $BL/6^{NZB}$ 18 males and 11 females; $BL/6^{C57\text{-}NZB}$ 41 males and 40 females. *p-value* <0.0001 for log-rank test (Mantel-Cox; Chi square: 36,85; Df: 4), Gehan-Breslow-Wilcoxon test and log-rank test for trend (Chi square: 18,17; Df: 1). **(F)** Heteroplasmy level at weaning (being 50% the maximum heteroplasmy) and frequency of premature death (<365 days) of the animals monitored in panel E. (0-10% n = 4; 10-20% n = 9; 20-30% n = 22; 30-40% n = 26; 40-50% n = 19).

Heteroplasmic mice showed additional signs of accelerated deterioration with age. Thus, biochemical analysis of plasma samples of 80-weeks-old mice of the three genotypes[238] revealed an increase of urea nitrogen in heteroplasmic mice, a hallmark of ageing related to the decrease of the excretion of fractional urea (FE urea) [239]. In addition, total proteins in plasma and the amount of albumin were decreased in the BL/6$^{C57\text{-}NZB}$ [240]. Finally, the C-reactive protein (CRP) was increased in the aged heteroplasmic mice. This is an inflammatory marker and an important risk factor associated with age and age related-diseases[241] (Figure 27D). The effects of heteroplasmy on organismal ageing were evaluated by a survival study. Most of the studies with heteroplasmic mice were focused on young animals, and we are not aware of any longevity study on the physiology of these heteroplasmic animals. Strikingly, the shape of the survival curve of the heteroplasmic animals reflected a highly heterogeneous population with an abnormal frequency of death events at relatively early age, indicating that, as a group, the health of the heteroplasmic animals may be compromised (Figure 27E). Heteroplasmy level between the two mtDNA variants range from 0%, when only one mtDNA haplotype is present, to a maximum of 50%, when the proportion of the two mtDNAs is identical. When the mice have more than 10-15% of heteroplasmy, we found a high correlation with very early death (Figure 27F).

V.2.D. Heteroplasmy, post-natal segregation and tissue performance

V.2.D.1. Evaluation of OXPHOS function in post-natal segregation: *in vitro* mouse adult fibroblast analysis

The evaluation of post-natal OXPHOS function and the investigation of the functional implications of heteroplasmy were first assessed by the generation of mouse adult fibroblasts (MAFs). Different cell clones were generated from homoplasmic and heteroplasmic mice. If glucose was substituted by galactose as the carbon source, cell growth in heteroplasmic cell cultures was impaired (Figure 28A-D). Doubling times in glucose (5mM) and in galactose (5 mM) media were calculated for each cell line from different clones (Table 14, Figure 28A-D). All the cell lines had an impaired growth rate when they were changed into galactose as a substrate. The doubling time was increased 68% with mtDNA C57, 155% in cells with NZB mtDNA and 443% in heteroplasmic cells. The analysis of mitochondrial membrane potential was significantly higher in the heteroplasmic MAFs (Figure 28E). Interestingly, and contrarily to what we found in MEFs, the production of ROS per maximum respiratory rate by mtDNA NZB carrying MAFs matched that of the heteroplasmic counterparts (Figure 28F). ROS levels are the result of the balance between ROS production and scavenging. Mitochondrial ROS production is directly proportional to both, oxygen utilization or oxygen consumption rate (OCR) and the membrane potential. When comparing BL/6^{NZB} and BL/6^{C57} MAFs and MEFs, we observed that mitochondrial membrane potential in MEFs was similar between homoplasmic cells. However, it was significantly higher for homoplasmic BL/6^{NZB} MAFs (Figure 28E, F). This causes the burst in mitochondrial ROS production in BL/6^{NZB} with respect to BL/6^{C57} MAFs while it is not different between homoplasmic MEFs.

Table 14. MAF cell culture doubling times. The doubling time of each cell line was determined using data from the growth curves. The average of the cell doubling times was calculated using nonlinear regression-Gaussian equation. Two different clones of heteroplasmic cell lines were used for the analysis.

Strain	Glucose 5 mM	Galactose 5 mM
BL/6^{C57}	19.86 hours	33.37 hours
BL/6^{NZB}	15.93 hours	40.72 hours
BL/6$^{C57\text{-}NZB}$	22.71 hours	123,4 hours

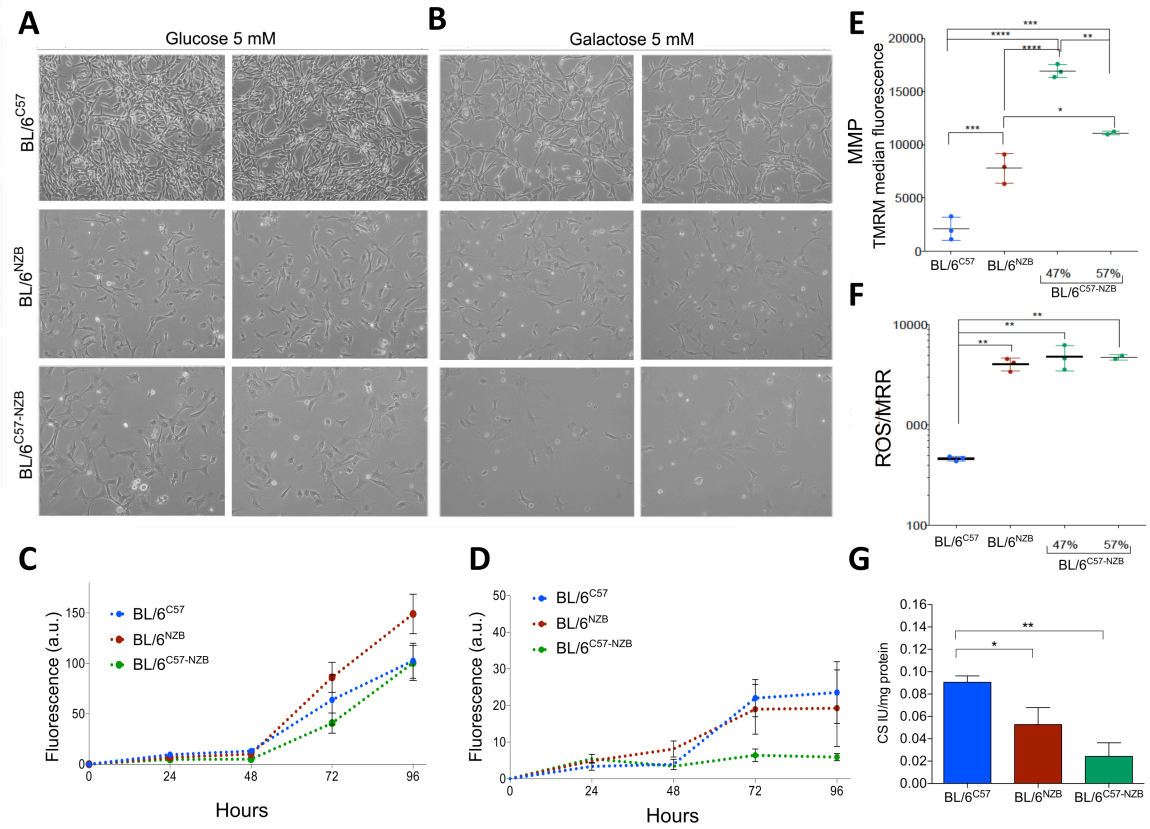

Figure 28. Mouse adult fibroblast cell culture characterization. **(A-B)** Mouse adult fibroblast cell cultures with different substrates, glucose (A) and galactose (B) (n = 2 different cell clones per genotype). **(C-D)** Growth curve of homoplasmic and heteroplasmic MAFs in the presence of 5 mM glucose (C) or 5 mM galactose (D) (n = 8 technical replicates per genotype). **(E)** Assessment of mitochondrial membrane potential (MMP) of the indicated cell lines. **(F)** ROS production normalized by the maximum respiration rate (MRR) for the indicated clone. **(G)** Enzymatic activity of citrate synthase (CS) per mg of total protein in MAFs of the indicated genotypes. **p-value* < 0.05, ***p-value* < 0.01, ****p-value* < 0.001, *****p-value* < 0.0001 assessed by ANOVA analysis. The two clones of heteroplasmic MAFs presented 47% and 57% of NZB mtDNA.

In heteroplasmic MEFs and MAFs, mitochondrial membrane potential was abnormally elevated, favouring ROS production, while OCR is decreased, diminishing ROS production. The overall balance is that ROS production per oxygen consumption is elevated in both, heteroplasmic MAFs and MEFs with respect to their homoplasmic counterparts (Figure 28E, F and Figure 24C, D). The increase in the differences in ROS production between MEFs and MAFs is due to the higher OXPHOS activity: basal OCR in MAFs is higher than that of MEFs. To determine mitochondrial content in the different MAF cell lines, we measured the citrate synthase activity in total protein extracts. Mitochondrial mass was higher in homoplasmic MAFs (Figure 28G).

Next, the respiratory capacity of the cell lines was analysed by SeaHorse^{TM} using different substrates. We found that both, basal and maximum respiratory capacities, were diminished in heteroplasmic MAFs regardless of the glucose concentration in the media (25 mM or 5 mM) (Figure 29A, B). Extracellular acidification rate (ECAR) is an indirect index of the glycolytic flux. The ratio ECAR/OCR was significantly elevated in heteroplasmic MAFs, an indicator of an enhanced glycolytic activity induced by heteroplasmy (Figure 29C, D). Each genotype in MAFs had a characteristic signature of OCR *vs.* ECAR, regardless of the use of coupled or uncoupled OCR. Heteroplasmic MAFs had a high acidification rate with low respiration, indicative of a shift from the oxidative to glycolytic metabolism. This analysis also revealed differences between the homoplasmic lines, showing that the BL/6^{C57} MAFs have higher ECAR/OCR balance than BL/6^{NZB} MAFs (Figure 29 C, D). All the cited parameters confirm that

heteroplasmic adult fibroblasts are more glycolytic than the homoplasmics. The shift to galactose as a carbon source did not impair the adaptation of the respiratory capacity of homoplasmic MAFs, while the heteroplasmic ones developed an abnormal respiratory profile. The status of the supercomplex levels and composition in the mtETC was assessed by Blue Native Electrophoresis (BNE) assay. When cultured in glucose as a carbon source, heteroplasmic MAFs revealed an imbalance in the assembly of the complexes with a significant reduction of complex I (CI), particularly in the super-assembled form. In galactose, BL/6$^{C57\text{-}NZB}$ MAFs could not grow, probably because they cannot increase sufficiently the amount of CI (Figure 29E).

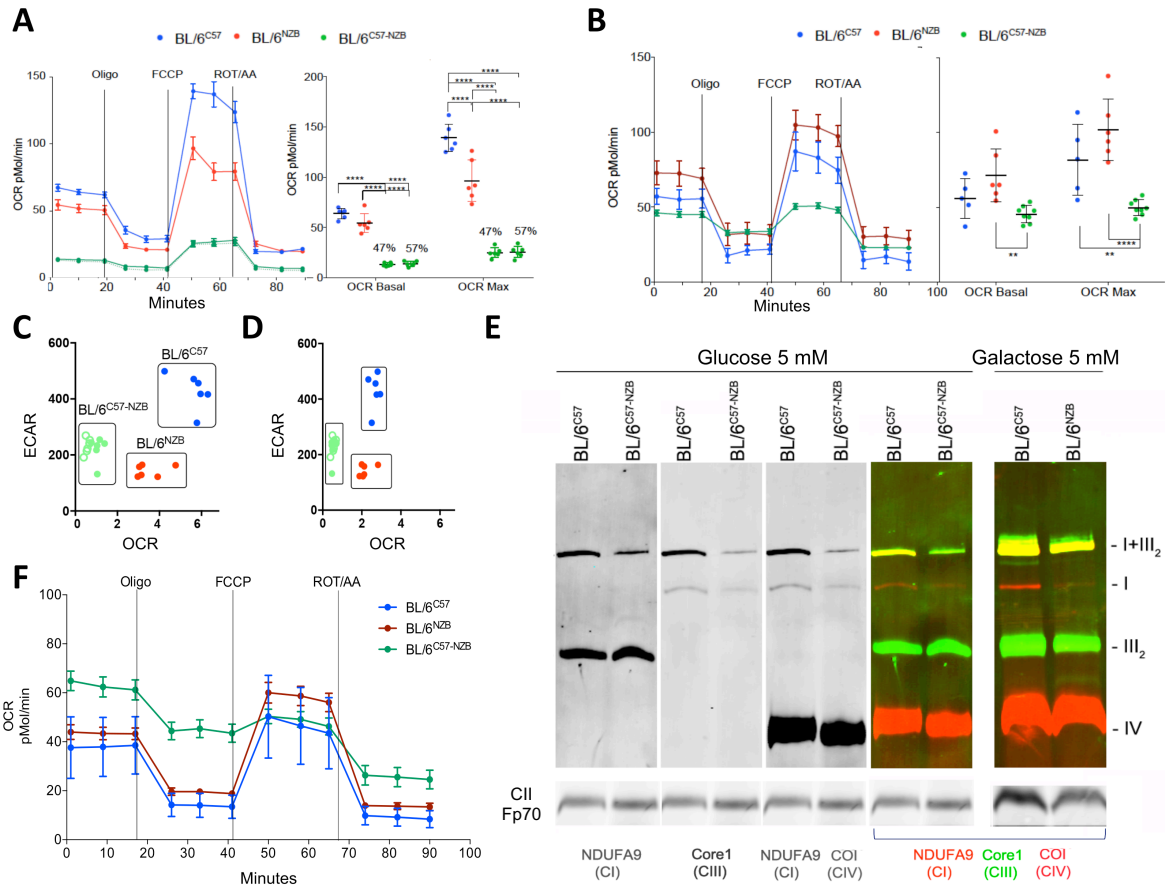

Figure 29. Mouse adult fibroblast cell culture characterization. **(A-B)** Estimation of the respiratory performance of homoplasmic and heteroplasmic mouse adult fibroblasts (MAFs) at high (A, 25 mM) or low (B, 5 mM) glucose supply. Panels are the summary of 5 to 6 independent assays per clone. The two clones of heteroplasmic MAFs had 47% and 57% of NZB mtDNA. **(C)** Representative profiles of acidification rate (ECAR) per oxygen consumption rate (OCR) as an index of glycolytic *vs.* OXPHOS metabolism of MAFs growing in complete media supplemented with 5 mM glucose (n = 2 different clones per genotype). **(D)** Representative profiles of oxygen consumption rates (OCR) versus extracellular acidification rate (ECAR) determined by SeaHorse^{TM} of MAFs growing in complete media supplemented with 5 mM galactose (n = 2 different clones per genotype). **(F)** Respiratory capacity of intact cells estimated by SeaHorse^{TM} using 5 mM galactose as cell culture condition. **(E)** Immunodetection of the indicated proteins after BNE of digitonin-solubilized mitochondria. SCs in MAFs were studied under glucose and galactose conditions.

V.2.D.2. Stable heteroplasmy impairs mitochondrial function and compromises tissue health

We reproduced previous results in the literature[163,165] regarding the segregation between non-pathological mtDNA variants. Thus, the removal of heteroplasmy appears to be the rule in most tissues, with notable exceptions affecting critical tissues that maintain stable heteroplasmy (heart, skeletal muscle, lung, bladder and eye) (Figure 22). One of the main conclusions of this work is that all studied tissues with stable heteroplasmy develop dysfunctional mitochondria.

V.2.D.3. Cardiac tissue analysis in heteroplasmic mice

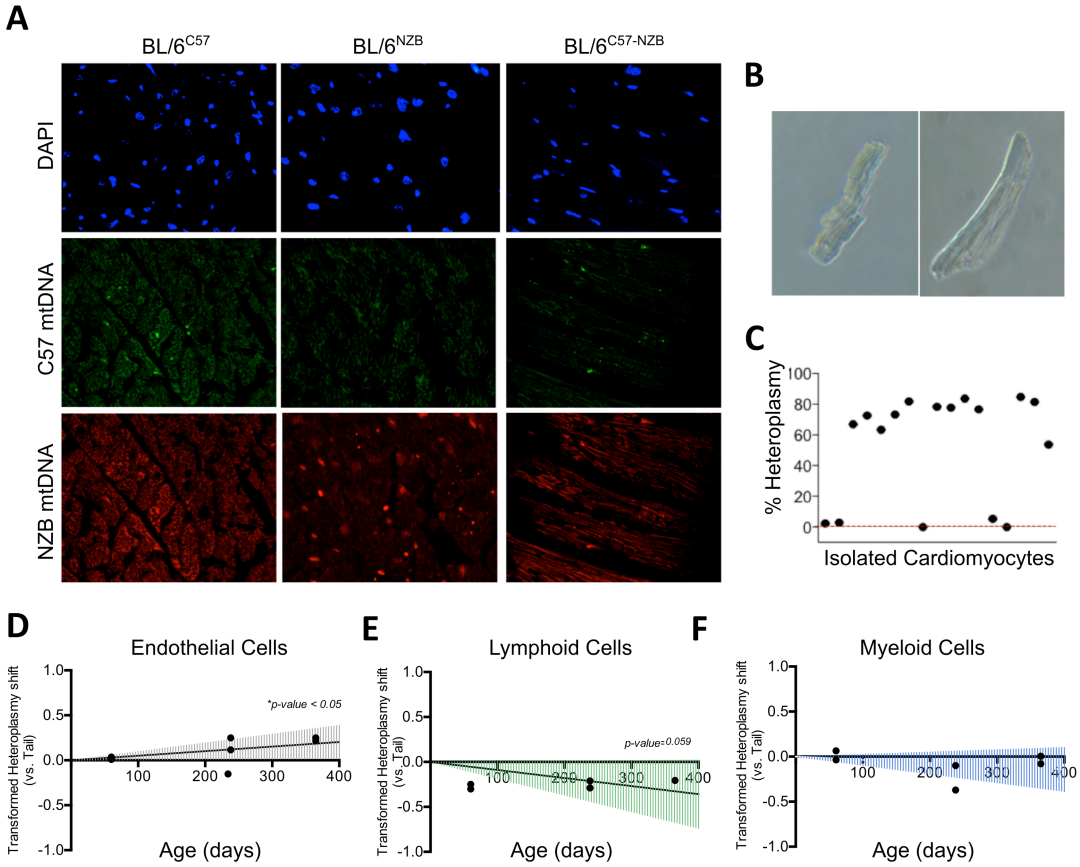

Figure 30. Impact of heteroplasmy on MAFs metabolic performance. **(A)** *In situ* detection of the two mtDNA sequence variants (C57 and NZB) in fresh frozen mouse cardiac tissue (12-weeks-old mice). In red, NZB mtDNA; in green C57 mtDNA; in blue, cell nucleus. **(B-C)** Isolated cardiomyocytes (B) and posterior evaluation of intracellular mtDNA heteroplasmy in single cells (n = 4 heteroplasmic 20-weeks-old mice). **(D-F)** Evaluation of the transformed heteroplasmy shift using tail as the reference tissue in isolated cardiac cell populations from heteroplasmic mice at different ages. (D) Endothelial cells, (E) lymphoid cells and (F) myeloid cells. Each dot corresponds to a different animal. **p-value* < 0.05, significance of linear regression coefficients.

First, the study of heteroplasmy in cardiomyocytes was performed to evaluate the co-existence of the two mtDNAs in the same cytoplasm. *In situ* detection of mitochondrial DNA using padlock probes and rolling cycle amplification (RCA) in cardiomyocytes confirmed that most of the cells harboured the two mtDNA haplotypes in their cytoplasms (Figure 30A). Isolation of adult cardiomyocytes and posterior analysis by PCR and RFLP of single cardiomyocytes revealed again the intracellular heteroplasmy (Figure 30B, C). Surprisingly, we found a population of cardiomyocytes that had only C57 mtDNA but none of the analysed cells reached 100% of NZB mtDNA (Figure 30C). To know which was the mtDNA segregation profile in the rest of cardiac cells and which was the contribution of the cardiomyocytes into the total

cardiac tissue measurement of heteroplasmy, we sorted the main cell populations: endothelial cells and different immune cell populations (total lymphoid and myeloid lineages) (Figure 30D-F).

V.2.D.3.a. Biochemical profile and evaluation of heart anatomical features and ultrastructure

The variable impact of heteroplasmy on health in middle to late adulthood prompted us to perform a detailed analysis of the phenotypes to identify early differences induced by heteroplasmy in different organs. The first evidence of tissue damage was found after a routine analysis of plasma biochemical parameters, which revealed an abnormal elevation creatine kinase (CK) and the myocardial isoform creatine kinase-MB (CK-MB) at 12 weeks of age, suggesting myocardial and/or muscle damage (Figure 31A). Interestingly, their levels are normalized at older ages (Figure 31A). In agreement with these findings, Evans blue staining revealed scattered cardiomyocyte death in 20-weeks-old heteroplasmic mice (Figure 31B, C), but no evidences of fibrosis at this age either with Sirius red or thrichrome staining were detected (Figure 31D-F).

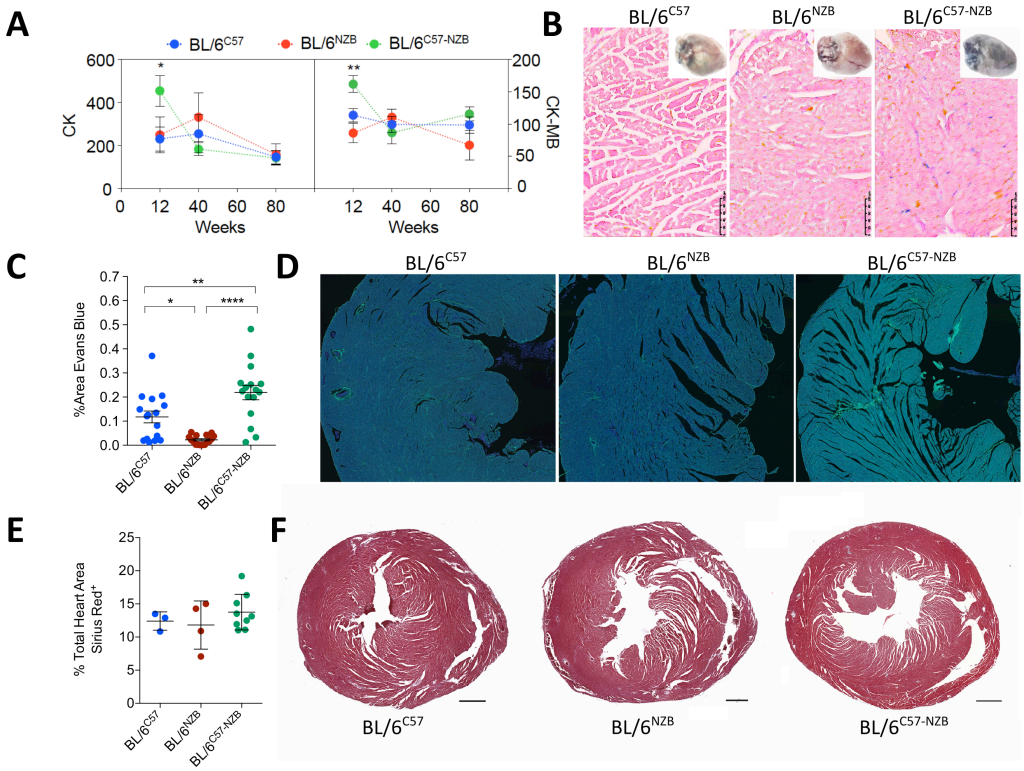

Figure 31. Analysis of cardiac structure and damage. **(A)** Longitudinal analysis of creatine kinase (CK) and creatine kinase-MB (CK-MB) in plasma samples. Data given as means ± s.e.m. (n=10 homoplasmic individuals per indicated age; n=20 heteroplasmic 12-weeks-old mice; n=10 heteroplasmic individuals 40- and 80-weeks-old heteroplasmic mice. **(B)** Evans blue staining of representative hearts of homoplasmic *vs.* heteroplasmic 20-weeks-old hearts. Blue intensity indicates cell damage. Histological sections of the hearts treated in panel B showing a very disperse distribution of the damaged cardiomyocytes in heteroplasmic hearts. **(C)** Quantification of the Evans blue staining in histological sections. * *p-value* < 0.05, ***p-value* < 0.01, ****p-value* < 0.0001 assessed by ANOVA analysis. **(D-E)** Cardiac picrosirius red staining (D) and estimation of the percentage of collagen area per total tissue (E) in 20-weeks-old homoplasmic and heteroplasmic mice. Each dot corresponds to a single animal. **(F)** Masson's trichrome staining of cardiac sections of homoplasmic and heteroplasmic mice (20-weeks old mice, n=5 per genotype). In blue, myocardial fibrosis. Scale bars correspond to 0.5 mm.

A detailed analysis of the ultrastructure of cardiac tissue by transmission electron microscopy (TEM) revealed dramatic alterations in young heteroplasmic mice (12-weeks-old animals) (Figure 32). A mix of cardiac-fibre mitochondria with dense and sparse matrices were found only in the heteroplasmic hearts, while the homoplasmic organs showed an uniform distribution either all-dense or all-sparse-matrix mitochondria. In addition, only heteroplasmic hearts showed necrotic fibres, sarcomere disruption, abnormal intercalated disk and connections between cardiomyocytes and multiple signs of vacuolated and disrupted mitochondria. 80-weeks-old BL/6^{C57} hearts showed a drastic loss of ultrastructural organization of the mitochondria which is however much better preserved in old BL/6^{NZB} animals (Figure 32A) as previously reported[16] (Figure 14D). Again, the aged heteroplasmic hearts manifested a variety of ultrastructural alterations (Figure 32B).

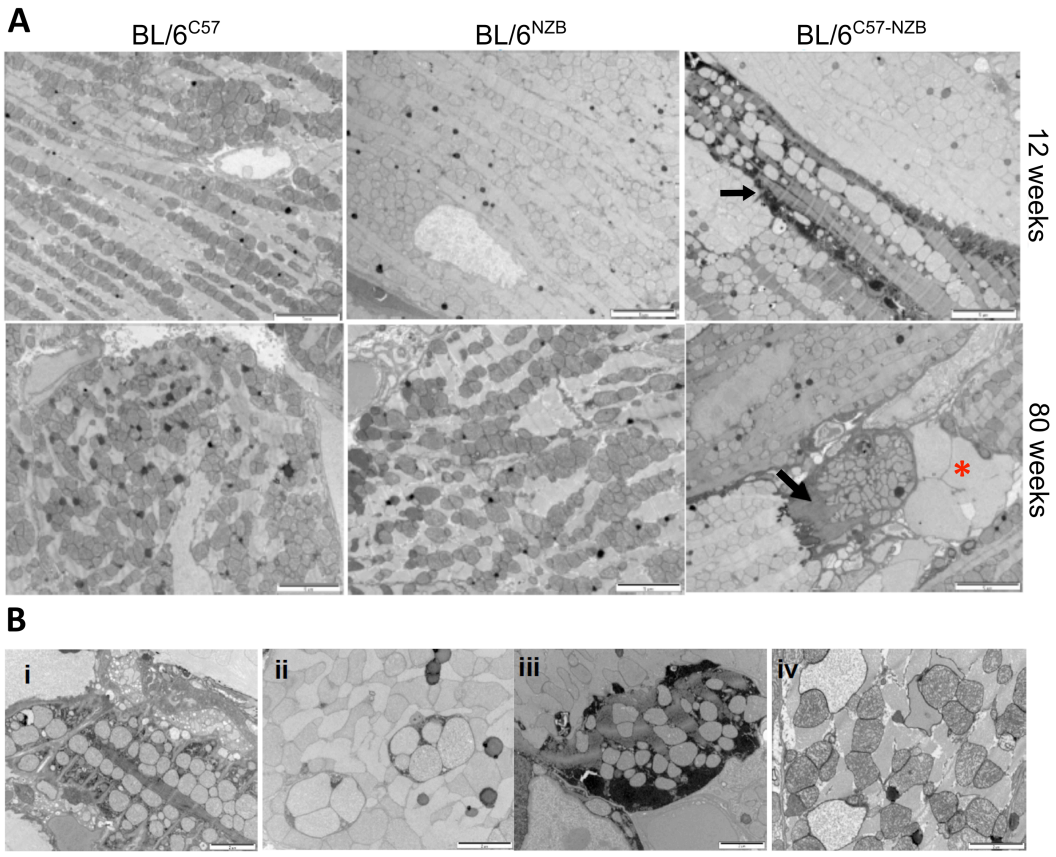

Figure 32. Analysis of cardiac ultrastructure. **(A)** Representative TEM images of the heart at two different ages of the heteroplasmic and homoplasmic animals (n = 5). Arrows indicate abnormal and necrotic fibres. Red asterisk indicates a fibrotic scar. **(B)** Representative TEM images showing specific features observed in hearts from heteroplasmic 12-weeks-old animals: i) Necrotic fibre; ii) mitochondria in phagosomes; iii) damaged cardiomyocyte; iv) vacuolated mitochondria and mitochondrial swelling phenomena (n = 5).

In parallel, we performed a complete histological analysis of the liver, as an example of a tissue that can select one of the mtDNA haplotypes (NZB) during the life of the animal. Whilst no significant histological differences among strains were found in liver from young individuals (Figure 33A), livers from 80-weeks-old mice showed signs of inflammation both in heteroplasmic BL/6$^{C57-NZB}$ and conplastic BL/6^{NZB} mice and steatosis in the control BL/6^{C57} group (Figure 33A). In addition, TEM analysis in 12-weeks-old mice revealed differences in mitochondrial electron density between BL/6^{C57} and BL/6^{NZB} mitochondria, and the appearance of the two types of electron density in mitochondrial matrix with morphological differences in

the heteroplasmic animals (Figure 33B). Also, we noticed an increase in the interaction between endoplasmic reticulum and mitochondria in the conplastic and heteroplasmic samples (Figure 33B).

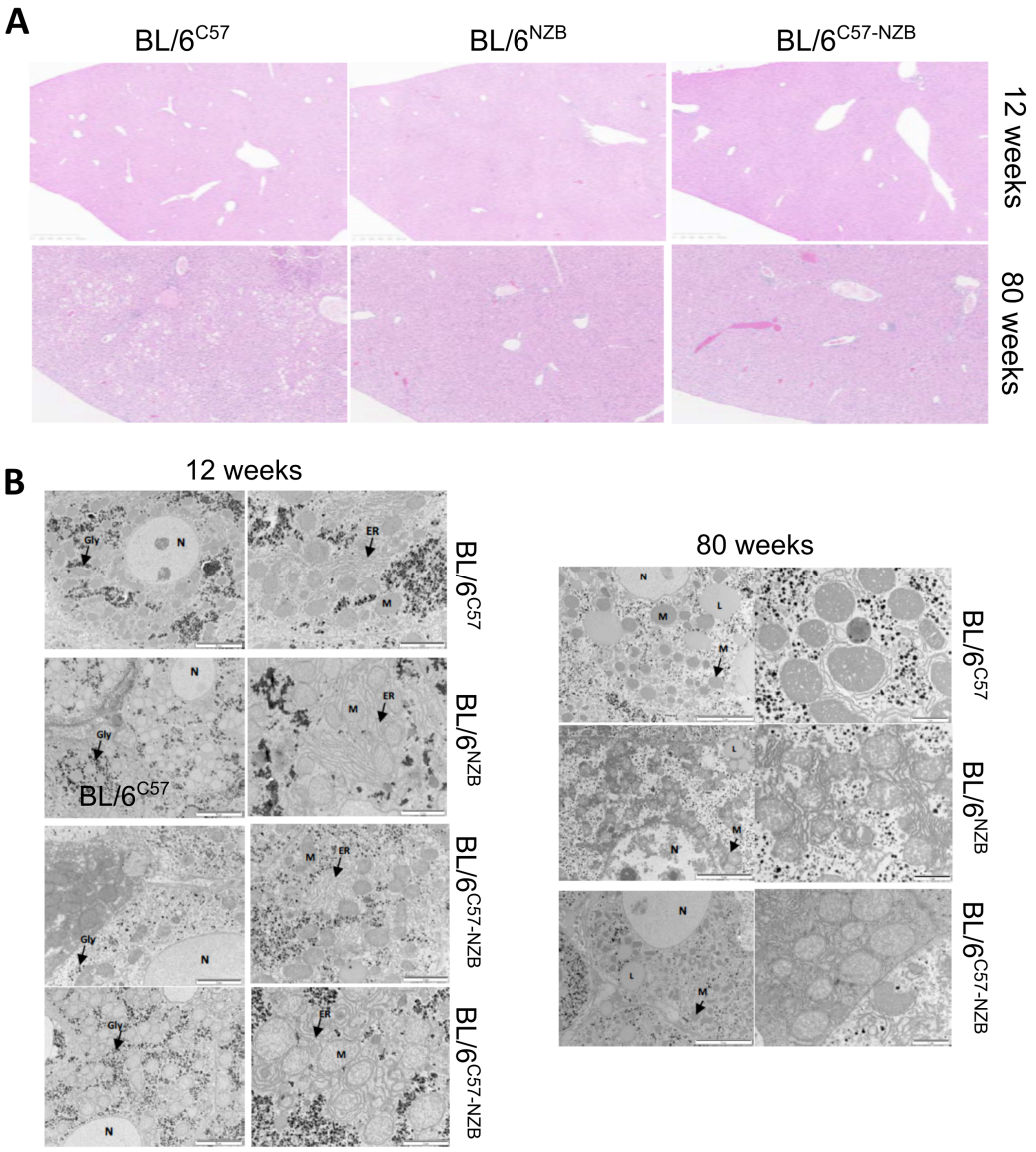

Figure 33. Analysis of liver anatomy and ultrastructure. (A) Representative H&E images of the liver at two different ages of the heteroplasmic and homoplasmic animals (n = 5). **(B)** Representative TEM images of hepatocytes from male livers of the indicated age and strain (n = 4-5). M: Mitochondria; ER: endoplasmic reticulum; L: lipid droplets; N: nucleus; Gly: glycogen.

V.2.D.3.b. Mitochondrial dynamics, OXPHOS performance and mtUPR assessment

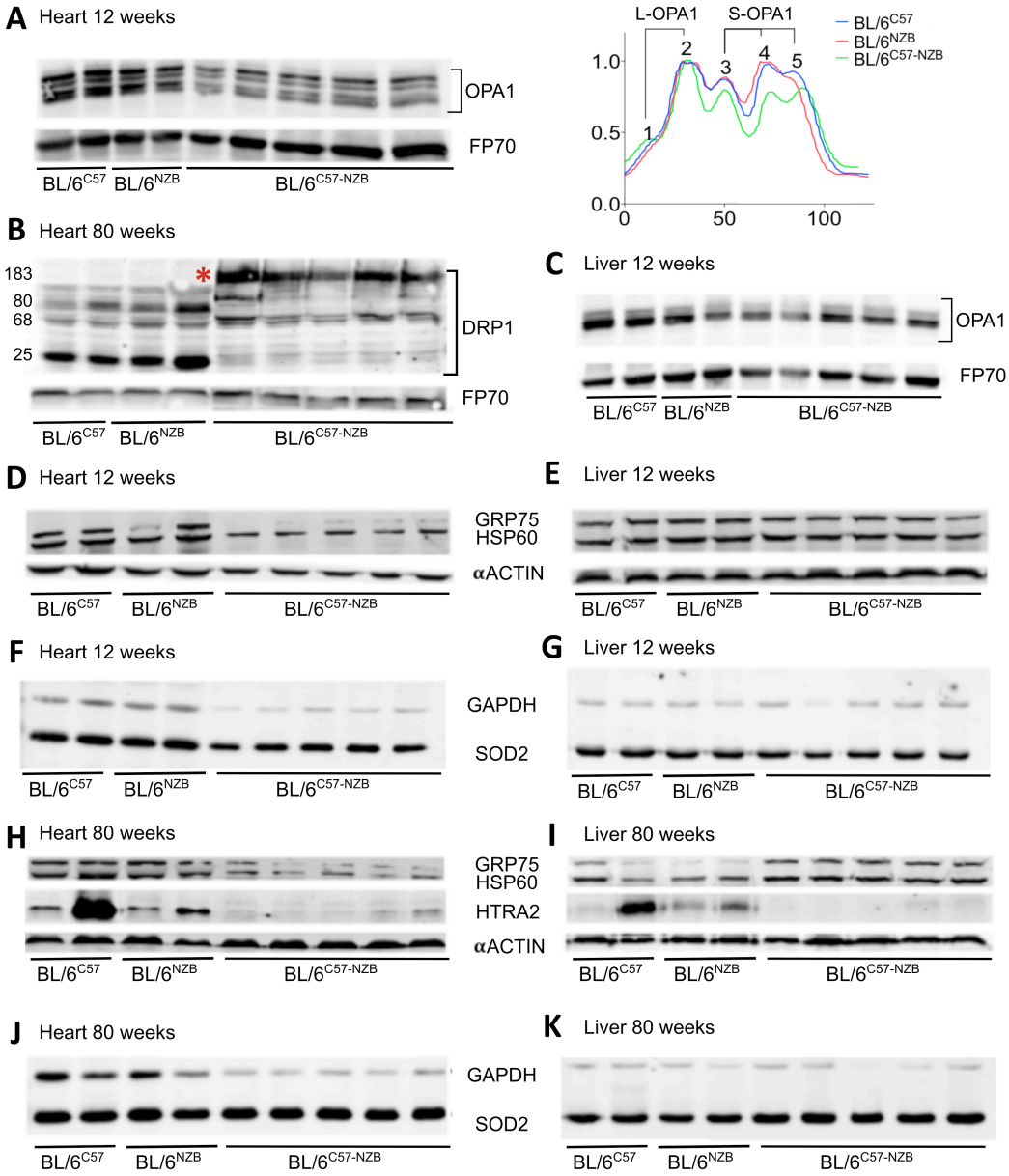

Figure 34. Western blot evaluation of selected proteins involved in mitochondrial dynamics, mitochondrial UPR and antioxidant defences. (A) OPA1 processing in cardiac tissue of 12-weeks-old homoplasmic and heteroplasmic mice. (Left) Western Blot evaluation and (right) peak profile of different processed isoforms of the protein. Red lines correspond to BL/6^{NZB} hearts, blue lines to BL/6^{C57} and green, BL/6$^{C57-NZB}$ hearts. L-OPA1: Long isoforms. S-OPA1: Short/proteolised isoforms. Y-axis: Relative signal of each band. X-axis: membrane position. **(B)** DRP1 protein evaluation (80 weeks of age). Red asterisk: ubiquitinated DRP-1 protein. **(C)** Analysis of OPA1 processing by Western blot in livers of the indicated genotypes. **(D-E)** GRP75 and HSP60 protein expression in hearts (D) and livers (E) of 12-weeks-old homoplasmic and heteroplasmic mice. **(F-G)** Evaluation of mitochondrial superoxide dismutase (SOD2) in cardiac (F) and liver (G) tissues. **(H-K)** Analysis of elderly BL/6^{C57}, BL/6^{NZB} and BL/6$^{C57-NZB}$ animals (80-weeks-old mice). Proteins related to mtUPR (GRP75, HTRA2 and HSP60) were evaluated in heart (H) and liver (I). SOD2 analysis in heart (J) and liver (K). In A-C, FP70 (CII) was used as a mitochondrial protein loading control. In D-E, H-I actin was used as loading control. In F-G and J-K, GAPDH was used as loading control. NZB mtDNA content assessed in the tail of heteroplasmic mice used in the experiment varies between 40-60%.

The study of mitochondrial dynamics in heart and liver helped us to understand the differences in the status of the cells in tissues that can, from those that cannot segregate mtDNA. We analysed the proteolysis of OPA1, a nuclear-encoded mitochondrial inner membrane protein (IMM) which plays a major role in

mitochondrial quality control, the formation of cristae junctions and the release of cytochrome c to trigger apoptosis[242]. OPA1 drives the fusion of the IMM and can be processed by two different proteases, YME1L and OMA1. We observed a decrease in the relative proportion of processed OPA1 bands in cardiac tissue of heteroplasmic mice (Figure 34A, B). This is in agreement with a reduced mitochondrial fission or fragmentation[243]. In liver, the short isoforms of OPA1 were predominant in all the strains (Figure 34C) and mitochondria were more fragmented than in the heart. It suggests that smaller mitochondria may facilitate the segregation and selection of one of the two mtDNA haplotypes. Interestingly, in the heart of aged BL/6$^{C57\text{-}NZB}$ mice we found the ubiquitinised form of the mitochondrial fission factor dynamin related protein 1 (DRP1) (Figure 34B). This post-translational modification placed the protein at 183 kDa. It was reported that ubiquitinasation of DRP1 affects its function and can act indirectly as a blocker of mitophagy[244]. During stress conditions hyperfused mitochondrial network may restrict mitophagy response, suggesting that mitochondrial size control is an important feature of the mitophagy process[244]. However, several studies have demonstrated that mitochondrial fission is necessary but not sufficient for mitophagy[244]. The chaperones HSP60 (cytosolic) and GRP75 (mitochondrial) help during protein folding and restructuration of tertiary structure trying to avoid aggregates[218]. With only 12 weeks of age, heteroplasmic hearts presented a strong decrease in the amount of the mitochondrial chaperone GRP75 and, although less pronounced, a decrease in the expression of HSP60 (Figure 34D). This reduction could be also observed in the heteroplasmic hearts of 80-weeks-old mice (Figure 34H). However, heteroplasmic livers maintained unaffected the levels of both chaperones at young age and elevated levels than in homoplasmic livers at older age (Figure 34E, I). In addition to that, we noticed a significant increase in the expression of the superoxide dismutase 2 (SOD2) only in young and old heteroplasmic hearts, since it was not affected in liver (Figure 34 F-G, J-K). The serine-protease HTRA2 (also termed Omi) is located in the IMM and has a crucial role in the degradation of oxidized proteins. Interestingly, HTRA2 protease expression was barely detected in old heteroplasmic hearts and livers in comparison with the homoplasmic controls (Figure 34H, I). These changes suggest that heteroplasmy induces oxidative and proteostatic stress in heart that seem to be sustained along the life of the animals while liver does not manifest it[245].

We next inquired if mitochondrial function was affected by the heteroplasmic condition. First, we determined the ATP synthesis capacity of heart and liver isolated mitochondria at two different ages, 12 and 20-weeks-old. The evidence of cardiomyocyte damage in plasma at 12 weeks of age (high values of CK and CK-MB) (Figure 31A) was paralleled with a significant decrease in mitochondrial capacity to synthesize ATP, either with glutamate or succinate (Figure 35A). In spite the fact that loss of heart cells is no longer observed at older age (Figure 35C), the lower capacity in ATP generation by heart mitochondria was maintained in 20-weeks-old heteroplasmic animals (Figure 35A). Interestingly, although the ATP synthesis capacity of liver mitochondria from heteroplasmic mice at 12 weeks of age was also reduced with respect to that of homoplasmic ones, it was recovered at 20 weeks of age (Figure 35B). Therefore, heteroplasmy had a negative impact on ATP synthesis capacity in both tissues in young mice. These results suggest that liver may combat it by inducing strong mtDNA segregation. In that way, C57 mtDNA may be actively eliminated and mitochondrial performance restored (Figure 22, Figure 35B).

On the other hand, cardiac tissue is unable to resolve heteroplasmy (Figure 22) and to recover mitochondrial function. However, the loss of cardiomyocytes is prevented at older ages. We hypothesized that cardiomyocytes may compensate the impairment in mitochondrial function by shifting its metabolism from oxidative towards glycolytic metabolism. A decrease in the proportion of assembled CV in heteroplasmic heart mitochondria was confirmed by BNE (Figure 35D). Therefore we demonstrated that with only 12 weeks of age there was a shift in cardiac tissue metabolism from β-oxidation to glycolysis in BL/6$^{C57\text{-}NZB}$ mice. The reorganisation of the OXPHOS system in heteroplasmic heart mitochondria at 12 weeks of age involves the superassembly of complexes. A reduction in the respirasome (CI+CIII$_2$+CIV)

and CI+CIII$_{2\ SL}$, a decrease of complex CIV dimer and total CIV and an increase of the ratio CIII$_2$/CI+CIII$_2$ were found in heteroplasmic hearts (Figure 35E). In the case of the liver, no significant differences were obtained with complex I and complex III immunodetection, but a slight reduction in CIV was detected (Figure 35F).

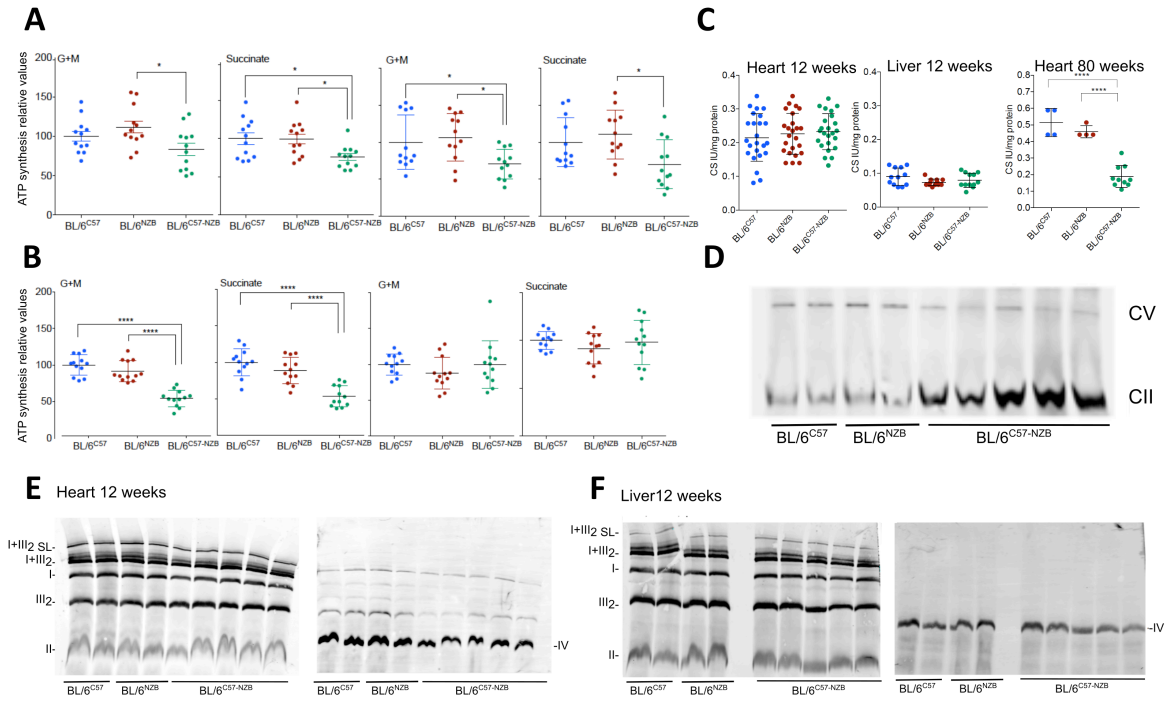

Figure 35. Western blot evaluation of selected proteins involved in mitochondrial dynamics, mitochondrial UPR and antioxidant defences. (A-B) Cardiac (A) and liver (B) mitochondrial ATP synthesis rate driven by glutamate plus malate (G+M, left) or succinate (right) at 12 and 20 weeks of age. Biological replicates: 6 per genotype and per age. **p-value* < 0.05, ***p-value* < 0.01, ****p-value* < 0.001, ANOVA analysis. **(C)** CS activity in cardiac tissue or liver tissue (middle) in young animals and CS activity in cardiac tissue of 80-weeks-old homoplasmic and heteroplasmic mice at the indicated age. ****p-value* < 0.001, ANOVA analysis. **(D)** BNE evaluation of CV (ATP-β) formation in hearts of 12-weeks-old mice. **(E-F)**. Blue native gel electrophoresis of heart (E) and liver (F) tissues from 12-weeks-old homoplasmic and heteroplasmic mice. Left: NADUFA9 (CI), Core1 (CIII) and FP70 (CII). Right, COX5B (CIV). FP70 (CII) was used as a loading control.

Mitochondrial respiratory capacity, respiratory supercomplexes and mitochondrial cristae shape are linked[13]. The observed changes in the proportion of long *vs*. short isoforms of OPA1 in heteroplasmic heart mitochondria strongly suggest that the ultrastructure of mitochondrial cristae was affected. To directly assess if that was the case, we measured mitochondrial cristae thickness for the three strains by TEM. We found that cristae of heart mitochondria of heteroplasmic individuals are shorter and present loss of integrity (black arrows) (Figure 36A, B). We also found an increased proportion in calcifications deposits in the cristae area of the heteroplasmic mitochondria as well as regions of mitochondria with no electron density (Figure 36A). Taken together, these results suggest that low OPA1 levels and cristae could be associated to an impaired supercomplexes assembly in BL/6$^{C57\text{-}NZB}$ mice. Similar analysis performed in liver samples revealed an increase of cristae in mitochondria from BL/6^{C57} mice compared to those in BL/6^{NZB} and BL/6$^{C57\text{-}NZB}$. A small proportion of the mitochondria of heteroplasmic livers had shorter and more disperse cristae and lack of electron density that may be related to the loss of OXPHOS performance in the liver of these animals. In addition, we noticed an increase in the ribosome load of the endoplasmic reticulum associated with mitochondria of heteroplasmic liver samples (red asterisk) (Figure 36C).

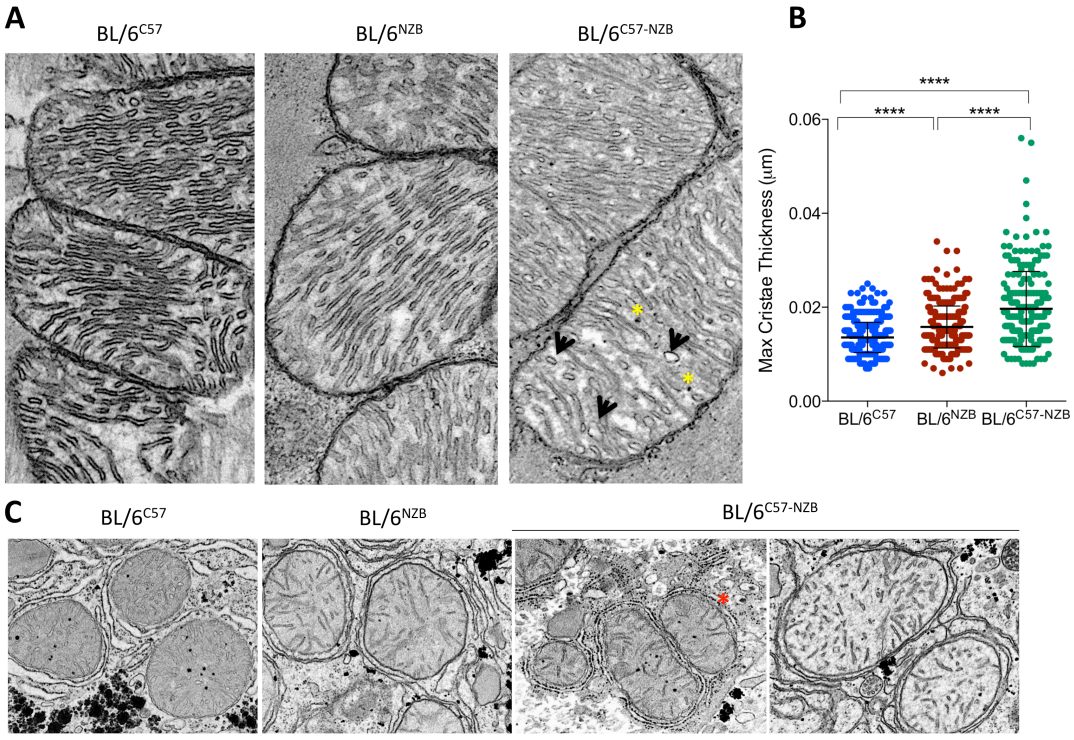

Figure 36. TEM analysis of mitochondrial ultrastructure. **(A-B)** Electron microscopy analysis of cardiac mitochondrial morphology. (A) Representative images of IMF mitochondria within cardiomyocytes. Yellow asterisks: calcium deposition spots; Black arrows: relaxed cristae in the IMM. (B) Quantification of maximal cristae thickness between cardiac mitochondria of 12-weeks-old BL/6^{C57}, BL/6^{NZB}, BL/6$^{C57-NZB}$ mice. **(C)** Representative images illustrating mitochondria ultraestructure in liver samples of 12-weeks-old mice. Red asterisk: ER-mitochondria interaction site.

V.2.D.3.c. The presence of heteroplasmy at any level induces a defined cellular status

We previously demonstrated that different non-pathological mtDNA variants have different heart transcriptomic profiles[16]. In the heteroplasmic mice, that have a mix between the two mtDNA (BL/6$^{C57-NZB}$), we expected to have a mix of transcriptomic changes between both homoplasmic hearts (BL/6^{C57} and BL/6^{NZB}). Surprisingly, the principal component analysis (PCA) of these mice in the left ventricle (LV) and in the liver revealed a totally different profile, far away from the homoplasmic animals regardless of the level of heteroplasmy they presented. This suggests that the heteroplasmy itself induces a defined cellular status (Figure 37A, B).

When considering only the transcripts that were significantly modified in expression, hierarchical clustering of heart and liver transcriptome confirmed the differences between homoplasmic and heteroplasmic individuals and also suggested that the heteroplasmic samples tend to group according to the degree of heteroplasmy (Figure 37C, D). We performed the functional analysis of sets of differentially expressed genes across the strains using DAVID and Ingenuity Pathways Analysis (IPA). To better understand how the heart responses to heteroplasmy, we performed a contrast analysis of the GO and IPA categories between homoplasmic and heteroplasmic hearts (Figure 37E). The analysis defined 4 major clusters of differential regulated pathways. Cluster 1 can be subdivided in 4 groups: autophagy and ubiquitination (clusters 1a and 1d), intracellular membrane organization (cluster 1b) and nuclear transport (cluster 1c). In all cases these pathways were upregulated in heteroplasmic hearts and may reflect hyper-activation of repairing intracellular mechanisms. Cluster 2 showed downregulation of pathways involved in immune response. Cluster 3 reflected the increase in metabolic processes leading to the utilization of glucose (cluster 3a) and the over-activation of the mitochondrial, and more precisely OXPHOS, gene expression (cluster 3b).

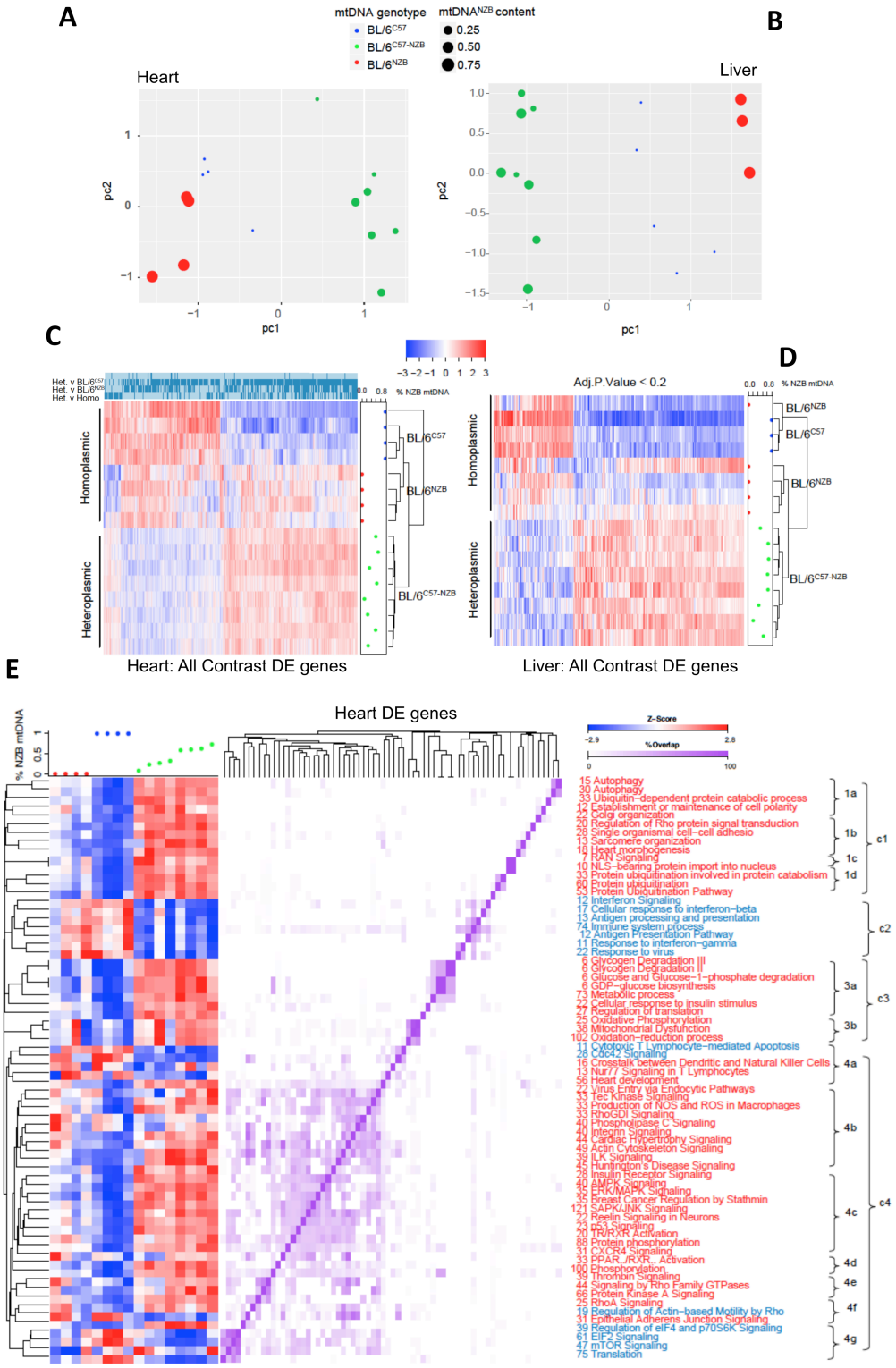

Figure 37. Transcriptomic analysis of heart and liver tissues. (A-B) Principal component analysis on the batch-corrected transcriptomes from heart (A) and liver (B) samples. Dot size represents the % of mtDNA NZB for each heteroplasmic mouse. **(C-D)** Clustered heat map of the profiles of differentially expressed heart (C) and liver (D) genes at any conditions (*adj.p-value* < 0.05 for heart samples dark blue on top panel and *adj.p-value* < 0.2 for liver samples). For this analysis data has not been batch corrected, but batch has been taken into account as a blocking variable in the model. Z-score of expression value of each sample (blue-red scale). Right panel shows the level of mtDNA NZB. Liver samples did not show any significant difference at an *adj.p-value* < 0.05 and for representation purposes we increased this *p-value* cut-off to 0.2. Samples still cluster according to their condition suggesting that cells are still sensing the conplastic and heteroplasmic condition. **(E)** Functional analysis from differentially expressed genes in the heart (HDE) between conditions. Significantly enriched (*adj.p-value* < 0.2) GO of biological processes obtained from DAVID platform plus canonical pathways from Ingenuity platform are clustered according to the number of genes they shared (purple heatmap). The number accompanying the functional category name

indicates the HDE genes in that category (blue for functions/pathways downregulated in heteroplasmic *vs.* homoplasmic mice and red for upregulation). Left panel represents the average transcriptional profile of the HDE genes present in each category across the different conditions, indicated as % mtDNA NZB content in the plot above.

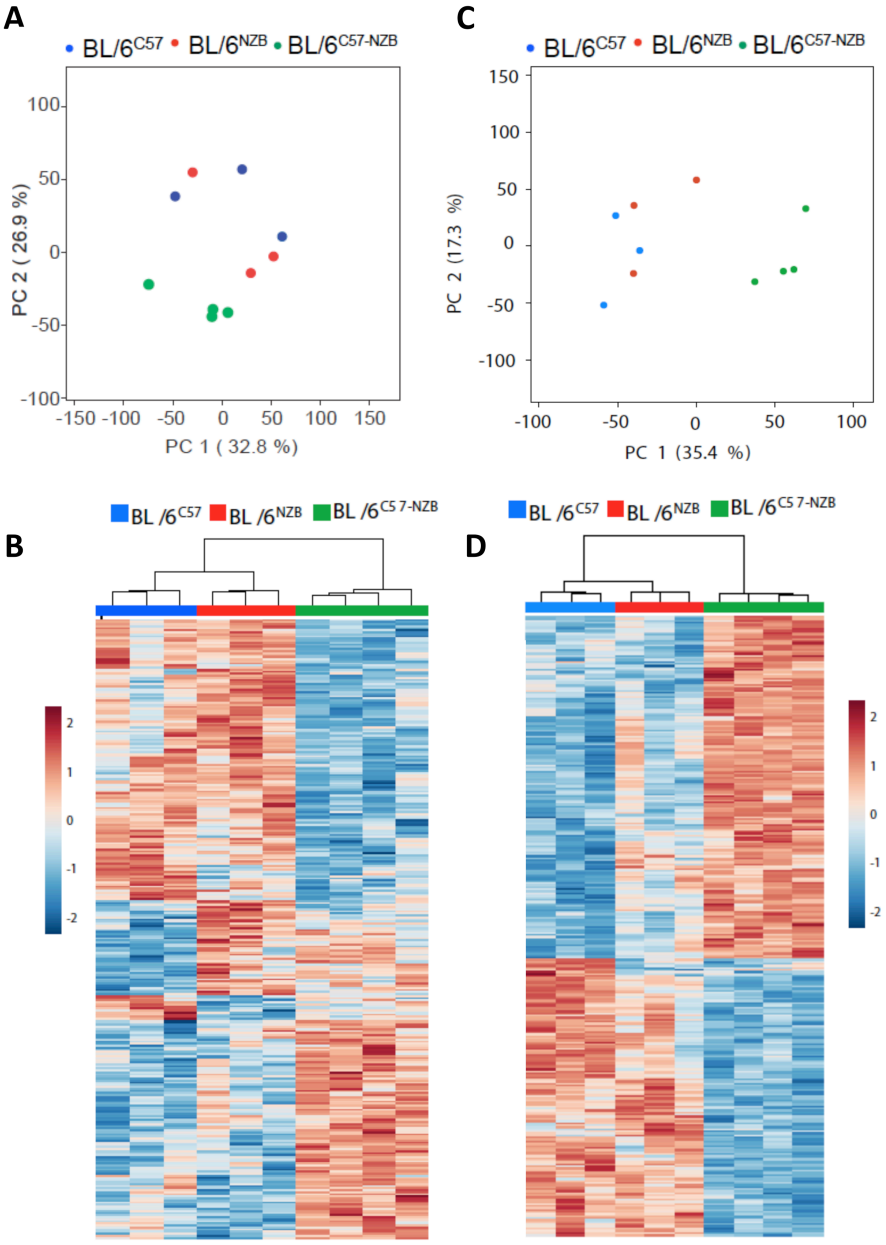

Figure 38. Heart and liver proteomic analysis. (A-B) Heart proteomic analysis of 12-weeks-old mice showing the principal component analysis (A) and the hierarchical clustering of the ANOVA 300 significantly different proteins (B). **(C-D)** Liver proteomic analysis of 12-weeks-old individuals. Principal component analysis (PCA) of liver samples (C) and hierarchical clustering analysis with the 300 significantly altered proteins (D).

Both are coherent with the observed increase in glucose uptake and OXPHOS protein damage in heteroplasmic hearts. Cluster 4 is more heterogeneous, illustrates the activation of a variety of general signalling pathways. Several of them are related to cell stress and nutrient sensing (Tec Kinase Signalling, SAPK/JNK signalling, p53 signalling, AMPK signalling). Notably, the mTOR, eIF4/P70S6K, and eIF2 signalling are downregulated (Figure 37E). This observation is in agreement with the recent proposal that mTORC1 stress response is specific for mtDNA expression diseases[246].

V.2.D.3.d. Proteomic analysis determines why ATP production is decreased in heteroplasmic hearts

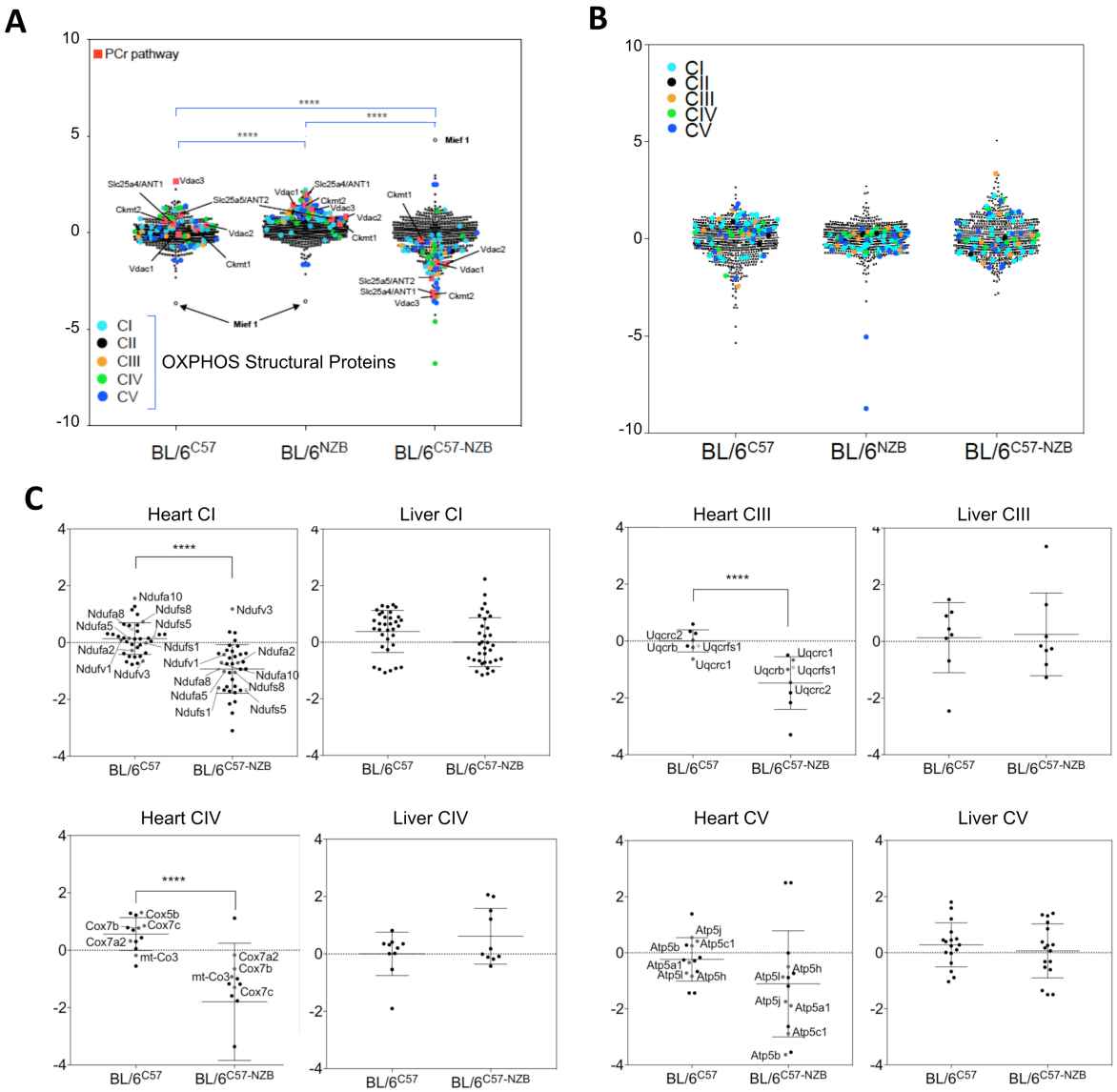

Figure 39. Proteomic analysis of structural OXPHOS components in hearts and livers of young homoplasmic and heteroplasmic mice. **(A)** Analysis of OXPHOS components and the mitochondrial elements of the phosphocreatine (PCr) pathway in hearts of 12-weeks-old homoplasmic and heteroplasmic mice. **(B)** Analysis of the total structural OXPHOS components in liver samples. **(C)** Zq graphics showing the overall amount of the proteins of the indicated complex between the two mice strains (12-weeks-old BL/6^{C57} and BL/6$^{C57\text{-}NZB}$ mice). **p-value* < 0.05, ***p-value* < 0.01, ****p-value* < 0.001, **** *p-value* <0.0001 assessed by ANOVA analysis.

Principal component analysis (PCA) in heart samples from individuals with over 30% heteroplasmy confirmed that overall the proteome of the heteroplasmic individuals is significantly different from that of the homoplasmic animals (Figure 38A). Hierarchical clustering analysis performed with the 300 more altered proteins showed a generalized decrease in mitochondrial proteins in heteroplasmic hearts (95 out of 134, FDR 9.9 e-22), and those involved in oxidative phosphorylation were significantly downregulated (57 proteins FDR 1.74 e-26) (Figure 38B). The set of upregulated proteins (106) involved homeostatic processes aimed to maintain the cell structure, such as those related to cytoskeletal reorganization (FDR 0.015). Interestingly, proteins involved in phagosome formation were also upregulated (FDR 0.0097). This

result may indicate a dysfunctional accumulation of mitochondria in stalled phagosomes. PCA and the hierarchical clustering in liver samples also confirmed the separation between the three genotypes (Figure 38C, D). Among the 117-downregulated proteins in the liver of heteroplasmic mice, 30 are involved in cytoplasmic ribosome assembly, translation and its regulation (FDR 2.34 e-12). This may be consequence of an activated UPR. The upregulated proteins, 136 in total, are involved in a variety of homeostatic functions, 42 of them are involved in macromolecular localization (FDR 0.001) (Figure 38D).

A decrease in the expression of proteins related to REDOX reactions, energy derivation by oxidation of organic compounds (i.e. organonitrogen compound metabolic process) and the generation of precursor metabolites and energy were observed in cardiac tissue of heteroplasmic mice. In this set of proteins, molecular functions as catalytic activity, cofactor binding and coenzyme binding were also negatively enriched. In the second set of proteins, ATP synthesis, proton transport and respiratory electron transport chain presented less expression in heteroplasmic hearts. In the same direction, the molecular functions that were downregulated are the proton-ion transmembrane transporter activity, oxidoreduction reactions and NADH dehydrogenase activity. The analysis also confirmed the differences in mtUPR among homoplasmic and heteroplasmic strains, including other proteins more than in the Western blot analysis as TRAP1, HSPE1, and HSPA9. The downregulation of OPA1 and DRP1 (also termed DNM1L) was also found.

We analyzed the mitoproteome and found that heteroplasmic hearts showed a reduction in all the protein components of the OXPHOS system (nuclear and mtDNA-encoded), which suggests a reduction of the mitochondrial capacity to provide energy (Figure 39A, C). In agreement with this interpretation, a decrease in the amount of the two isoforms of the ADP/ATP translocase at the mitochondrial inner membrane (ANT2 ubiquitously expressed in mice and ANT1, the skeletal muscle and heart isoform) was observed (Figure 39A). Additionally the amount of mitochondrial creatine kinase (CKMT2), fundamental in the maintenance of the myocardial high-phosphate metabolism[247], and the protein components of the mitochondrial outer membrane pore (VDAC1, VDAC2 and VDAC3), responsible for the release of phosphocreatine from the mitochondrial intermembrane space, were also reduced in heteroplasmic hearts (Figure 39A). In summary, all the mitochondrial components responsible to provide energy for heart contraction were strongly reduced in cardiac tissue of BL/$6^{C57\text{-}NZB}$. Heteroplasmic livers, however, did not show any decline in OXPHOS structural proteins (Figure 39B-C).

V.2.D.3.e. Cardiac function assessment in heteroplasmic mice

The findings obtained by proteomics prompted us to perform a detailed analysis of the *in vivo* cardiac bioenergetic metabolism. First, the glucose demands were investigated by [^{18}F]-FDG PET/CT uptake analysis in homoplasmic and heteroplasmic young animals (20-week-old males). We described elsewhere that homoplasmic adult NZB and C57 mtDNA carrying mice differ in the relative weight gain and in the homeostasis of glucose and FA metabolism[16]. Here, we found that heteroplasmic mice show an unusual and significant increase in heart glucose uptake (Figure 40A), very prominent in the case of the right ventricle (Figure 40B). We segmented the right ventricle (RV) and left ventricle (LV) from CT scans and the average of three-four mean standardized uptake values (SUV) from different manually delimited heart regions were obtained to estimate LV/RV FDG uptake (Figure 40B).

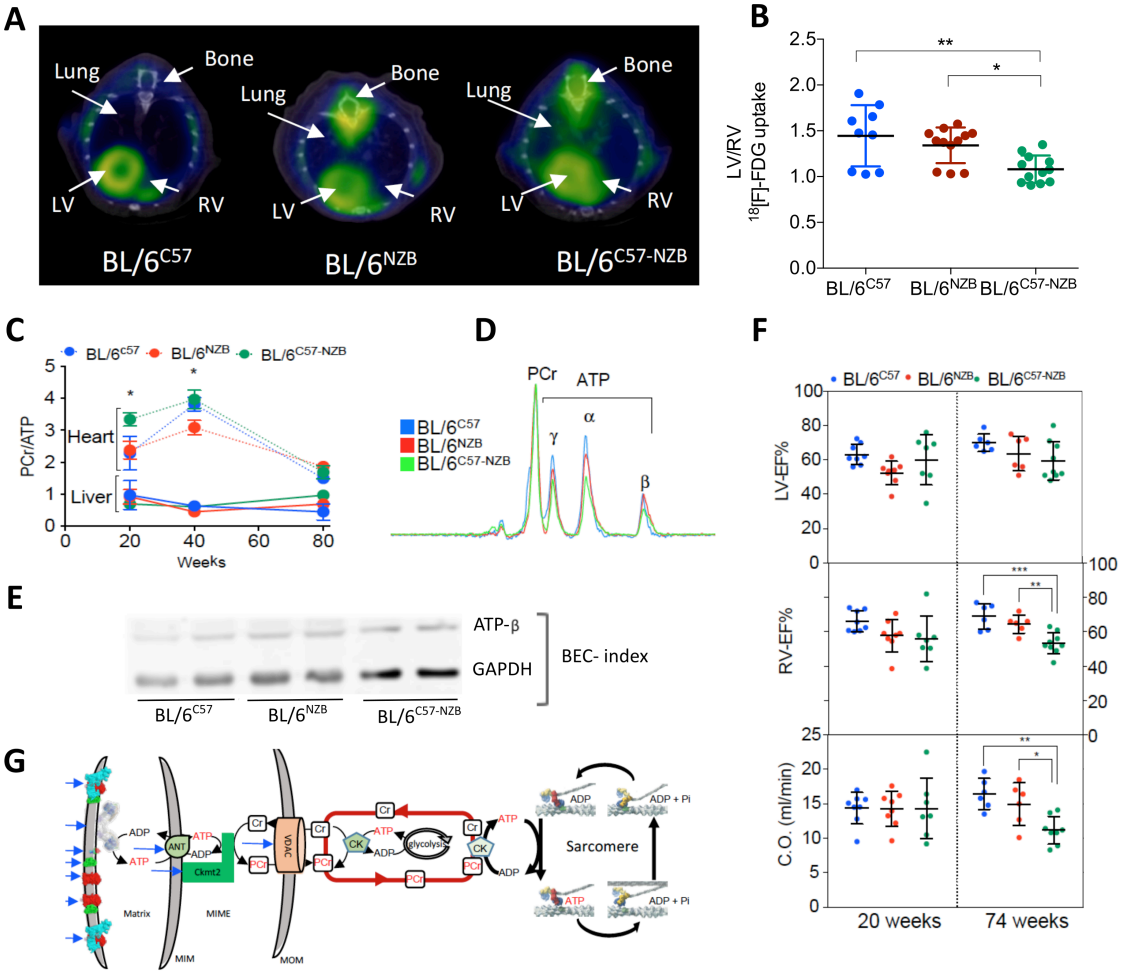

Figure 40. *In vivo* assessment of cardiac performance. **(A-B)** Axial fused PET/CT representative images of homoplasmic and heteroplasmic 20-weeks-old mice (n = 4-5) (A) and quantitative analysis of the increase in the relative RV and lung glucose uptake ([^{18}F]-FDG) (B). LV: left ventricle, RV: right ventricle. **(C)** Analysis of heart and liver performance. Longitudinal analysis by ^{31}P-MRS of the phosphocreatine/ATP ratio in heart and liver of the indicated mouse strains (n = 3-8). **(D)** Heart ^{31}P-MRS stacked spectra of 20-weeks-old mice. **(E)** Representative Western blot showing BEC-index immunodetection in 12-weeks-old heart samples. **(F)** MRI analysis of heart function in the indicated mouse strains at 20- or 74-weeks-old animals. Each dot represents a single animal. **(G)** Diagram illustrating the alterations in the bioenergetics/PCr pathway in heteroplasmic animals revealed by the multiple approaches analysis of the heart function.

In vivo Magnetic Resonance Spectroscopy (^{31}P-MRS) revealed that, in addition to the elevated FDG uptake, heteroplasmic hearts had an increase in the phosphocreatine/ATP (PCr/ATP) ratio. The highest PCr/ATP ratio was maintained in heart of 40-week-old animals, the age in which an increase in the ratio was observed in homoplasmic BL/6^{C57} with respect to BL/6^{NZB} in agreement with its earlier mitochondrial decline. This ratio dropped in all strains at advanced age (80-weeks-old mice). In accordance with the proteomic data, liver did not reveal differences in any of the bioenergetic parameters (Figure 39B, Figure 40C). We hypothesized that cardiomyocytes may compensate the impairment in mitochondrial function by shifting its metabolism from oxidative towards glycolytic metabolism. We explored this possibility assessing the relative proportion between both of them in whole tissue homogenates by the Bioenergetic Cellular Index (BEC) [236]. This index was decreased in the hearts of the heteroplasmic animals with respect to the homoplasmic ones (Figure 40E). These results showed that heteroplasmy causes the reduction of the overall capacity of the heart mitochondria to supply PCr to the sarcomere, and that glucose consumption through glycolysis is activated to compensate it (Figure 40G).

At 20 weeks of age, heart functional parameters assessed by MRI, as right and left ventricle ejection fractions (RV-EF and LV-EF) and cardiac output (CO) were similar between homoplasmic and heteroplasmic individuals (Figure 40F). However, at 74-weeks-old, age in which heteroplasmic mice start to die suddenly, RV-EF was significantly reduced (Figure 40F). The decrease in RV contractility and a low cardiac output have been described associated to a reduced RV function [248]. In our case, we observed a decrease in CO accompanied also the low RV-EF (Figure 40F).

In summary, we observed a sustained reduction in the contribution of heteroplasmic mitochondria to the pool of ATP as an early landmark of mtDNA heteroplasmy, which is resolved in liver but not in heart, presumably because heteroplasmy persists in the latter. The normal heart function at young age in heteroplasmic animals is preserved by a shift to a more glycolytic metabolism. The abnormal metabolic phenotype in cardiac tissue starts at 20 weeks old in heteroplasmic mice, although adapted to maintain the pumping capacity of the heart. It is only at the age of 70-74 weeks, when heteroplasmic mice show alterations in cardiac function and heart failure. On the other hand, the functional and structural differences observed in the liver did not suggest mitochondrial impairment or damage. We found that the liver became close to 100% NZB in the elderly heteroplasmic mice, but at 12-20 weeks old is still heteroplasmic. Notably the heteroplasmy was only monitored in the overall tissue. There are no data on how heteroplasmy evolves in the individual hepatocytes. As a hypothesis, cells that have a grade of heteroplasmy that is harmful would be the first that may become mostly NZB mtDNA. This fact may be an explanation of why liver of heteroplasmic mice recovers mitochondrial function before the total removal of heteroplasmy.

We found that the cell recognizes mtDNA heteroplasmy and can adapt its transcriptome and proteome profiles regardless the existence of mtDNA selection or persistent heteroplasmy. However, the pathways implicated in this adaptation are rather different between tissues, more focused on the downregulation of mitochondrial dependent metabolism in heart and skeletal muscle and focused on the downregulation of gene expression in lung and liver. Upregulated genes, although are particular in each tissue, are indicators of an overall increase in the homeostatic maintenance. This pattern may be suggestive of a primary damage of the mitochondrial function in heart, likely due to their inability to select one mtDNA haplotype, that compromises its metabolic performance. The liver may reflect a mixed response to a successful adaptation to the presence of two mtDNAs that lead to the selective elimination of one of them together with a metabolic adaptation to the damage in heart and skeletal muscle performance. It is very interesting the early affectation of lung function. The proteomic analysis reveals a complex response that may be consequence of the lack of segregation likely leading to pulmonary hypertension that contribute to the heart right ventricle dysfunction.

V.2.D.4. How non-pathological variants of mtDNA can affect pulmonary function

Studies in human transmitochondrial cybrid cell lines demonstrated that different mtDNA haplogroups could mediate the expression profile of nuclear-encoded genes, most of them associated to immune response pathways that play a central role in several human respiratory diseases as well as their progression and phenotypic severity[249]. It was proposed that differences in the ability to resist oxidation between mtDNA haplogroups have to be considered in chronic obstructive pulmonary disease (COPD) susceptibility[250]. However, there is not a clear association between mitochondrial DNA variants and the prevalence of pulmonary disorders. We found differences in mitochondrial physiology induced by wild type mtDNA variants in the conplastic strains BL/6^{C57} and BL/6^{NZB} (i.e. ROS production, OXPHOS efficiency and differences in ageing profile)[16]. These parameters may play a central role in lung

performance. Due to the lung tissue complexity, elucidating the role of mitochondria in pulmonary diseases is a challenging task.

In the present work we have shown that the heteroplasmy proportion in eighteen different tissues does not remain constant along the lifespan of the mice. Most of the tissues select for one of the variants of mtDNA. Lung was one of the few organs that did not show mtDNA segregation (Figure 22). Studying the mtDNA segregation at the level of tissue does not consider the cellular complexity of them. Lung cell complexity is wide, but pulmonary artery smooth muscle cells (PASMCs), fibroblast and endothelial cells might be the most relevant components on pulmonary remodelling associated with mitochondrial mediated metabolic alterations[69]. As it is showed in our previous analysis of mtDNA segregation during lifespan of heteroplasmic mice, smooth muscle, cardiac muscle or skeletal muscle cannot select for one the mtDNA variants. Based on these findings, heteroplasmic mouse strains are considered a valuable model to understand the molecular basis of mitochondrial impairment and mtDNA in pulmonary physiology.

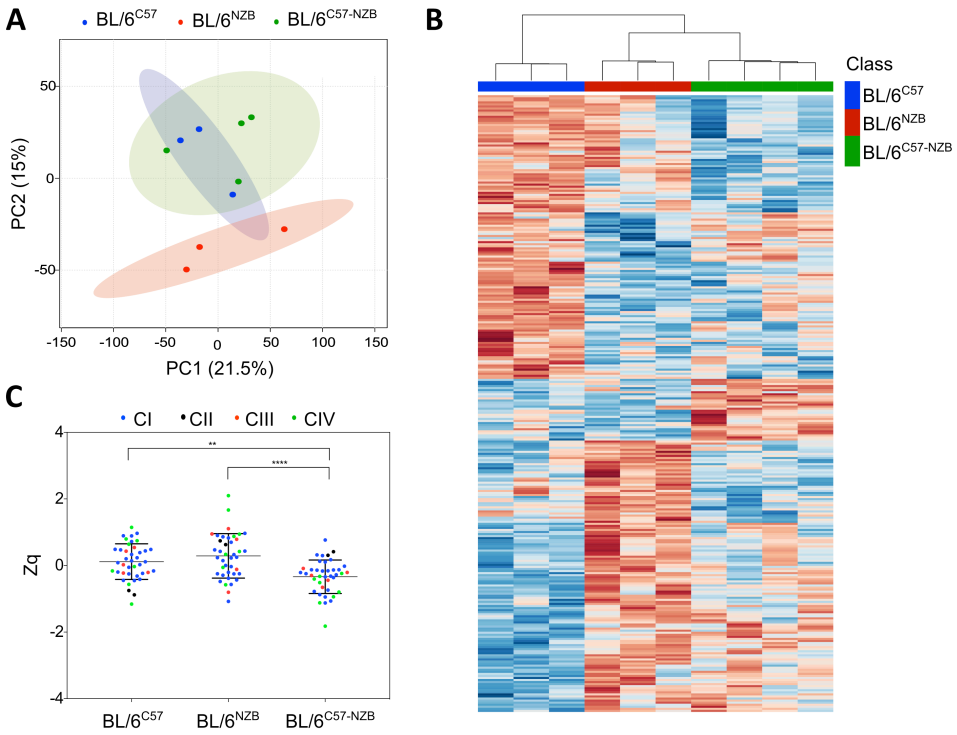

Figure 41. Lung proteomic analysis. Lung proteomic analysis of 12-weeks-old mice showing the principal component analysis **(A)**, the hierarchical clustering of the ANOVA 300 significantly different genes **(B)** and the analysis of structural components of the mitochondrial electron transport chain **(C)**. (n = 3 for the each homoplasmic strain and n = 4 for the heteroplasmic mice). ***p-value* < 0.01, **** *p-value* < 0.0001, ANOVA analysis.

We performed proteomic analysis from the whole lung tissue of 12-weeks-old homoplasmic and heteroplasmic mice. Principal component analysis showed no drastic differences in the lung between the proteomes (Figure 41A). Despite of this, the hierarchical clustering of the 300 more divergent proteins separated the heteroplasmic samples (Figure 41B). Heteroplasmic samples showed a significant downregulation of proteins located in the nucleus (34 proteins with a FDR of 1.4e-06) and among them those regulating RNA splicing (11 proteins, FDR 1.5e-07) and poly(A)RNA binding (26 proteins, FDR 3.7e-11) (Table 15).

Table 15. Pathway analysis of differentially expressed proteins.

GO	Pathway	p-value
0008380	RNA splicing	5.95x10-15
0000377	RNA splicing, via transesterification reactions with bulged adenosine as nucleophile	1.14x10-14
0000398	mRNA splicing, via spliceosome	1.14x10-14
0000375	RNA splicing, via transesterification reactions	1.14x10-14
0006397	mRNA processing	1.14x10-13
0016071	mRNA metabolic process	1.71x10-13
1903311	Regulation of mRNA metabolic process	8.70x10-11
1903312	Negative regulation of mRNA metabolic process	4.72x10-6
0051171	Regulation of nitrogen compound metabolic process	1.10x10-5
0010608	Posttranscriptional regulation of gene expression	1.58x10-5

Interestingly, we found a significant decrease in proteins of the mitochondrial respiratory chain (Figure 41C), but not of those of the H^+-ATP synthase. It was described before that mutations in mitochondrial complex IV (cytochrome c oxidase) subunit COX5A could cause PAH[251]. Heteroplasmic 12-weeks-old mice presented an important decrease in this complex IV subunit among others (Figure 41C).

Transmission electron microscopy analysis in lungs from 12-weeks-old mice revealed abnormal mitochondrial ultrastructure in the alveolar system, specifically in alveolar epithelial cells (AECs) type II, but not in bronchiole epithelium (Figure 42A). One of the principal features that heteroplasmic mice show was the accumulation of collagen in alveolar walls when they are young (12-weeks-old mice). It was described that damaged mitochondrial DNA can lead to an increase in apoptosis of AECs, being related to pulmonary fibrosis[70]. In addition, TEM analysis revealed an excess of lamellar bodies, differences in nuclei morphology (convoluted nucleus with cavitation) and more and abnormal morphology of the mitochondria (damaged, vacuolated, and swelling mitochondria) in AECs type II of heteroplasmic mice (Figure 42A, B).

Lamellar bodies are specialized organelles responsible for surfactant packaging within AECs type II. This surface-active lipoprotein complex is necessary to stabilize the alveoli by the reduction of surface tension at the air-liquid interface, preventing the alveolar collapse during end-exhalation[252]. Surfactant also acts as a host defence and pathogen barrier. We then inquired if the increase of lamellar bodies (Figure 42B-D) was associated with any deregulation of the surfactant synthesis or delivery. After analysing components of the pulmonary surfactant, we observed an increase of the surfactant protein A (SP-A), foreseeing an alteration of this specific cellular metabolism (Figure 42E). SP-A and SP-D are synthesized and secreted by alveolar epithelial (AECs) type II and Clara cells, playing a crucial role in the immunomodulatory effects of resident macrophages[71]. These proteins recognize pathogen associated molecular patterns (PAMPs) and carry out their role as opsonins, agglutinins and immunomodulators[253]. It is well known the role of SP-A and SP-D in the regulation of tissue homeostasis and immune response as cleanser of apoptotic cells after interacting with macrophages[254]. DNA and mitochondrial DNA exposed on the cell surface of early and late apoptotic cells could be a possible ligand for cysteine-rich domain CRD and collagen-like regions of the collectins SP-A and SP-D[255,256]. Interactions with cell surface ligands on inflammatory cells as macrophages promote or block the phagocytic activity as well as the synthesis of cytokines and ROS[253]. Among the different clusters of proteins differentially expressed, those related to the

immune system were highlighted and presented significant *p-value* in the Gene Ontology (GO) analysis (Table 16). The interaction with alveolar macrophages is based on that[253].

Among the total proteins analysed, a significant upregulation was observed in the neutrophil gelatinase-associated lipocalin (LCN2), associated with apoptosis and innate immunity; intercellular adhesion molecule 1 (ICAM1), which is a ligand for the leucocyte adhesion protein LFA-1 (integrin alpha-l/beta-2); the myosin-Ig (MYO1g), required during immune response for detection of rare antigen-presenting cells by regulating T-cell migration and in Fc-gamma receptor phagocytosis and the protein Annexin A1 (ANXA1), regulator of the inflammatory process by enhancing signalling pathways triggered by T-cell activation, involved in the differentiation and proliferation of them[257]. Alveolar macrophages are the most abundant immune cell population in lung tissue playing a critical role in adaptive and innate immune response. They represent the most important sentinels both for non-specific phagocytic defence system and for antigen triggered immunity via activation of T-lymphocytes and neutrophils recruitment[258]. The analysis of macrophages as F4/80 positive lung tissue areas in histology from the whole lungs of the three strains ($BL/6^{C57}$, $BL/6^{NZB}$ and $BL/6^{C57\text{-}NZB}$) demonstrated an abnormal increase of macrophages in those lungs from heteroplasmic mice, supporting the increase in the activation of immune response in them (Figure 43A, B).

Table 16. Gene Ontology (GO) enrichment analysis of immune system-related pathways genes altered in heteroplasmic lung tissue.

GO	Pathway	p-value
0006955	Immune response	0.0056
0045087	Innate immune response	0.0103
0002684	Positive regulation of immune system process	0.0194
0002460	Adaptive immune response: recombination of immune receptors built from immunoglobulin superfamily domains	0.0524
0002252	Immune effector process	0.0786
0002682	Regulation of immune system process	0.0786
0002250	Adaptive immune response	0.0961

It is well-known that oxidative stress in mitochondrial DNA damage induce autophagy and inflammation[259]. As we faced before, there are differences in ROS production in cells containing different mitochondrial DNA variants under the same nuclear background[16]. The increased inflammation observed in lungs could be originated by the released mtDNA or non-functional mitochondria during processes of autophagy in AECs. To prove it, autophagy markers were analysed in 12-weeks-old mice lung sections by Western blot to assess the implication of ROS in autophagic pathway (Figure 43C, D). We evaluated LC3 protein (microtubule-associated protein 1 light chain 3), a soluble protein that expresses splice variants LC3A, LC3B and LC3C. All these isoforms can show post-translational modifications, mainly lipidations. Upon autophagic signals, the cytosolic form of LC3 (LC3-I, 18 kDa), is modified by lipidation to form LC3-II (16 kDa) to be recruited to the autophagosome membranes and being degraded during the process of fusion between autophagosomes and lysosomes. The ratio LC3-I/LC3-II is used to indicate the autophagic activity. LC3-II was only detected when significant numbers of autophagosomes are present in the samples. Interestingly, we observed a decrease in this ratio in samples from heteroplasmic mice, indicating an increase of autophagosome formation (Figure 43C). Samples from $BL/6^{C57\text{-}NZB}$ accumulated

the LC3-II 16kDa band. Recent studies place ATG proteins as regulators of autophagy[260]. ATG proteins were decreased in the heteroplasmic mice in comparison with any of the homoplasmic strains, mostly significant in the case of ATG5 (Figure 43C). ATG5 is implicated in both the autophagic and apoptotic response[261]. Similarly, we found low amount of GRP75 (also termed HSPA9) and an increased amount of HSP60 two chaperones related to cellular stress response, particularly endoplasmic reticulum and mitochondrial unfolded protein responses (mtUPR) (Figure 43D). Defective UPR and alterations in autophagy-lysosome pathway have been reported in lung pathologies as idiopathic pulmonary fibrosis (IPF)[74].

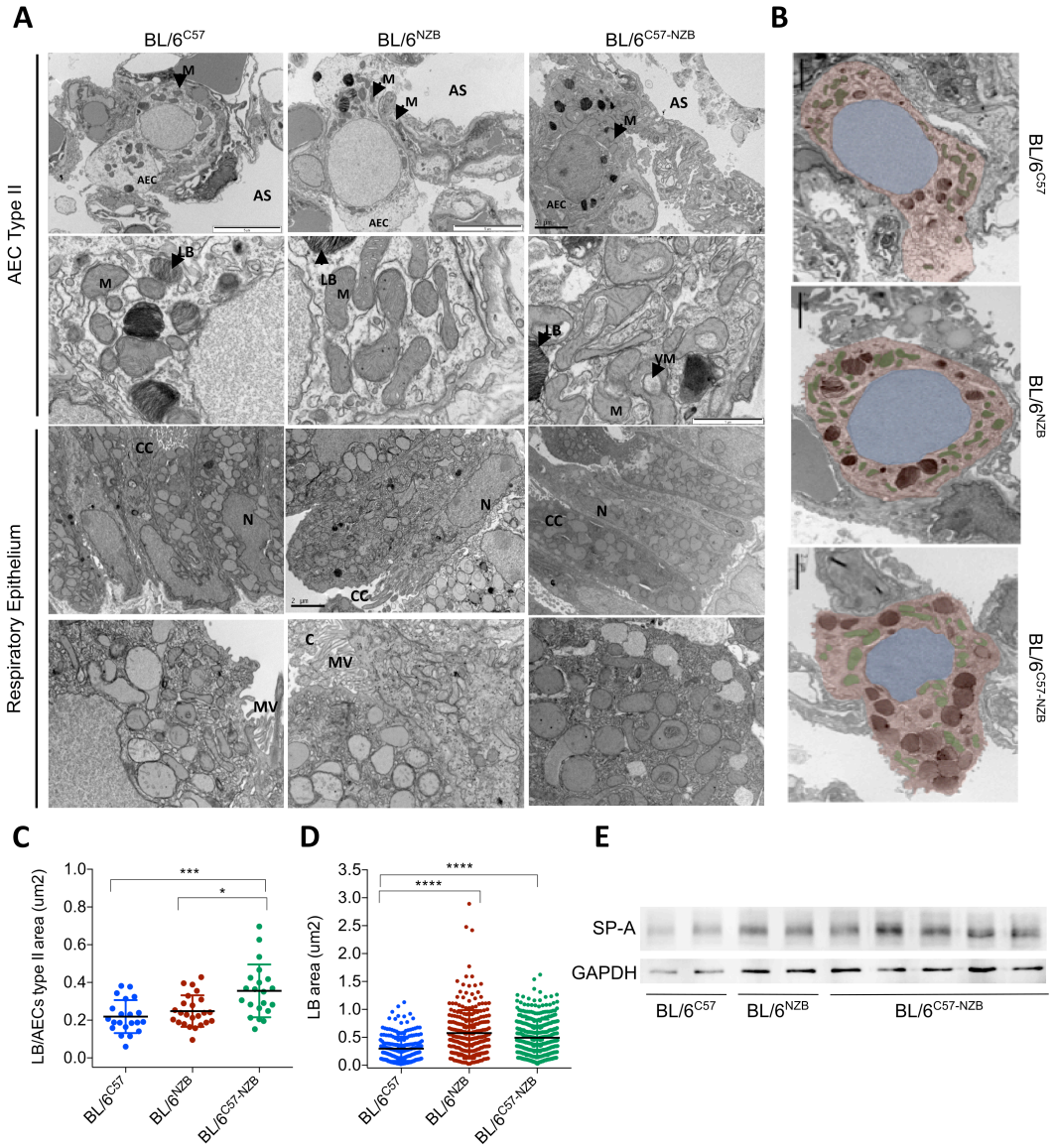

Figure 42. Evaluation of lung tissue ultrastructure. **(A)** TEM representative images of the alveolar epithelial type II cells and respiratory epithelium. M: mitochondria; MV: microvilli; CC: ciliated cells; N: nucleus; VM: vacuolated mitochondria; LB: lamellar body; AS: alveolar space; AEC: alveolar epithelial cell. **(B)** Details of type II AECs of homoplasmic and heteroplasmic lung tissues. In red, cell cytoplasm; blue, nuclei; green, mitochondria. **(C)** Quantitative analysis of the amount of lamellar bodies (LBs) per type II AECs area. **(D)** LB size in type II AECs of BL/6^{C57}, BL/6^{NZB} and BL/6$^{C57\text{-}NZB}$ mice. **(E)** Western blot analysis showing the expression of surfactant protein A (SP-A) and GAPDH enzyme in lungs. The analysis was done in 12-weeks-old males (n = 3 homoplasmic mice and n = 4-5 heteroplasmic mice). **p-value* < 0.05, ****p-value* < 0.001, **** *p-value* <0.0001 assessed by ANOVA analysis (C) and Kruskal-Wallis test (D).

To evaluate if the observed adaptations correlated with mitochondrial function, *ex vivo* analysis of ATP synthesis from isolated mitochondria of lung tissue from 12 and 20-week-old mice was performed (Figure 44 A, B). At 12 weeks of age, we observed a tendency in the decrease of ATP synthesis in mitochondria from heteroplasmic mice ($BL/6^{C57\text{-}NZB}$). We also measured the mitochondrial content by citrate synthase activity at the same age and no differences were found between the strains. At 20 weeks of age there were not differences between the energy productions. However, we observed low mitochondrial content measured by citrate synthase activity in heteroplasmic mice. Due to the complexity of cell composition in lung tissue, more experiments are necessary to be done to clarify which cells are more affected in terms of the reduced mitochondrial content.

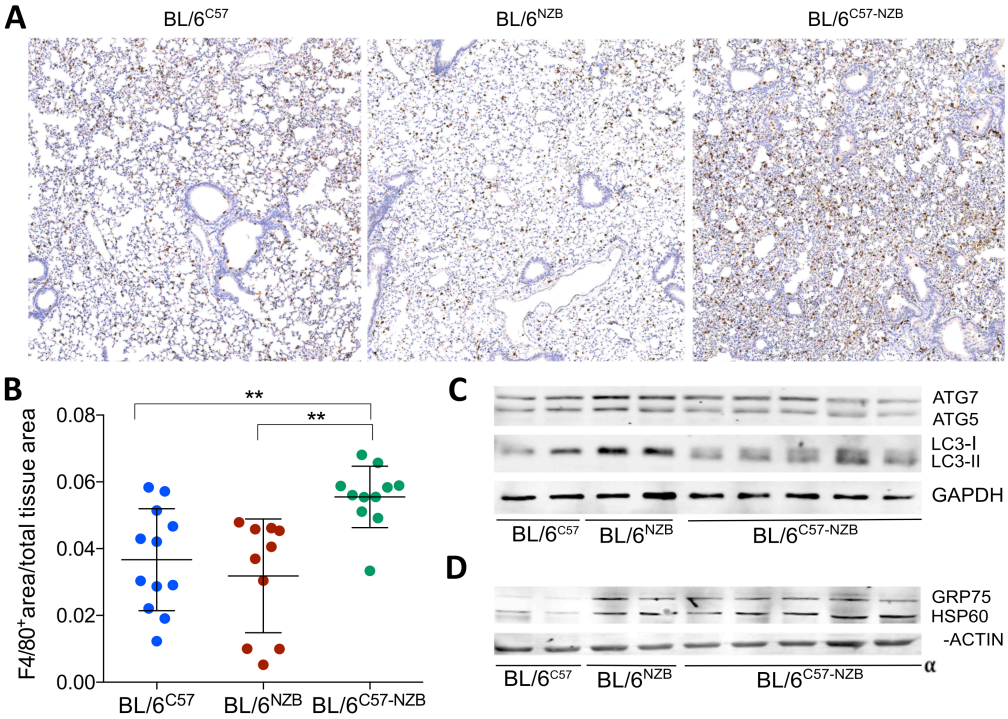

Figure 43. Lung tissue analysis. (A) Histological analysis of lung tissue (F4/80 staining). **(B)** Total expression of F4/80 per area of tissue (n = 5 tissue samples per genotype; 20-weeks-old mice). ***p-value* < 0.01, assessed by ANOVA analysis. **(C-D)** Western blot analyses of proteins involved in autophagy (C) and mtUPR (D).

Alterations in mitochondria during PAH and other related respiratory pathologies can disrupt oxygen sensing, with a concomitant increased the hypoxic environment. Two of the enzymatic activities that are affected are the mitochondrial superoxide dismutase (SOD2) and mitochondrial aconitate hydratase (ACO2). In addition, a decrease on sirtuin activity was reported in IPF patients can lead to the dysregulation of mitochondrial biogenesis and metabolism[74], consequent with the alterations in antioxidant enzymatic activity from mitochondrial superoxide dismutase SOD2. The analysis of the expression of these proteins were performed by proteomic high-throughput analysis (Figure 44E) and Western blot (SOD2, Figure 44F) when animals were young (12-weeks-old mice). An increase in the expression of these proteins was observed in lung tissue of $BL/6^{C57\text{-}NZB}$ mice in comparison with the $BL/6^{C57}$ and $BL/6^{NZB}$ strains. On the other hand, the cytoplasmic isoform of aconitase (ACO1) remained substantially unmodified in homoplasmic strains and even less expressed in the heteroplasmic ones. The implication of mitochondrial ROS in pulmonary disorders as PH is still under debate[81,262]. Studies in rats reported a rise in the activity of the mitochondrial complexes I, II, III and IV and mtROS in lung with age, and a subsequent increase in the post-translational modifications in proteins of the mtETC and lipid

peroxidation[263]. Our analysis shows a senescence-associated phenotype in lungs of middle age heteroplasmic mice (BL/6$^{C57-NZB}$) with a reduction of complex I, II, III and IV proteins, increased ROS and evident signs of fibrosis assessed by electron microscopy and histological analysis.

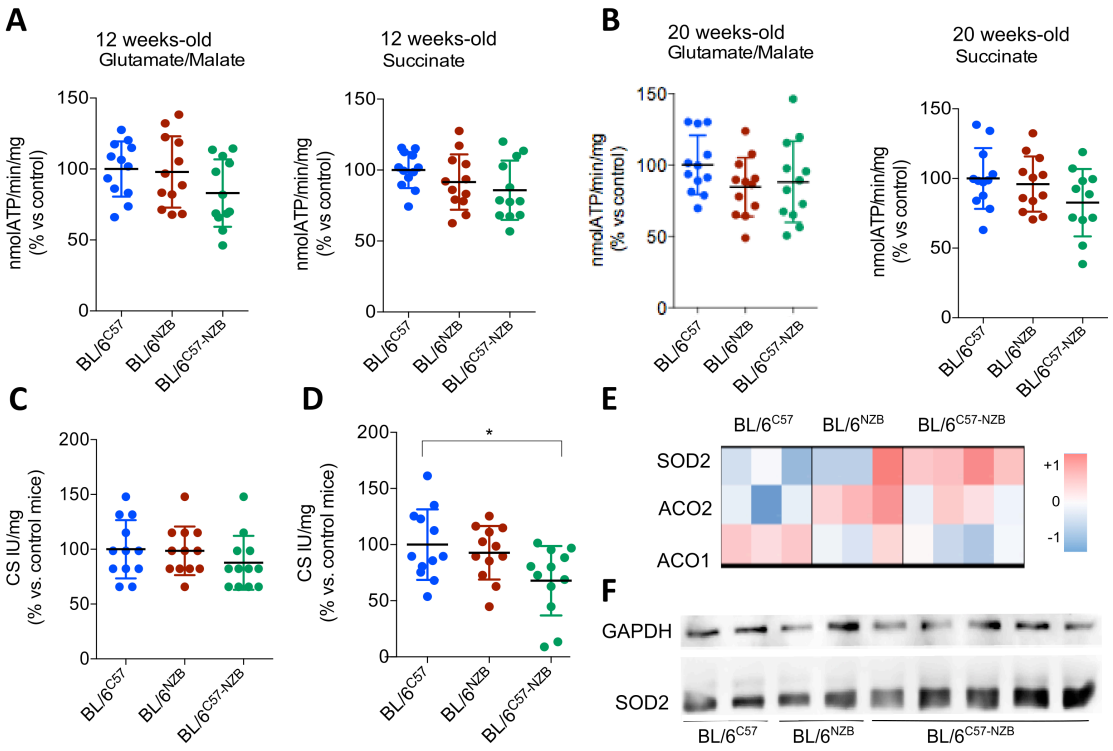

Figure 44. Evaluation of mitochondria performance in lung tissues. **(A-B)** *Ex vivo* ATP production rates in isolated mitochondria from 12-weeks-old (A) and 20-weeks-old (B) homoplasmic and heteroplasmic mice in the presence of the indicated substrates. (n = 6 mice per group; 2 technical replicates per individual). **(C-D)** Citrate synthase activity in lung tissues of 12-weeks-old (C) and 20-weeks-old (D) homoplasmic and heteroplasmic mice. (n = 6 mice per group; 2 technical replicates per individual). Graph shows the enzymatic activity per mg of total lung protein. **p-value* < 0.05 determined by ANOVA test. In A-D control mice correspond to BL/6^{C57} strain. **(E)** Heat map showing the relative expression of the different antioxidant SOD2 (mitochondrial), ACO2 (mitochondrial) and ACO1 (cytosolic) proteins measured by MS/MS (Zq values) (n = 3 homoplasmic mice and n = 4 heteroplasmic mice of 12 weeks of age). **(F)** Representative Western blot analysis of SOD2 (GAPDH as a loading control) in 12-weeks-old mice.

Metabolic status in pulmonary circulation and in the right ventricle (RV) is critical to assess vascular pulmonary dysfunction. PAH is associated with a shift in cell metabolism from fatty acid oxidation towards glucose oxidation[264]. An imbalance between glucose and fatty acid oxidation in mitochondria can promotes RV disfunction[83]. To elucidate the possible role of mtDNA in such metabolic switch, *in vivo* metabolic analysis was performed in the three mice strains. To assess the use of glucose in both cases, we performed a PET/CT analysis for the uptake of [^{18}F]-fluorodeoxyglucose ([^{18}F]-FDG). Analysis of *in vivo* PET/CT images with the PET radiotracer [^{18}F]-FDG revealed an increase in the glucose uptake of the lungs of 20-weeks-old heteroplasmic individuals (Figure 45A). We also observed this increment in the *ex vivo* analysis of the lungs using the gamma counter after 4 hours of intravenous injection of the probe (Figure 45A). These results suggest a switch to a more glycolytic metabolism that might be an indicative of diminished OXPHOS performance. A glycolytic switch in the RV reduces its contractility and promotes an inactivation of the mitochondria-mediated apoptosis in pulmonary artery smooth muscle cells[66]. The right ventricle ejection fraction (RV-EF) is an excellent predictor for the prognosis of this pathology[265,83]. Based on that findings, we analysed the RV-EF and cardiac output (CO) using cardiac magnetic resonance imaging (MRI) in young and aged animals. Heteroplasmic mice presented a significant decrease in right

ventricle ejection fraction when they were more than 70 weeks old (Figure 40F). We also performed a longitudinal study characterising pulmonary features after evidences of loss of function of the heart. Aortic cardiac output (CO) performance assessed by echocardiography remained constant in homoplasmic mice ($BL/6^{C57}$ and $BL/6^{NZB}$) during the whole experiment (Figure 45B-D). In the heteroplasmic mice we observed an increase in CO at 60 weeks of age. This may reveal a compensatory increase of blood delivery to cover the oxygen demands, because at this stage the heteroplasmic mice already presented alterations in cardiac and pulmonary performance. About 10 weeks later, only heteroplasmic animals manifested a decreased in cardiac output.

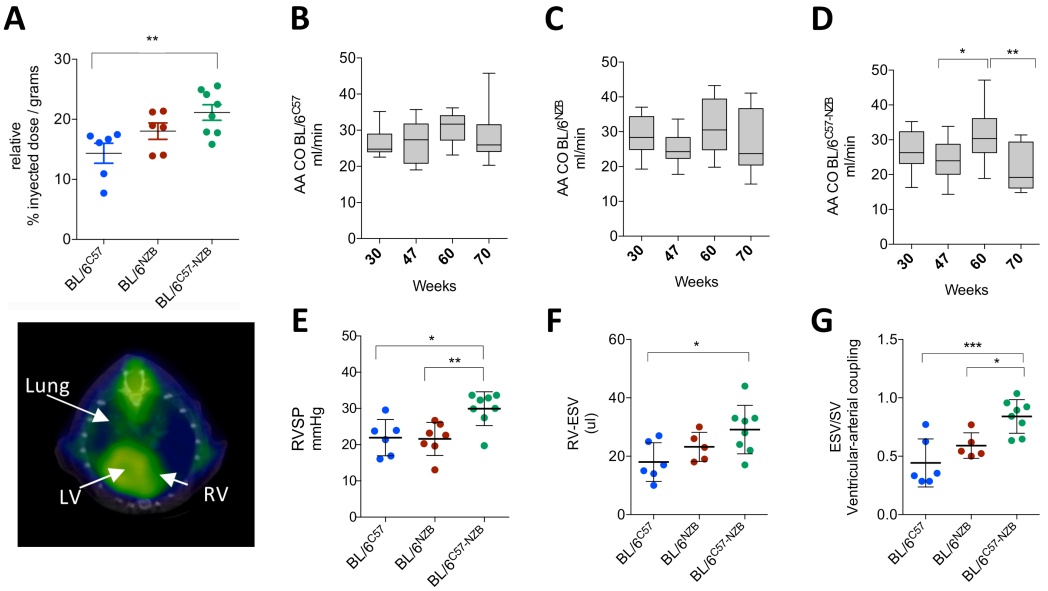

Figure 45. *In vivo* assessment of pulmonary performance. **(A)** *Ex vivo* quantitative analysis of [^{18}F]-FDG uptake in excised lung tissue from 20-weeks-old mice (n = 6 homoplasmic mice and n = 8 heteroplasmic mice) assessed by gamma counter (top) and *in vivo* representative axial PET/CT image of a 20-weeks-old heteroplasmic mouse showing abnormal [^{18}F]-FDG uptake in lung tissue (bottom). **(B-D)** *In vivo* echocardiographic examinations of cardiac output (CO). The longitudinal study was performed in the aorta artery (AA) in homoplasmic mice (B-C) and heteroplasmic mice (D) (n = 12-15 mice per group and age). **(E)** *In vivo* measurement of the right ventricular systolic pressure (RVSP) after RV catheterization in 74-weeks-old mice. **(F-G)** MRI assessment of the right ventricle end-systolic volume (RV-ESV) (F) and the right ventricular-arterial coupling (G) in 74-weeks-old homoplasmic and heteroplasmic mice. In E-G each dot corresponds to a different individual**.** **p-value* < 0.05, ***p-value* < 0.01, ****p-value* < 0.001 determined by ANOVA test.

The analysis of the relation between the systolic pressure and ventricular volume contributes to understand the blood flow performance and the interaction between the right ventricle and the pulmonary system[266]. Independently of the aethiology of the disease, pulmonary arteries narrowing, increased pulmonary vascular resistance (PVR) and the elevated ventricular systolic pressure (RVSP) are characteristics of PH. Right heart catheterization is the only technique available that provides crucial information regarding the load imposed on the RV and its response to this burden, essential to finally diagnose PH[267]. We assessed the *in vivo* ventricular systolic pressure in young (12-weeks-old) and aged (74-weeks-old) mice (Figure 45E). Experiments were performed in closed-chest living animals by inserting the catheter via the right jugular vein and advanced to the RV. In young animals, these measurements showed no significant differences. However, we observed an increase in the right ventricular systolic pressure (RVSP) in elderly heteroplasmic mice in comparison with the homoplasmic strains in the age in which most of them start to die. This increase correlates with the decrease in RV-EF at the same age of the heteroplasmic mice. Cardiac MRI was used to calculate the total right ventricle end-systolic volume (RV-ESV) and stroke volume (SV) (Figure 45F). We observed the expected increase in the RV-ESV. RV-ESV and SV assessments were necessary to calculate the ventricular-arterial coupling, which was significantly

increased in heteroplasmic mice (BL/6$^{C57\text{-}NZB}$) (Figure 45G). This parameter was described for a better understanding of RV uncoupling considering the volume of blood that remains in the RV. A consideration of both arterial load and ventricular performance, as well as the degree of matching between the two are necessary for this assessment[268]. In early stages of the pathology (60-weeks-old mice) the ventricular function and load are coupled adequately. Heteroplasmic mice show heart failure when they were more than 70-weeks-old; right ventricle is unable to enhance its contractility proportionally to the increase of the load that continues to increase since the beginning stage of the disease. All the measured parameters led us to conclude with the evidence of pulmonary hypertension in aged heteroplasmic mice, probably secondary to pulmonary fibrosis.

Changes in lung and RV metabolism are important as an early symptom of the pathology. The elucidation of the molecular mechanism of that metabolic impairment is necessary to develop new diagnostic tools, treatments and improve the prevention in diseases such as PAH[269]. Our results suggest how of the possible mechanisms involved in PF and PH, which are closely connected. Based on them, it is fundamental to analyse the role of mitochondria during the whole process and try to find therapeutic interventions targeting metabolic pathways or at an organelle level.

Diversity in mtDNA and mismatch between nDNA and mtDNA can arise from natural and/or artificial processes:

Lung tissue transplantation in humans, which introduces different mtDNA/nDNA matches within the same individuals. Different variants of mtDNA could interfere at a cellular level of adaptation and in the global homeostatic response in the patient. A mismatch between nDNA and mtDNA could improve metabolic disorders. MtDNA random mutation in somatic cells followed by somatic segregation and amplification is an underscored common phenomenon. These background mutations can be then amplified in ageing[270] or under pathological conditions as cancer[271] . The accumulation of somatic variants of mtDNA during ageing could also promotes alterations in the global metabolism of the individuals.

Mitochondrial transfer in damaged tissues. This mitochondrial repopulation *in situ* has been proposed to have therapeutic value in lung disorders[272] among others. It was proposed that, in a mouse model of acute lung injury, mitochondrial transfer from bone-marrow-derived stromal cells, by direct airway-instillation to the pulmonary alveoli was able to repair the damage[272] . This approach would unavoidably generate mtDNA heteroplasmy and the short-term benefits reported may generate in the long run a heteroplasmic derived-disease. Autologous transplantation or mtDNA matching would be recommended to prevent potential negative consequences of mtDNA heteroplasmy.

Different single mutations and deletions, inherited or spontaneous, in mitochondrial DNA are the cause of a wide variety of mitochondrial diseases (MITOMAP, http://www.mitomap.org). Also mutations in nDNA can alter mitochondrial performance or alterations in proteins or RNA molecules that are present in the organelle[273]. These disorders usually affect multiple organs varying its severity symptoms. Impairment in brain tissue leads patients to have dementia, strokes, mental retardation or neuropathic pain. Muscles are the more damaged tissues that are being studies in patients for years; gastrointestinal problem, weakness and in cardiac muscle problems with conductivity and cardiomyopathy appear. Although lung is one of the tissues that requires high amount of energy, its study is neglected in patients with mitochondrial diseases in terms of diagnosis or treatment[274]. The early affectation of pulmonary tissue in our mouse models was unexpected, because in patients with mitochondrial dysfunction the analysis of lung performance is rarely performed[64]. Our results highlight the unforeseen relationship between mitochondrial function and lung

affectation, as well as developed new early diagnostic tools and the necessity to find new therapeutic solutions based on the knowledge of mitochondrial impairment.

Our results also strongly call for the potential relevance of pulmonary malfunction in mitochondrial disorders, suggesting that alterations in lung could be an underlying cause to the primary pathology. We are proposing that mitochondrial dysfunction plays a central role in some lung pathologies and in the process of lung ageing, directly connected with the transition from normal lung physiology to a pathological state.

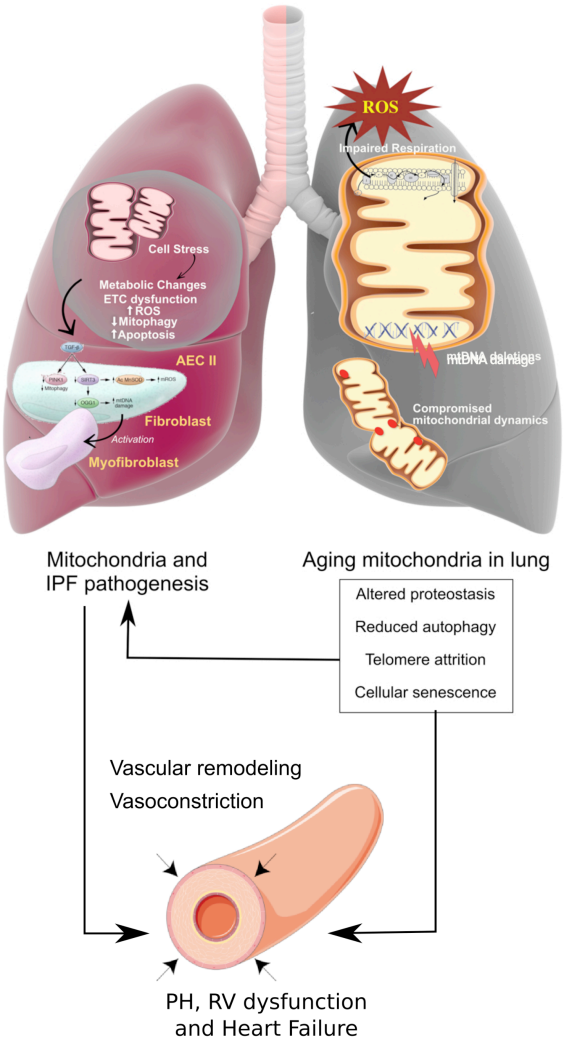

Figure 46. Lung diseases and mitochondrial dysfunction. Summary of the obtained results showing how lung tissue might be damaged by the co-existence of two non-pathological mitochondrial DNA variants. The existence of intrinsic mismatch between mtDNA and nDNA reveals lifelong metabolic consequences and alterations in pulmonary performance.

V.2.D.5. All tissues with stable heteroplasmy develop dysfunctional mitocondria

The deep impact of heteroplasmy on heart and lung mitochondria and metabolism while liver mitochondrial function was preserved prompted us to evaluate the metabolism of other tissues that do not resolve heteroplasmy: skeletal muscle and eye.

V.2.D.5.a. MtDNA heteroplasmy induces skeletal muscle degeneration with ageing

One of the more striking consequences of heteroplasmy was the massive loss of skeletal muscle with age.

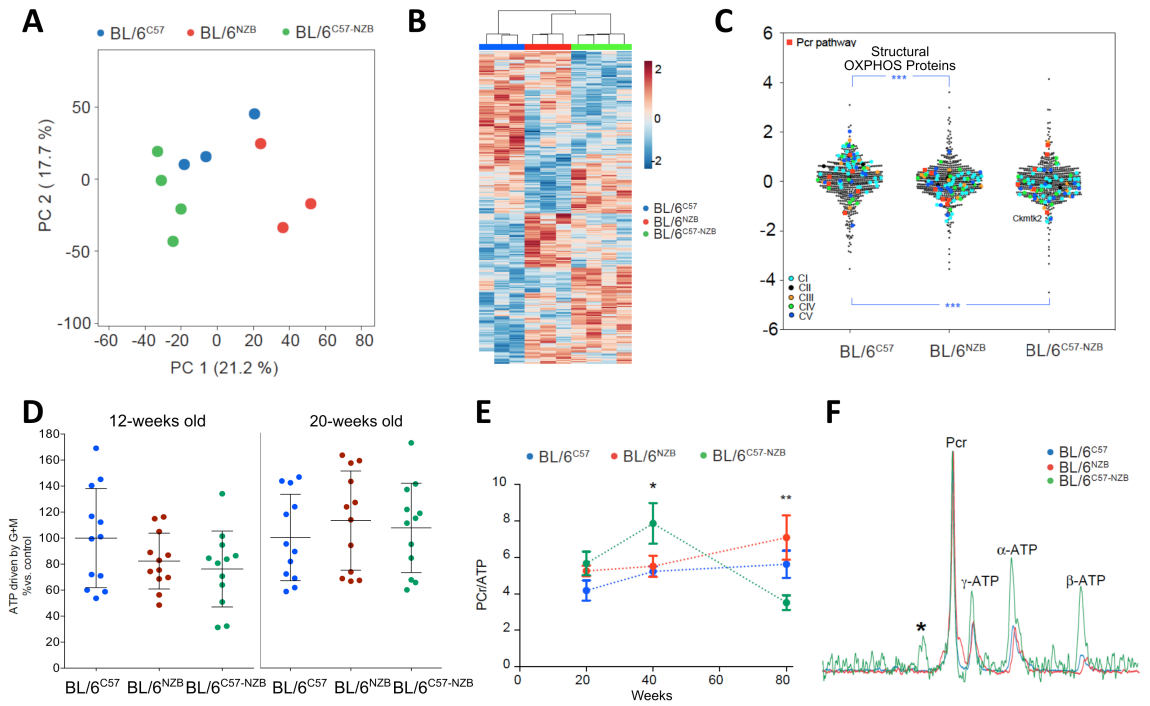

Figure 47. Evaluation of skeletal muscle performance in heteroplasmic mice. Gastrocnemius skeletal muscle proteomic analysis of 12-weeks-old mice showing the principal component analysis **(A)**, the hierarchical clustering of the ANOVA 300 significantly different proteins **(B)** and the analysis of the mitoproteome **(C)**, where the structural OXPHOS components and the mitochondrial elements of the phosphocreatine (PCr) pathway are highlighted (n = 3 homoplasmic samples and n = 4 heteroplasmic samples). **(D)** ATP synthesis rate in skeletal muscle mitochondria driven by glutamate plus malate (G+M) in homoplasmic and heteroplasmic mice of 12 and 20 weeks of age. **(E)** Longitudinal analysis by ^{31}P-MRS of the PCr/ATP ratio in the skeletal muscle (soleus) of the indicated mouse strain (n = 5-9 mice per group and age). **(F)** Representative skeletal muscle (soleus) ^{31}P-MRS stacked spectra of 80-weeks-old mice. The asterisk corresponds to PDE (phosphodiesters). In C, D and E lines mean ± SD. Differences are assessed by ANOVA analysis. **p-value* < 0.05, ***p-value* < 0.01, ****p-value* < 0.001, *****p-value* < 0.0001.

Proteomic analysis of muscle samples at 12 weeks of age corroborated the specific common profile to heteroplasmic individuals demonstrating again that heteroplasmy is sensed by skeletal muscle (47A-C). Hierarchical clustering of the 300 more significantly changed proteins separated heteroplasmic samples from the homoplasmic ones (Figure 47B). In skeletal muscle, mitochondrial proteins (50 out of 96 FDR 5.26e-6) and those involved in OXPHOS (14, FDR 1.9e-2) were reduced. Proteins increased in heteroplasmic samples (92) were enriched in those involving endoplasmic/sarcoplasmic reticulum (29 proteins, FDR 3.0e-4) and calcium homeostasis (7 proteins, FDR 4.7e-2). The detailed analysis of the mitoproteome revealed a higher content of CI structural subunits in BL/6^{C57} than in BL/6^{NZB} or BL/6$^{C57\text{-}NZB}$ muscles (Figure 47C). The overall limited alteration in OXPHOS components (Figure 47C) is in agreement with the absence of signs of skeletal muscle impairment at this age and suggests that mitochondrial performance is maintained in skeletal muscle at the age of 20 weeks, when the heart already showed signs of dysfunction. In fact, there were no significant differences in *ex vivo* ATP synthesis, either in 12 or 20-weeks-old heteroplasmic mice (Figure 47E). ^{31}P-MRS studies also revealed a normal PCr/ATP ratio in 20-weeks-old animals (Figure 47E), which is coherent with the unaffected protein levels of the PCr pathway (Figure 47C, in red).

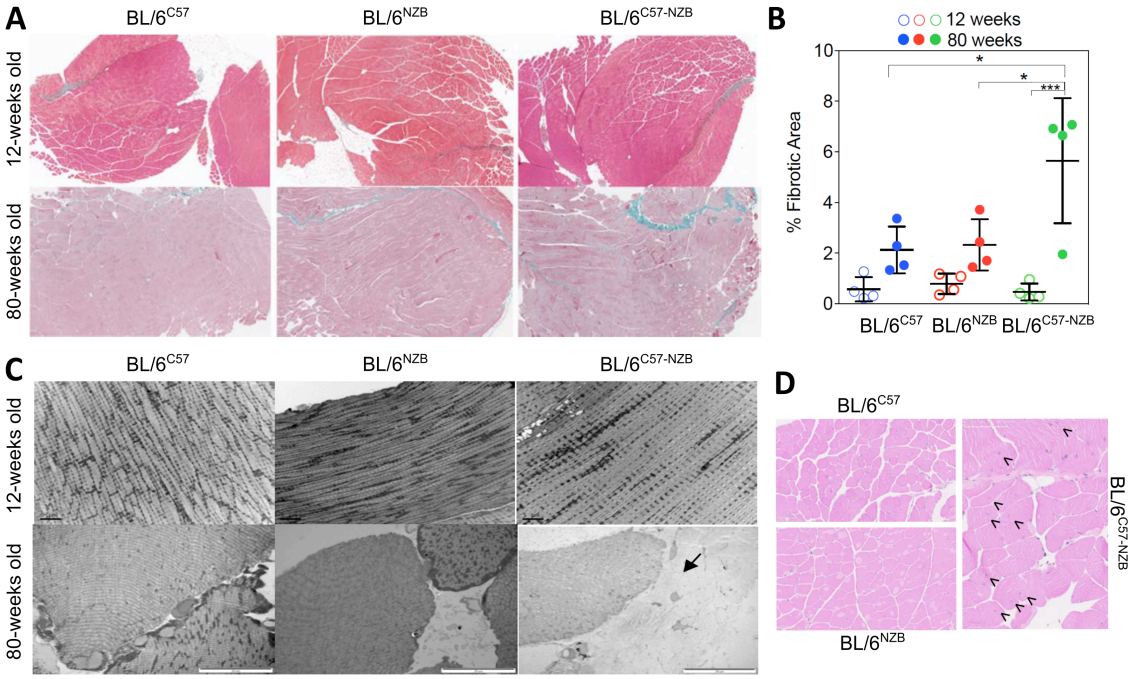

Figure 48. Analysis of skeletal muscle - gastrocnemius. (A-B) Trichromic staining images and analysis in skeletal muscle at the indicated age and strain. Each dot represents an individual mouse. **(C)** Analysis of skeletal muscle collagen and fibrosis at the indicated age and mouse strain (n = 4). **(D)** Histopathological representative images of homoplasmic and heteroplasmic 80-weeks-old skeletal muscles. Arrows indicate central nuclei. Lines: mean ± SD. Differences are assessed by ANOVA analysis. **p-value* < 0.05, ****p-value* < 0.001.

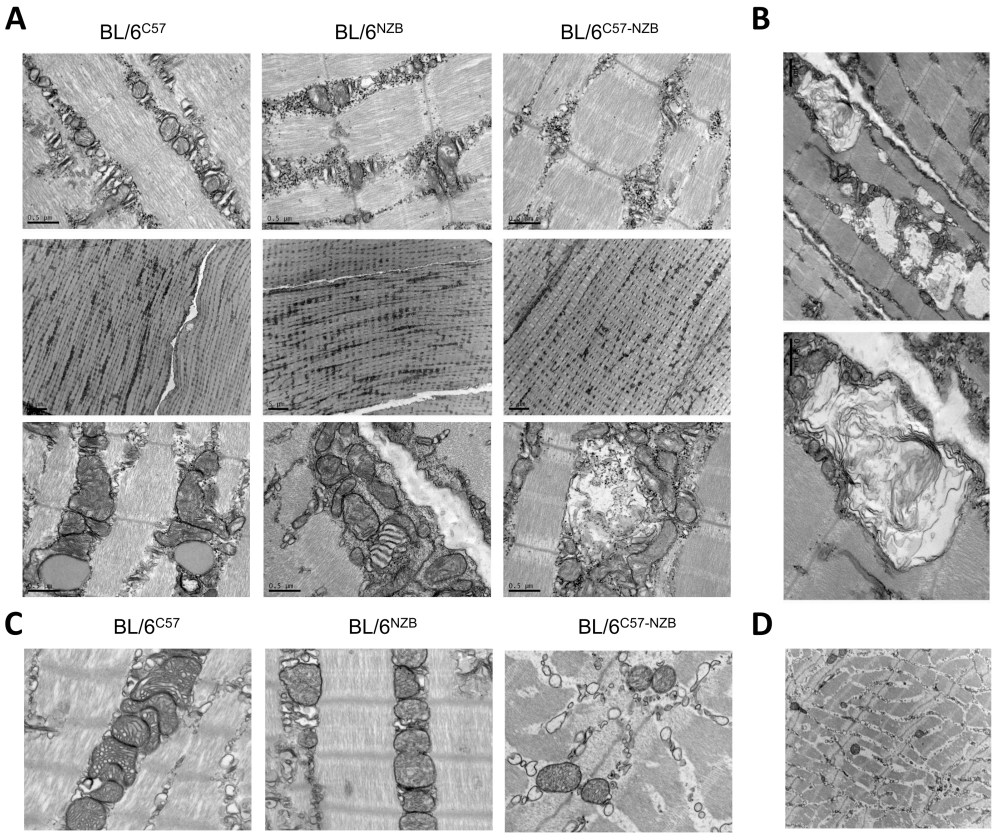

Figure 49. Ultrastructural analysis of skeletal muscle - gastrocnemius. (A-C) TEM representative analyses of 12-weeks-old mice BL/6^{C57}, BL/6^{NZB} and BL/6$^{C57\text{-}NZB}$. (A) TEM image showing panoramic view of the fibres in the skeletal muscles, the status of the myofilaments and mitochondria and lipid droplets associations. (B) Detail at different EM objectives of accumulation of membranes, phagosomes and mitochondrial swelling phenomena within muscle fibres. (C) Detail of IMF mitochondrial network in gastrocnemius muscle of the three strains. **(D)** Representative image of an aged heteroplasmic skeletal muscle (80-weeks-old mice) in which disrupted fibre and loss of mitochondria content can be noticed.

In agreement with the progressive loss of muscle mass with age, skeletal muscle PCr/ATP ratio was abnormally elevated in heteroplasmic animals at older age, 40-weeks-old (Figure 47E), suggesting a change in the mitochondrial bioenergetic efficiency. Indeed, the PCr/ATP ratio drastically dropped at 80-weeks-old (Figure 47E, F), specifically in heteroplasmic animals. Histological evaluation of 80-week-old skeletal muscles (gastrocnemius) of heteroplasmic mice showed abnormal levels of fibrosis (Figure 48A, B), an elevated proportion of central nuclei and strong evidence of muscle degeneration (Figure 48D). Evident changes in muscle ultrastructure were revealed by TEM (Figure 48C). Low mitochondria number and high amount of completely disrupted muscle fibres were observed in aged heteroplasmic mice (Figure 49 A-D). Also, we studied the mitochondrial ultrastructure, and intermitochondrial junctions (IMJ) were lost in BL/6$^{C57\text{-}NZB}$ and most of the mitochondria showed a decrease in the number of cristae as compared with the homoplasmic mice (Figure 48C). This was accompanied with a massive loss of muscle mass. Strikingly, sporadic cases of rear leg paralysis were observed only in old heteroplasmic individuals (6 out of 81 individuals).

V.2.D.5.b. Heteroplasmy induces structural and functional abnormalities in the eye

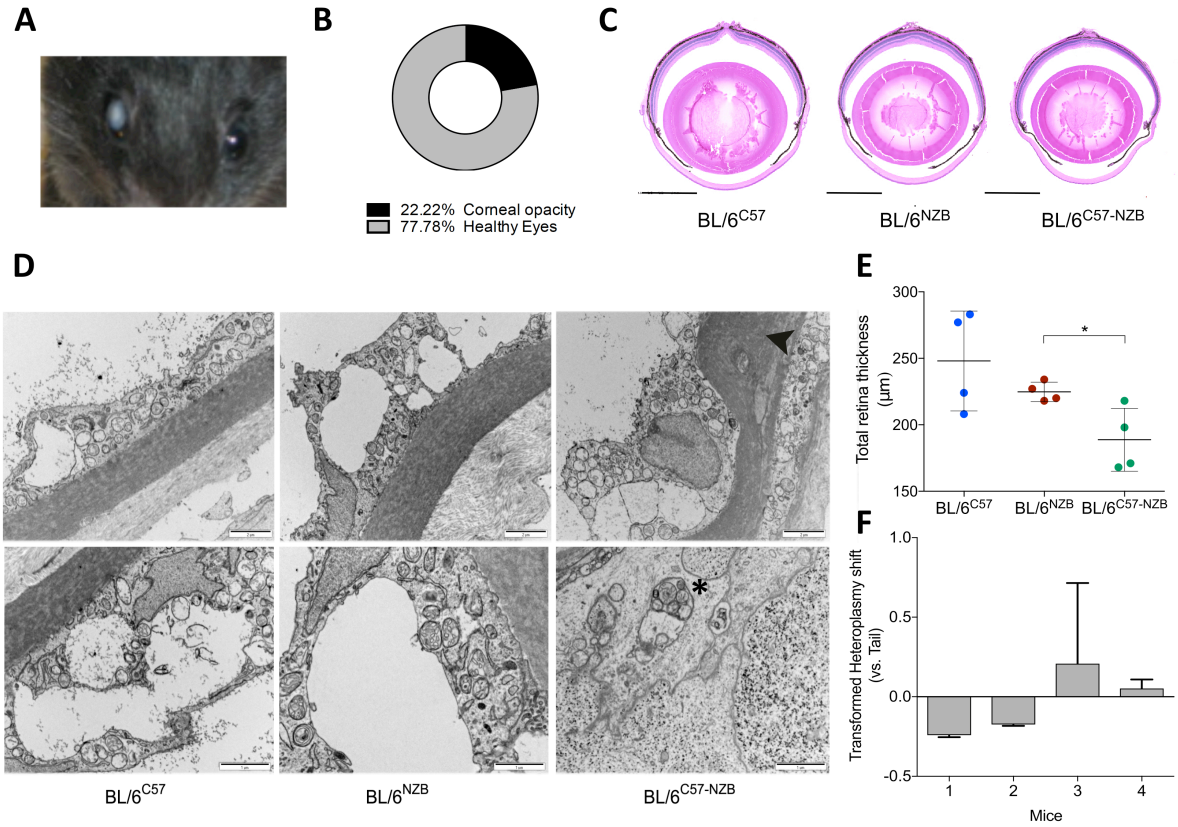

Figure 50. Functional and structural analyses of the eye in heteroplasmic mice. (A) Representative image of corneal opacity found in heteroplasmic animals**. (B)** Percentage of heteroplasmic mice presenting corneal dysfunction during their lifespan (n = 45 individuals) **(C)** Histological analysis of eyes from homoplasmic and heteroplasmic mice and quantification of the total retina thickness in the three strains. Scale bar: 1 mm; haematoxilin-eosin staining. **(D)** TEM analysis of corneal endothelial cells and Descemet's membrane. Arrowhead: thickening of the Descemet's membrane, an indicator of corneal impairment**.** Asterisk: phagosome with mitochondrial content inside in heteroplasmic corneal endothelium. **(E)** Measurement of the total retina thickness of heteroplasmic mice. **p-value* < 0.05 assessed by ANOVA test. In C-E, n = 4 12-weeks-old animals were used for the analyses. **(F)** Transformed heteroplasmy shift assessed by PCR and posterior RFLP with *BamHI* enzyme in cochlea of heteroplasmic mice (n = 4).

A higher incidence of eye problems in heteroplasmic animals was evident from the very beginning (Figure 50A, B). Systematic histopathological analysis of the eye at 12 weeks of age revealed structural abnormalities in the retina of heteroplasmic animals (Figure 50C). Retina have ten different layers formed by different cell types[275]. The thickness of the layers was measured in histological sections using haematoxylin and eosin (HE) staining. The studied layers were the ganglion cell layer, the inner plexiform layer, the inner nuclear layer (where bipolar cells where located, Müller and amacrine cells), the outer synaptic layer, photoreceptors (rods and cones) and the outer nuclear layer. In the case of the BL/6$^{C57\text{-}NZB}$ mice, the layers that contribute more to the decrease of the total retina thickness, are the ganglion cell layer (GCL) and the inner limiting membrane, formed by astrocytes and the end feet of Müller cells (Figure 50C, E). It was previously described that the retinal thickness decreases with age[276]. This is specifically associated with degeneration, the loss of photoreceptors and cells in the ganglion cell layer,[277] which are prone to disappear in comparison with the cones[278]. Contrary to retina, cornea was apparently normal by histopathology. However, EM analysis revealed that cornea ultrastructure was also impaired (Figure 50D). Different regions of the cornea were analysed and no significant differences were observed in the epithelium, the Bowman's membrane layer or the stroma. However, the structure and thickness of the Descemet's membrane (DM) is altered in heteroplasmic mice (Figure 50D, arrowhead). DM is a specialized basement membrane of the endothelium and its thickness increases with ageing, but also after endothelial damage[279]. The damage in the endothelium is the major cause of corneal opacity[280,281]. It was possible to observe in this region of the cornea from heteroplasmic mice the accumulation of mitochondria within phagosomes (black asterisk) suggesting stalled mitophagy (Figure 50D).

Common features of the tissues that cannot select for one mtDNA haplotype are a high mitochondrial content, highly structured cytoplasm and post-mitotic cells constitute them. These factors may require a more complex mtDNA turnover and segregation. To corroborate this statement, we decided to study mtDNA segregation in the most defined and organized structure of the mouse ear: the cochlea. The two cochleae of each mouse (taken from the left and right ears) were excised and analysed in the same way as the rest of the tissues for heteroplasmy content in the elderly animals. As it can be appreciated, the percentage of NZB mtDNA in the tissue is almost identical to that of the tail, confirming that there is no segregation in this tissue with the age (Figure 50F). All these evidences suggest that although there is a functional component behind the segregation of mtDNA, structural and compartmental limitations are added to it.

V.2.E. Elucidating a new mechanistic model: why heteroplasmy is harmful in tissues that do not resolve it?

To explain in which way heteroplasmy is harmful in tissues that cannot resolve it during the life of the mice, a high-throughput determination of the landscape of post-translational modifications (PTMs) was determined in liver (tissue that resolves heteroplasmy), heart and skeletal muscle (tissues that cannot segregate mtDNA) (Figure 51). The proteomic analysis was based in a new computational approach[197] from high-throughput mass spectrometry data (MS/MS). Tissues from 12-weeks-old males were collected.

No significant changes were found between homoplasmic strains at that age in any of the tissues analysed (Figure 51A). When we compared BL/6^{C57} with heteroplasmic mice, interestingly, a marked tissue-specific change in the PTMs landscape was revealed (Figure 51B). The most affected tissue was the heart, with a significant increase in oxidative PTMs affecting Tyr, Trp, Pro, Asn, Phe, His, Asp and Cys residues (Figure 51B). The peptide modifications were lower in heteroplasmic liver and skeletal muscle when compared to homoplasmic samples (Figure 51A, B). A detailed study of the PTMs landscape of skeletal muscle in 12-weeks-old heteroplasmic mice revealed lower amount of modifications in comparison

to the homoplasmic individuals, while at the same age, the heart showed a highly modified PTMs landscape. Heart impairment was earlier than skeletal muscle degeneration. This may reflect higher self-repairing capacity in skeletal muscle compared to cardiac tissue.

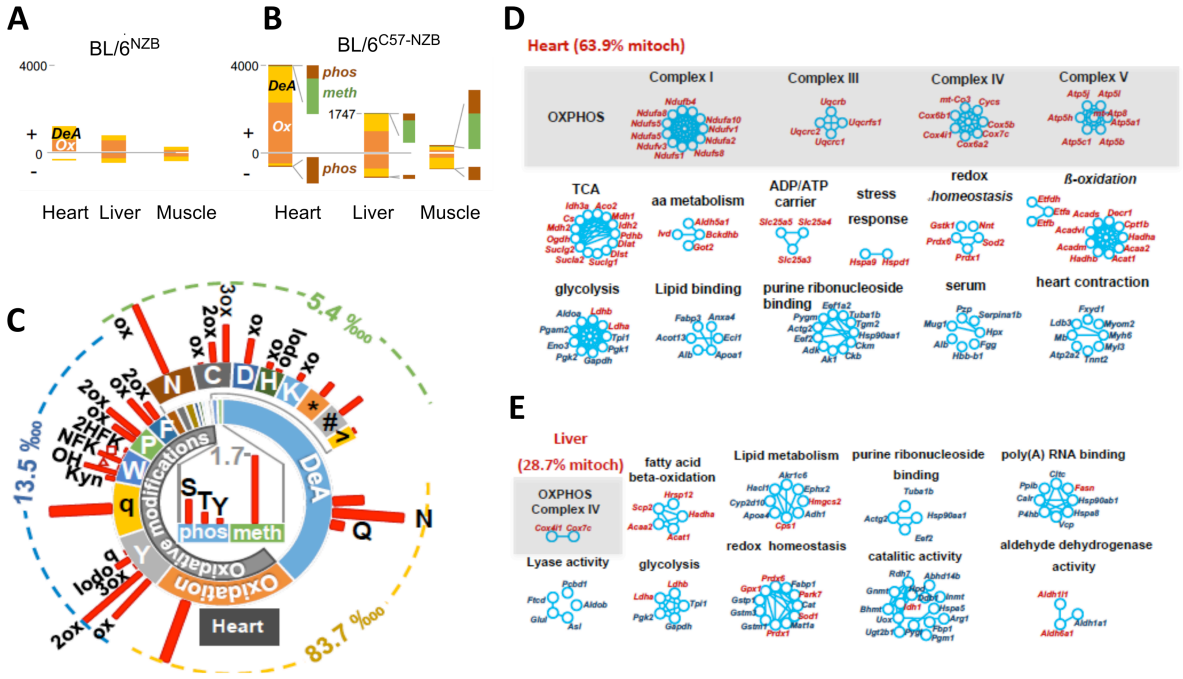

Figure 51. Alterations produced in the modified peptidome by heteroplasmy. **(A-B)** Number of peptides containing PTMs that were significantly increased (+) or decreased (-) in the indicated (A) BL/6^{NZB} (n = 3) or (B) BL/6$^{C57\text{-}NZB}$ (n = 4) mouse tissues in relation to BL/6^{C57} (n = 3). **(C)** Statistically significant PTMs increase in heteroplasmic mouse hearts according to the type of modification and the modified residue. The circular inner bars show the peptide proportion for each modification in the basal state, and the radial red bars represent the proportion of peptides of each type (in parts per 10,000) that are increased in heteroplasmic tissues. For the sake of clarity, 3 different scales are used depending on the type of modification. DeA, deamidation; meth, methylation; phos, phosphorylation; MC, missed cleavages; Chem, chemical derivatives produced by sample preparation; TMT, extra addition of the isobaric labelling reagent; Adducts, Na, K and ammonia adducts. Capital letters indicate the single letter amino acid code. Ox, oxidation; 2ox, dioxidation; 3ox, trioxidation; Kyn, Trp to kynurenine; OH, Trp to hydroxytryptophan; NFK, Trp to N-formyl kynurenine; 2HFK, Trp to 2-hydroxy formyl kynurenine; red triangle, Trp to oxolactone; red square, Trp to quinone; q, quinone, Tyr to quinone; Iodo, iodination; *, Met to homocysteic acid; #, Met to homoserine. **(D-E)** Proteins harbouring PTMs grouped by function in heart (D) or liver (E). Red colour indicates mitochondrial localization.

Oxidations in modified proteins were also revealed in several components of relevant metabolic pathways (TCA cycle, ß-oxidation, redox homeostasis, amino acid metabolism). ADP/ATP carrier, mitochondrial chaperones and antioxidant proteins were also highlighted. There were about 65% of mitochondrial proteins of the total affected by PTMs in the heart and less than 30% of them modified in the liver (Figure Figure 51D, E). This fact reinforces the mitochondiral functional impact of unresolved heteroplasmy. This is beautifully illustrated by one of the most ROS-sensitive enzymes in the cell, aconitase, which has a mitochondrial matrix isoform (ACO2) and a cytoplasmic isoform (ACO1). While ACO2 was severely modified in heteroplasmic with respect to control hearts, it was unaffected in liver (Figure 52A). On the other hand, ACO1 remain substantially unmodified in both tissues. Assessment of oxidative stress in fresh heart slices was performed using dihydroethidium (DHE) staining (Figure 52B, C). The analysis corroborated the *in vitro* increase in ROS production in heteroplasmic cells.

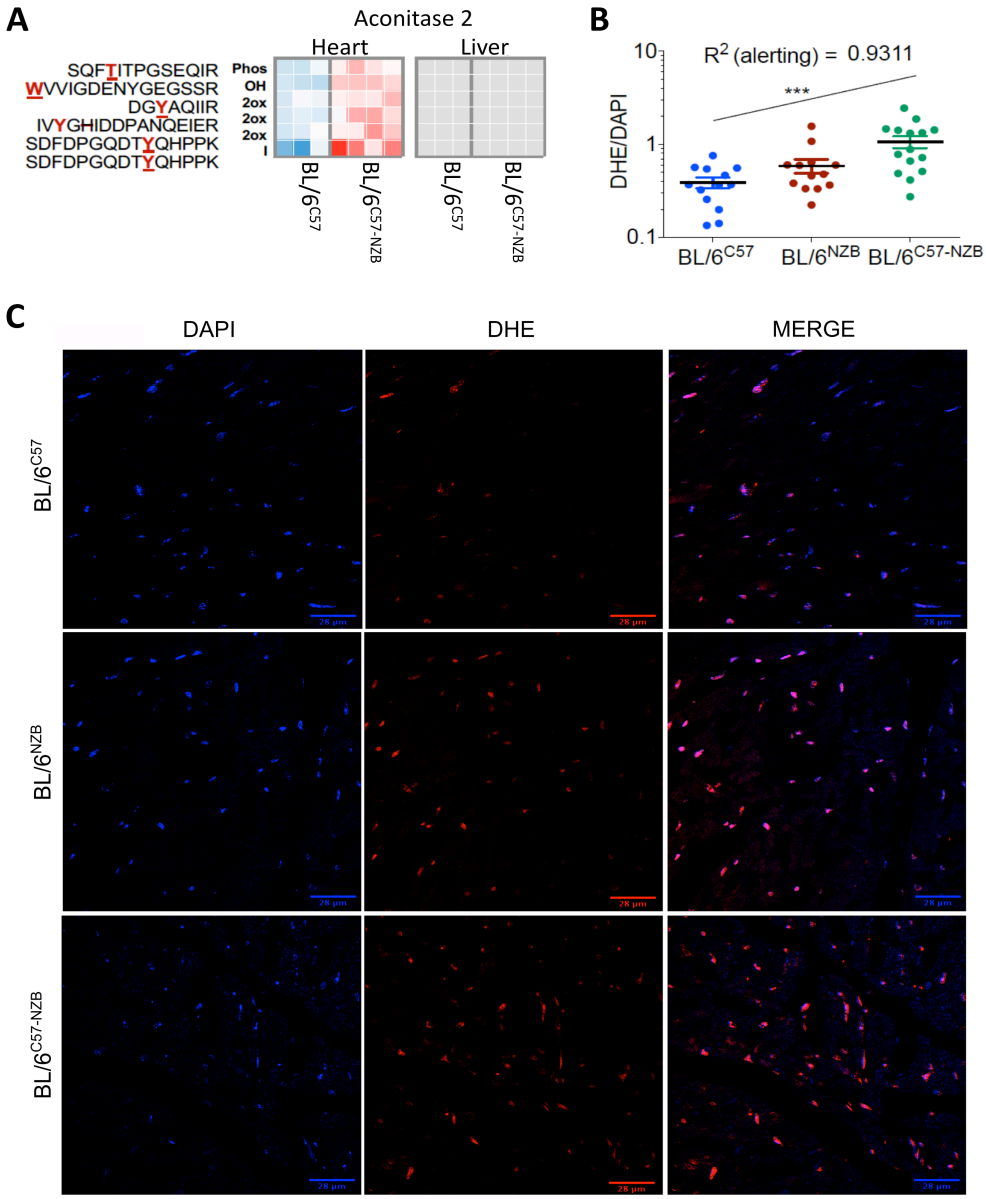

Figure 52. Heteroplasmy causes generalized oxidative damage in heart mitochondrial proteins. (A) ACO2 peptides containing the indicated PTMs and the quantitative changes observed between BL/6^{C57} and BL/6$^{C57\text{-}NZB}$ hearts or livers. **(B-C)** Estimation of ROS by DHE staining in fresh heart slices from 20-week-old animals of the indicated genotype.

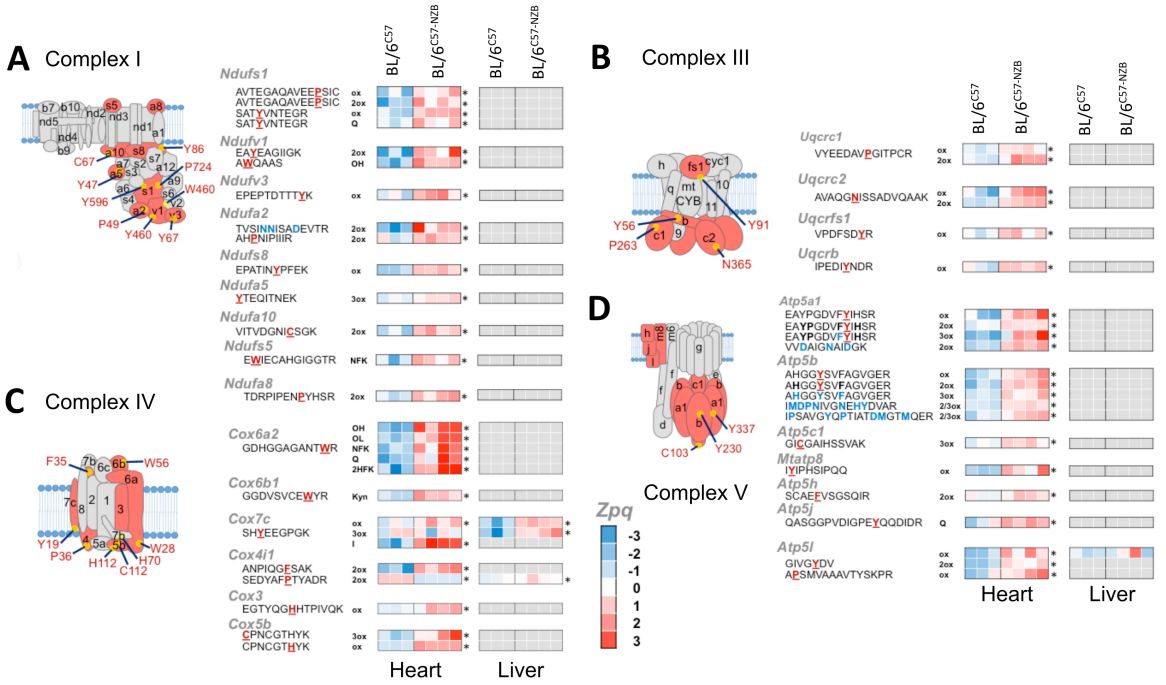

Figure 53.Post-translational modifications induced by heteroplasmy in OXPHOS proteins. (A-D) Scheme of heteroplasmy-induced PTMs in proteins of complex I, complex III, complex IV and complex V of the OXPHOS system. PTM-containing proteins are highlighted in red, with the spatial position of the modified residue indicated. The heat maps show statistically significant changes in abundance (*Zpq*) of the indicated peptides in heart and liver from control mice (BL/6^{C57}) and heteroplasmic mice (BL/6$^{C57\text{-}NZB}$). Gray squares indicate that the modified peptide was not detected in the sample. Modified residues that are unambiguously assigned are underlined bold red letters; tentatively assigned sites are in bold blue letters. Asterisks correspond to significant changes between control and heteroplasmic samples according to Student's t-test (*p-value < 0.05). The modification type is indicated in the column to the right of the peptide sequences. Ox: oxidation; 2ox: dioxidation; 3ox: trioxidation; Kyn, Trp to kynurenine; OH, Trp to hydroxytryptophan; NFK, Trp to N-formyl kynurenine; 2HFK, Trp to 2-hydroxy formyl kynurenine; OL, Trp to oxolactone; Q, Trp to quinone; I, iodination.

Among the non-mitochondrial proteins differentially affected by changes in PTMs in heart we found proteins involved in glycolysis, lipid binding and contraction (Figure 51D). We detected an increase in oxidative alterations in proteins of complexes I, III, IV and V in heteroplasmic hearts, which correlates with the reduction in the amount of protein, but that rise was not detected in liver (Figure 51D, 53A-D). ROS are able to target proteins located in mitochondrial matrix, OMM, IMM, intermembrane space or cytosol. However, most of the ROS produced by CI are released into mitochondrial matrix and those produced by CIII to the intermembrane space[35]. According to this, most of the modified peptides found in our analysis are located in the matrix side of the inner membrane, suggesting that CI-derived ROS are the major source of ROS in our model (Figure 53 A-D). We modelled the structure of mETC complexes and functional predicted modified amino acids were mapped onto them (Figure 54A-D). The obtained results revealed that the heteroplasmy condition may damage OXPHOS proteins and furthermore, the PTMs can compromise their enzimatic activity.

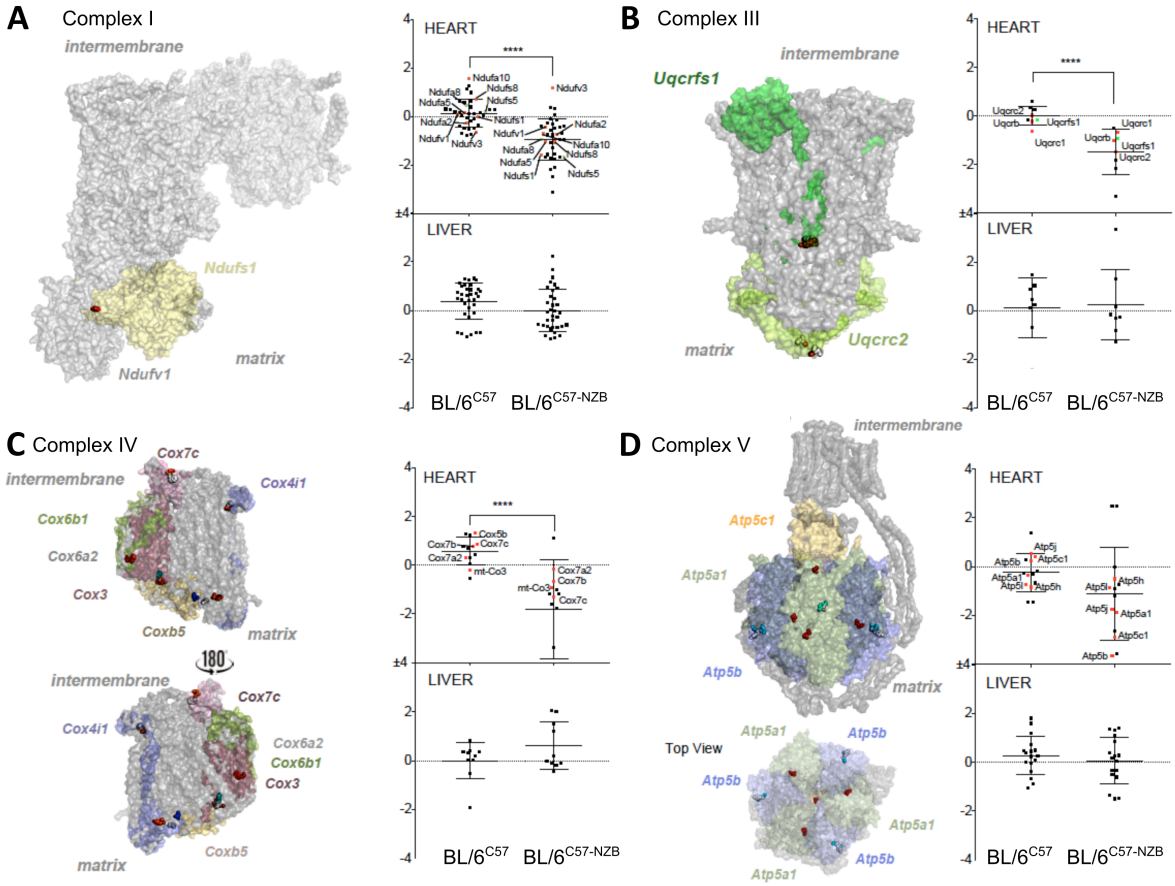

Figure 54. Predicted modified amino acids in complexes of the mtETC. (A-D) Protein peptides of the indicated complex highlighting altered PTMs in amino acids with predicted functional relevance (exposed residues with 9 or 8 conservation score, red colour) and structural residues (buried residues with 9 conservation score, blue colour). Those PTM residues close to a functional residue; orange colour, or a structural residue; cyan colour, are coloured in white. The Zq graphics show the overall amount of the proteins of the indicated complex between the two mice strains. Red dots: mtDNA encoded proteins.

V.2.F. Discussion

Since mtDNA heteroplasmy is heavily combated in nature in most of the eukaryotes (mtDNA bottlenecks, uniparental germline transmission, etc), there is a reasonable concern about the fact that the generation of mtDNA heteroplasmy could be harmful for the individual. Here, we show that young animals tolerate well the presence of more than one mtDNA haplotype within the same cytoplasm. However, during ageing, mtDNA heteroplasmy promotes malfunction of the heart and lung and skeletal muscle wasting, leading to premature ageing-like symptoms.

Based on our results, two mtDNAs with similar regulatory requirements are not noticed by the cell, but two mtDNAs with different regulatory requirements may generate a conflict is formulated. Because of this reason, most of the studied tissues can select one of the two confronted mtDNAs in the heteroplasmic mice and cells may sense the divergent responses between them. To solve the conflict, cells select the haplotype that better fits their OXPHOS requirements. What we found is that the features that depend only on the proportion of each mtDNA haplotype confronted are not associated with dysfunction, but the features that are associated with the heteroplasmic status are hallmarks of dysfunction. Tissues that cannot resolve heteroplasmy cannot optimize the homeostatic response and sub-optimal OXPHOS performance is established in the cells. This situation may lead to an increase in ROS generation. Furthermore, the

comprehensive analysis of the PTMs indicates that unresolved heteroplasmy triggers damaging oxidative stress. It is yet unclear why some tissues fail to remove heteroplasmy. Heart, skeletal muscle, bladder and eye are made of post-mitotic cells with a highly-structured cytoplasm and elevated mitochondrial content, factors that may make mtDNA segregation challenging.

The interaction between different mtDNAs within the same cytoplasm is a fascinating biological problem with evolutionary, physiological, pathological and ethical implications. It has come to the forefront of public awareness with the to debate about the use of mitochondrial replacement therapy in human oocytes to prevent transmission of mtDNA-linked diseases[173,212,282], and the proposal of treating infertility by injecting young donor oocyte cytoplasm to oocytes of sub-fertile women[283]. MtDNA segregation can be a potential and underexplored issue in new reproductive strategies. In addition, in the last two years, a new medical application likely to cause heteroplasmy is under investigation: the use of mitochondrial transfer *in vivo* between donor cells (mesenchymal) used as therapeutic vehicle and the cells in recipient tissues; or by the injection of mitochondria in the blood stream that is proposed that can colonize damaged cells in the body. Haplotype matching could be necessary to ameliorate any expected issues from mtDNA incompatibility. Beyond the overexposed relevance of fertility, we believe that the simple presence of two slightly different mtDNAs in the same cell might cause ageing phenotypes is particularly intriguing and suggests that the mild somatic mutations that are heavily propagated in our tissues might have a role in ageing.

V.3. Results III: Crosstalk between mtDNA and nDNA in health, ageing and disease

V.3.A. Elucidating the driving force of mitochondrial DNA segregation

V.3.A.1. Nuclear control of mitochondrial DNA segregation

The segregation of heteroplasmic mtDNA in mammalian was described in the late 1980s as a critical factor in the severity and progression of mitochondrial disorders caused by pathogenic mtDNA mutations. However, mtDNA segregation also occurs between non-pathological variants[154,155,163,165]. One of the unsolved but very relevant questions is the identification of the driving forces of segregation. In the present study, we investigate the mechanisms and principles that govern mtDNA segregation using heteroplasmic mouse models and by inducing genetic, pharmacological and nutritional interventions. Those interventions were evaluated in germline transmission, mitotic and post-mitotic segregation to study the segregation behaviour and their impact on the organismal physiology.

Previous works generated an open debate about the physiological impact of heteroplasmy between non-pathological mtDNA variants[162,165,284,285]. Most of these studies only investigated the individuals in the juvenile age and there is no information on the long-term impact of heteroplasmy. Here we studied the *in vivo* and *ex vivo* metabolic features during the whole life of the mice. In addition, most of the published studies did not ensure the homogeneity of the nuclear background. For example, some C57BL/6 mice sub-strains have a natural mutation that inactivates the gene *Nnt* (C57BL/6J mice) that codifies for the nicotinamide nucleotide transhydrogenase (NNT), a mitochondrial inner membrane protein that use the proton gradient to transform NADH into NADPH. Futhermore, all the C57BL/6 strains and at least one Balb/c substrain, are naturally mutants for the supercomplex assembly factor 1 (SCAF1[113]), responsible for the superassembly between complexes III and IV. The results that are presented in this work show that the presence or absence of functional NNT or SCAF1[113] proteins modulates the pathological phenotype of the heteroplasmy.

In the studies performed by Shoubridge *et al.* (1997), Balb/c mtDNA was confronted with NZB mtDNA in Balb/c nuclear background. The presence or absence of NNT and SCAF1[113] proteins in their nuclear background is still unknown[165]. Other groups used C57BL/6 background but the substrain was not well defined. The homoplasmic mice (BL/6^{C57} and BL/6^{NZB}) and the heteroplasmic mice used in this work (BL/6$^{C57\text{-}NZB}$) have C57BL/6 nuclear background mutant for SCAF1[113] and wild type for NNT.

V.3.A.2. Previous results

Segregation of mtDNA in heteroplasmic mice (C57BL/6 nDNA and C57-NZB mtDNA, called during this chapter control or wilt type heteroplasmic mice) was assessed in 18 different tissues during the whole lifespan of the mice[175]. Our results reproduced previous studies in which most of tissues progressively select for one of the alternative variants of mtDNA. However, heteroplasmy remains stable in few tissues[154,163,165,229] (Figure 55).

To further characterize the driving force for the selective mtDNA segregation, this analysis was also performed under experimental actions mimicking a variety of genetic and environmental conditions. The purpose of the interventions was to modify mitochondrial performance and to study its impact on the kinetics of segregation for each tissue. First, we investigated the ablation of PGC1α, a co-activator of nuclear receptors and a major regulator of mitochondrial biogenesis[286].

In the absence of PGC1α, the rate of segregation in brain and skeletal muscle was significantly modified: brain shifted its preference from NZB mtDNA to non-selection towards any mtDNA, while the non-selection of any mtDNA variant in skeletal muscle from control heteroplasmic mice shifted towards C57 mtDNA selection (Figure 55). Next, environmental changes were induced by treating mice pharmacologically with (a) N-Acetyl-L-Cysteine (NAC), an antioxidant and reductant; (b) dichloroacetate (DCA), an inhibitor of pyruvate dehydrogenase kinase (PDHK) (the inhibition of PDHK activates PDH and enhances the oxidization of pyruvate by mitochondria increasing OXPHOS activity[287,288]); and (c) hypercaloric diet with high fat content (HFD) to induce a severe metabolic alteration based on cellular adaptation to fuel use. We found that NAC induces an overall reduction in the segregation efficiency (Figure 55). DCA exacerbates the mtDNA segregation rates and, in case of gut, selected the preferred mtDNA variant (C57 instead of NZB mtDNA) (Figure 55). Finally, HFD promotes a striking alteration in the segregation rate and direction of mtDNA variants in gut (Figure 55).

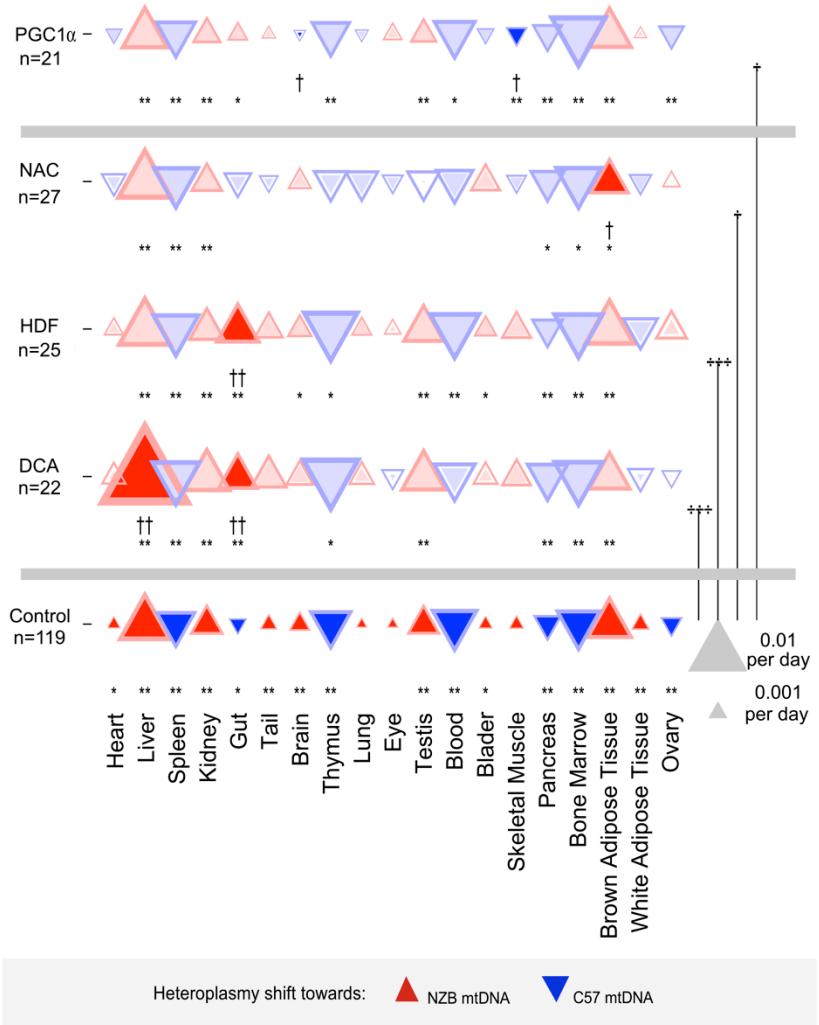

Figure 55. Post-natal mtDNA segregation can be amplified or suppressed by modulation of organismal metabolism. Summary matrix of tissue-specific segregation patterns in basal conditions. Triangles denote magnitude and direction of inferred segregation (upwards for increasing heteroplasmy). Control row shows segregation inferred with no experimental intervention. Experimental rows show the inferred segregation resulting from chemical and genetic perturbations. Sidebars denote levels of statistical support for a model where perturbations affect the overall pattern of segregation (LRT; ****p-value* < 0.001; **p-value* < 0.05; *ns* not significant). Individual tissues where significant differences from control behaviour are observed are highlighted and significance level of that difference reported (bootstrap percentile method; †† p < 0.01, † p < 0.05). In all cases asterisks mark significant differences from zero segregation (bootstrap percentile method with Bonferroni correction; ***p-value* < 0.01, **p-value* < 0.05).

V.3.A.3. Somatic mtDNA segregation and mitochondrial dynamics, redox balance and OXPHOS function.

V.3.A.3.a. Effects of mitochondrial dynamics

One of the main features of mitochondria is that they are dynamic organelles that can divide and remodel their membrane by fission-fusion processes constantly. The equilibrium between these two processes can be modified according to different stress conditions (i.e. environmental changes, hypoxia, metabolic remodelling). Mitochondrial fusion has been considered a pro-survival mechanism but fission has the opposite role in cell physiology[289]. Fission is related to autophagy and removal of dysfunctional mitochondria via mitophagy[290]. Mitochondrial dynamics is in the focus of most of the studies involving mtDNA segregation. Tissue-specific response to mtDNA segregation in heteroplasmic mice with mutated protein dynamin-related protein 1 (DRP1) involved in mitochondrial fission has been reported[160]. Other fusion proteins (MFN1, MFN2 and OPA1) may play a crucial role in mtDNA nucleoids segregation[290].

To evaluate whether or not the mechanism of fragmentation and removal of damaged mitochondria (and its role during mitochondrial stress conditions) is related to mtDNA segregation and how they interfere with the *in vivo* heteroplasmic phenotype, we generated the heteroplasmic mice with the ablation of OMA1. OMA1 is a stress-induced zinc metalloproteinase that in combination with YME1L cleaves OPA1 in different isoforms triggering mitochondrial fragmentation[14,243,291,292]. Cristae shape and mitochondrial function are connected; OPA1 regulates the morphology of the cristae improving OXPHOS performance by stabilization of respiratory supercomplexes[13]. Thus, the processing of OPA1 by OMA1 protease has important implications in the adaptive response to metabolic stress. It was published before that deletion of OMA1 implies a preservation of the inner mitochondrial membrane cristae shape improving mitochondrial performance under stress and protecting cardiomyocytes and neurons against apoptosis[293,294,295].

V.3.A.3.b. Effects of optimization of cellular metabolism

To form functional respiratory complexes, the different subunits of the complexes need to be assembled properly. At the same time, complexes can super-assemble into supercomplexes, quaternary structures that allow mitochondria to reach an optimum performance based on a dynamic supramolecular organization[85,104,296]. The dynamism of the supercomplexes assembly determines electron flux from different substrates. In 2013, our group discovered one of the factors that modulates the reorganization of these quaternary structures and that consolidates the basis of the mtETC plasticity model: the supercomplex assembly factor 1 (SCAF1, also named COX7A2L)[297]. SCAF1^{113} is required for the superassembly of mitochondrial respiratory complexes III and IV[142]. Instead the wild type version of 113 amino acids (SCAF1^{113}) C57BL/6 mice harbour a microdeletion that eliminates two amino acids of the complete sequence, rendering the protein non-functional (SCAF1^{111}). As a consequence, C57BL/6 mice cannot superassemble complex III and IV. Despite of it, the animals are healthy and fertile, but they lose the versatility in the proper adaptation of OXPHOS to environmental changes[297].

V.3.A.3.c. Effects of ROS detoxification in heteroplasmy

Respiratory supercomplex dynamics can be regulated by redox reactions, which modify specific cysteine-thiol groups in the subunits of the complexes[32]. The mtETC generates ROS that act as specific second messengers modifying residues in proteins involved in redox signalling (i.e. thiol-modifications)[298]. The *Nnt* gene encodes an integral protein (NNT, nicotinamide nucleotide transhydrogenase) located in the inner mitochondrial membrane. Its enzymatic activity promotes the transfer of hydride shuttling between NADH and NADPH taking advantage of the proton motive

force across the mitochondrial inner membrane. The transhydrogenation reaction is coupled to respiration and ATP hydrolysis processes. NNT is required to maintain cellular homeostasis and ROS regulation and detoxification[299,300].

We described a novel stage of strong mtDNA segregation around the pre-implantation stage in embryo development and the segregation at this stage was completely abolished if NAC was provided to the BL/6$^{C57-NZB}$ pregnant mice in their drinking water[175]. Our study also showed that the physiological changes that differentiate NZB from C57 mtDNA conplastic animals rely on the higher basal ROS production by NZB mtDNA[16]. Many of those differences are abolished in NNT^{KO} conplastic mice[301].

V.3.A.4. Generation of new heteroplasmic animal models

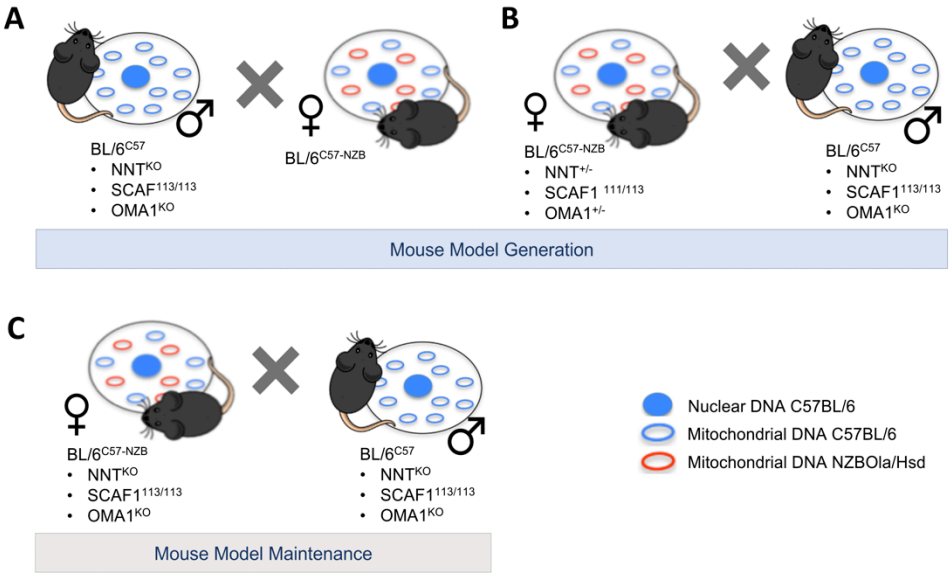

Figure 56. Nuclear genetic modifications in heteroplasmic mice. (A-B) General diagram of the strains generation and **(C)** maintenance. Strain nomenclature: control or wild type heteroplasmic mice (BL/6$^{C57-NZB}$); OMA1 knockout heteroplasmic mouse model (BL/6$^{C57-NZB}$ OMA1^{KO}); heteroplasmic mouse model with NNT mutated gene (BL/6$^{C57-NZB}$ NNT^{KO}) and heteroplasmic mice with SCAF1 functional isoform (BL/6$^{C57-NZB}$ SCAF1^{113}).

To evaluate if the mechanisms of (a) fragmentation and removal of damaged mitochondria, under stress; (b) the relevance of ROS signalling/detoxification; or (c) the role of the superassembly of the respiratory complexes in the mtDNA segregation and in the *in vivo* heteroplasmic phenotype, three novel heteroplasmic mouse models were generated: (1) mice without OMA1 (OMA1^{KO}), (2) mice without NNT (NNT^{KO}) or (3) mice harbouring the wild type form of SCAF1 (SCAF1^{113}).

We generated OMA1^{KO} and NNT^{KO} heteroplasmic mice backcrossing heteroplasmic females with OMA1^{KO} or NNT^{KO} males (Figure 56A, B). OMA1 metalloprotease regulates cristae remodelling and mitochondrial function upon severe stress, but is not essential under normal circumstances[302]. C57BL/6JOlaHsd original strain is wild type for NNT. The *Nnt* gene suffered a spontaneous mutation in the C57BL/6J strain provided directly by Jackson Laboratories[303]. Heteroplasmic females with the C57BL/6JOlaHsd nuclear background were backcrossed with males with C57BL/6J nuclear background in order to generate NNT^{KO} heteroplasmic mice (Figure 56). Then, the genetic ablations of *Oma1* and *Nnt* were confirmed by different approaches (See Material and Methods).

Thus, heteroplasmic mouse strain with SCAF1^{113} was generated to re-evaluate if the recovery/loss of structural plasticity of the OXPHOS system has any impact on the mtDNA selection and segregation rate, or on the heteroplasmic mice physiology. The B6J.129S2-Cox7a2l (BL/6^{C57} SCAF1^{113}) strain was

produced by crossing purebred female C57BL/6JOlaHsd mice containing the sort allele of COX7A2L ($SCAF1^{111}$) with purebred male 129S2/ SvPasCrlf containing the long allele of COX7A2L ($SCAF1^{113}$) both in homozygosis. The resulting heterozygous offspring was backcrossed until the F15 to obtain purebred C57BL/6JOlaHsd background mice containing the long form of COX7A2L in homozygous. Males $BL/6^{C57}$ $SCAF1^{113}$ were crossed with heteroplasmic females ($BL/6^{C57\text{-}NZB}$ $SCAF1^{113}$) to maintain the breeding colony of these mice (Figure 56).

V.3.A.5. MtDNA haplotype preference in germline and embryo development

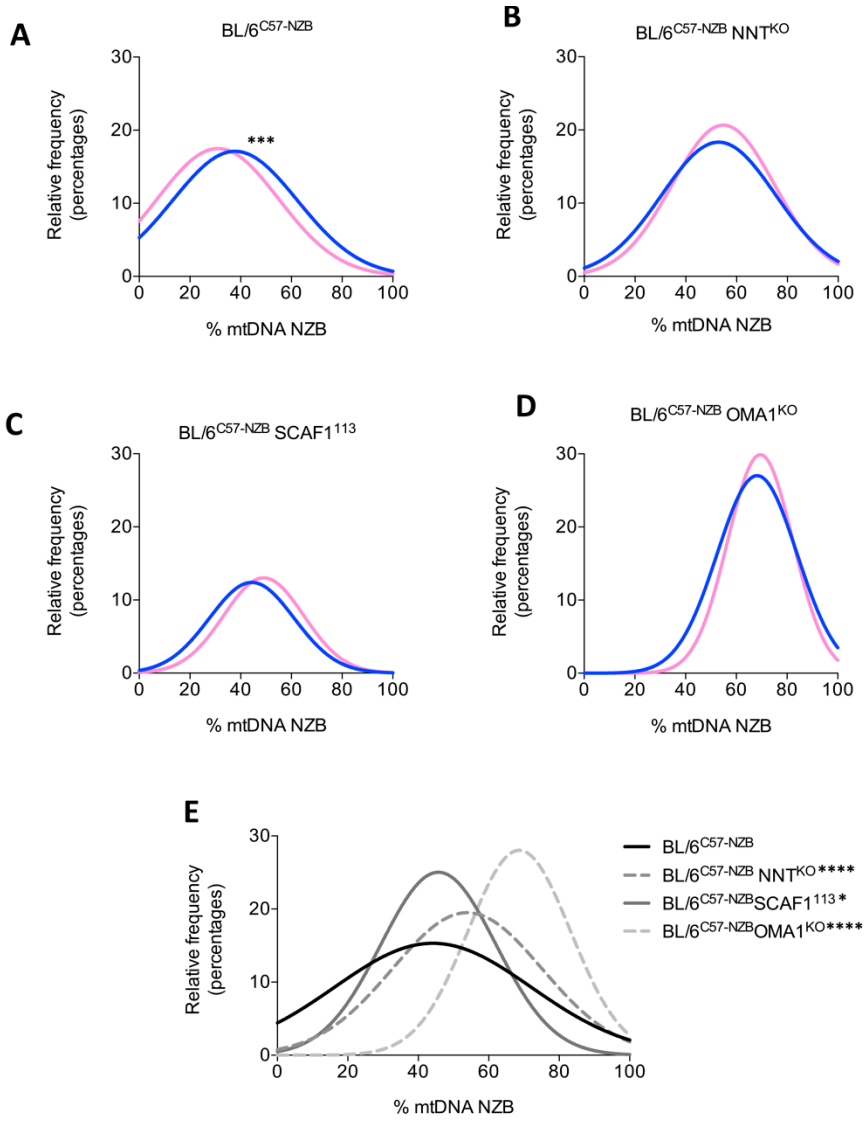

Figure 57. Heteroplasmy is sensed and mtDNA segregated prenatally. (A-D) Distribution profiles in the heteroplasmy of the offspring (males and females) for the different strains. In (A), distribution profiles for both sexes are not normal (skewness 0.135 and 0.476. and kurtosis -0.7114 and -0.5474 for males and females, respectively). In **(B-D)** KS normality test was not significant for the different distribution profiles. **(E)** Distribution profiles between different heteroplasmic nuclear backgrounds. The different strain profiles were compared to the wild type heteroplasmic mice. KS test, **p-value* < 0.05, *****p-value* < 0.0001.

First, we evaluated how the nuclear modifications impact on the mother-to-pup transmission of heteroplasmy. For that, tail heteroplasmy levels of different strains were measured once the pups were weaned. Heteroplasmy germline transmission in the heteroplasmic control mice ($BL/6^{C57\text{-}NZB}$), was biased

towards C57 mtDNA, with a proportion close to homoplasmic pups of C57:NZB 45:1 (Figure 57A). The ablation of NNT eliminated the preference towards C57 mtDNA (Figure 57B) allowing the birth of homoplasmic NZB animals. This tendency in favour of NZB mtDNA was exacerbated in OMA1^{KO} animals (Figure 57D) while the SCAF1^{113} pups showed no preference for any of the haplotypes (Figure 57C).

D'Agostino & Pearson omnibus normality test was employed to assess the normality of the distribution of heteroplasmy levels among the litters. Only BL/6$^{C57\text{-}NZB}$ OMA1^{KO} and BL/6$^{C57\text{-}NZB}$ SCAF1^{113} mice presented normal distribution of the values (BL/6$^{C57\text{-}NZB}$ and BL/6$^{C57\text{-}NZB}$ NNT^{KO} showed *****p-value* < 0.0001) (Figure 57). Gaussian distribution was not observed in control heteroplasmic mice and the first results indicated that nuclear modifications alter the distribution of heteroplasmy in the offspring (Figure 57A-D). Different distribution profile between females and males was only revealed in control heteroplasmic mice (Kolmogorov-Smirnov, KS test, *p-value* <0.0001) (Figure 57A). Comparison between each genotype with the control heteroplasmic group with KS test showed differences between the BL/6$^{C57\text{-}NZB}$ strain and the three different nuclear backgrounds: BL/6$^{C57\text{-}NZB}$ NNT^{KO} mice and BL/6$^{C57\text{-}NZB}$ OMA1^{KO} (KS test, *****p-value* <0.0001) and BL/6$^{C57\text{-}NZB}$ SCAF1^{113} (KS test, **p-value* < 0.05) (Figure 57E).

As for the heteroplasmic control mice (BL/6$^{C57\text{-}NZB}$), 18 different tissues were analysed during the whole life of the individuals. Liver, lung, kidney, ovary, testes, heart (left ventricle), brain (cerebral cortex), skeletal muscle (gastrocnemius muscle), bladder, gut (duodenum), thymus, eye, pancreas, spleen, bone marrow, blood, brown adipose tissue and white adipose tissue (gonadal adipose tissue) were excised from mice and genotyped for mtDNA variants. We assessed the percentage of heteroplasmy and used a mathematical model used to understand and predict stochastically the evolution of mtDNA populations in the heteroplasmic strains.

Changes in heteroplasmy (h) of each tissue during the whole lifespan were reported with respect to a reference value (h_0). This reference value is the reference tissue, which has neutral segregation. The reference tissue was obtained after analysing more than 20 animals with more than six months of age. The heteroplasmy of each tissue was correlated to the tail heteroplasmy when the animal was weaned (3-4 weeks of age) and the tissue with a correlation coefficient closest to 1 was chosen. Eye was inferred to be the slowest segregating tissue, and thus the closest to the initial heteroplasmy.

Transformed heteroplasmy was obtained from the model $\Delta h = \beta t = \log((h(h_0\text{-}1))/(h_0(h\text{-}1)))$, as described in Johnston and Jones (2016)[208]. This mathematical model has been previously supported by experimental results[208]. Tissues were clustered in three groups (NZB mtDNA selection, no mtDNA selection and C57 mtDNA selection) depending on the significance of the slope obtained from the analysis (plotting delta h against time and performing a linear regression).

V.3.A.6. Post-natal analysis of selective mtDNA segregation in tissues

V.3.A.6.a. Effects of NNT mutation in post-natal mtDNA segregation

BL/6$^{C57\text{-}NZB}$ NNT^{KO} mice differed in segregation rate of some tissues and important changes in the direction of mtDNA variant selection were reported compared to the original control heteroplasmic mice (Figure 58). In this case, tissues such as skeletal muscle or bladder segregated towards NZB mtDNA. Other tissues like the WAT, thymus and spleen decreased notably their rate of segregation towards C57 mtDNA. Overall in most proliferative tissues the lack of NNT protein promoted a decrease in rate of segregation. This is the case of bone marrow, thymus and spleen. Due to the impact on the health of the animals, it is particularly interesting that the lack of NNT induced segregation in skeletal muscle (Figure 58).

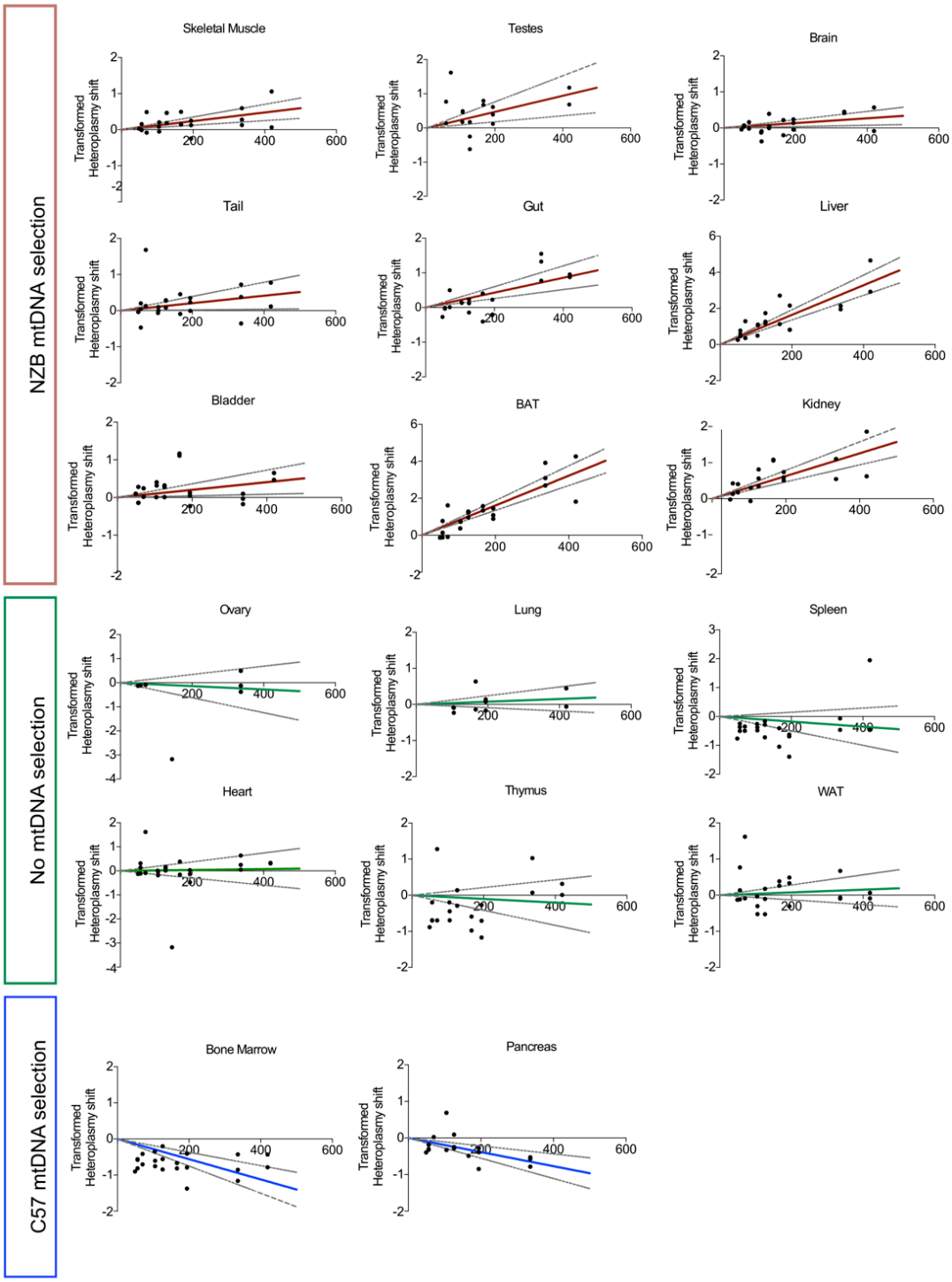

Figure 58. MtDNA segregation in BL/6$^{C57\text{-}NZB}$ NNT^{KO} mice. X-axis: age (days); Y-axis: transformed heteroplasmy shift (calculated *vs.* eye). Black dots are experimental data of single mice across their lifespan (X-axis). Red, green and blue lines correspond to the mean and grey lines show 95% confidence intervals of inferred segregation trajectories. Positive values indicate a relative increase of the NZB mtDNA and negative values a relative increase of the C57 mtDNA. Lines in green show no significant segregation.

V.3.A.6.b. Effects of SC reorganization in post-natal mtDNA segregation

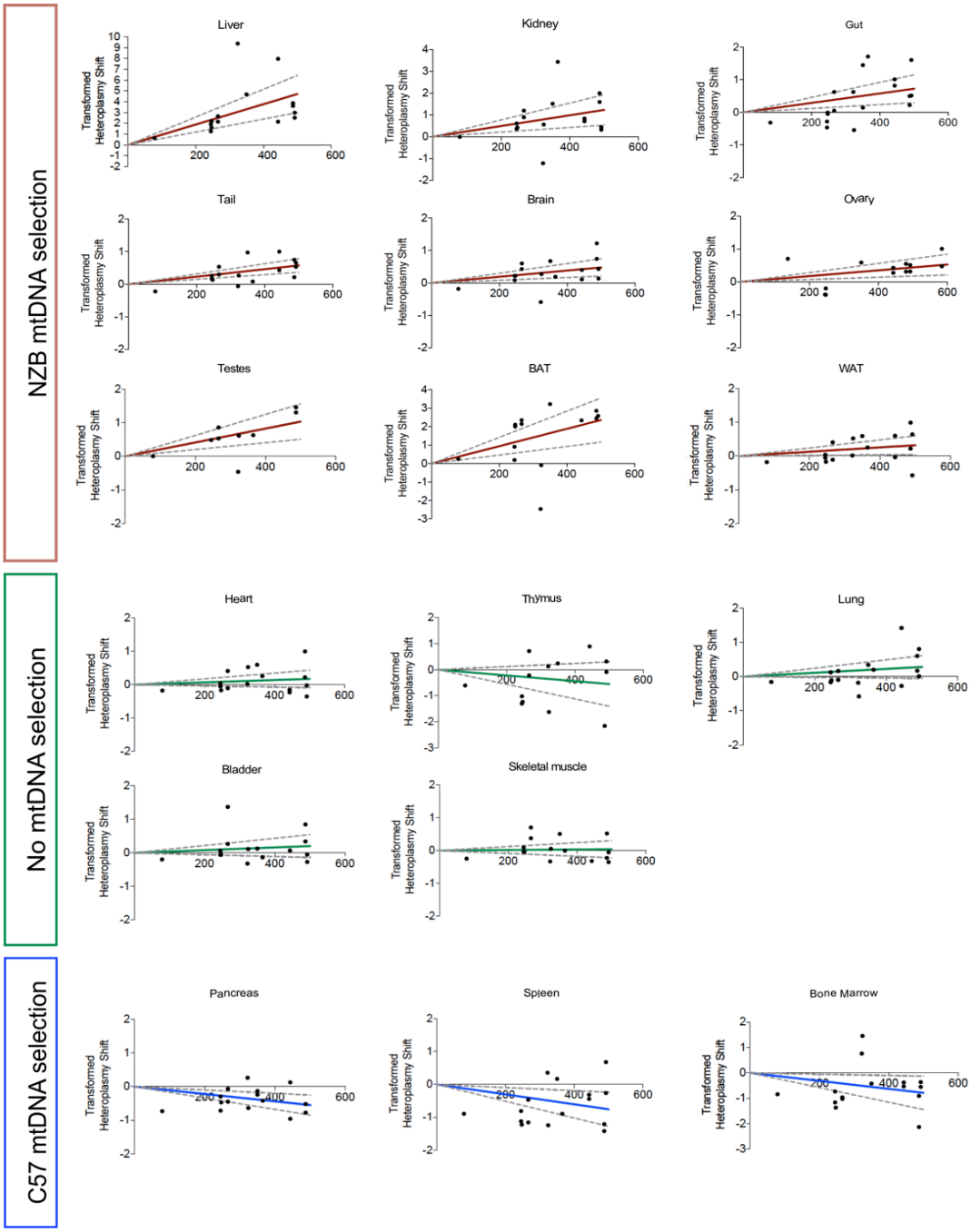

Figure 59. MtDNA segregation in BL/6$^{C57\text{-}NZB}$ SCAF1^{113} mice. X-axis: age (days); Y-axis: Transformed heteroplasmy shift (calculated *vs.* eye). Black dots are experimental data of single mice across their lifespan (x-axis). Red, green and blue lines correspond to the mean and grey lines show 95% confidence intervals of inferred segregation trajectories. Positive values indicate relative increase of the NZB mtDNA and negative values the relative increase of the C57 mtDNA. Lines in green show no significant segregation.

As in the previous case, heteroplasmic animals expressing SCAF1^{113} had a notably impact on the mtDNA segregation behaviour. Heart, skeletal muscle, bladder and ovary could not select for one of the mtDNA haplotypes, as it was the case in the control heteroplasmic mice. However, it was found that thymus that strongly segregates towards C57 mtDNA in control heteroplasmic mice, could not resolve heteroplasmy in this situation. Others tissues like bone marrow or spleen, showed a decrease in their

segregation rate (Figure 59). Some of the tissues that were unable to resolve heteroplasmy (i.e. ovary, tail and gut) selected NZB mtDNA in the presence of SCAF1^{113} (Figure 59).

V.3.A.6.c. OMA1 does not have significant impact on the mtDNA segregation behaviour

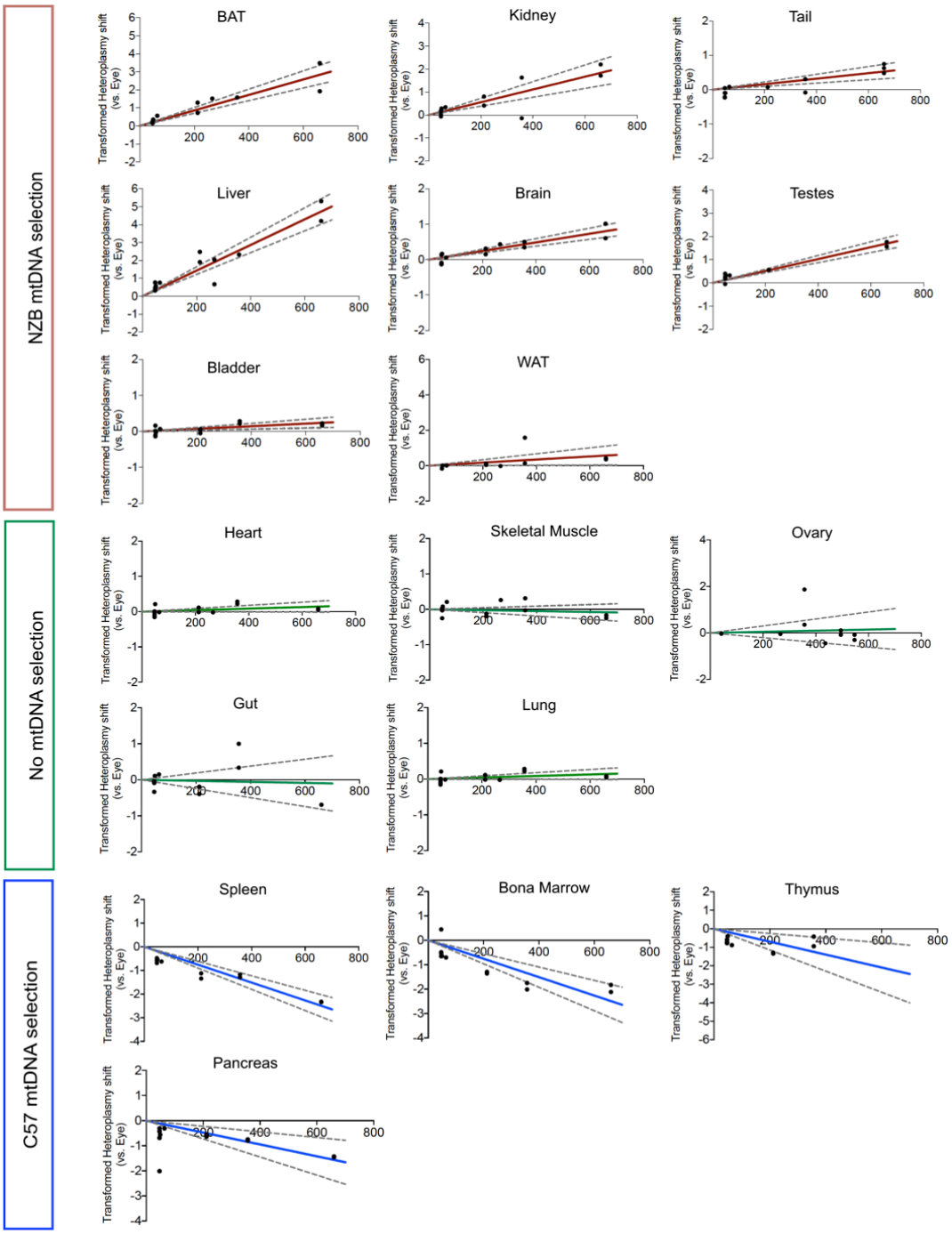

Figure 60. MtDNA segregation in BL/6$^{C57\text{-}NZB}$ OMA1^{KO} mice. X-axis: age (days); Y-axis: transformed heteroplasmy shift (calculated *vs.* eye). Black dots are experimental data of single mice across their lifespan (X-axis). Red, green and blue lines correspond to the mean and grey lines show 95% confidence intervals of inferred segregation trajectories. Positive values indicate relative increase of the NZB mtDNA and negative values the relative increase of the C57 mtDNA. Lines in green show no significant segregation.

In summary, no significant changes occured in post-natal mtDNA segregation in BL/6$^{C57\text{-}NZB}$OMA1^{KO} with respect to the control heteroplasmic animals (Figure 60). In case of BL/6$^{C57\text{-}NZB}$ SCAF1^{113} and

BL/6$^{C57\text{-}NZB}$ NNT^{KO}, most of the tissues tended towards NZB mtDNA haplotype. Those tissues that selected mtDNA C57 had a decreased rate of segregation in comparison to the heteroplasmic control mice. Thus, the optimization of the energy production and the redox balance play a fundamental role in the communication between nucleus and mitochondria.

V.3.A.7. Phenotypic and metabolic consequences of nuclear gene modifications

V.3.A.7.a. Assessment of metabolic performance and mitochondrial characterization in mouse adult fibroblasts

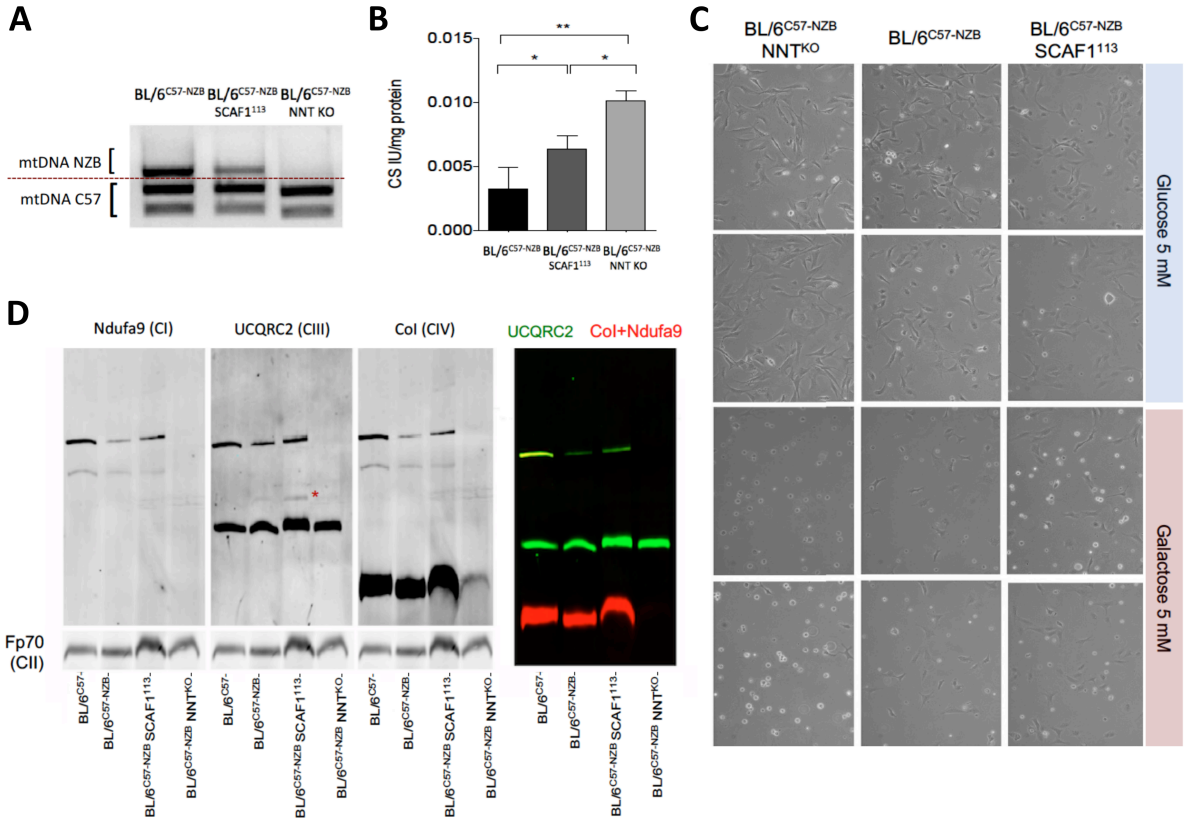

Figure 61. Characterization of heteroplasmic MAFs with nuclear genes modifications. **(A)** Analysis of heteroplasmy in MAFs (PCR and RFLP). The analysis was done in the fifth passage after MAFs immortalization (25 mM glucose as a carbon source). Initial cell culture heteroplasmy: BL/6$^{C57\text{-}NZB}$, 56%; BL/6$^{C57\text{-}NZB}$ SCAF1^{113}, 40.2%; BL/6$^{C57\text{-}NZB}$ NNT^{KO}, 67% NZB mtDNA. **(B)** Mitochondrial content assessed by citrate synthase activity in total protein MAFs homogenates. *p-value < 0.05, **p-value < 0.01, ANOVA test. **(C)** Representative images of the different MAF cell lines in culture with different substrates as carbon sources (5 mM glucose and 5 mM galactose). **(D)** BNE analysis of the unmodified and modified heteroplasmic MAFs. MAFs were cultured in complete medium with 25 mM glucose. The antibodies used for immunodetection were NDUFA9 (CI), UQCRC2 (CIII), COI (CIV) and FP70 (CII). Three different clones of each cell line were used for the experimental evaluation.

Mouse adult fibroblasts (MAFs) were generated from the different heteroplasmic strains to evaluate mitochondrial performance. Control heteroplasmic MEFs under normal culture media conditions (25 mM glucose) did not show mtDNA segregation along the passages[175]. In the case of MAFs, it was also found that the percentage of heteroplasmy did not change until the fifteenth passage in the same concentration of glucose. BL/6$^{C57\text{-}NZB}$ SCAF1^{113} MAFs did not modify the behaviour of control heteroplasmic MAFs. However, NNT^{KO} heteroplasmic MAFs lose almost 100% NZB mtDNA variant in the fifth passage after immortalization (Figure 61A).

All the experiments were performed between passage 10 and passage 12 and the level of heteroplasmy was similar to the results reported in the fifth passage (Figure 61A) for all the used clones. First, we checked the mitochondrial mass per total protein in the cell lines. There were significant variations in the mitochondrial content among them. Thus, $SCAF1^{113}$ and NNT^{KO} cells contained more mitochondria than original heteroplasmic MAFs, being NNT^{KO} the cell line that had the highest mitochondrial mass (Figure 61B). Interestingly, all the heteroplasmic MAFs presented difficulties to grow in galactose as carbon source (Figure 61C). Only the MAFs that harbour the functional isoform of SCAF1 protein ($BL/6^{C57\text{-}NZB}$ $SCAF1^{113}$) could survive more than 24 hours in 5 mM galactose. The better performance in galactose of the heteroplasmic $SCAF1^{113}$ compared with the control heteroplasmic MAFs prompted us to investigate the status of the electron transport chain. BNE analysis revealed that control heteroplasmic MAFs ($BL/6^{C57\text{-}NZB}$) assembled less CI and presented higher ratio between CI free and $CI+CIII_2$ than that of homoplasmic C57 (Figure 61D). Both parameters were improved in heteroplasmic $SCAF1^{113}$ cells, in which the majority of CI was associated with $CIII_2$, and worsened in NNT^{KO} heteroplasmic cell line that revealed a striking reduction in overall CI and CIV (Figure 61D). Notably the total amount of free $CIII_2$ was similar in NNT^{KO} heteroplasmic cells to the other heteroplasmic and homoplasmic cell lines (Figure 61D). As expected, the supercomplex $CIII_2$+CIV was only observed in the cells that expressed the protein $SCAF1^{113}$ ($BL/6^{C57\text{-}NZB}$ $SCAF1^{113}$)[142](Figure 61D, asterisk), but no respirasome was observed in any of the heteroplasmic cells.

Next, it was evaluated the respiration performance in the MAF cell lines by SeaHorse™ assay under normal cell culture conditions (25 mM glucose) (Figure 62A). Control heteroplasmic MAFs ($BL/6^{C57\text{-}NZB}$) had less basal and maximal OCR when compared with the genetically modified $SCAF1^{113}$ heteroplasmic cell lines. Due to the limitation in heteroplasmic cell growth in galactose, only the comparison between the supercomplex organization in $BL/6^{C57\text{-}NZB}$ $SCAF1^{113}$ and the homoplasmic MAFs was possible (Figure 62B, C). With galactose as substrate, a substantial increase in the supercomplex $CIII_2$+CIV and the appearance of $CI+CIII_2$+CIV, the respirasome, was observed only in heteroplasmic $SCAF1^{113}$ cells (Figure 62C). A significant increase in the CIII proportion associated with CI ($CI+CIII_2$) in homoplasmic MAFs was also induced by galactose (Figure 62C). Seahorse assays were performed with galactose as substrate and we found that the respiratory capacity of the mitochondria in heteroplasmic MAFs with $SCAF1^{113}$ was similar to the homoplasmic MAFs with mtDNA NZB (Figure 62B). The profile of control heteroplasmic MAFs was the typical observed in apoptotic cells, unable to survive with galactose as a carbon source (Figure 62B). Despite the differences in mtETC reorganization, the ROS production (measured as H_2O_2 levels) was similar between control heteroplasmic MAFs and the heteroplasmic mice expressing $SCAF1^{113}$ (Figure 62D).

To confirm the differences in mitochondrial content and to have additional information about the mitochondrial dynamic status of the different heteroplasmic MAF models, we performed immunofluorescence assays (Figure 63). Immunodetection of TOM20 was used for the staining of the mitochondrial outer membrane and phalloidin for staining the cytoskeleton (F-actin) (Figure 63A). To understand the different profiles of mitochondrial networks, we also performed the immunostaining of homoplasmic MAFs ($BL/6^{C57}$). Interestingly, the cell shape and size varied between different heteroplasmic models. Control homoplasmic MAFs showed the most elongated mitochondria network (Figure 63A). In homoplasmic MAFs, mitochondria were spread through the whole cytoplasm with high concentration of them in the perinuclear region (Figure 63B). This distribution was modified in control heteroplasmic MAFs where mitochondria are more randomly distributed within the cell, with significant lower clustering around the perinuclear region. $BL/6^{C57\text{-}NZB}$ $SCAF1^{113}$ MAFs showed a pattern of mitochondrial distribution very similar to the homoplasmic MAFs recovering the higher density of mitochondria surrounding the nucleus (Figure 63B).

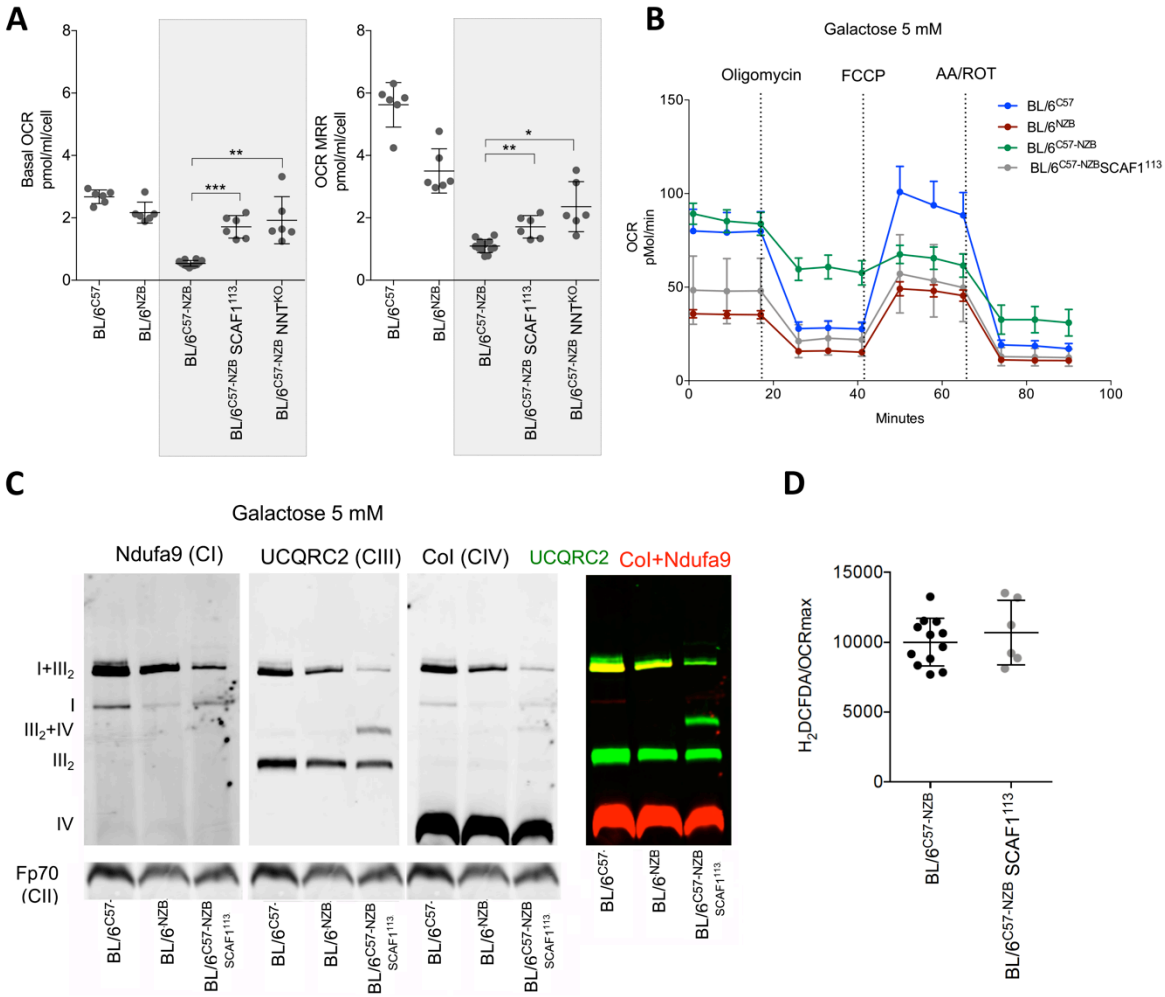

Figure 62. Mitochondrial performance evaluation in MAFs from modified heteroplasmic mice. **(A)** Oxygen consumption rates (OCR and OCR MRR) determined by SeaHorse™. N = 5 independent assays per clone. Cells were grown in 5 mM glucose. **p-value* < 0.05, ***p-value* < 0.01, ****p-value* < 0.001 assessed by ANOVA test. **(B)** Representative profiles of oxygen consumption rates (OCR) determined by SeaHorse™ in cells cultured in medium with 5 mM galactose. **(C)** BNE analysis of the unmodified and modified heteroplasmic MAFs. MAFs were cultured in complete medium with 25 mM glucose. The antibodies used for immunodetection were NDUFA9 (CI), UQCRC2 (CIII), COI (CIV) and FP70 (CII). Three different clones of each cell line were used for the experimental evaluation. **(D)** H_2DCFDA mediated ROS levels quantification in MAFs in 25 mM glucose medium. N = 3 clones of each immortalized cell line; 2-3 technical replicates.

In case of NNT^{KO} heteroplasmic MAFs, we found a high rate of mitochondrial fragmentation, and most of the mitochondria were stacked in the periphery of the cell (Figure 63B). An intriguing feature observed only in $BL/6^{C57\text{-}NZB}$ NNT^{KO} MAFs was the presence of extracellular vesicles or spots containing mitochondria and cytoskeleton (Figure 63B). Those vesicles could be found also in the periphery of the cells. Interestingly, the concentration of mitochondria in these vesicles assessed as the relative fluorescence intensities of TOM20 were highest than in other any area of the cytoplasm (Figure 63B). This observation could suggest the selective removal of mitochondria by exocytosis.

Besides mitochondrial distribution, the quantitative analysis of the ratio between fluorescence signal from mitochondria and actin (TOM20/F-ACTIN ratio) was performed as an index of mitochondrial content. This analysis indicated that heteroplasmic control fibroblasts have less mitochondrial mass per cell than homoplasmic ones (Figure 63C), confirming in that way the analysis obtained by CS activity per total protein amount (Figure 28G and Figure 61B). Interestingly, the expression of $SCAF1^{113}$ and the ablation of NNT increased the mitochondrial content (Figure 63A, C).

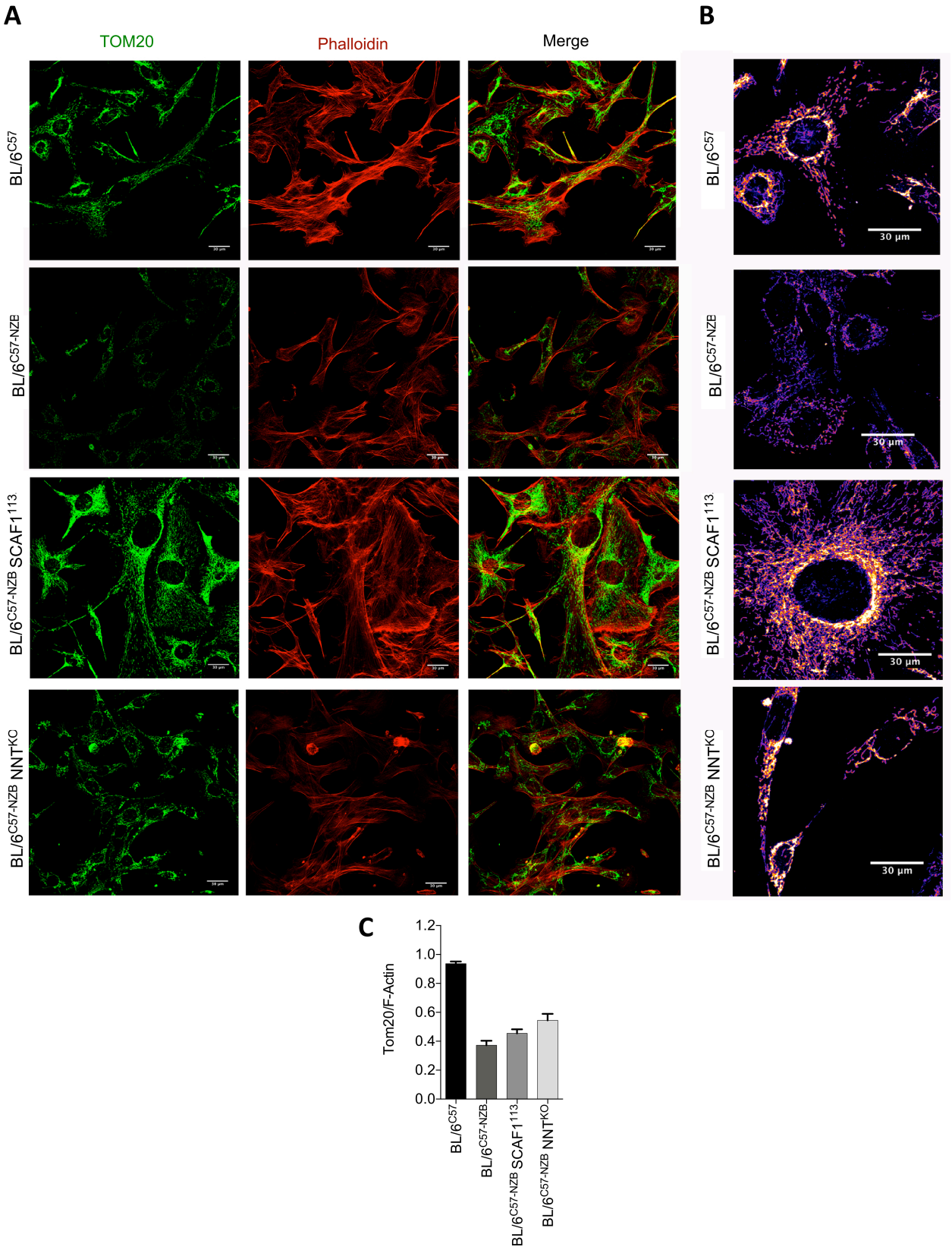

Figure 63. Confocal imaging analysis of mitochondrial networks in MAFs. (A) Confocal imaging of the mitochondrial networks. TOM20: mitochondrial marker in green. Phalloidin: F-actin marker, in red**. (B)** Densitometry imaging analysis of mitochondrial network distribution within the cells using TOM20 as mitochondrial marker. **(C)** Ratio of TOM20/F-Actin intensities in MAFs. Three different clones were used for the analyses. ***p-value* < 0.01, ****p-value* < 0.001, ANOVA analysis.

V.3.A.7.b. Study of cardiac and mitochondrial ultrastructure in genetically modified heteroplasmic mice

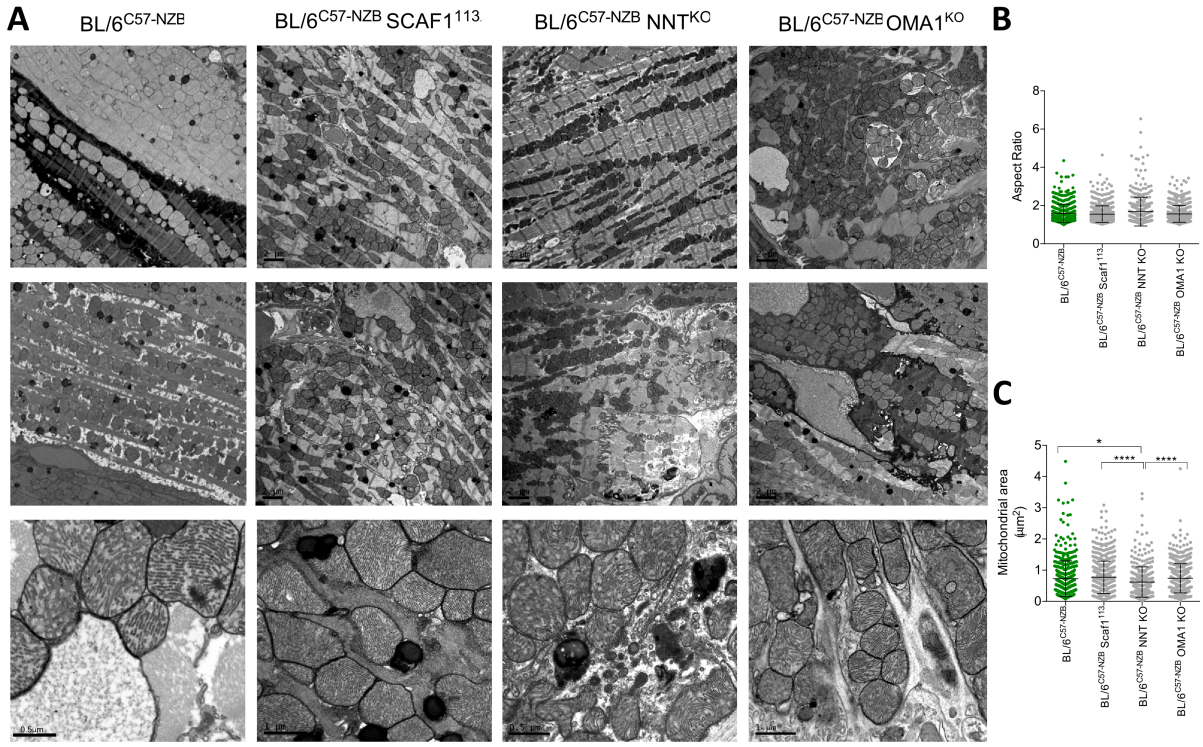

Figure 64. Ultrastructural analysis of hearts from genetically modified heteroplasmic mice. (A) Representative TEM images showing specific features observed in hearts from different heteroplasmic 12-weeks-old animals. Top-middle: 5x magnification; bottom: 40x magnification. **(B-C)** Morphometric analysis of manually segmented mitochondria. Aspect ratio as a parameter of mitochondrial elongation (B) and mitochondrial size (C). N = 5 mice per genotype. **p-value* < 0.05, *****p-value* < 0.0001 assessed by one-way ANOVA tests.

The observation of changes in the mitochondrial content and dynamics in cultured heteroplasmic MAFs with specific alterations in nuclear-encoded mitochondrial genes raised the question if this was relevant at the organismal level. To answer the question, we analysed the ultrastructure of cardiac tissue of the different heteroplasmic mouse strains by TEM. The differences in cardiac mitochondrial between homoplasmic and heteroplasmic mice were described before (*Results II*). Heteroplasmic mitochondria were characterised by an increase in size, the accumulation of them into autophagic vesicles and the reduction in the overall lipid droplet content (Figure 32). The expression of SCAF1^{113} in heteroplasmic mice induced a better lipid mobilization into the cardiomyocytes revealed by an increase in the amount and the distribution of lipid droplets, which were closer to IMF mitochondria (Figure 64A). In addition, the cardiac myographs also showed an increase in the number of cristae and better cristae shape and definition in BL/6$^{C57\text{-}NZB}$ SCAF1^{113} mitochondria (Figure65A-C).

The ablation of NNT in heteroplasmic animals impacted on the mitochondrial size. TEM analysis revealed that mitochondria are smaller, and they present more relaxed cristae than in the control heteroplasmic mice. In addition, sarcomeres were also shorter than in control mice, and the number of lipid droplets in cardiac fibres was significantly reduced (Figure 64A).

Finally, the ablation of OMA1 induced an increase in the number of mitochondria but in a disorganized fashion (Figure 64A). There was an increase in the number of disperse necrotic fibres and the accumulation of mitochondria into autophagosomes, suggesting higher difficulty in the removal of mitochondria either

because the increased content of dysfunctional organelles or due to an impaired autophagy (Figure 64A, asterisk). No significant changes were observed in mitochondrial area and morphometry although the ablation of the protein OMA1 in homoplasmic mice presented differences in cardiac mitochondrial ultrastructure[293].

V.3.A.7.c. Analysis of mitochondrial performance

Cristae shape and respiratory chain structure and function are closely associated[13]. Analysis of cristae morphology and thickness revealed that the removal of the NNT in heteroplasmic mice induced longer and more relaxed cristae (Figure 65A-C). On the other hand, SCAF1^{113} promoted better organization; homogeneity in shape and density in the mitochondrial cristae and the packaging of IMM was more similar to the homoplasmic strains (Figure 36 A-B and Figure 65A-C).

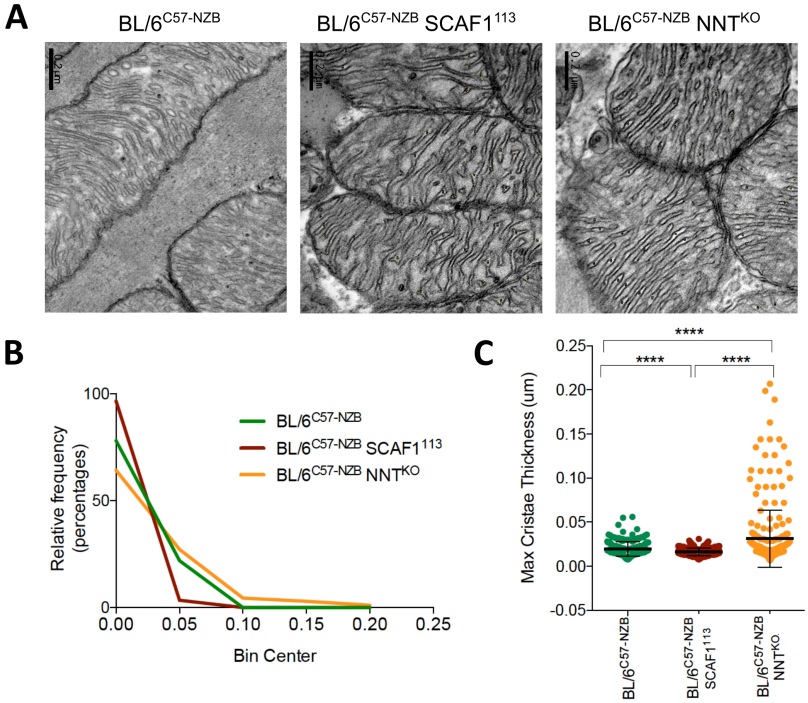

Figure 65. Analysis of the mitochondrial ultrastructure and cristae shape in heteroplasmic mice. (A) Representative TEM images showing cristae morphology of cardiac mitochondria. 80x magnification. **(B)** Frequency distribution of maximal cristae thickness in BL/6$^{C57-NZB}$, BL/6$^{C57-NZB}$ SCAF1^{113}, and BL/6$^{C57-NZB}$ NNT^{KO} mitochondria. **(C)** Maximal cristae thickness measurements in cardiac mitochondria. Each dot corresponds to a different cristae measurement. N = 5 mice per genotype, 12-weeks-old mice. ****p-value < 0.0001, one-way ANOVA test.

We next inquired if the synchronization in providing OXPHOS subunits was affected in heteroplasmic mice. We evidenced an imbalance between mitochondrial and nuclear-encoded proteins of CIV in BL/6$^{C57-NZB}$ that was partially compensated in NNT^{KO} and SCAF1^{113} heteroplasmic animals (Figure 66A). Ultrastructural evidences of better conservation of cristae in cardiac mitochondria in BL/6$^{C57-NZB}$ SCAF1^{113} and the different appearance in NNT^{KO} heteroplasmic mice prompted us to study the potential impact on the organization of supercomplexes and bioenergetics (Figure 66B-E). The removal of NNT increased the content of respiratory complexes, with an increase in total CIV, CIII and CI levels. However, the proportion of CI containing SCs remained significantly lower than in homoplasmic hearts. Only in case of the BL/6$^{C57-NZB}$ SCAF1^{113} hearts (Figure 66D), $CIII_2$+CIV could be observed accompanied with an overall increase in the level of all complexes and SCs. BNE allowed us to evaluate ATP synthase formation. We found an increase in CV in both heteroplasmic strains (NNT^{KO} and SCAF1^{113}) compared to wild type

heteroplasmic mice (Figure 66C). BNE analyses suggested that the OXPHOS impairment in heteroplasmic cardiac mitochondria was partially compensated by the loss of NNT or the repression of SCAF1^{113}; hearts may have recovered their oxidative capacity. This was also suggested by the BEC index, an increase in OXPHOS *versus* glycolysis in SCAF1^{113} heteroplasmic hearts (Figure 66B). On the contrary, we found similar expression of β-ATPase and GAPDH between BL/6$^{C57\text{-}NZB}$ and BL/6$^{C57\text{-}NZB}$ OMA1^{KO} suggesting that the ablation of this protease does not restore OXPHOS performance (Figure 66B).

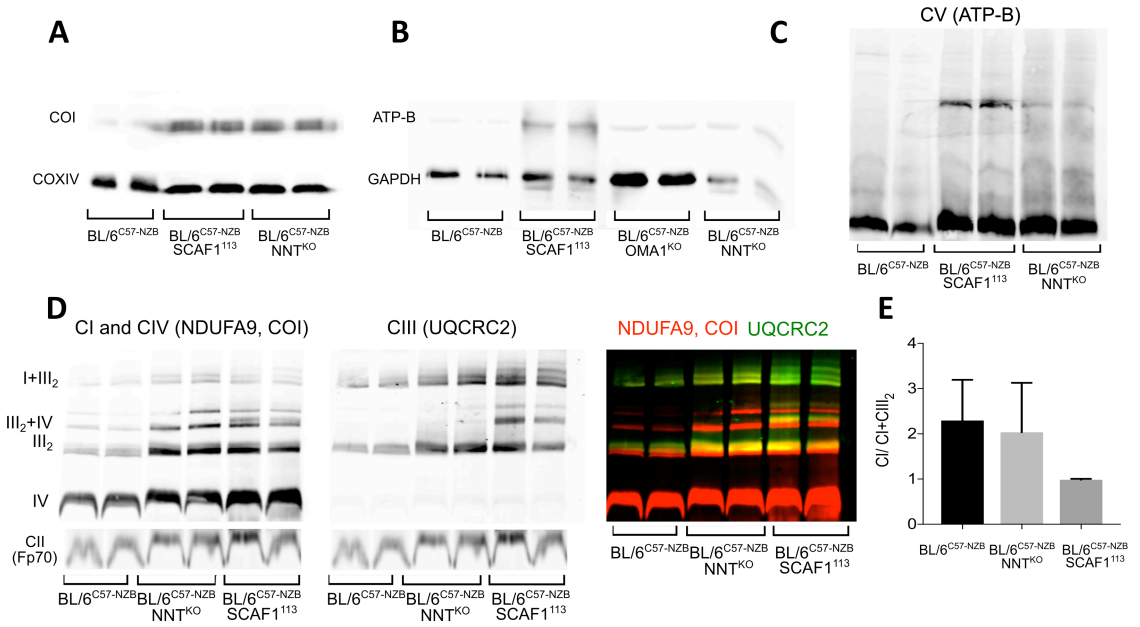

Figure 66. Analysis of mitochondrial features in heart of heteroplasmic mice lacking NNT and expressing SCAF1^{113} protein. **(A)** Representative Western blot showing the expression of a mitochondrial-encoded protein (COI) *vs.* a nuclear-encoded protein (COXIV). **(B)** Bioenergetic cellular (BEC) index in total cardiac tissue from BL/6$^{C57\text{-}NZB}$, BL/6$^{C57\text{-}NZB}$ SCAF1^{113}, BL/6$^{C57\text{-}NZB}$ OMA1^{KO} and BL/6$^{C57\text{-}NZB}$ NNT^{KO} mice. **(C-E)** Blue native electrophoresis of heart samples from 12-weeks-old modified heteroplasmic mice. (C) Analysis of complex V (β-ATP). (D) Left: Complex I (NDUFA9), complex IV (COI) and complex II (FP70). Middle: Complex I (UQCRC2). Right: Merged immunodetection of the indicated proteins and colours after BNGE of digitonin-solubilized mitochondria from the different strains. (E) Ratio of free complex I to supercomplexed complex I, determined from the CI Western blot in (D). Hearts from 12-weeks-old mice were used for the analysis.

V.3.A.7.d. Impact on whole animal physiology

The absence of OMA1 protease did not modify, to any detectable degree, the pattern of mtDNA segregation when compared to control heteroplasmic animals suggesting that its ablation is silent for the heteroplasmic status.

However, an exacerbation of the pathological phenotype in the BL/6$^{C57\text{-}NZB}$ OMA1^{KO} mice was found when the animals were young (12-weeks-old mice). Thus, TEM analysis revealed more cardiac tissue damage accompanied with an increase in CK and CK-MB plasma levels at the same age, similar to the original heteroplasmic mice (Figure 67A). Interestingly, the level of heteroplasmy correlated with the increase of both enzymes in plasma; this was the unique strain that showed a significant linear correlation between those parameters (Figure 67B, C). This suggest that either (a) the ablation of OMA1 preserves the removal of damaged cardiomyocytes during cardiac homeostasis (for these mechanisms, the animals with more heteroplasmy would be the most defective mice) or (b) the ablation of OMA1 exacerbates the pathological phenotype. The results implicate that mitochondrial dynamics is also implied in maintaining a healthy status of mitochondria in heteroplasmic cells. We described elsewhere that the ablation of OMA1

protects cardiac tissue from heart failure under different insults[293]. This protection may be due to the prevention of cardiomyocyte apoptosis. As shown before, apoptosis is an important pathway in lung cell populations under different stress conditions. Because of the pathological cardiac phenotype, lung function was studied to evaluate potential changes with respect to the heteroplasmic mice presenting OMA1. The assessment of ROS in fresh lung tissue revealed an exacerbated increase in superoxide levels (DHE signal) in heteroplasmic mice with the ablation of OMA1 (Figure 67D, E). This was accompanied by increased levels of partial pressure of oxygen ($mmHgO_2$) in BL/6^{C57} OMA1^{KO} mice revealed by blood gasometry (Figure 67F). Together with that, we found a decrease in the inflammatory cell populations in BL/$6^{C57\text{-}NZB}$ OMA1^{KO} in comparison with BL/$6^{C57\text{-}NZB}$ (Figure 67G), probably due to the reduction in cell death. These differences are characteristics of heteroplasmic animals since analysis of homoplasmic mice (BL/6^{C57}) and BL/6^{C57} OMA1^{KO} did not reveal differences in those parameters (Figure 67H).

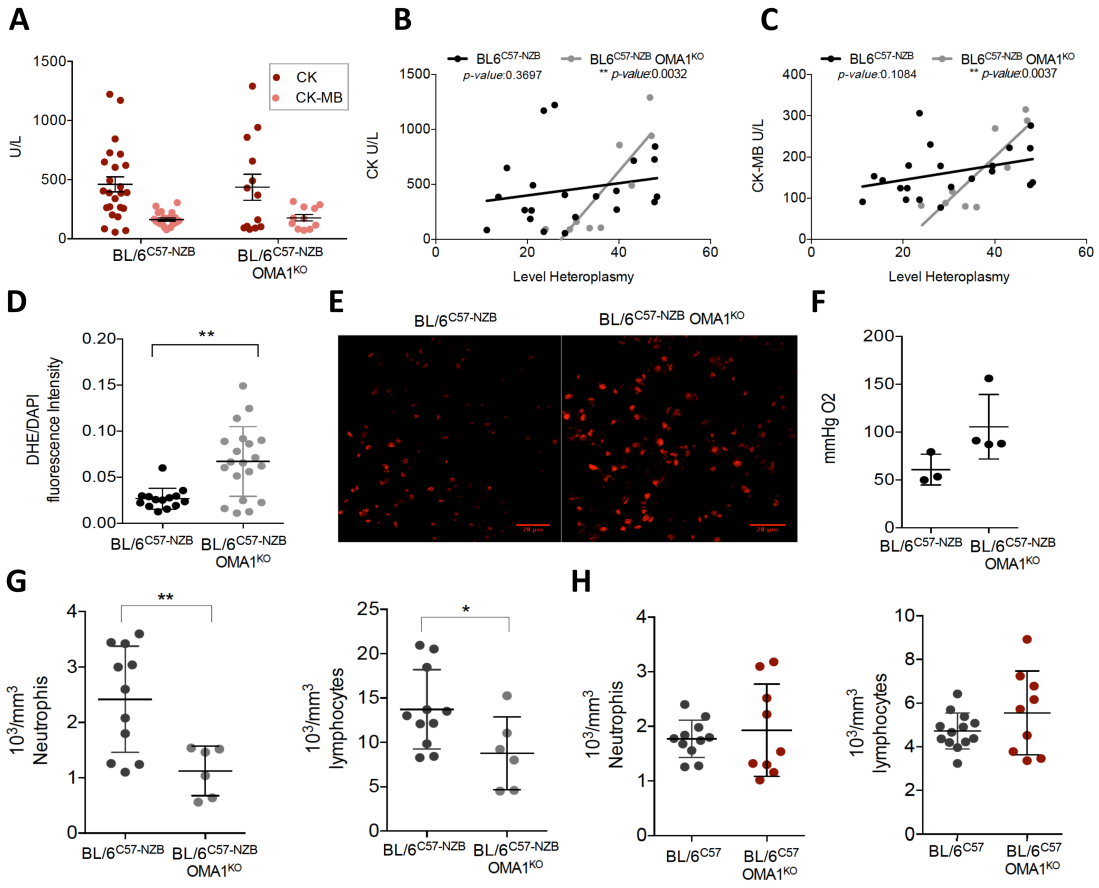

Figure 67. Analysis of heteroplasmic mice lacking OMA1 protein. (A) Blood analysis of cardiac damage indicated by increased plasma CK and CK-MB. 12-weeks-old males of the indicated genotype**. (B-C)** Correlation between the cardiac damage assessed by CK (B) and CK-MB (C) plasma concentrations in (A) and the level of heteroplasmy. **(D-E)** Analysis of ROS (DHE staining) in fresh cardiac sections from 20-weeks-old mice; quantification of the levels (D) and representative lung confocal images (E). **(F)** Gasometric determination of O_2 partial pressure in blood from 20-weeks-old mice. (n = 3-4 mice) **(G-H)** Haematological evaluation of the indicated strains at 12 weeks of age. Each dot corresponds to one mouse. *p-value<0.05, **p-value < 0.001 assessed by ANOVA test.

BL/$6^{C57\text{-}NZB}$ NNT^{KO} modified the segregation of mtDNA mainly affecting tissues related to immune response. Haematological analysis revealed that heteroplasmy induces an increase in monocytes, leucocytes and neutrophils. Interestingly, in BL/$6^{C57\text{-}NZB}$ NNT^{KO} mice neutrophilia disappears and the number of monocytes and lymphocytes decreased compared to control heteroplasmic mice (Figure 68A). Again, the effect of NNT ablation was characteristic of the heteroplasmic status since homoplasmic mice with (BL/6^{C57}) or without (BL/6^{C57} NNT^{KO}) showed no differences between both groups of animals (Figure

68B). Haematological analysis of control heteroplasmic animals indicated a tendency to increase the haematocrit (HCT). Low oxygen levels caused by heart damage, pulmonary fibrosis, bone marrow overproduction or kidney disease among others may cause the abnormal values[304,305]. The ablation of NNT recovered the HCT levels (Figure 68C).

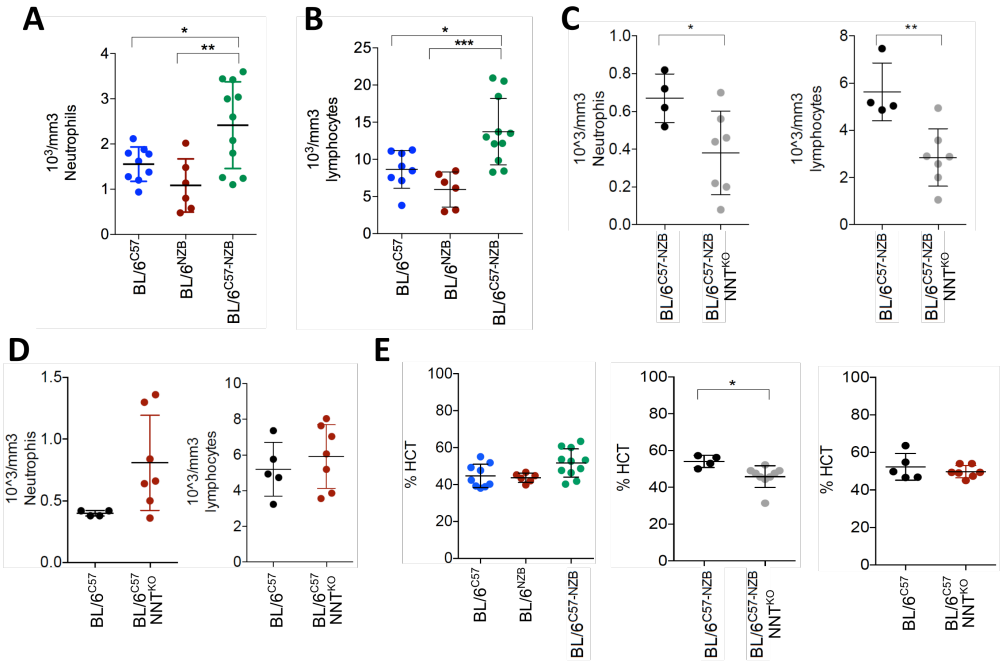

Figure 68. Analysis of heteroplasmic mice lacking NNT protein. (A-D) Haematological evaluation of inflammatory status of homoplasmic and heteroplasmic mice (A-B), wild type heteroplasmic mice and heteroplasmic mice NNT^{KO} (C), and C57BL/6 mice wild type and mutant for NNT protein (D) at 12 weeks of age. **(E)** Haematocrit analysis of the indicated mouse strains at 12 weeks of age. Each dot corresponds to a different animal. **p-value* < 0.05, ***p-value* < 0.01, one-way ANOVA test.

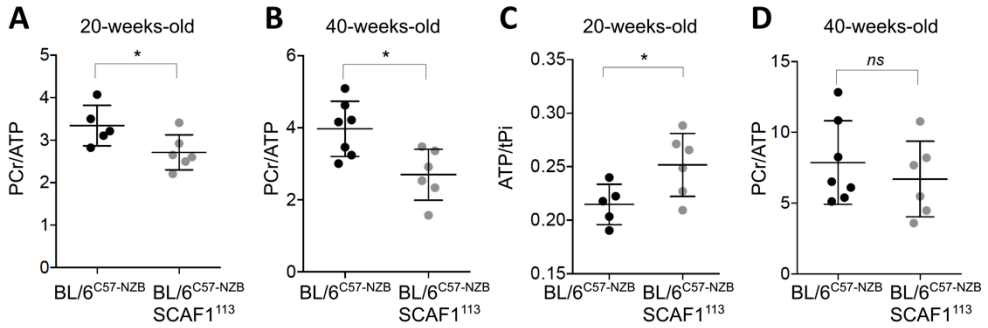

Figure 69. *In vivo* analysis of the high-phosphate metabolism in $BL/6^{C57\text{-}NZB}$ $SCAF1^{113}$ cardiac and skeletal muscle. (A-B) Analysis by ^{31}P-MRS of the PCr/ATP ratio in (A) cardiac muscle of 20-weeks-old mice, (B) 40-weeks-old heteroplasmic mice. **(C)** Ratio ATP/ total (t) Pi in hearts from the indicated genotypes at 20 weeks of age. **(D)** *In vivo* assessment of PCr/ATP ratio in soleus skeletal muscle (40-weeks-old mice). Each dot represents a different animal (n = 5-7). **p-value* < 0.05, ANOVA test.

The impact of $SCAF1^{113}$ was investigated in heart and skeletal muscle by *in vivo* $^{31}P/^{1}H$ MRS. Heart high-phosphate metabolism was monitored at 20 and 40 weeks of age. The increase in PCr/ATP ratio that revealed an impaired heart metabolism in $BL/6^{C57\text{-}NZB}$ mice was prevented by the expression of $SCAF1^{113}$ that recovered the values of homoplasmic mice (Figure 69A, B). In the case of the skeletal muscles, the analysis was focused at 40 weeks of age because in 20-weeks-old control heteroplasmic mice we could not

find any alterations (Figure 69C). PCr/ATP ratio increased in heteroplasmic animals regardless of the expression of SCAF1^{113} in skeletal muscle (soleus) (Figure 69C).

V.3.A.7.e. Lifelong consequences of nuclear gene modifications in heteroplasmic mice

BL/6$^{C57\text{-}NZB}$ NNT^{KO} and SCAF1^{113} mice did not present different aspect to the control heteroplasmic mice until they reached the adulthood (10-12 weeks of age). As it was reported before, one of the features of the heteroplasmic mice (BL/6$^{C57\text{-}NZB}$) is that females were bigger than usual, reaching similar weight than the males (Figure 26B, C and Figure 70A). This feature was also observed in heteroplasmic mice SCAF1^{113} (Figure 70A). However, the ablation of NNT eliminated these gender specific differences; weight was re-established despite their heteroplasmic condition (Figure 70A). The ageing phenotype score improved with the ablation of NNT or the expression of SCAF1^{113}. When animals were more than 350 days, they looked healthier than the BL/6$^{C57\text{-}NZB}$, which started to lose hear, manifested kyphosis and reduced weight (Figure 70B). Also, the agility of the mice was improved (Figure 15B) in comparison with the control heteroplasmic mice that had reduced activity.

Control heteroplasmic mice manifested a significant decrease in cardiac output with age (around 74 weeks of age). The MRI analysis of RV-EF and SVP confirmed that the mortality of the strain might be related to heart failure and pulmonary hypertension. The analysis of heart function by echocardiography revealed a striking recovery only in BL/6$^{C57\text{-}NZB}$ SCAF1^{113} mice when compared with BL/6$^{C57\text{-}NZB}$ NNT^{KO} and control heteroplasmic mice (Figure 70C).

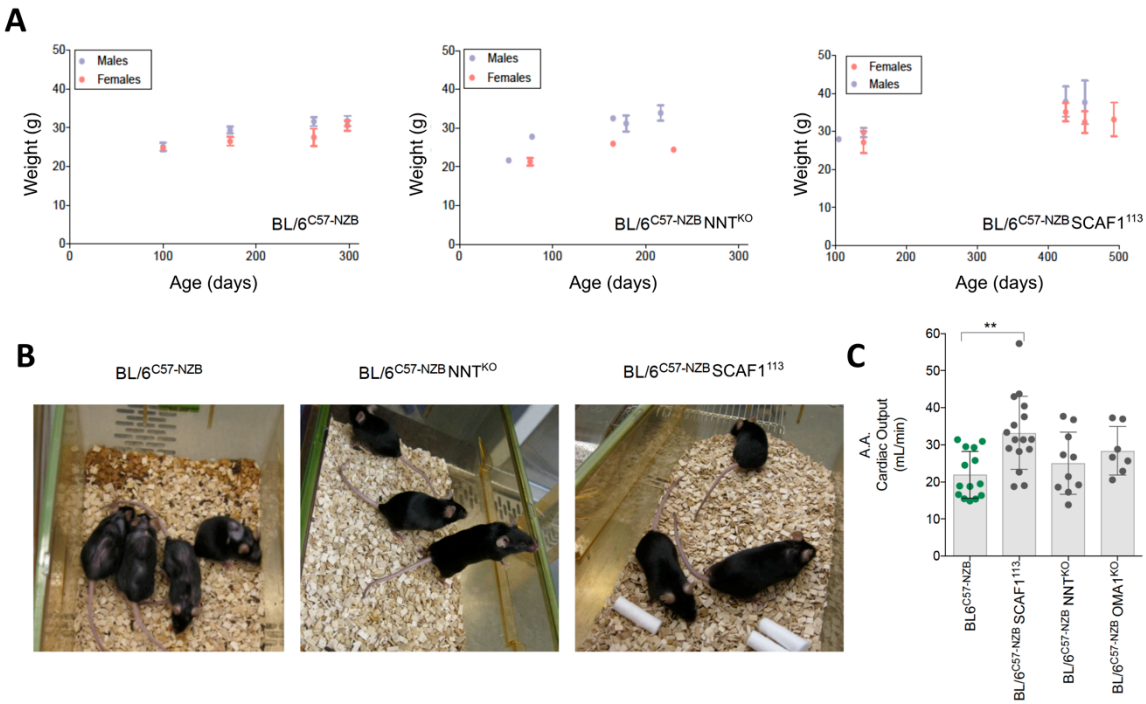

Figure 70. Impact of nuclear gene modifications on heteroplasmic mice ageing phenotype. (A) Weight gain (chow diet, n = 7-10 males and females per genotype, mean ± s.e.m., two-tailed t-test. **(B)** Representative pictures of aged females of the indicated strain. BL/6$^{C57\text{-}NZB}$: 349 days of age; BL/6$^{C57\text{-}NZB}$ SCAF1^{113} 492 days of age; BL/6$^{C57\text{-}NZB}$ NNT^{KO}. 578 days of age. **(C)** Assessment of cardiac output in 74-weeks-old mice of the indicated genotype. Each dot represents a single animal. (BL/6$^{C57\text{-}NZB}$: 14 males; BL/6$^{C57\text{-}NZB}$ SCAF1^{113}: 17 mice; BL/6$^{C57\text{-}NZB}$ NNT^{KO}: 10 males; BL/6$^{C57\text{-}NZB}$ OMA1^{KO}: 7 males). Mean ± SD. ***p-value* < 0.01, one-way ANOVA test.

V.3.A.8. Modulation of the cellular status by activation of physiological processes

V.3.A.8.a. MtDNA segregation in liver regeneration process

To test the hypothesis that fuel preference and/or proliferative status dictate the heteroplasmic shift, liver hepatectomy was performed in adult mice to induce its regression to highly proliferative status and regeneration. Partial hepatectomy (removal of 75% of liver tissue) induces cell proliferation until the original mass of the liver is restored. Most of the changes in metabolism occur during the first 24 hours[306]. After these changes, a replicative phase in which DNA synthesis is very active occurs[306].

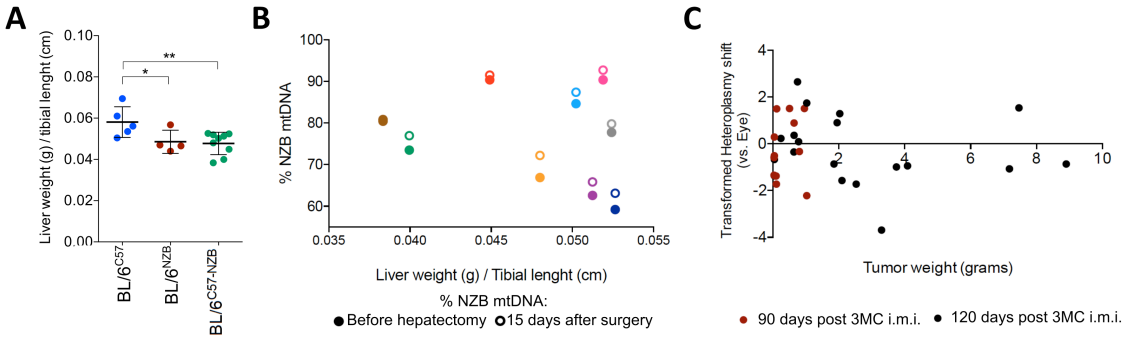

Figure 71. Evaluation of mtDNA segregation in tissues with different metabolic status. (A-B) Evaluation of heteroplasmic condition in liver regeneration. (A) Recovery weight of the liver after 15 days post hepatectomy surgery. N = 5 mice per homoplasmic genotype and n = 10 heteroplasmic mice. (B) Measured percentage of NZB mtDNA in liver before and after hepatectomy (15-days-post surgery). Each colour corresponds to a different individual. Filled dots are measurements before surgery and non-filled dots correspond to the amount of NZB mtDNA after liver regeneration. **(C)** Transformed heteroplasmy shift estimated *vs.* tail in 3MC-induced fibrosarcomas. Each dot corresponds to an individual heteroplasmic mouse. Red dots: 90 days post 3MC intramuscular injection. Black dots: 120 days post 3MC injection. Analyses were done in 8-12-weeks-old mice. **p-value* < 0.05, ***p-value* < 0.01, one-way ANOVA test.

Hepatectomy surgery was performed in 10-weeks-old males. Fifteen days after the tissue removal, mice were euthanized and total liver regeneration and the percentage of mtDNA haplotypes were measured. Total liver weight after 15 days of the hepatectomy revealed that livers from homoplasmic mice presenting mtDNA C57 have better recovery in total liver tissue compared with BL/6^{NZB} and BL/6$^{C57\text{-}NZB}$ mice (Figure 71A). To evaluate mtDNA segregation, excised livers at day 0 (tissue samples excised during liver surgery) were compared with regenerated livers at day 15 (Figure 71B). The analysis revealed that (a) the rate of mtDNA segregation does not correlate with the total recovery of liver weight and (b) all the regenerated liver samples had an increase in NZB mtDNA compared to the samples at day 0 (Figure 71B). The same percentage of each haplotype was found independently of the hepatic region analysed. Liver is the organ that more actively segregates in favour of NZB mtDNA. These results indicate that the NZB mtDNA is selected independently of the proliferative status of hepatocytes (Figure 71A, B).

V.3.A.8.b. Tumour development

High frequency of homoplasmic-mutated mtDNA has been reported in different human tumours. This observation has been interpreted as a consequence of proliferation advantage of cells carrying mtDNA mutations, the tumorigenic properties of the mutations or by the replication advantage of mutated mtDNA. Other studies suggest the mtDNA selection does not require any metabolic or tumorigenic particularities, only the selection by chance in tumour progenitor cells[307]. Most of the tumours have a rapid cell proliferation, are highly glycolytic and present low level of OXPHOS[308]. It has been postulated that amino acid changes in different proteins of mtETC may induce the selection of mitochondria that promotes higher glycolytic phenotype.

To our knowledge, the analysis of segregation or selection between non-pathological mtDNA variants in tumours has not been done until now. We considered that the evolution of heteroplasmy in tumours could provide further information about the kinetics and influential factors that drive mtDNA segregation, since it is a situation in which cells need to proliferate in a context of cell competition. To analyse that, we induced fibrosarcomas in BL/6$^{C57\text{-}NZB}$ mice by intramuscular administration of 3-methylcholanthrene (3-MC). These tumours present K-*ras* (Kirsten rat sarcoma viral oncogene*)* or K-*ras* and N-*ras* proto-oncogene activation[309,310]. They are oncogenes that encode membrane proteins with intrinsic GTPase activity that shuttle between Golgi apparatus and plasma membrane in case of N-*ras*[311]. Furthermore, these chemically-induced fibrosarcomas are highly sensitive to the activity of p53 and the response towards DNA damage is persistently activated[312]. It was reported that mutations in mt-ND4 and mt-ND6 affect the tumorigenicity of the cells in multiple human cancers[308]. Our two mtDNA haplotypes have aminoacidic differences in proteins of complex I that could affect the selection of one of them.

We followed the tumour using *in vivo* imaging techniques (MRI) in heteroplasmic and homoplasmic mice, showing no significant growth differences between the two conditions. Tumours were excised after 90 and 120 days post intramuscular injection and the percentage of heteroplasmy analysed (Figure 71C). When tumours started to be visible (around 90 days post 3-MC administration), weight tumour and heteroplasmy shift between the tumour and the tail of the mice were correlated: bigger tumours select always for one of the two mtDNA variants rejecting the heteroplasmic condition. Tumours that could not select one of the mtDNA haplotypes grew less. A closer look into the transformed heteroplasmy shift of 120 days post 3-MC injection induced fibrosarcomas indicated a selection towards C57 mtDNA in the biggest tumours (Figure 71C). In conclusion, (a) tumours that cannot resolve heteroplasmy grow less than tumours than can select one or another mtDNA variants, and (b) tumours shift towards C57 mtDNA in most of the cases, supporting the hypothesis that cells with a more glycolytic metabolism have a better growth with this mtDNA variant.

V.3.A.8.c. T cell activation in immune responses

Lymphocytes systematically selected C57 mtDNA in heteroplasmic mice. In addition these cells are quite interesting since they shift their proliferative and metabolic programs upon natural stimulus. Thus, the transition from a quiescent phase to the proliferation status of naïve T cells requires the modulation of the mitochondrial biogenesis and metabolism[313]. We decided to perform two different *in vivo* and *in vitro* approaches to evaluate the impact of the metabolic program on mtDNA segregation upon T cell activation. Two different murine groups, naïve and immunized mice of each genotype, were analysed. Mice were immunized intravenously with the model antigen ovalbumin (OVA) combined with the invariant NKT cell agonist IMM60 and the TLR4 agonist monophosphoril lipid A (MPLA). Splenocytes of naïve and immunized mice were evaluated to assess the mitochondrial performance. TOM20 immunodetection, used as OMM marker to assess mitochondrial content, was significant lower in naïve heteroplasmic mice compared to any of the homoplasmic strains. However, after 7 days of immunization, an increase in mitochondrial mass was observed only in heteroplasmic mice (Figure 72A). BEC index showed that heteroplasmic splenocytes present less OXPHOS activity in naïve mice. However, after mice immunization, the increase in the CV subunit expression was only significant in BL/6$^{C57\text{-}NZB}$ splenocytes (*p-value*=0.006) (Figure 72B). We could also notice differences between the immunized conplastic animals (Figure 72B).

Seven days after vaccination, naïve and immunized mice were euthanized. $CD4^+$ and $CD8^+$ memory (T_M), effector (T_E) and naïve (T_N) T cells were sorted according to the expression of CD62L and CD44 and the percentage of heteroplasmy was measured in each population (Figure 72C, D). Effector T cells use

glucose to generate NADPH and ribose through pentose phosphate pathway (PPP) and their metabolism mainly relies in glycolysis[314]. Resting CD4 and CD8 T cells rely predominantly on oxidative metabolism[315]. The obtained results show: (a) transformed heteroplasmic shift is negative in all T cell populations independently if the mice are immunized or not, confirming that C57 mtDNA is accumulated in T cells (Figure 72 C, D). The shift towards mtDNA C57 seems to be more pronounced in immunized mice, whose values were also more homogeneous (Figure 72E); (b) an increase in NZB mtDNA only in $CD8^+$ memory cells (T_M) in naïve mice; (c) an increase in NZB mtDNA in $CD8^+$ memory cells (T_M) and effector cells (T_E) in immunized mice; and (d), no differences between $CD4^+$ T cell subsets (Figure 72C-E). Activated $CD4^+$ T cells remain more oxidative and had greater maximal respiratory capacity and increased mitochondrial biogenesis than activated $CD8^+$ T cells, which proliferate more rapidly and rely on glucose metabolism by aerobic glycolysis as a primary metabolic program. The main difference between $CD8^+$ T_E and T_M is that T_M cells present substantial mitochondrial spare respiratory capacity (SRC) to produce energy in response to stress[316]. As a result we found an increase in NZB mtDNA in $CD8^+$ T_M in naïve and immunized mice despite the overall tendency of T cells to accumulate C57 mtDNA, (Figure 72C-E) that may be explained by the mitohormesis phenomena, a consequence of nDNA/mtDNA mismatch that attribute more capacity to these cells to respond to stress conditions and by the necessity of promoting mitochondrial biogenesis and exacerbating the expression of the carnitine palmitoyltransferase (CPT1a) to activate fatty acid oxidation (FAO)[323]. The selection of NZB mtDNA in $CD8^+$ memory T cells may be consequence of the higher FAO metabolism promoted by NZB mtDNA compared to C57 mtDNA variant.

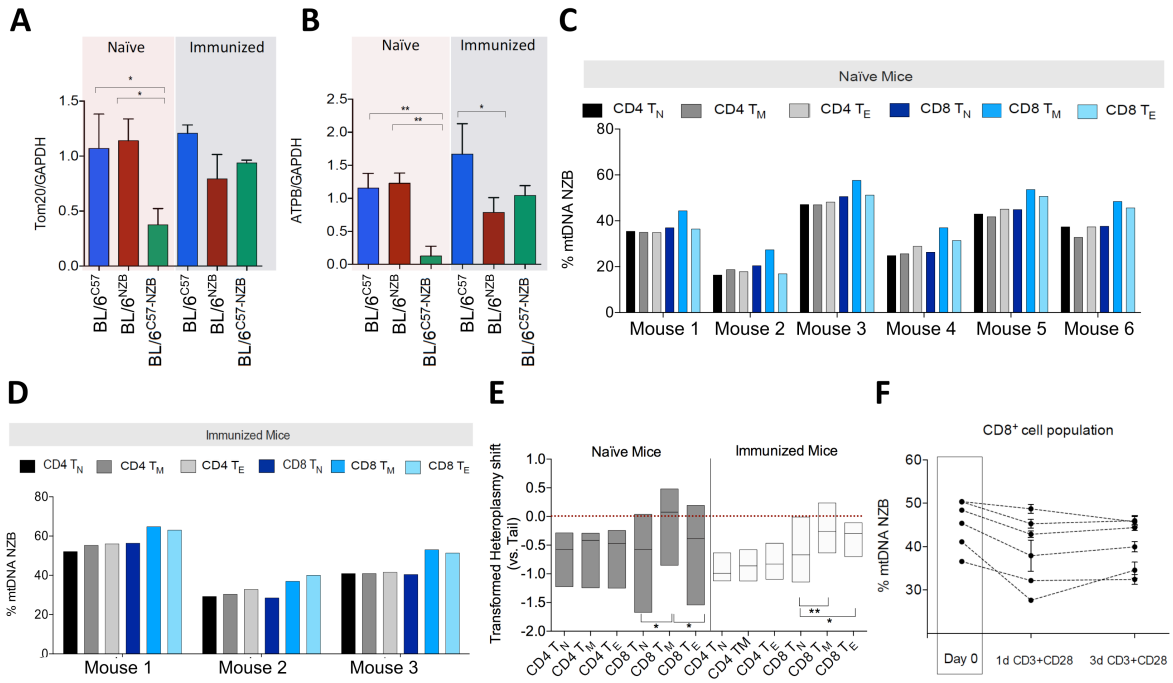

Figure 72. Impact of heteroplasmy on the immune response. **(A)** Analysis of the TOM20/GAPDH ratio estimating the amount of mitochondria in naïve and immunized mice. **(B)** BEC index (ATP-β/GAPDH) analysis. In A-B, data were obtained from Western blot assays of total splenocytes (15-weeks-old homoplasmic and heteroplasmic mice). **(C-D)** *In vivo* analysis of heteroplasmy in different sorted populations of $CD4^+$ and $CD8^+$ T cells in naïve (C) and immunized mice (D). **(E)** Transformed heteroplasmy shift (*vs.* tail) obtained from data in (C-D). T_N: naïve T cells. T_M: memory T cells; T_E: effector T cells. **(F)** *In vitro* analysis of heteroplasmy progression after $CD8^+$ T cell activation using anti-CD3/CD28 beads. Each dot represents the total cell population obtained from the spleen of one different heteroplasmic mouse (n = 6 heteroplasmic mice). In A-E, n = 5 naïve mice and n = 3 immunized mice. **p-value* < 0.05, ***p-value* < 0.01, one-way ANOVA tests.

To reproduce *in vitro* the polyclonal T cell stimulation and expansion, total $CD8^+$ T cells were isolated from heteroplasmic spleens and cultured. We assessed the initial percentage of NZB mtDNA after the isolation and analysed its temporal evolution. To mimic the stimulation by antigen-presenting cells *in vitro*,

we used an approach using beads coated with anti-CD3/CD28 (Figure 72F). The signal through the CD3 components of the TCR complex and CD28 as costimulatory molecule triggers a metabolic reprogramming based in proliferation and differentiation of the $CD8^+$ subset[315]. T cell activation occurs within the first hour of stimulation and reaches a plateau after 6 hours of incubation. The viability of the cells may be compromised during the first day of cell culture. The analysis revealed a shift towards C57 mtDNA in $CD8^+$ T cells upon activation (Figure 72F). This result reinforces the idea showed in the *in vivo* results, the overall T cell activation promotes the segregation towards C57 mtDNA (Figure 72E, F).

Immune synapses require of organelle reorganization within the cell[317,318]. Lymphocytes respond to extracellular signals with polarization of the cell (morphometric changes), migration (chemotaxis) and fusion-fission events in mitochondria[317]. The activation of T lymphocytes requires the localization of mitochondria in the periphery of the cell. An inadequate localization of the organelles impairs the ability of the lymphocytes to migrate[318]. Elucidating the role of mitochondrial genetics in immune cell metabolism and function combined with an understanding of the mechanisms regulating this process is quite challenging. To address these questions, heteroplasmic mice were used, which provide an opportunity to demonstrate mtDNA segregation in T cells, upon their *in vivo* and *in vitro* activation. In addition, we observed how differences in OXPHOS performance and ROS production generated by the two mtDNA haplotypes can modulate T cell function and differentiation. MtDNA haplotype profoundly impacts on the way immune cells respond to their environment, ultimately shaping immune cell function and fate.

V.3.A.8.d. Metabolic coupling between neurons and astrocytes

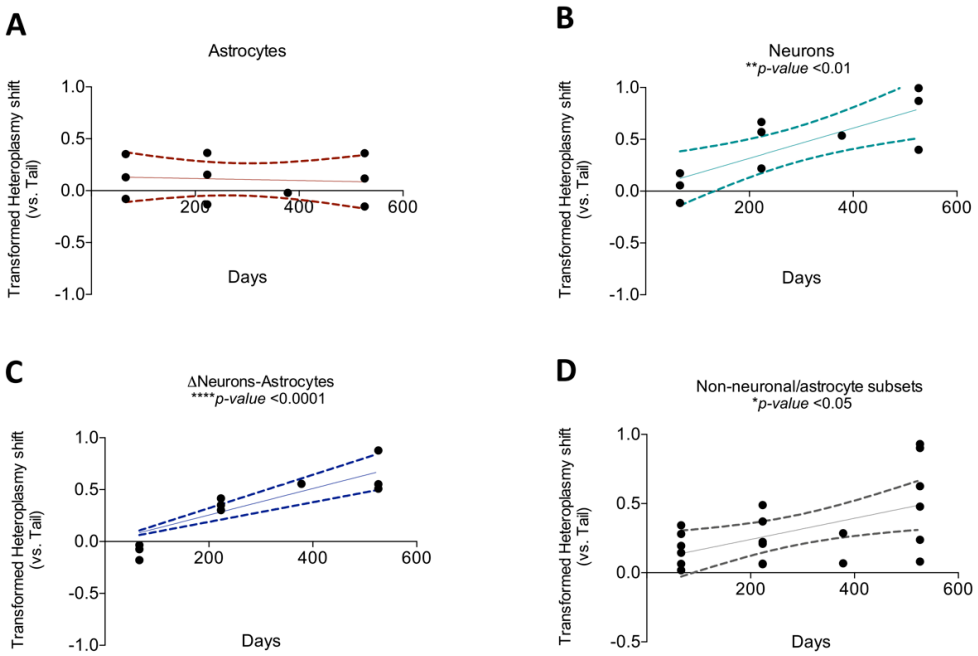

Figure 73. Analysis of heteroplasmy in brain cell populations. (A-B) Transformed heteroplasmy shift (*vs*. tail) in isolated astrocytes (A) and neurons (B). **(C)** Differences in heteroplasmy between astrocytes and neurons. Each dot corresponds to the difference between astrocytes and neurons in a single individual at the indicated age. **(D)** Transformed heteroplasmy shift in non-astrocyte/neuronal populations. Lines correspond to the mean and discontinuous lines show 95% confidence intervals of inferred segregation trajectories. Each dot corresponds to a different animal at the indicated age. * *p-value* < 0.05, ***p-value* < 0.01, ****p-value* < 0.001, linear regression.

The major concern in the assessment of the heteroplasmic shift in different tissues is that they contain heterogeneous cell populations that can have substantially different metabolic programs. This is particularly relevant in the case of the brain, in which different cell types with very diverse metabolism co-

exist within a single tissue section (i.e. neurons, astrocytes, oligodendrocytes, microglia). Astrocytes have different roles in the central nervous system (CNS), metabolic and energetic support, neuronal plasticity, maintenance of extracellular ion concentration, structural support and clearance and recycling of neurotransmitters (i.e. glutamate, GABA)[319]. Glutamate uptake into astrocytes stimulates aerobic glycolysis: a mechanism coupling neuronal activity to glucose utilization. On the other hand, neurons are mainly oxidative and among 80% of the activity in brain relies on them[319]. Oligondendrocytes and axons are metabolically coupled. Aerobic glycolysis generates pyruvate and lactate to power the axonal compartment. Glycogen is not present in neurons and low amount of this polysaccharide is found in dendritic cells. However, high amount of this glucose reservoir is used in astrocytes to promote the astrocytic synapses. Persistent enhancement of glycolysis in neurons leads to glucose intolerance, fat accumulation and weight gain, redox stress, neuronal dendrite shrinkage and short-term memory loss. The bioenergetic programs of neurons and astrocytes are coordinated by APC/C-Cdh1 by controlling PFKFB3 stability. APC/C-Cdh1 blocks PFKFB3 and consequently, the glycolytic pathway. At this moment, the pentaphosphate (PPP) pathway is activated to synthesize the intermediate ribulose 5-phosphate (R5P). The process is coordinated by the interconversion of $NADP^+$ to NADPH which is signalled by ROS[320]. MtETC organization in neurons and astrocytes is adapted to their metabolic profile and impacts on ROS generation. Neurons present an efficient electron transport with low ROS generation, but astrocytes generate high levels of ROS. Endogenous mitochondrial ROS production by astrocytes has profound signalling effects to regulate glucose metabolism ultimately affecting cognitive function[320].

V.3.A.8.e. Analysis of mtDNA segregation in brain cell populations

We measured the amount of mtDNA NZB in brain (specifically in cerebral cortex) during the whole life of the animals. The enormous complexity of the brain[321] based on several cell types and the metabolic interrelationship between them[322,323] and particularly the different metabolism of neurons and astrocytes, give us the opportunity to study a complete system and evaluate the driving force that triggers mtDNA segregation.

Analysis of heteroplasmy was performed at different ages covering the whole lifespan of these mice. We isolated astrocytes (left brain hemisphere) and neurons (right brain hemisphere) from the same heteroplasmic individual. Astrocytes did not manifest preference for any mtDNA haplotype (Figure 73A-C). However, neurons clearly selected for NZB mtDNA from birth to natural death (Figure 73B). When animals were young (8-weeks-old females), the amount of NZB mtDNA was higher in astrocytes than in neurons (Figure 73A). Neurons from heteroplasmic mice presented higher amount of NZB mtDNA than astrocytes when were studied at older ages showing more pronounced differences with the ageing process (Figure 73C). These results reinforce the idea that OXPHOS demands determine the preferred mtDNA variant.

We also analysed the cell fraction that was negative for astrocytes and neurons. That fraction was mostly composed of oligodendrocytes and microglia ("resting" or active form), but also of other cell types such as tanycytes (specialized ependymal-like glial cells), pericytes, and endothelial and epithelial cells[324]. Interestingly, that fraction strongly segregated towards mtDNA NZB (Figure 73D). Microglia is defined as the population of resident immune cells of the central nervous system (CNS). This kind of cells can divide *in situ* and may be recruited from the circulating monocyte pool and differentiate into resident microglia[325]. More studies are necessary to analyse if the status of differentiation between monocytes and microglia can promote mtDNA selection.

V.3.A.8.f. Functional analysis of brain in heteroplasmic mice

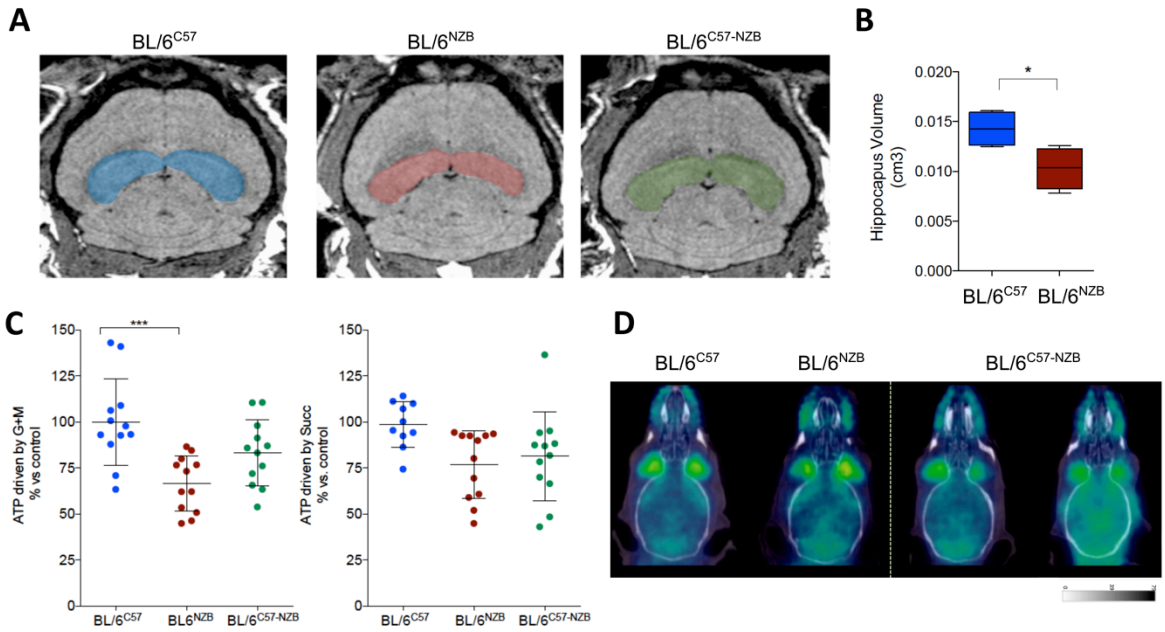

Figure 74. ***In vivo* and *ex vivo* brain metabolic performance in heteroplasmic mice. (A-B)** MRI analysis of brain from homoplasmic and heteroplasmic mice at 30 weeks of age. Representative images of the indicated genotypes (A) and quantification of total hippocampus volume in homoplasmic strains (B). **(C)** *Ex vivo* brain mitochondrial ATP synthesis rate driven by glutamate plus malate (G+M, left) or succinate (right) of 30-weeks-old mice. N = 6 mice per genotype, 2 technical replicates per condition. **(D)** Representative PET/CT images illustrating the distribution of the [^{18}F]-FDG uptake in the brain of 30-weeks-old homoplasmic and heteroplasmic mice (n = 6). **p-value* < 0.05, ****p-value* < 0.001, one-way ANOVA analysis.

In general, we associated lack of segregation with cellular impairment. Since no selection of any mtDNA by astrocytes was found, we inquired if tissue performance could be compromised in heteroplasmic mice due to their critical role in brain function. We performed a structural-functional analysis of the brain in 30-weeks-old mice using *in vivo* imaging techniques, MRI and PET/CT. We segmentated manually the brain areas, and we observed a decrease in the hippocampal total volume in BL/6^{NZB} in comparison with same regions of the BL/6^{C57} (Figure 74A, B). No significant differences between the conditions of homoplasmy and heteroplasmy were obtained (Figure 74A). These results corroborate a previous published work in congenic mice with respect to mtDNA (NZB/BINJ and CBA/H), that showed that mtDNA variants could alter brain morphology, sensory development, learning and exploration with the age of the animals[326]. The analysis of ATP synthesis in isolated mitochondria using the whole-brain of 20-weeks-old mice showed a trend to have higher efficiency of ATP production the BL/6^{C57} mitochondria. However, differences were only significant between conplastic mice with glutamate/malate as substrates (CI dependent) (Figure 74C). *In vivo* [^{18}F]-FDG PET/CT analysis revealed differences in the glucose uptake between brain regions. A visual inspection of the PET scans showed a different profile of [^{18}F]-FDG uptake in homoplasmic and heteroplasmic mice (Figure 74D). In homoplasmic mice, the pattern displayed well-defined regions with high glucose uptake clearly differentiated. We observed a huge heterogeneity in the heteroplasmic mice. The most significant changes compared to homoplasmic mice were in relation to (a) the clear increased uptake of this radioactive glucose analogue in some of the animals and (b) no differences in the distribution of the probe between areas of their brains (Figure 74D).

The analysis of the hippocampus area of 30-weeks-old mice by TEM revealed differences in microstructural composition and characterization. We observed an increase in the size of the axons and dendrites in the BL/6$^{C57\text{-}NZB}$ mice (Figure 75A, asterisks). Additionally, we found an increase of the thickness in myelin of the axons (Figure 75A, arrowhead), which has been previously described to have typical splits and ballooning changes during ageing[327,328]. Details of cellular components were analysed between hippocampus samples of heteroplasmic and homoplasmic mice (Figure 75B). We visualized differences in mitochondria, in shape and cristae electron density between neurons and astrocytes (Figure 75B). These functionally relevant parameters are indicators of differential activity of mitochondria in cells[322]. In addition, higher frequency of mitophagy was observed in neurons and astrocytes of heteroplasmic samples, although both populations showed a very heterogeneous phenotype. The glial cells had less cristae density and disrupted mitochondrial ultrastructure (Figure 75B, arrowhead). Other distinctive features of heteroplasmic brains were the rupture of the nucleus membrane and anomalies in nucleus shape, scattered necrotic cells (Figure 75C) and lipofuscin accumulation, which is usually present in neuronal ageing (Figure 75C, asterisk). Degenerated neurons are labelled dark in TEM preparations (Figure 75C) and are usually found in aged brain and characterized by an increase in filaments and irregular nuclei, although mostly preserving axosomatic synapsis[327].

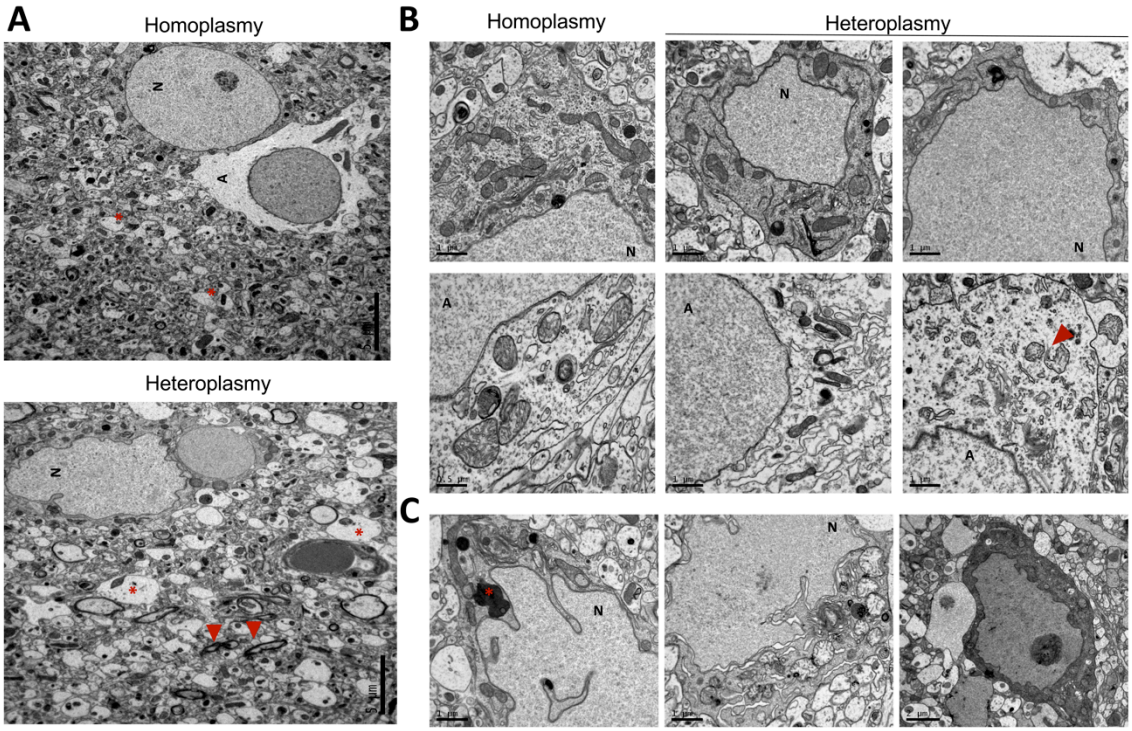

Figure 75. Ultrastructural analysis of hippocampus from homoplasmic and heteroplasmic mice. **(A)** Panoramic view of homoplasmic and heteroplasmic hippocampus. Red asterisks: alterations in axon size between homoplasmic and heteroplasmic mice. Red arrowheads: abnormal myelination in heteroplasmic mice**. (B)** Details of astrocytes and neurons. Red arrowhead indicates disrupted mitochondria. **(C)** Alterations in the ultrastructure of heteroplasmic brain cell populations. Left: lipofuscin accumulation and abnormal nucleus shape. Middle: loss of cristae in mitochondria of heteroplasmic cell. Right: necrotic cell. 30-weeks-old mice, n = 4 per genotype. N= neuron; A= astrocyte.

Histological analysis revealed the potential alterations in the total number of cells in the temporal and septal hippocampus, more specifically in the *Cornu Ammonis* (CA1, *stratum radiatum, lacunosum* and *moleculare*) and in the *dentate gyrus-hilus*, the input region of the hippocampus[329] (Figure 76A, B). The nucleus of the cells was stained with DAPI (blue) for an easy quantification of the number of cells. The astrocytes were immunoassayed with antibodies against the glial fibrillary acidic protein (GFAP, green), and microglia was immunostained against ionized calcium binding adaptor molecule 1 (IBA1, red)

(Figure 76). No differences in the total number of cells were found (Figure 76A, B). However, immunostaining of GFAP and IBA1 in temporal hippocampus revealed a trend in the increase in the microglia and a reduction of $GFAP^{+}$ cells (astroglia) in 30-weeks-old heteroplasmic brains (Figure 76 C, D). It is also important to notice the reduction in the biomarkers of ageing of $BL/6^{NZB}$ compared with $BL/6^{C57}$ (less microglia assessed by IBA1) (Figure 76D). Together with the TEM analysis, the results suggest that heteroplasmic mice lost functional cells in the area of the hippocampus.

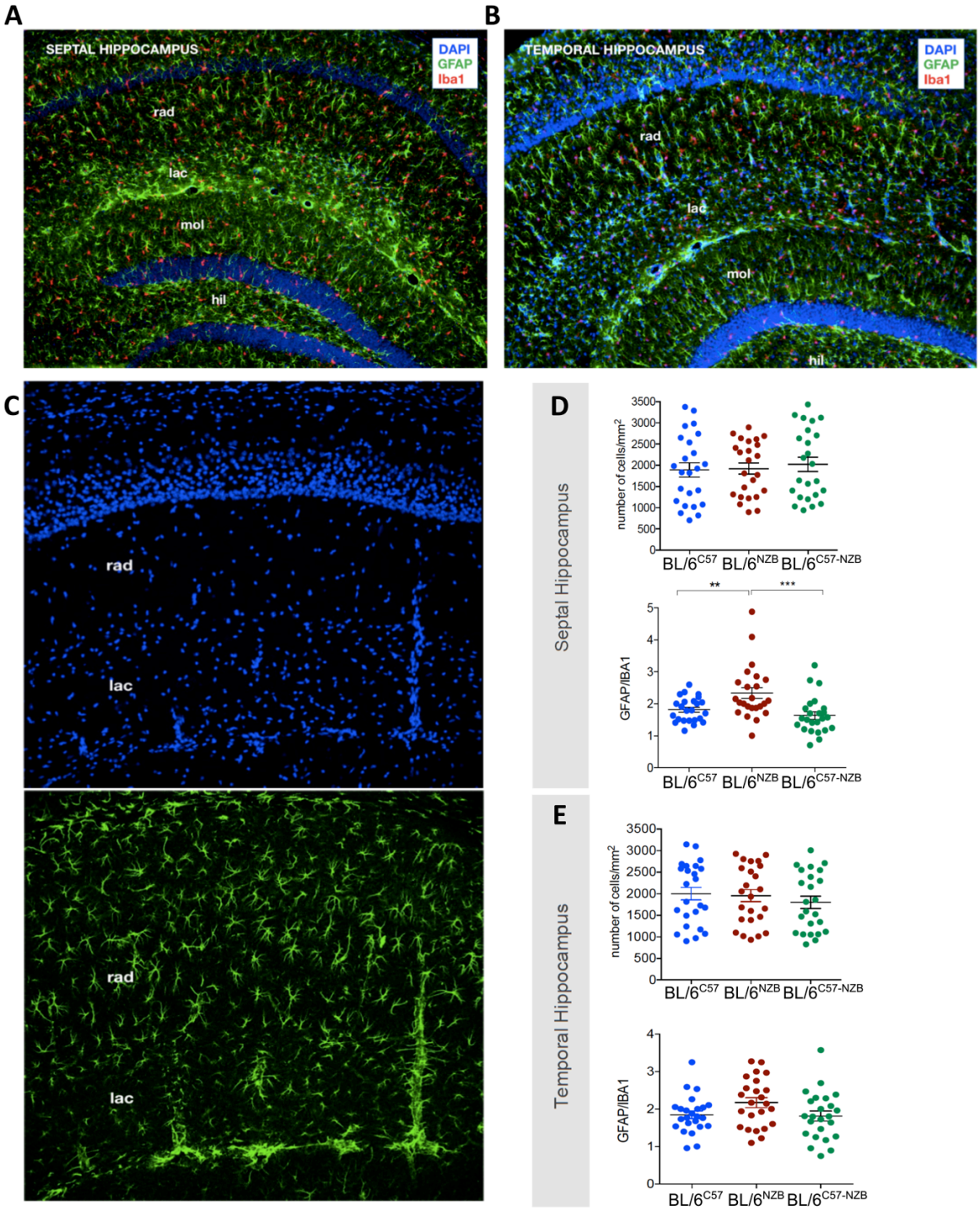

Figure 76. Confocal analysis of astroglia and microglia in the hippocampus of heteroplasmic mice. (A-C) Immunofluorescence microscopy images illustrating the labelling of GFAP and IBA1 in septal and temporal hippocampus from 30-weeks-old mice**. (D-E)** Quantification of the total number of cells per area and the ratio between $GFAP^{+}/IBA1^{+}$ in septal (D) and temporal (E) hippocampus of the sections in (A-C). Hil: *dentate gyrus hilus*. *Stratum* rad: *radiatum;* Lac: *lacunosum*; mol: *moleculare*.

Zhang *et al.* (2013) previously described that the hypothalamus has a critical role in systemic ageing[330]. We performed an histological examination of basal hypothalamus in the three strains (30-weeks-old mice) to evaluate the population of neural stem/progenitor cells (NSCs), specifically those present in the mediobasal hypothalamus, previously described to regulate the physiological homeostasis in the organism[331]. It was recently reported that the loss of the $Sox2^+$ hypothalamic cells in mice is a hallmark of ageing[331]. Data obtained from confocal imaging showed that heteroplasmic animals have a reduced proportion of $Sox2^+$ measured in the median eminence, the anatomical link between the hypothalamus and anterior pituitary[332] (Figure 77A-C). Furthermore, the number of astrocytes ($GFAP^+$ cells) was significant lower in the arcuate nucleus of the heteroplasmic mice (Figure 77B, D) although the microglia ($IBA1^+$ cells) remain similar to the homoplasmic counterparts (Figure 77B, bottom). In the same way, the analysis done in the substantia nigra revealed no changes between the three strains (Figure 77E).

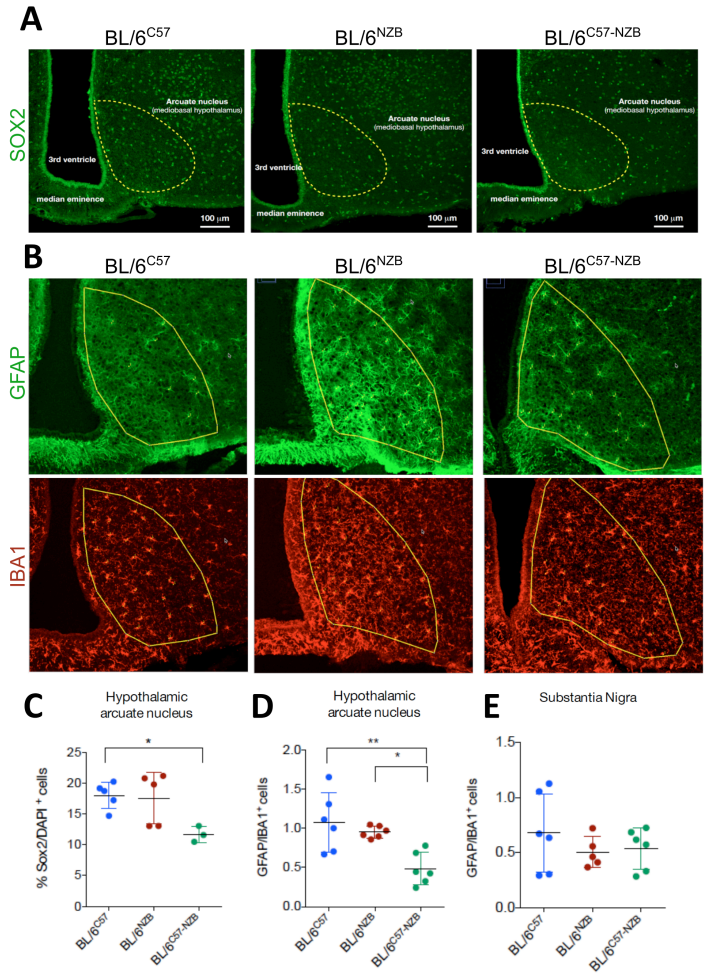

Figure 77. Confocal analysis of hypothalamic stem/progenitor cells, astroglia and microglia in brains from homoplasmic and heteroplasmic mice. Representative images of hypothalamic brain sections from homoplasmic and heteroplasmic mice at 30 weeks of age immunostained for SOX2 **(A)**, GFAP as a marker of astroglia **(B-top)** and IBA1 as a marker of microglia **(B-bottom)**. Total $SOX2^+$ cells **(C)**, the ratio of GFAP/IBA1 in hypothalamus **(D)** and in the substantia nigra **(E)** were estimated from (A-B). **p-value* < 0.05, ***p-value* < 0.01 assessed by ANOVA test. Each dot corresponds to an individual mouse.

One of the therapeutic tools that may generate heteroplasmy is the transfer of mtDNA from donor cells to damaged cells. This mitochondrial repopulation *in situ* has been also proposed in brain, where first transfer experiments of healthy mitochondria from astrocytes to neurons after an injury could help to recover the neurological function[150]. The obtained results indicate that if for any reason there is no mtDNA

match in the difference cell populations, it is important to take into consideration the prevention of the long-term adverse consequences on the whole tissue.

V.3.B. Discussion

Among the three nuclear loci found that affect the segregation of mtDNA in heteroplasmic mice, Gimap3 is the only expressed gene in hematopoietic tissues that mediates the segregation which favours C57 mtDNA in leukocytes[155,158]. Until now, it was the only nuclear gene shown to be capable of modifying mtDNA segregation in a tissue-specific way but its functional role and the mechanism responsible remain a mystery. The results presented above reveal novel genes potentially involved in metabolic optimization and in REDOX signalling, that can modify the profiles of mtDNA selection in the studied tissues. The SCAF1[113] protein reduces the intensity of segregation in tissues that select strongly towards C57 mtDNA (ie. pancreas, thymus, spleen or bone marrow). The NNT protein minimizes the segregation towards C57 mtDNA and activates the segregation in favour of NZB mtDNA (Figure 79). However, understanding how ROS signalling is transduced in the molecular mechanisms that drive non-random mtDNA segregation requires further investigation.

After the longitudinal study of heteroplasmic mice with different nuclear gene modifications, we demonstrated that the severity of the phenotype could be modulated. In the case of the SCAF1[113], even with only one copy of the functional protein, mice can delay the pathological phenotype induced by heteroplasmy. However, in any case, the heteroplasmy condition generates a disease phenotype. Different nuclear background and ages of the studied animals could be the reason why previously studies, driven for example with some C57BL/6 mice substrains, described neutrality of heteroplasmy between non-pathological mtDNA variants in young-adult heteroplasmic mice.

The long-lasting discussion about the random or non-random segregation of non-pathological mtDNA variants has been critical. How the cell directly discriminates the DNA sequence variants and if the assumption that mtDNA haplotypes do not promote functional differences have been controversially debated in different studies, including previous works from our group, which demonstrated *in vivo* that mtDNA variants generate different OXPHOS status[16,25]. In the context of the heteroplasmic mouse models, a range of functionally different OXPHOS allows defining a specific healthy status. Different OXPHOS are compatible with the characteristic healthy status because of the regulatory and adaptive response of the cell to specific OXPHOS requirements of different cell types. The two different mtDNA haplotypes require different regulatory responses based on OXPHOS function. The differences between our model and a model with pathological mtDNA variants reside in that the adaptive response and its regulation fail when the disease arises. In this doctoral thesis, it has been demonstrated that the segregation behaviour is indeed sensitive to OXPHOS requirements *in vivo*, and that segregation in the germline and in tissues is driven by functional selection.



Conclusions

VI. Conclusions

1. Interchanging mtDNA haplotypes modifies OXPHOS performance and reorganization supporting our hypothesis that mtDNA/nDNA matches in healthy individuals.

2. We have demonstrated the influence of the mtDNA variability on lipid and carbohydrate metabolism, which determines a different predisposition to diabetes, obesity and conspicuous differences in healthy ageing. This was achieved through the generation of functionally different OXPHOS systems supporting the conclusion that different mtDNA wild type haplotypes are phenotypically relevant.

3. We documented in detail that mtDNA heteroplasmy is actively combated during germline transmission, embryonic development and somatic life of most differentiated cells.

4. We propose a new active mechanism promoting homoplasmy in stages when the embryo contains pluripotent cells. Pluripotency favours homoplasmy in an OXPHOS-dependent manner.

5. MtDNA segregation is required to prevent loss of cell fitness caused by heteroplasmy. Persistent heteroplasmy of non-pathological mtDNA haplotypes in critical organs increases the likelihood of death at younger age and shows an overall premature ageing-like phenotype.

6. We demonstrated that mtDNA heteroplasmy alone, even when both mtDNA types are individually non-pathogenic, causes pathological conditions affecting mainly the tissues that are not able to resolve it: heart, lung and skeletal muscle as relevant examples.

7. Heteroplasmy strikingly affects cardiac tissue inducing oxidative damage to proteins of the OXPHOS system. We provide a new molecular mechanism explaining the structural and functional alterations found in cardiac mitochondria.

8. The metabolic differentiation program determines the preferred mtDNA haplotype.

9. MtDNA preference is cell-type specific and not tissue specific.

10. MtDNA selection is strongly modulated by the crosstalk between the nucleus and mitochondria.

11. The segregation behavior is indeed sensitive to OXPHOS requirements *in vivo*, and this segregation is driven by functional selection.

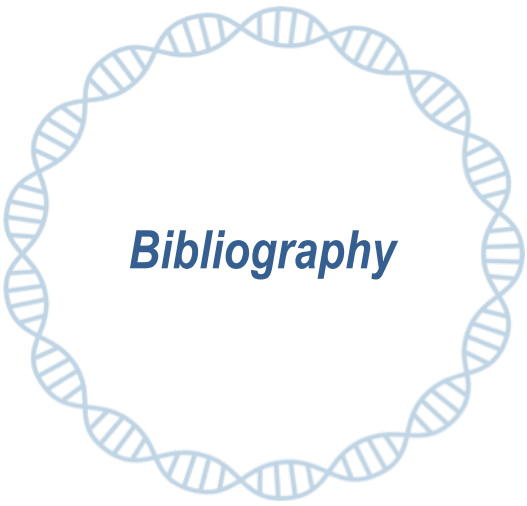

Bibliography

VII. Bibliography

1. Wai, T. & Langer, T. Mitochondrial Dynamics and Metabolic Regulation. *Trends Endocrinol. Metab.* 27, 105–117 (2016).
2. Roger, A. J., Muñoz-Gómez, S. A. & Kamikawa, R. The Origin and Diversification of Mitochondria. *Curr. Biol.* 27, R1177–R1192 (2017).
3. Mcbride, H. M., Neuspiel, M. & Wasiak, S. Review Mitochondria: More Than Just a Powerhouse. (2006). doi:10.1016/j.cub.2006.06.054
4. Cagin, U. & Enriquez, J. A. The complex crosstalk between mitochondria and the nucleus: What goes in between? *Int. J. Biochem. Cell Biol.* 63, 10–15 (2015).
5. Chandel, N. S. Essay Evolution of Mitochondria as Signaling Organelles. *Cell Metab.* 22, 204–206 (2015).
6. CHAFFEY, N. Alberts, B., Johnson, A., Lewis, J., Raff, M., Roberts, K. and Walter, P. Molecular biology of the cell. 4th edn. *Ann. Bot.* 91, 401–401 (2003).
7. Cogliati, S., Enriquez, J. A. & Scorrano, L. Mitochondrial Cristae: Where Beauty Meets Functionality. *Trends Biochem. Sci.* 41, 261–273 (2016).
8. Giorgi, C. *et al.* Mitochondria-Associated Membranes: Composition, Molecular Mechanisms, and Physiopathological Implications. *Antioxid. Redox Signal.* 22, 995–1019 (2015).
9. Cooper, G. M. *The cell : a molecular approach*. (ASM Press, 2000).
10. Galloway, C. A., Lee, H. & Yoon, Y. Mitochondrial morphology-emerging role in bioenergetics. *Free Radic. Biol. Med.* 53, 2218–28 (2012).
11. Picard, M., Wallace, D. C. & Burelle, Y. The rise of mitochondria in medicine. *Mitochondrion* 30, 105–16 (2016).
12. Picard, M. *et al.* Trans-mitochondrial coordination of cristae at regulated membrane junctions. *Nat. Commun.* 6, 6259 (2015).
13. Cogliati, S. *et al.* Mitochondrial cristae shape determines respiratory chain supercomplexes assembly and respiratory efficiency. *Cell* 155, 160–71 (2013).
14. Anand, R. *et al.* The i-AAA protease YME1L and OMA1 cleave OPA1 to balance mitochondrial fusion and fission. *J. Cell Biol.* 204, 919–929 (2014).
15. Rovira-Llopis, S. *et al.* Mitochondrial dynamics in type 2 diabetes: Pathophysiological implications Foundation for the Promotion of Health and Biomedical Research in the. (2017). doi:10.1016/j.redox.2017.01.013
16. Latorre-Pellicer, A. *et al.* Mitochondrial and nuclear DNA matching shapes metabolism and healthy ageing. *Nature* 535, 561–565 (2016).
17. Herbers, E., Kekäläinen, N. J., Hangas, A., Pohjoismäki, J. L. & Goffart, S. Tissue specific differences in mitochondrial DNA maintenance and expression. *Mitochondrion* (2018). doi:10.1016/J.MITO.2018.01.004
18. Matsuyama, S. & Reed, J. C. Mitochondria-dependent apoptosis and cellular pH regulation. *Cell Death Differ.* 7, 1155–1165 (2000).
19. Perry, S. W., Norman, J. P., Barbieri, J., Brown, E. B. & Gelbard, H. A. Mitochondrial membrane potential probes and the proton gradient: a practical usage guide. *Biotechniques* 50, 98–115 (2011).
20. Wallace, D. C. Bioenergetics in human evolution and disease: implications for the origins of biological complexity and the missing genetic variation of common diseases. *Philos. Trans. R. Soc. Lond. B. Biol. Sci.* 368, 20120267 (2013).
21. Lemasters, J. J., Theruvath, T. P., Zhong, Z. & Nieminen, A.-L. Mitochondrial calcium and the permeability transition in cell death. *Biochim. Biophys. Acta - Bioenerg.* 1787, 1395–1401 (2009).
22. Campello, S., Strappazzon, F. & Cecconi, F. Mitochondrial dismissal in mammals, from protein degradation to mitophagy. *Biochim. Biophys. Acta - Bioenerg.* 1837, 451–460 (2014).
23. Acín-Pérez, R. *et al.* ROS-triggered phosphorylation of complex II by Fgr kinase regulates cellular adaptation to fuel use. *Cell Metab.* 19, 1020–1033 (2014).
24. Murphy, M. P. How mitochondria produce reactive oxygen species. *Biochem. J.* 417, 1–13 (2009).
25. Moreno-Loshuertos, R. *et al.* Differences in reactive oxygen species production explain the phenotypes associated with common mouse mitochondrial DNA variants. *Nat. Genet.* 38, 1261–1268 (2006).
26. Moreno-Loshuertos, R. *et al.* Evolution meets disease: penetrance and functional epistasis of mitochondrial tRNA mutations. *PLoS Genet.* 7, e1001379 (2011
27. Murphy, M. P. Understanding and preventing mitochondrial oxidative damage. *Biochem. Soc. Trans.* 44, 1219–1226 (2016).
28. Kloner, R. A. *et al.* New and revisited approaches to preserving the reperfused myocardium. *Nat. Rev.*

Cardiol. 14, 679–693 (2017).
29. Formentini, L. *et al.* Mitochondrial ROS Production Protects the Intestine from Inflammation through Functional M2 Macrophage Polarization. *Cell Rep.* 19, 1202–1213 (2017).
30. Lin, M. T. & Beal, M. F. *Mitochondrial dysfunction and oxidative stress in neurodegenerative diseases*. 443, 787–795 (Nature Publishing Group, 2006).
31. Topf, U. *et al.* Quantitative proteomics identifies redox switches for global translation modulation by mitochondrially produced reactive oxygen species. *Nat. Commun.* 9, 324 (2018).
32. Guarás, A. *et al.* The CoQH2/CoQ Ratio Serves as a Sensor of Respiratory Chain Efficiency. *Cell Rep.* 15, 197–209 (2016).
33. Dröse, S. Differential effects of complex II on mitochondrial ROS production and their relation to cardioprotective pre- and postconditioning. *Biochim. Biophys. Acta - Bioenerg.* 1827, 578–587 (2013).
34. Murphy, M. P. How mitochondria produce reactive oxygen species. *Biochem. J* 417, 1–13 (2009).
35. Bleier, L. *et al.* Generator-specific targets of mitochondrial reactive oxygen species. *Free Radic. Biol. Med.* 78, 1–10 (2015).
36. Quinlan, C. L. *et al.* Mitochondrial complex II can generate reactive oxygen species at high rates in both the forward and reverse reactions. *J. Biol. Chem.* 287, 27255–64 (2012).
37. Balsa, E. *et al.* NDUFA4 is a subunit of complex IV of the mammalian electron transport chain. *Cell Metab.* 16, 378–86 (2012).
38. Hirst, J., King, M. S. & Pryde, K. R. The production of reactive oxygen species by complex I. *Biochem. Soc. Trans.* 36, 976–80 (2008).
39. Ganini, D., Santos, J. H., Bonini, M. G. & Mason, R. P. Switch of Mitochondrial Superoxide Dismutase into a Prooxidant Peroxidase in Manganese-Deficient Cells and Mice. *Cell Chem. Biol.* 0, (2018).
40. Klaips, C. L., Jayaraj, G. G. & Hartl, F. U. Pathways of cellular proteostasis in aging and disease. *J. Cell Biol.* 217, 51–63 (2018).
41. Nargund, A. M., Fiorese, C. J., Pellegrino, M. W., Deng, P. & Haynes, C. M. Mitochondrial and nuclear accumulation of the transcription factor ATFS-1 promotes OXPHOS recovery during the UPR(mt). *Mol. Cell* 58, 123–33 (2015).
42. Melber, A. & Haynes, C. M. UPR mt regulation and output: a stress response mediated by mitochondrial-nuclear communication. *Nat. Publ. Gr.* 1–15 (2018). doi:10.1038/cr.2018.16
43. Wrobel, L. *et al.* Mistargeted mitochondrial proteins activate a proteostatic response in the cytosol. *Nature* 524, 485–488 (2015).
44. Jovaisaite, V., Mouchiroud, L. & Auwerx, J. The mitochondrial unfolded protein response, a conserved stress response pathway with implications in health and disease. *J. Exp. Biol.* 217, 137–43 (2014).
45. Corazzari, M., Gagliardi, M., Fimia, G. M. & Piacentini, M. Endoplasmic Reticulum Stress, Unfolded Protein Response, and Cancer Cell Fate. *Front. Oncol.* 7, 78 (2017).
46. Bravo, R. *et al.* Endoplasmic reticulum and the unfolded protein response: dynamics and metabolic integration. *Int. Rev. Cell Mol. Biol.* 301, 215–90 (2013).
47. Harding, H. P. *et al.* An integrated stress response regulates amino acid metabolism and resistance to oxidative stress. *Mol. Cell* 11, 619–33 (2003).
48. Richard, V. R. *et al.* Macromitophagy is a longevity assurance process that in chronologically aging yeast limited in calorie supply sustains functional mitochondria and maintains cellular lipid homeostasis. *Aging (Albany. NY).* 5, 234–69 (2013).
49. Ashrafi, G. & Schwarz, T. The pathways of mitophagy for quality control and clearance of mitochondria. (2013). doi:10.1038/cdd.2012.81
50. Lazarou, M. Keeping the immune system in check: a role for mitophagy. *Immunol. Cell Biol.* 93, 3–10 (2015).
51. Shi, R., Guberman, M. & Kirshenbaum, L. A. Mitochondrial quality control: The role of mitophagy in aging. *Trends Cardiovasc. Med.* (2017). doi:10.1016/J.TCM.2017.11.008
52. López-Otín, C., Blasco, M. A., Partridge, L., Serrano, M. & Kroemer, G. The hallmarks of aging. *Cell* 153, 1194–217 (2013).
53. HARMAN, D. Free Radical Theory of Aging: An Update: Increasing the Functional Life Span. *Ann. N. Y. Acad. Sci.* 1067, 10–21 (2006).
54. Höhn, A. *et al.* Happily (n)ever after: Aging in the context of oxidative stress, proteostasis loss and cellular senescence. *Redox Biol.* 11, 482–501 (2017).
55. HARMAN, D. Aging: a theory based on free radical and radiation chemistry. *J. Gerontol.* 11, 298–300 (1956).
56. Miquel, J. An update on the oxygen stress-mitochondrial mutation theory of aging: genetic and evolutionary implications. *Exp. Gerontol.* 33, 113–26
57. Barja, G. en *Progress in molecular biology and translational science* 127, 1–27 (2014).
58. Reiter, R. *et al.* Mitochondria: Central Organelles for Melatonin′s Antioxidant and Anti-Aging Actions.

Molecules 23, 509 (2018).
59. Lee, H.-C. & Wei, Y.-H. en 311–327 (2012). doi:10.1007/978-94-007-2869-1_14
60. Laberge, R.-M. *et al.* Mitochondrial DNA damage induces apoptosis in senescent cells. *Cell Death Dis.* 4, e727–e727 (2013).
61. Shirakabe, A., Ikeda, Y., Sciarretta, S., Zablocki, D. K. & Sadoshima, J. Aging and Autophagy in the Heart. *Circ. Res.* 118, 1563–76 (2016).
62. Tian, Y. *et al.* Mitochondrial Stress Induces Chromatin Reorganization to Promote Longevity and UPR(mt). *Cell* 165, 1197–1208 (2016).
63. Instituto Nacional de Estadistica. (Spanish Statistical Office). en <http://www.ine.es/>
64. Piantadosi, C. A. & Suliman, H. B. Mitochondrial Dysfunction in Lung Pathogenesis. *Annu. Rev. Physiol* 79, 495–515 (2017).
65. Liu, X. & Chen, Z. The pathophysiological role of mitochondrial oxidative stress in lung diseases. *J. Transl. Med.* 15, (2017).
66. Ryan, J., Dasgupta, A., Huston, J., Chen, K.-H. & Archer, S. L. Mitochondrial dynamics in pulmonary arterial hypertension. *J. Mol. Med.* 93, 229–242 (2015).
67. Hsia, C. C. W., Hyde, D. M. & Weibel, E. R. Lung Structure and the Intrinsic Challenges of Gas Exchange. doi:10.1002/cphy.c150028
68. Cloonan, S. M. & Choi, A. M. K. Mitochondria in lung disease. *J. Clin. Invest.* 126, 809–20 (2016).
69. Pak, O. *et al.* Mitochondrial Hyperpolarization in Pulmonary Vascular Remodeling. Mitochondrial Uncoupling Protein Deficiency as Disease Model. *Am. J. Respir. Cell Mol. Biol.* 49, 358–367 (2013).
70. Kim, S.-J., Cheresh, P., Jablonski, R. P., Williams, D. B. & Kamp, D. W. The Role of Mitochondrial DNA in Mediating Alveolar Epithelial Cell Apoptosis and Pulmonary Fibrosis. *Int. J. Mol. Sci.* 16, 21486–519 (2015).
71. Madhukaran, S. P. *et al.* Expression of surfactant proteins SP-A and SP-D in murine decidua and immunomodulatory effects on decidual macrophages. *Immunobiology* 221, 377–386 (2016).
72. Win, T. *et al.* Pulmonary 18F-FDG uptake helps refine current risk stratification in idiopathic pulmonary fibrosis (IPF). *Eur. J. Nucl. Med. Mol. Imaging* 1–10 (2018). doi:10.1007/s00259-017-3917-8
73. Es Selman, M. & Pardo, A. Revealing the Pathogenic and Aging-related Mechanisms of the Enigmatic Idiopathic Pulmonary Fibrosis An Integral Model. doi:10.1164/rccm.201312-2221PP
74. Mora, A. L., Bueno, M. & Rojas, M. Mitochondria in the spotlight of aging and idiopathic pulmonary fibrosis. *J. Clin. Invest.* 127, 405–414 (2017).
75. Edgar, D. & Trifunovic, A. The mtDNA mutator mouse: Dissecting mitochondrial involvement in aging. *Aging (Albany. NY).* 1, 1028–32 (2009).
76. Jacob, J. *et al.* Likelihood of pulmonary hypertension in patients with idiopathic pulmonary fibrosis and emphysema. *Respirology* (2017). doi:10.1111/resp.13231
77. Seeger, W. *et al.* Pulmonary Hypertension in Chronic Lung Diseases. *J. Am. Coll. Cardiol.* 62, D109–D116 (2013).
78. Farkas, L., Gauldie, J., Voelkel, N. F. & Kolb, M. Pulmonary Hypertension and Idiopathic Pulmonary Fibrosis. *Am. J. Respir. Cell Mol. Biol.* 45, 1–15 (2011).
79. Galiè, N. *et al.* 2015 ESC/ERS Guidelines for the Diagnosis and Treatment of Pulmonary Hypertension. *Rev. Española Cardiol. (English Ed.* 69, 177 (2016).
80. Talati, M. & Hemnes, A. Fatty acid metabolism in pulmonary arterial hypertension: role in right ventricular dysfunction and hypertrophy. *Pulm Circ* 5, 269–278 (2015).
81. Dromparis, P. & Michelakis, E. D. *Mitochondria in vascular health and disease. Annual review of physiology* 75, (2013).
82. Talati, M. & Hemnes, A. Fatty acid metabolism in pulmonary arterial hypertension: role in right ventricular dysfunction and hypertrophy. *Pulm Circ* 5, 269–278 (2015).
83. Talati, M. & Hemnes, A. Fatty acid metabolism in pulmonary arterial hypertension: role in right ventricular dysfunction and hypertrophy. *Pulm. Circ.* 5, 269–78 (2015).
84. Farha, S. *et al.* Mitochondrial Haplogroups and Risk of Pulmonary Arterial Hypertension. *PLoS One* 11, e0156042 (2016).
85. Enríquez, J. A. Supramolecular organization of respiratory complexes. *Annu. Rev. Physiol.* 78, 533–561 (2016).
86. Stewart, J. B., Freyer, C., Elson, J. L. & Larsson, N.-G. Purifying selection of mtDNA and its implications for understanding evolution and mitochondrial disease. *Nat. Rev. Genet.* 9, 657–662 (2008).
87. Miller, S. *et al. Handbook of flavoproteins : Volume 1 oxidases, dehydrogenases and related systems.* (De Gruyter, 2012).
88. Watmough, N. J. & Frerman, F. E. The electron transfer flavoprotein: Ubiquinone oxidoreductases. *Biochim. Biophys. Acta - Bioenerg.* 1797, 1910–1916 (2010).
89. Enríquez, J. A., Sánchez-Cabo, F. & Vázquez, J. S. Hypothesis Driven versus Hypothesis-free: Filling

the Gaps in CoQ Biosynthesis. *Cell Metab.* 24, 525–526 (2016).
90. Servet, C., Ghelis, T., Richard, L., Zilberstein, A. & Savoure, A. Proline dehydrogenase: a key enzyme in controlling cellular homeostasis. *Front. Biosci. (Landmark Ed.* 17, 607–20 (2012).
91. Fukuda, R. *et al.* HIF-1 Regulates Cytochrome Oxidase Subunits to Optimize Efficiency of Respiration in Hypoxic Cells. *Cell* 129, 111–122 (2007).
92. Guerrero-Castillo, S. *et al.* The Assembly Pathway of Mitochondrial Respiratory Chain Complex I. *Cell Metab.* 25, 128–139 (2017).
93. Quirós, P. M. *et al.* ATP-dependent Lon protease controls tumor bioenergetics by reprogramming mitochondrial activity. *Cell Rep.* 8, 542–56 (2014).
94. Keilin, D. & Hartree, E. F. Activity of the cytochrome system in heart muscle preparations. *Biochem. J.* 41, 500–2 (1947).
95. Chance, B., Williams, G.R. Holmes, W.F. & Higgins J. Respiratory enzymes in oxidative phosphorylation. V. A mechanism for oxidative phosphorylation. *J. Biol. Chem.* 217, 439–51 (1955).
96. C hance, B., Williams, G.R. Respiratory enzymes in oxidative phosphorylation. IV. The respiratory chain. *J. Biol. Chem.* 217, 429–38 (1955).
97. Chance, B., Williams, G.R. A method for the localization of sites for oxidative phosphorylation. *Nature* 176, 250–4 (1955).
98. Hackenbrock, C. R., Chazotte, B. & Gupte, S. S. The random collision model and a critical assessment of diffusion and collision in mitochondrial electron transport. *J. Bioenerg. Biomembr.* 18, 331–68 (1986).
99. Mitchell, P. Coupling of phosphorylation to electron and hydrogen transfer by a chemi-osmotic type of mechanism. *Nature* 191, 144–8 (1961).
100. Gupte, S. S. & Hackenbrock, C. R. Multidimensional diffusion modes and collision frequencies of cytochrome c with its redox partners. *J. Biol. Chem.* 263, 5241–7 (1988).
101. Schägger, H. & Pfeiffer, K. The ratio of oxidative phosphorylation complexes I-V in bovine heart mitochondria and the composition of respiratory chain supercomplexes. *J. Biol. Chem.* 276, 37861–7 (2001).
102. Schägger, H. Blue-native gels to isolate protein complexes from mitochondria. *Methods Cell Biol.* 65, 231–44 (2001).
103. Acín-Pérez, R., Fernández-Silva, P., Peleato, M. L., Pérez-Martos, A. & Enriquez, J. A. Respiratory active mitochondrial supercomplexes. *Mol. Cell* 32, 529–39 (2008).
104. Acin-Perez, R. & Enriquez, J. a. The function of the respiratory supercomplexes: The plasticity model. *Biochim. Biophys. Acta - Bioenerg.* 1837, 444–450 (2014).
105. Lapuente-Brun, E. *et al.* Supercomplex Assembly Determines Electron Flux in the Mitochondrial Electron Transport Chain. *Science (80-.).* 340, 1567–1570 (2013).
106. Guo, R., Zong, S., Wu, M., Gu, J. & Yang, M. Architecture of Human Mitochondrial Respiratory Megacomplex I2III2IV2. *Cell* 170, 1247–1257.e12 (2017).
107. Giles, R. E., Blanc, H., Cann, H. M. & Wallace, D. C. Maternal inheritance of human mitochondrial DNA. *Proc. Natl. Acad. Sci. U. S. A.* 77, 6715–9 (1980).
108. Hayashi, J. I., Yonekawa, H., Gotoh, O., Watanabe, J. & Tagashira, Y. Strictly maternal inheritance of rat mitochondrial DNA. *Biochem. Biophys. Res. Commun.* 83, 1032–8 (1978).
109. Hutchison, C. A., Newbold, J. E., Potter, S. S. & Edgell, M. H. Maternal inheritance of mammalian mitochondrial DNA. *Nature* 251, 536–8 (1974).
110. HUDSON, B. & VINOGRAD, J. Catenated Circular DNA Molecules in HeLa Cell Mitochondria. *Nature* 216, 647–652 (1967).
111. Verma, M. & Kumar, D. en *Encyclopedia of Cancer* 2331–2333 (Springer Berlin Heidelberg, 2011). doi:10.1007/978-3-642-16483-5_3765
112. Shoubridge, E. A. Mitochondrial DNA segregation in the developing embryo. *Hum. Reprod.* 15 Suppl 2, 229–34 (2000).
113. Taylor, R. W. & Turnbull, D. M. Mitochondrial DNA mutations in human disease. *Nat. Rev. Genet.* 6, 389–402 (2005).
114. Eyre-Walker, A. & Awadalla, P. Does Human mtDNA Recombine? *J. Mol. Evol.* 53, 430–435 (2001).
115. Torregrosa-Muñumer, R. *et al.* PrimPol is required for replication reinitiation after mtDNA damage. *Proc. Natl. Acad. Sci. U. S. A.* 114, 11398–11403 (2017).
116. Carr, S. M. *et al.* Phylogeographic genomics of mitochondrial DNA: Highly-resolved patterns of intraspecific evolution and a multi-species, microarray-based DNA sequencing strategy for biodiversity studies. *Comp. Biochem. Physiol. Part D Genomics Proteomics* 3, 1–11 (2008).
117. Kong, Q.-P. *et al.* Phylogeny of East Asian Mitochondrial DNA Lineages Inferred from Complete Sequences. *Am. J. Hum. Genet.* 73, 671–676 (2003).
118. Stewart, J. B. & Chinnery, P. F. The dynamics of mitochondrial DNA heteroplasmy: implications for

human health and disease. *Nat. Rev. Genet.* 16, 530–542 (2015).
119. Wei, W., Gomez-Duran, A., Hudson, G. & Chinnery, P. F. Background sequence characteristics influence the occurrence and severity of disease-causing mtDNA mutations. *PLOS Genet.* 13, e1007126 (2017).
120. Tranah, G. J. *et al.* Mitochondrial DNA variation in human metabolic rate and energy expenditure. (2011). doi:10.1016/j.mito.2011.04.005
121. Ruiz-Pesini, E. *et al.* Human mtDNA haplogroups associated with high or reduced spermatozoa motility. *Am. J. Hum. Genet.* 67, 682–696 (2000).
122. Holt, I. J., Harding, A. E. & Morgan-Hughes, J. A. Mitochondrial DNA polymorphism in mitochondrial myopathy. *Hum. Genet.* 79, 53–7 (1988).
123. Zeviani, M. *et al.* Deletions of mitochondrial DNA in Kearns-Sayre syndrome. *Neurology* 38, 1339–46 (1988).
124. Poulton, J. Mitochondrial DNA and genetic disease. *Arch. Dis. Child.* 63, 883–5 (1988).
125. Wallace, D. C. *et al.* Familial mitochondrial encephalomyopathy (MERRF): genetic, pathophysiological, and biochemical characterization of a mitochondrial DNA disease. *Cell* 55, 601–10 (1988).
126. Holt, I. J., Harding, A. E. & Morgan-Hughes, J. A. Deletions of muscle mitochondrial DNA in patients with mitochondrial myopathies. *Nature* 331, 717–719 (1988).
127. Pohjoismäki, J. L. O., Goffart, S. & Spelbrink, J. N. Replication stalling by catalytically impaired Twinkle induces mitochondrial DNA rearrangements in cultured cells. *Mitochondrion* 11, 630–634 (2011).
128. Hudson, G. *et al.* Clinical expression of Leber hereditary optic neuropathy is affected by the mitochondrial DNA-haplogroup background. *Am. J. Hum. Genet.* 81, 228–33 (2007).
129. Brown, M. D., Torroni, A., Reckord, C. L. & Wallace, D. C. Phylogenetic analysis of Leber's hereditary optic neuropathy mitochondrial DNA's indicates multiple independent occurrences of the common mutations. *Hum. Mutat.* 6, 311–25 (1995).
130. Ma, H. *et al.* Incompatibility between Nuclear and Mitochondrial Genomes Contributes to an Interspecies Reproductive Barrier. *Cell Metab.* 24, 283–94 (2016).
131. Krzywanski, D. M. *et al.* Endothelial Cell Bioenergetics and Mitochondrial DNA Damage Differ in Humans Having African or West Eurasian Maternal AncestryCLINICAL PERSPECTIVE. *Circ. Cardiovasc. Genet.* 9, 26–36 (2016).
132. Chalkia, D. *et al.* Association Between Mitochondrial DNA Haplogroup Variation and Autism Spectrum Disorders. *JAMA Psychiatry* 74, 1161 (2017).
133. Duhn, P. H., Sode, J., Hagen, C. M., Christiansen, M. & Locht, H. Mitochondrial haplogroups in patients with rheumatoid arthritis: No association with disease and disease manifestations. *PLoS One* 12, e0188492 (2017).
134. Kalman, B. *et al.* Large scale screening of the mitochondrial DNA reveals no pathogenic mutations but a haplotype associated with multiple sclerosis in Caucasians. *Acta Neurol. Scand.* 99, 16–25 (1999).
135. Collerton, J. *et al.* Frailty and mortality are not influenced by mitochondrial DNA haplotypes in the very old. *Neurobiol. Aging* 34, 2889.e1-2889.e4 (2013).
136. Hudson, G. *et al.* No evidence of an association between mitochondrial DNA variants and osteoarthritis in 7393 cases and 5122 controls. *Ann. Rheum. Dis.* 72, 136–9 (2013).
137. Hudson, G. *et al.* No consistent evidence for association between mtDNA variants and Alzheimer disease. *Neurology* 78, 1038–1042 (2012).
138. Amo, T., Yadava, N., Oh, R., Nicholls, D. G. & Brand, M. D. Experimental assessment of bioenergetic differences caused by the common European mitochondrial DNA haplogroups H and T. *Gene* 411, 69–76 (2008).
139. Lomax, M. I. & Grossman, L. I. Tissue-specific genes for respiratory proteins. *Trends Biochem. Sci.* 14, 501–3 (1989).
140. Pierron, D. *et al.* Cytochrome c oxidase: evolution of control via nuclear subunit addition. *Biochim. Biophys. Acta* 1817, 590–7 (2012).
141. Vijayasarathy, C. *et al.* Variations in the subunit content and catalytic activity of the cytochrome c oxidase complex from different tissues and different cardiac compartments. *Biochim. Biophys. Acta - Biomembr.* 1371, 71–82 (1998).
142. Cogliati, S. *et al.* Mechanism of super-assembly of respiratory complexes III and IV. *Nature* 539, 579–582 (2016).
143. Guerrero-Castillo, S., Cabrera-Orefice, A., Huynen, M. A. & Arnold, S. Identification and evolutionary analysis of tissue-specific isoforms of mitochondrial complex I subunit NDUFV3. *Biochim. Biophys. Acta* 1858, 208–217 (2017).
144. Song, W.-H., Yi, Y.-J., Sutovsky, M., Meyers, S. & Sutovsky, P. Autophagy and ubiquitin–proteasome system contribute to sperm mitophagy after mammalian fertilization. *Proc. Natl. Acad. Sci.* 113, E5261–

E5270 (2016).
145. Kang, E. *et al.* Age-Related Accumulation of Somatic Mitochondrial DNA Mutations in Adult-Derived Human iPSCs. *Cell Stem Cell* 18, 625–36 (2016).
146. Kirches, E. MtDNA As a Cancer Marker: A Finally Closed Chapter? *Curr. Genomics* 18, 255–267 (2017).
147. Ye, K., Lu, J., Ma, F., Keinan, a. & Gu, Z. Extensive pathogenicity of mitochondrial heteroplasmy in healthy human individuals. *Proc. Natl. Acad. Sci.* 1403521111- (2014). doi:10.1073/pnas.1403521111
148. Kennedy, S. R., Salk, J. J., Schmitt, M. W. & Loeb, L. A. Ultra-sensitive sequencing reveals an age-related increase in somatic mitochondrial mutations that are inconsistent with oxidative damage. *PLoS Genet.* 9, e1003794 (2013).
149. Agnati, L. F. *et al.* A new hypothesis of pathogenesis based on the divorce between mitochondria and their host cells: possible relevance for Alzheimer's disease. *Curr. Alzheimer Res.* 7, 307–22 (2010).
150. Hayakawa, K. *et al.* Transfer of mitochondria from astrocytes to neurons after stroke. *Nature* 535, 551–5 (2016).
151. Kitani, T., Kami, D., Matoba, S. & Gojo, S. Internalization of isolated functional mitochondria: involvement of macropinocytosis. *J. Cell. Mol. Med.* 18, 1694–1703 (2014).
152. Holt, I. J., Harding, A. E. & Morgan-Hughes, J. A. Deletions of muscle mitochondrial DNA in mitochondrial myopathies: sequence analysis and possible mechanisms. *Nucleic Acids Res.* 17, 4465–9 (1989).
153. Burgstaller, J. P., Johnston, I. G. & Poulton, J. Mitochondrial DNA disease and developmental implications for reproductive strategies. *Mol. Hum. Reprod.* 21, 11–22 (2015).
154. Burgstaller, J. P. *et al.* MtDNA segregation in heteroplasmic tissues is common in vivo and modulated by haplotype differences and developmental stage. *Cell Rep.* 7, 2031–2041 (2014).
155. Battersby, B. J., Loredo-Osti, J. C. & Shoubridge, E. a. Nuclear genetic control of mitochondrial DNA segregation. *Nat. Genet.* 33, 183–186 (2003).
156. Jenuth, J. P., Peterson, A. C. & Shoubridge, E. A. Tissue-specific selection for different mtDNA genotypes in heteroplasmic mice. *Nat. Genet.* 16, 93–5 (1997).
157. Battersby, B. J. & Shoubridge, E. A. Selection of a mtDNA sequence variant in hepatocytes of heteroplasmic mice is not due to differences in respiratory chain function or efficiency of replication. *Hum. Mol. Genet.* 10, 2469–2479 (2001).
158. Jokinen, R. *et al.* Gimap3 regulates tissue-specific mitochondrial DNA segregation. *PLoS Genet.* 6, e1001161 (2010).
159. Strauss, K. A. *et al.* Severity of cardiomyopathy associated with adenine nucleotide translocator-1 deficiency correlates with mtDNA haplogroup. *Proc. Natl. Acad. Sci.* 110, 3453–3458 (2013).
160. Jokinen, R., Marttinen, P., Stewart, J. B., Neil Dear, T. & Battersby, B. J. Tissue-specific modulation of mitochondrial DNA segregation by a defect in mitochondrial division. *Hum. Mol. Genet.* 25, 706–714 (2016).
161. Jokinen, R. *et al.* Quantitative Changes in Gimap3 and Gimap5 Expression Modify Mitochondrial DNA Segregation in Mice. *Genetics* 200, 221–235 (2015).
162. Acton, B. M., Lai, I., Shang, X., Jurisicova, A. & Casper, R. F. Neutral mitochondrial heteroplasmy alters physiological function in mice. *Biol. Reprod.* 77, 569–576 (2007).
163. Sharpley, M. S. *et al.* Heteroplasmy of mouse mtDNA is genetically unstable and results in altered behavior and cognition. *Cell* 151, 333–343 (2012).
164. Lane, N. The Problem with Mixing Mitochondria. *Cell* 151, 246–248 (2012).
165. Jenuth, J. P., Peterson, A. C. & Shoubridge, E. A. Tissue-specific selection for different mtDNA genotypes in heteroplasmic mice. *Nat. Genet.* 16, 93–95 (1997).
166. van den Ouweland, J. M. *et al.* Mutation in mitochondrial tRNA(Leu)(UUR) gene in a large pedigree with maternally transmitted type II diabetes mellitus and deafness. *Nat. Genet.* 1, 368–71 (1992).
167. Lerman-Sagie, T. *et al.* Dramatic improvement in mitochondrial cardiomyopathy following treatment with idebenone. *J. Inherit. Metab. Dis.* 24, 28–34 (2001).
168. Hernández-Camacho, J. D., Bernier, M., López-Lluch, G. & Navas, P. Coenzyme Q10 Supplementation in Aging and Disease. *Front. Physiol.* 9, 44 (2018).
169. Gammage, P. A., Rorbach, J., Vincent, A. I., Rebar, E. J. & Minczuk, M. Mitochondrially targeted ZFNs for selective degradation of pathogenic mitochondrial genomes bearing large-scale deletions or point mutations. *EMBO Mol Med* 6, 458–466 (2014).
170. Hashimoto, M. *et al.* MitoTALEN: A General Approach to Reduce Mutant mtDNA Loads and Restore Oxidative Phosphorylation Function in Mitochondrial Diseases. *Mol. Ther.* 23, 1592–9 (2015).
171. Bacman, S. R., Williams, S. L., Pinto, M., Peralta, S. & Moraes, C. T. Specific elimination of mutant mitochondrial genomes in patient-derived cells by mitoTALENs. *Nat. Med.* 19, 1111–3 (2013).
172. Lee, H.-S. *et al.* Rapid mitochondrial DNA segregation in primate preimplantation embryos precedes

somatic and germline bottleneck. *Cell Rep.* 1, 506–15 (2012).
173. Craven, L. *et al.* Pronuclear transfer in human embryos to prevent transmission of mitochondrial DNA disease. *Nature* 465, 82–85 (2010).
174. Wolf, D. P., Mitalipov, N. & Mitalipov, S. Mitochondrial replacement therapy in reproductive medicine. *Trends Mol. Med.* 21, 68–76 (2015).
175. Latorre-Pellicer, A. Sistema OXPHOS: Integración funcional de dos genomas. (Universidad Autónoma de Madrid, 2014).
176. McGrath, J. & Solter, D. Nuclear transplantation in the mouse embryo by microsurgery and cell fusion. *Science* 220, 1300–2 (1983).
177. Laipis, P. J. Construction of heteroplasmic mice containing two mitochondrial DNA genotypes by micromanipulation of single-cell embryos. *Methods Enzymol.* 264, 345–57 (1996).
178. Jenuth, J. P., Peterson, A. C., Fu, K. & Shoubridge, E. A. Random genetic drift in the female germline explains the rapid segregation of mammalian mitochondrial DNA. *Nat. Genet.* 14, 146–51 (1996).
179. Meirelles, F. V & Smith, L. C. Mitochondrial genotype segregation in a mouse heteroplasmic lineage produced by embryonic karyoplast transplantation. *Genetics* 145, 445–51 (1997).
180. Nagy, A. *Manipulating the mouse embryo : a laboratory manual*. (Cold Spring Harbor Laboratory Press, 2003).
181. Lawitts, J. A. & Biggers, J. D. Culture of preimplantation embryos. *Methods Enzymol.* 225, 153–64 (1993).
182. MGI-Rules and Guidelines for Nomenclature of Mouse and Rat Strains. <http://www.informatics.jax.org/mgihome/nomen/2007_strains.shtml#mice>
183. Schindelin, J., Rueden, C. T., Hiner, M. C. & Eliceiri, K. W. The ImageJ ecosystem: An open platform for biomedical image analysis. *Mol. Reprod. Dev.* 82, 518–29 (2015).
184. Schindelin, J. *et al.* Fiji: an open-source platform for biological-image analysis. *Nat. Methods* 9, 676–682 (2012).
185. Treuting, P. M. & Dintzis, S. M. *Comparative anatomy and histology : a mouse and human atlas*. (Academic, 2012). <https://www.sciencedirect.com/science/book/9780123813619>
186. Lopez-Fabuel, I. *et al.* Complex I assembly into supercomplexes determines differential mitochondrial ROS production in neurons and astrocytes. *Proc. Natl. Acad. Sci. U. S. A.* 113, 13063–13068 (2016).
187. Cochemé, H. M. *et al.* Using the mitochondria-targeted ratiometric mass spectrometry probe MitoB to measure H2O2 in living Drosophila. *Nat. Protoc.* 7, 946–958 (2012).
188. Logan, A. *et al.* Using exomarkers to assess mitochondrial reactive species in vivo. *Biochim. Biophys. Acta - Gen. Subj.* 1840, 923–930 (2014).
189. Robinson, M. D., McCarthy, D. J. & Smyth, G. K. edgeR: a Bioconductor package for differential expression analysis of digital gene expression data. *Bioinformatics* 26, 139–40 (2010).
190. Subramanian, A. *et al.* Gene set enrichment analysis: a knowledge-based approach for interpreting genome-wide expression profiles. *Proc. Natl. Acad. Sci. U. S. A.* 102, 15545–50 (2005).
191. Leek, J. T., Johnson, W. E., Parker, H. S., Jaffe, A. E. & Storey, J. D. The sva package for removing batch effects and other unwanted variation in high-throughput experiments. *Bioinformatics* 28, 882–3 (2012).
192. Martínez-Bartolomé, S. *et al.* Properties of average score distributions of SEQUEST: the probability ratio method. *Mol. Cell. Proteomics* 7, 1135–45 (2008).
193. Navarro, P. *et al.* General statistical framework for quantitative proteomics by stable isotope labeling. *J. Proteome Res.* 13, 1234–47 (2014).
194. García-Marqués, F. *et al.* A Novel Systems-Biology Algorithm for the Analysis of Coordinated Protein Responses Using Quantitative Proteomics. *Mol. Cell. Proteomics* 15, 1740–60 (2016).
195. Navarro, P. *et al.* General statistical framework for quantitative proteomics by stable isotope labeling. *J. Proteome Res.* 13, 1234–47 (2014).
196. Xia, J. & Wishart, D. S. Using MetaboAnalyst 3.0 for Comprehensive Metabolomics Data Analysis. *Curr. Protoc. Bioinforma.* 55, 14.10.1-14.10.91 (2016).
197. Bagwan, N. *et al.* Comprehensive quantification of the modified proteome reveals oxidative heart damage in mitochondrial heteroplasmy. *Cell Rep.* In press, (2018).
198. Wiśniewski, J. R., Ostasiewicz, P. & Mann, M. High recovery FASP applied to the proteomic analysis of microdissected formalin fixed paraffin embedded cancer tissues retrieves known colon cancer markers. *J. Proteome Res.* 10, 3040–9 (2011).
199. Bonzon-Kulichenko, E., Garcia-Marques, F., Trevisan-Herraz, M. & Vázquez, J. Revisiting Peptide Identification by High-Accuracy Mass Spectrometry: Problems Associated with the Use of Narrow Mass Precursor Windows. *J. Proteome Res.* 14, 700–710 (2015).
200. Subramanian, A. *et al.* Gene set enrichment analysis: a knowledge-based approach for interpreting genome-wide expression profiles. *Proc. Natl. Acad. Sci. U. S. A.* 102, 15545–50 (2005).

201. Teichholz, L. E., Kreulen, T., Herman, M. V & Gorlin, R. Problems in echocardiographic volume determinations: echocardiographic-angiographic correlations in the presence of absence of asynergy. *Am. J. Cardiol.* 37, 7–11 (1976).
202. Navarro, S. J. *et al.* The C57BL/6J Mouse Strain Background Modifies the Effect of a Mutation in Bcl2l2. *G3 (Bethesda).* 2, 99–102 (2012).
203. Fernández-Vizarra, E. Isolation of biogenetically competent mitochondria from mammalian tissues and cultured cells. *Methods* 26, 292–297 (2002).
204. Vives-Bauza, C., Yang, L. & Manfredi, G. en *Methods in cell biology* 80, 155–171 (2007).
205. Birch-Machin, M. A. & Turnbull, D. M. Assaying mitochondrial respiratory complex activity in mitochondria isolated from human cells and tissues. *Methods Cell Biol.* 65, 97–117 (2001).
206. Bradford, M. M. A rapid and sensitive method for the quantitation of microgram quantities of protein utilizing the principle of protein-dye binding. *Anal. Biochem.* 72, 248–254 (1976).
207. Larsson, C., Grundberg, I., Söderberg, O. & Nilsson, M. In situ detection and genotyping of individual mRNA molecules. *Nat. Methods* 7, 395–397 (2010).
208. Johnston, I. G. & Jones, N. S. Evolution of Cell-to-Cell Variability in Stochastic, Controlled, Heteroplasmic mtDNA Populations. *Am. J. Hum. Genet.* 99, 1150–1162 (2016).
209. Mancuso, M., Filosto, M., Orsucci, D. & Siciliano, G. Mitochondrial DNA sequence variation and neurodegeneration. *Hum. Genomics* 3, 71–8 (2008).
210. Woodson, J. D. & Chory, J. Coordination of gene expression between organellar and nuclear genomes. *Nat. Rev. Genet.* 9, 383–395 (2008).
211. Reinhardt, K., Dowling, D. K. & Morrow, E. H. Mitochondrial Replacement, Evolution, and the Clinic. *Science (80-.).* 341, 1345–1346 (2013).
212. Chinnery, P. F. *et al.* The Challenges of Mitochondrial Replacement. *PLoS Genet.* 10, e1004315 (2014).
213. Eyre-Walker, A. Mitochondrial Replacement Therapy: Are Mito-nuclear Interactions Likely To Be a Problem? *Genetics* 205, 1365–1372 (2017).
214. Walther, T. C. & Farese, R. V. Lipid Droplets and Cellular Lipid Metabolism. *Annu. Rev. Biochem.* 81, 687–714 (2012).
215. Varela-López, A., Quiles, J. L., Cordero, M., Giampieri, F. & Bullón, P. Oxidative Stress and Dietary Fat Type in Relation to Periodontal Disease. *Antioxidants (Basel, Switzerland)* 4, 322–44 (2015).
216. Kuna, A. & Achinna, P. Mono unsaturated fatty acids for CVD and diabetes: A healthy choice. *Int. J. Nutr. Pharmacol. Neurol. Dis.* 3, 236 (2013).
217. Reily, C. *et al.* Mitochondrially targeted compounds and their impact on cellular bioenergetics. *Redox Biol.* 1, 86–93 (2013).
218. Quirós, P. M., Langer, T. & López-Otín, C. New roles for mitochondrial proteases in health, ageing and disease. *Nat. Rev. Mol. Cell Biol.* 16, 345–359 (2015).
219. Pelosi, E. *et al.* Constitutively active Foxo3 in oocytes preserves ovarian reserve in mice. *Nat. Commun.* 4, 1843 (2013).
220. Chu, Y.-L., Xu, Y.-R., Yang, W.-X. & Sun, Y. The role of FSH and TGF-β superfamily in follicle atresia. *Aging (Albany. NY).* 10, 305–321 (2018).
221. Rossi, D. J., Bryder, D. & Weissman, I. L. Hematopoietic stem cell aging: mechanism and consequence. *Exp. Gerontol.* 42, 385–90 (2007).
222. Challen, G. A., Boles, N., Lin, K.-Y. K. & Goodell, M. A. Mouse hematopoietic stem cell identification and analysis. *Cytom. Part A* 75A, 14–24 (2009).
223. Ristow, M. & Schmeisser, K. Mitohormesis: Promoting health and lifespan by increased levels of reactive oxygen species (ROS). *Dose-Response* 12, 288–341 (2014).
224. Yun, J. & Finkel, T. Mitohormesis. *Cell Metab.* 19, 757–66 (2014).
225. Srivastava, S. The Mitochondrial Basis of Aging and Age-Related Disorders. *Genes (Basel).* 8, (2017).
226. Johnston, I. G. *et al.* Stochastic modelling, Bayesian inference, and new in vivo measurements elucidate the debated mtDNA bottleneck mechanism. *Elife* 4, e07464 (2015).
227. Taylor, K. D. & Pikó, L. Mitochondrial biogenesis in early mouse embryos: expression of the mRNAs for subunits IV, Vb, and VIIc of cytochrome c oxidase and subunit 9 (P1) of H(+)-ATP synthase. *Mol. Reprod. Dev.* 40, 29–35 (1995).
228. Hämäläinen, R. H. *et al.* mtDNA Mutagenesis Disrupts Pluripotent Stem Cell Function by Altering Redox Signaling. *Cell Rep.* 11, 1614–24 (2015).
229. Takeda, K., Takahashi, S., Onishi, A., Hanada, H. & Imai, H. Replicative advantage and tissue-specific segregation of RR mitochondrial DNA between C57BL/6 and RR heteroplasmic mice. *Genetics* 155, 777–83 (2000).
230. Wai, T., Teoli, D. & Shoubridge, E. A. The mitochondrial DNA genetic bottleneck results from replication of a subpopulation of genomes. *Nat. Genet.* 40, 1484–1488 (2008).
231. Dunning, K. R. *et al.* Beta-Oxidation Is Essential for Mouse Oocyte Developmental Competence and

Early Embryo Development1. *Biol. Reprod.* 83, 909–918 (2010).
232. Benveniste, H. *et al.* Maternal-fetal in vivo imaging: a combined PET and MRI study. *J. Nucl. Med.* 44, 1522–30 (2003).
233. Zanotti-Fregonara, P. *et al.* Absorbed 18F-FDG dose to the fetus during early pregnancy. *J. Nucl. Med.* 51, 803–5 (2010).
234. Leung, K. *6-Deoxy-6-[18F]fluoro-D-fructose*. *Molecular Imaging and Contrast Agent Database (MICAD)* (2004). en <http://www.ncbi.nlm.nih.gov/pubmed/22049574>
235. Lopci, E. *et al.* PET radiopharmaceuticals for imaging of tumor hypoxia: a review of the evidence. *Am. J. Nucl. Med. Mol. Imaging* 4, 365–84 (2014).
236. Cuezva, J. M. *et al.* The bioenergetic signature of lung adenocarcinomas is a molecular marker of cancer diagnosis and prognosis. *Carcinogenesis* 25, 1157–63 (2004).
237. Bayona-Bafaluy, M. P., Blits, B., Battersby, B. J., Shoubridge, E. a & Moraes, C. T. Rapid directional shift of mitochondrial DNA heteroplasmy in animal tissues by a mitochondrially targeted restriction endonuclease. *Proc. Natl. Acad. Sci. U. S. A.* 102, 14392–14397 (2005).
238. Fernández, I., Peña, A., Del Teso, N., Pérez, V. & Rodríguez-Cuesta, J. Clinical biochemistry parameters in C57BL/6J mice after blood collection from the submandibular vein and retroorbital plexus. *J. Am. Assoc. Lab. Anim. Sci.* 49, 202–206 (2010).
239. Musch, W., Verfaillie, L. & Decaux, G. Age-Related Increase in Plasma Urea Level and Decrease in Fractional Urea Excretion: Clinical Application in the Syndrome of Inappropriate Secretion of Antidiuretic Hormone. *Clin. J. Am. Soc. Nephrol.* 1, 909–914 (2006).
240. Viani, A., Rizzo, G., Carrai, M. & Pacifici, G. M. The effect of ageing on plasma albumin and plasma protein binding of diazepam, salicylic acid and digitoxin in healthy subjects and patients with renal impairment. *Br. J. Clin. Pharmacol.* 33, 299–304 (1992).
241. Tang, Y., Fung, E., Xu, A. & Lan, H.-Y. C-reactive protein and ageing. *Clin. Exp. Pharmacol. Physiol.* 44, 9–14 (2017).
242. Alavi, M. V & Fuhrmann, N. Dominant optic atrophy, OPA1, and mitochondrial quality control: understanding mitochondrial network dynamics. *Mol. Neurodegener.* 8, 32 (2013).
243. MacVicar, T. D. B. & Lane, J. D. Impaired OMA1-dependent cleavage of OPA1 and reduced DRP1 fission activity combine to prevent mitophagy in cells that are dependent on oxidative phosphorylation. *J. Cell Sci.* 127, 2313–25 (2014).
244. Tanaka, A. *et al.* Proteasome and p97 mediate mitophagy and degradation of mitofusins induced by Parkin. *J. Cell Biol.* 191, 1367–1380 (2010).
245. Lin, Y.-F. *et al.* Maintenance and propagation of a deleterious mitochondrial genome by the mitochondrial unfolded protein response. *Nature* 533, 416–419 (2016).
246. Suomalainen, A. & Battersby, B. J. Mitochondrial diseases: the contribution of organelle stress responses to pathology. *Nat. Rev. Mol. Cell Biol.* (2017). doi:10.1038/nrm.2017.66
247. Spindler, M. *et al.* Mitochondrial creatine kinase is critically necessary for normal myocardial high-energy phosphate metabolism. *Am. J. Physiol. Circ. Physiol.* 283, H680–H687 (2002).
248. Piao, L., Marsboom, G., Archer, S. L. & Professor, H. J. Mitochondrial metabolic adaptation in right ventricular hypertrophy and failure. doi:10.1007/s00109-010-0679-1
249. Cristina Kenney, M. *et al.* Molecular and Bioenergetic Differences between Cells with African versus European Inherited Mitochondrial DNA Haplogroups: Implications for Population Susceptibility to Diseases. *Biochim Biophys Acta* 1842, 208–219 (2014).
250. Zheng, S. *et al.* Role of mtDNA haplogroups in COPD susceptibility in a southwestern Han Chinese population. *Free Radic. Biol. Med.* 53, 473–481 (2012).
251. Baertling, F. *et al.* Mutation in mitochondrial complex IV subunit COX5A causes pulmonary arterial hypertension, lactic acidemia, and failure to thrive. *Hum. Mutat.* 38, 692–703 (2017).
252. Andreeva, A. V., Kutuzov, M. A. & Voyno-Yasenetskaya, T. A. Regulation of surfactant secretion in alveolar type II cells. *Am. J. Physiol. Cell. Mol. Physiol.* 293, L259–L271 (2007).
253. Sano, H. & KUROKI, Y. The lung collectins, SP-A and SP-D, modulate pulmonary innate immunity. *Mol. Immunol.* 42, 279–287 (2005).
254. Schagat, T. L., Wofford, J. A. & Wright, J. R. Neutrophils Macrophage Phagocytosis of Apoptotic Surfactant Protein A Enhances Alveolar Surfactant Protein A Enhances Alveolar Macrophage Phagocytosis of Apoptotic Neutrophils. *J Immunol J. Immunol. by guest January* 166, 2727–2733 (2001).
255. Palaniyar, N., Nadesalingam, J. & Reid, K. B. M. Innate immune collectins bind nucleic acids and enhance DNA clearance in vitro. *Ann. N. Y. Acad. Sci.* 1010, 467–70 (2003).
256. Palaniyar, N., Clark, H., Nadesalingam, J., Hawgood, S. & Reid, K. B. M. Surfactant protein D binds genomic DNA and apoptotic cells, and enhances their clearance, in vivo. *Ann. N. Y. Acad. Sci.* 1010, 471–5 (2003).

257. D'Acquisto, F. *et al.* Impaired T cell activation and increased Th2 lineage commitment in Annexin-1-deficient T cells. *Eur. J. Immunol.* 37, 3131–42 (2007).
258. Byers, D. E. & Holtzman, M. J. Alternatively activated macrophages and airway disease. *Chest* 140, 768–774 (2011).
259. Van Houten, B., Hunter, S. E. & Meyer, J. N. Mitochondrial DNA damage induced autophagy, cell death, and disease. *Front. Biosci. (Landmark Ed.* 21, 42–54 (2016).
260. Wesselborg, S. & Stork, B. Autophagy signal transduction by ATG proteins: from hierarchies to networks. *Cell. Mol. Life Sci.* 72, 4721–57 (2015).
261. Norman, J. M., Cohen, G. M. & Bampton, E. T. W. The in vitro cleavage of the hAtg proteins by cell death proteases. *Autophagy* 6, 1042–56 (2010).
262. Crosswhite, P. & Sun, Z. Nitric Oxide, Oxidative Stress and Inflammation in Pulmonary Arterial Hypertension. doi:10.1097/HJH.0b013e328332bcdb
263. Braidy, N. *et al.* Age related changes in NAD+ metabolism oxidative stress and Sirt1 activity in wistar rats. *PLoS One* 6, e19194 (2011).
264. Sutendra, G. & Michelakis, E. D. The Metabolic Basis of Pulmonary Arterial Hypertension. *Cell Metab.* 19, 558–573 (2014).
265. Tonelli, A. R., Zein, J. & Ioannidis, J. P. A. Geometry of the randomized evidence for treatments of pulmonary hypertension. *Cardiovasc. Ther.* 31, e138-46 (2013).
266. Kuehne, T. *et al.* Magnetic resonance imaging analysis of right ventricular pressure-volume loops: in vivo validation and clinical application in patients with pulmonary hypertension. *Circulation* 110, 2010–6 (2004).
267. Lai, Y.-C., Potoka, K. C., Champion, H. C., Mora, A. L. & Gladwin, M. T. Pulmonary Arterial Hypertension: The Clinical Syndrome. *Circ. Res.* 115, 115–130 (2014).
268. García-Álvarez, A. *et al.* Noninvasive Monitoring of Serial Changes in Pulmonary Vascular Resistance and Acute Vasodilator Testing Using Cardiac Magnetic Resonance. *J. Am. Coll. Cardiol.* 62, 1621–1631 (2013).
269. Harvey, L. D. & Chan, S. Y. Emerging Metabolic Therapies in Pulmonary Arterial Hypertension. *J. Clin. Med.* 6, (2017).
270. Payne, B. A. I. *et al.* Universal heteroplasmy of human mitochondrial DNA. doi:10.1093/hmg/dds435
271. Mitochondrial Enzyme Defi ciencies in Inherited Neoplasia. <https://www.ncbi.nlm.nih.gov/pmc/articles/PMC1297557/pdf/pmed.0020401.pdf>
272. Islam, M. N. *et al.* Mitochondrial transfer from bone marrow-derived stromal cells to pulmonary alveoli protects against acute lung injury. doi:10.1038/nm.2736
273. Molnar, M. J. Mitochondrial diseases. *Handb. Clin. Neurol.* 145, 147–155 (2017).
274. United Mitochondrial Disease Foundation. What is Mitochondrial Disease? – UMDF. <https://www.umdf.org/what-is-mitochondrial-disease/>
275. Ouyang, H. *et al.* Ocular Stem Cell Research from Basic Science to Clinical Application: A Report from Zhongshan Ophthalmic Center Ocular Stem Cell Symposium. *Int. J. Mol. Sci.* 17, 415 (2016).
276. Alamouti, B. & Funk, J. Retinal thickness decreases with age: an OCT study. *Br. J. Ophthalmol.* 87, 899–901 (2003).
277. Celebi, A. R. C. & Mirza, G. E. Age-Related Change in Retinal Nerve Fiber Layer Thickness Measured With Spectral Domain Optical Coherence Tomography. *Investig. Opthalmology Vis. Sci.* 54, 8095 (2013).
278. Gao, H. & Hollyfield, J. G. Aging of the human retina. Differential loss of neurons and retinal pigment epithelial cells. *Invest. Ophthalmol. Vis. Sci.* 33, 1–17 (1992).
279. Tuft, S. J., Williams, K. A. & Coster, D. J. Endothelial repair in the rat cornea. *Invest. Ophthalmol. Vis. Sci.* 27, 1199–204 (1986).
280. Tan, D. T., Dart, J. K., Holland, E. J. & Kinoshita, S. Corneal transplantation. *Lancet* 379, 1749–1761 (2012).
281. Chen, J. *et al.* Descemet's Membrane Supports Corneal Endothelial Cell Regeneration in Rabbits. *Sci. Rep.* 7, 6983 (2017).
282. Tachibana, M. *et al.* Mitochondrial gene replacement in primate offspring and embryonic stem cells. *Nature* 461, 367–372 (2009).
283. Woods, D. & Tilly, J. Autologous Germline Mitochondrial Energy Transfer (AUGMENT) in Human Assisted Reproduction. *Semin. Reprod. Med.* 33, 410–421 (2015).
284. Sondheimer, N. *et al.* Neutral mitochondrial heteroplasmy and the influence of aging. *Hum. Mol. Genet.* 20, 1653–1659 (2011).
285. Jokinen, R. *et al.* Quantitative Changes in Gimap3 and Gimap5 Expression Modify Mitochondrial DNA Segregation in Mice. en <https://www.ncbi.nlm.nih.gov/pmc/articles/PMC4423365/pdf/221.pdf>
286. Wu, Z. *et al.* Mechanisms Controlling Mitochondrial Biogenesis and Respiration through the

Thermogenic Coactivator PGC-1. *Cell* 98, 115–124 (1999).
287. Michelakis, E. D., Webster, L. & Mackey, J. R. Dichloroacetate (DCA) as a potential metabolic-targeting therapy for cancer. *Br. J. Cancer* 99, 989–94 (2008).
288. Stockwin, L. H. *et al.* Sodium dichloroacetate selectively targets cells with defects in the mitochondrial ETC. *Int. J. Cancer* 127, 2510–2519 (2010).
289. Ong, S.-B. & Gustafsson, A. B. New roles for mitochondria in cell death in the reperfused myocardium. *Cardiovasc. Res.* 94, 190–6 (2012).
290. Carelli, V. *et al.* Mitochondria: Biogenesis and mitophagy balance in segregation and clonal expansion of mitochondrial DNA mutations. *Int. J. Biochem. Cell Biol.* 63, 21–24 (2015).
291. Head, B., Griparic, L., Amiri, M., Gandre-Babbe, S. & Van Der Bliek, A. M. Inducible proteolytic inactivation of OPA1 mediated by the OMA1 protease in mammalian cells. *J. Cell Biol.* 187, 959–966 (2009).
292. Baker, M. J. *et al.* Stress-induced OMA1 activation and autocatalytic turnover regulate OPA1-dependent mitochondrial dynamics. *EMBO J.* 33, 578–93 (2014).
293. Acín-Pérez R., Lechuga-Vieco A.V., Muñoz M.M., Nieto-Arellano R., Torroja C., Sánchez-Cabo F., Jiménez C., González-Guerra A., Carrascoso I.; Benincá C., Moral-Quirós P., López-Otin C., Castellano J.M., Ruíz-Cabello J., Jiménez-Borreguero L.J., E. J. . Ablation of the stress protease OMA1 protects against heart failure. *Sci. Transl. Med.* In press, (2018).
294. McBride, H. & Soubannier, V. Mitochondrial Function: OMA1 and OPA1, the Grandmasters of Mitochondrial Health. *Curr. Biol.* 20, R274–R276 (2010).
295. Korwitz, A. *et al.* Loss of OMA1 delays neurodegeneration by preventing stress-induced OPA1 processing in mitochondria. *J. Cell Biol.* 212, 157–66 (2016).
296. Moreno-Loshuertos, R. & Enríquez, J. A. Respiratory supercomplexes and the functional segmentation of the CoQ pool. *Free Radic. Biol. Med.* 100, 5–13 (2016).
297. Lapuente-Brun, E. *et al.* Supercomplex assembly determines electron flux in the mitochondrial electron transport chain. *Science (80-.).* 340, 1567–70 (2013).
298. Dröse, S., Brandt, U. & Wittig, I. Mitochondrial respiratory chain complexes as sources and targets of thiol-based redox-regulation. *Biochim. Biophys. Acta - Proteins Proteomics* 1844, 1344–1354 (2014).
299. Willems, P. H. G. M., Rossignol, R., Dieteren, C. E. J., Murphy, M. P. & Koopman, W. J. H. Cell Metabolism Perspective Redox Homeostasis and Mitochondrial Dynamics. (2015). doi:10.1016/j.cmet.2015.06.006
300. Mannella, C. A., Lederer, W. J. & Jafri, M. S. The connection between inner membrane topology and mitochondrial function. *J. Mol. Cell. Cardiol.* 62, 51–57 (2013).
301. Hirose, M. *et al.* Lifespan effects of mitochondrial mutations. *Nature* 540, E13–E14 (2016).
302. Quirós, P. M., Ramsay, A. J. & López-Otín, C. New roles for OMA1 metalloprotease. *Adipocyte* 2, 7–11 (2013).
303. The Jackson Laboratory. C57BL/6J Mouse strain datasheet.
304. High red blood cell count Causes - Mayo Clinic. en <https://www.mayoclinic.org/symptoms/high-red-blood-cell-count/basics/causes/sym-20050858>
305. Sarma, P. R. *Red Cell Indices*. *Clinical Methods: The History, Physical, and Laboratory Examinations* (Butterworths, 1990). <http://www.ncbi.nlm.nih.gov/pubmed/21250103>
306. Ferri, D. *et al.* Ultrastructural zonal heterogeneity of hepatocytes and mitochondria within the hepatic acinus during liver regeneration after partial hepatectomy. *Biol. Cell* 97, 277–288 (2005).
307. Coller, H. A. *et al.* High frequency of homoplasmic mitochondrial DNA mutations in human tumors can be explained without selection. *Nat. Genet.* 28, 147–150 (2001).
308. Yeung, K. Y. *et al.* The identification of mitochondrial DNA variants in glioblastoma multiforme. *Acta Neuropathol. Commun.* 2, 1 (2014).
309. Balmain, A. & Brown, K. Oncogene activation in chemical carcinogenesis. *Adv. Cancer Res.* 51, 147–82 (1988).
310. Barbacid, M. ras Genes. *Annu. Rev. Biochem.* 56, 779–827 (1987).
311. Nussinov, R., Tsai, C.-J. & Jang, H. Oncogenic Ras Isoforms Signaling Specificity at the Membrane. *Cancer Res.* 78, 593–602 (2018).
312. Efeyan, A. *et al.* Limited role of murine ATM in oncogene-induced senescence and p53-dependent tumor suppression. *PLoS One* 4, e5475 (2009).
313. Ron-Harel, N. *et al.* Mitochondrial Biogenesis and Proteome Remodeling Promote One-Carbon Metabolism for T Cell Activation. *Cell Metab.* 24, 104–17 (2016).
314. Gerriets, V. A. & Rathmell, J. C. Metabolic pathways in T cell fate and function. *Trends Immunol.* 33, 168–73 (2012).
315. Cao, Y., Rathmell, J. C. & Macintyre, A. N. Metabolic Reprogramming towards Aerobic Glycolysis Correlates with Greater Proliferative Ability and Resistance to Metabolic Inhibition in CD8 versus CD4

T Cells. *PLoS One* 9, e104104 (2014).
316. van der Windt, G. J. W. *et al.* Mitochondrial Respiratory Capacity Is a Critical Regulator of CD8+ T Cell Memory Development. *Immunity* 36, 68–78 (2012).
317. Campello, S. *et al.* Orchestration of lymphocyte chemotaxis by mitochondrial dynamics. *J. Exp. Med.* 203, 2879–86 (2006).
318. Quintana, A. *et al.* T cell activation requires mitochondrial translocation to the immunological synapse. *Proc. Natl. Acad. Sci.* 104, 14418–14423 (2007).
319. Magistretti, P. J. & Allaman, I. A cellular perspective on brain energy metabolism and functional imaging. *Neuron* 86, 883–901 (2015).
320. Bolaños, J. P. Bioenergetics and redox adaptations of astrocytes to neuronal activity. *J. Neurochem.* 139, 115–125 (2016).
321. Schitine, C., Nogaroli, L., Costa, M. R. & Hedin-Pereira, C. Astrocyte heterogeneity in the brain: from development to disease. *Front. Cell. Neurosci.* 9, 76 (2015).
322. Bélanger, M., Allaman, I. & Magistretti, P. J. Brain Energy Metabolism: Focus on Astrocyte-Neuron Metabolic Cooperation. *Cell Metab.* 14, 724–738 (2011).
323. Fernandez-Fernandez, S., Almeida, A. & Bolaños, J. P. Antioxidant and bioenergetic coupling between neurons and astrocytes. *Biochem. J.* 443, 3–11 (2012).
324. Freire-Regatillo, A., Argente-Arizón, P., Argente, J., García-Segura, L. M. & Chowen, J. A. Non-Neuronal Cells in the Hypothalamic Adaptation to Metabolic Signals. *Front. Endocrinol. (Lausanne).* 8, 51 (2017).
325. Lawson, L. J., Perry, V. H. & Gordon, S. Turnover of resident microglia in the normal adult mouse brain. *Neuroscience* 48, 405–15 (1992).
326. Roubertoux, P. L. *et al.* Mitochondrial DNA modifies cognition in interaction with the nuclear genome and age in mice. *Nat. Genet.* 35, 65–69 (2003).
327. Ludvigson, A. E., Luebke, J. I., Lewis, J. & Peters, A. Structural abnormalities in the cortex of the rTg4510 mouse model of tauopathy: a light and electron microscopy study. *Brain Struct. Funct.* 216, 31–42 (2011).
328. Bowley, M. P., Cabral, H., Rosene, D. L. & Peters, A. Age changes in myelinated nerve fibers of the cingulate bundle and corpus callosum in the rhesus monkey. *J. Comp. Neurol.* 518, 3046–64 (2010).
329. Jonas, P. & Lisman, J. Structure, function, and plasticity of hippocampal dentate gyrus microcircuits. *Front. Neural Circuits* 8, 107 (2014).
330. Zhang, G. *et al.* Hypothalamic programming of systemic ageing involving IKK-β, NF-κB and GnRH. *Nature* 497, 211–216 (2013).
331. Zhang, Y. *et al.* Hypothalamic stem cells control ageing speed partly through exosomal miRNAs. *Nature* 548, 52–57 (2017).
332. McCartney, C. R. & Marshall, J. C. en *Yen & Jaffe's Reproductive Endocrinology* 3–26.e8 (Elsevier, 2014). doi:10.1016/B978-1-4557-2758-2.00001-9.

